ISSN: 2153-1196 Vol. 7, No. 8, April 2016

Scientific Research Publishing

Journal of Modern Physics

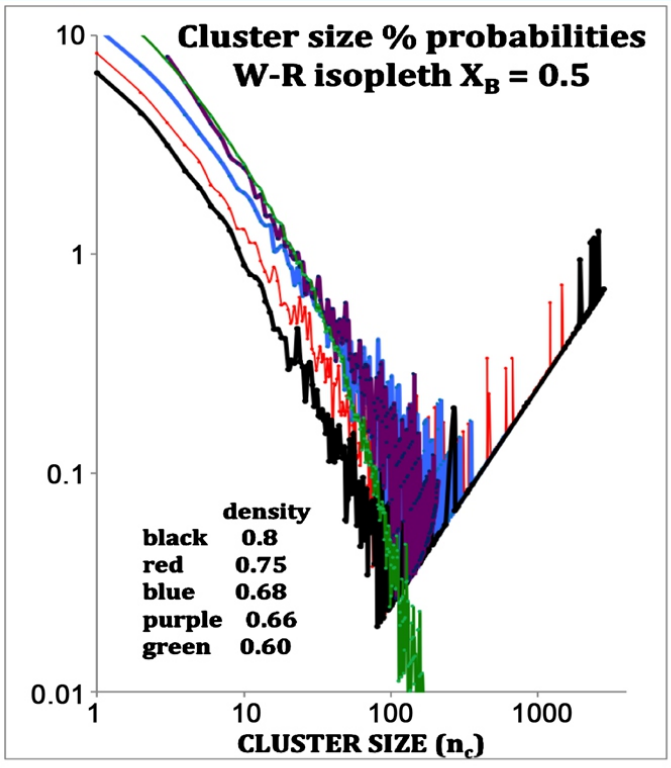

(a)

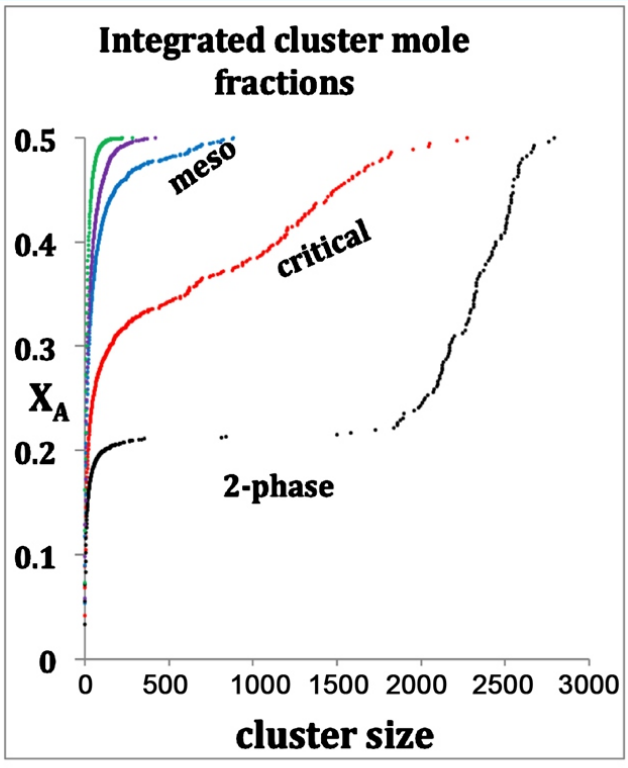

(b)

ISSN: 2153-1196

www.scirp.org/journal/jmp

Journal Editorial Board

ISSN: 2153-1196 (Print) ISSN: 2153-120X (Online)
http://www.scirp.org/journal/jmp

Journal of Modern Physics, 2016, 7, 729-862
Published Online April 2016 in SciRes. http://www.scirp.org/journal/jmp

Table of Contents

Volume 7 Number 8 April 2016

The figure on the front cover is from the article published in Journal of Modern Physics, 2016, Vol. 7, No. 8, pp. 760-773 by Leslie V. Woodcock.

Journal of Modern Physics (JMP)

Journal Information

SUBSCRIPTIONS

The *Journal of Modern Physics* (Online at Scientific Research Publishing, www.SciRP.org) is published monthly by Scientific Research Publishing, Inc., USA.

Subscription rates:

Print: $89 per issue.
To subscribe, please contact Journals Subscriptions Department, E-mail: sub@scirp.org

SERVICES

Advertisements
Advertisement Sales Department, E-mail: service@scirp.org

Reprints (minimum quantity 100 copies)
Reprints Co-ordinator, Scientific Research Publishing, Inc., USA.
E-mail: sub@scirp.org

COPYRIGHT

PRODUCTION INFORMATION

For manuscripts that have been accepted for publication, please contact:
E-mail: jmp@scirp.org

Journal of Modern Physics, 2016, 7, 729-736
Published Online April 2016 in SciRes. http://www.scirp.org/journal/jmp
http://dx.doi.org/10.4236/jmp.2016.78069

On a Quantum Gravity Fractal Spacetime Equation: QRG ≃ HD + FG and Its Application to Dark Energy—Accelerated Cosmic Expansion

Mohamed S. El Naschie

Department of Physics, University of Alexandria, Alexandria, Egypt
Email: Chaossf@aol.com

Received 18 April 2016; accepted 25 April 2016; published 28 April 2016

Abstract

The paper suggests that quantum relativistic gravity (QRG) is basically a higher dimensionality (HD) simulating relativity and non-classical effects plus a fractal Cantorian spacetime geometry (FG) simulating quantum mechanics. This more than just a conceptual equation is illustrated by integer approximation and an exact solution of the dark energy density behind cosmic expansion.

Keywords

Fractal Cantorian Spacetime, Quantum Relativity, Superstrings, Transfinite Set Theory, Extra Spacetime Dimensions, Quantum Physics, Dark Energy, Accelerated Cosmic Expansion, Cosmic Topology, Hyperbolic Geometry, E-Infinity Theory, Post Modernistic Physics

1. Introduction

Post modernistic research in theoretical physics [1]-[20] notably that connected to superstrings [21]-[25], loop quantum gravity [26] [27], fractal-Cantorian spacetime [28]-[30], M-theory [24] [30] [31] and a host of other theories [1] [2] [17]-[19] is most if not all pointing towards a rather firm fact that higher dimensionality and fractal geometry can be used to simulate relativity as well as quantum mechanics and possibly replace them, at least partially and at a minimum in basic situations where relativity and quantum mechanics are both relevant in equal measure [1]-[4] [32] [33]. Looking a little back in history, this is actually the achievement of visionaries and a few towering figures of science which are not credited sufficiently with pointing to what in our opinion is

How to cite this paper: El Naschie, M.S. (2016) On a Quantum Gravity Fractal Spacetime Equation: QRG ≃ HD + FG and Its Application to Dark Energy—Accelerated Cosmic Expansion. *Journal of Modern Physics*, **7**, 729-736.
http://dx.doi.org/10.4236/jmp.2016.78069

the superior direction of geometrizing and "topologizing" physics and cosmology in a most general way [1] [2] [15] such as F. Gauss [3], J. Bolya, N. Lobachevsky, H. Minkowski [3], J. von Neumann and A. Connes [34]. All apart from these pioneers, the recent contributions to the theory of fractal spacetime and the E-infinity theory of G. Ord, L. Nottale and the present author are almost exclusively going in the same direction constituting the subject of the paper at hand [4] [6] [8].

In the present work which is anticipating a sweeping new revolution in the way, we will be doing physics in 10 to 20 years, [1]-[54], we will illustrate the above by giving in a relatively short and concentrated form various, and on its face value, classical derivations of the fundamental major problem of the supposedly "missing" dark energy density of the cosmos amounting to 95.5 to 96 percent of the total theoretically expected value [33]-[36].

To keep the length of the present paper to a minimum we start from what we called in a recent paper [37] "The real Einstein" beauty $E = kmc^2$ where k is essentially related to the familiar Lorentzian factor γ with a twist. Thus in the present paper we introduce $k = \gamma$ as being the topological energy density factor of a generalization of Einstein's famous equation [1] [38] [39]

$$E = \gamma mc^2 \tag{1}$$

where E is the energy, m is the mass and c is the speed of light while $\gamma = 1$ is evidently related to the absolute maximal energy density possible $E = mc^2$ [40]. The deep meaning of the above as well as the controversial aspect connected to rest mass, real mass conversion to energy, difference and similarity to Newton kinetic energy $E(k) = (1/2)mv^2$ where v is the classical velocity of a particle as well as Einstein's leap to a fully fledged generalization of similar earlier discoveries of $E = mc^2$ by Poincare and others will not be discussed here in the depth it requires [35]-[39]. Instead to cover these fundamental aspects, the reader is advised to consult first the outstanding work of Prof. W. Rindler and Prof. L.B. Okun [40] [41] and second the earlier work of the present author and the references cited therein [35]-[39].

2. A More than Noteworthy Hidden Connection between Riemann's Powerful Curvature Tensor [42]-[44] and I. Dvoretzky's Magnificent Theorem Regarding Measure Concentration [45]-[48]

We are invoking here nothing connected directly to the theory of relativity or quantum mechanics and yet we will arrive to a result which can be understood deeply only via these two pillars of modern physics [1] [3] [4]. The main idea behind the following analysis of dark energy is the intuitive picture that extra dimensions are where things can be there but not directly seen nor in fact measured by us 3-dimensional beings and with time being only a parameter not given to us in a tangible, physical way let alone the fifth dimension of Kaluza and Klein nor Witten's eleven dimensional spacetime of his M-theory which is way above our non-mathematical intuitive grasp. Confining ourselves to n dimensional Riemannian tensor $R^{(n)}$ one could take the view with considerable justification, that $R^{(5)}$, *i.e.* five dimensions is about the limit of accessible physics in the experimental possibilities of a 3 + 1 dimensional conscious and well equipped observer. At the same time it is an educated guess that M-theory is real and $R^{(11)}$ is probably one of the best ways to describe not only theoretical high energy physics but the entire cosmos. To put this to a pragmatic test we calculate the vital independent components of the most important driving force in Einstein's relativity, namely the Riemann tensor. For n dimensions this number is given by [42]-[44] [54]

$$R^{(n)} = n^2\left(n^2 - 1\right)\Big/12 \tag{2}$$

Setting $n = 5$ and $n = 11$ one finds [54]

$$R^{(5)} = 50 \tag{3}$$

and

$$R^{(11)} = 2110 \tag{4}$$

respectively. Assuming that all these components have almost the same statistical weight, then the difference between 50 and 2110 measures clearly the sparseness of the associated space and consequently the totality of the average curvature. Similarly the ratio between 50 and 2110 is a measure of the density of the energy which is likened in the theory of relativity mainly to the curvature as it is in the case a simple elastic wire in the theory of

engineering elasticity. Viewing the complex problem in this quite simplistic way leads us directly to estimating $\gamma(O)$, *i.e.* the density of the probably accessible energy which we can normally measure directly and call it aptly and logically, ordinary energy as follows [42]-[44] [54]:

$$\gamma(O)=\frac{R^{(5)}}{R^{(11)}}=50/121\simeq 0.04\simeq 4\% \tag{5}$$

Consequently the rest of the energy filling not only $D = 5$ but also $D = 11$ must be given by the so called dark energy density which is given logically by [35]-[39]

$$\gamma(D)=1-\gamma(O)=1-0.04\simeq 0.958\simeq 96\% \tag{6}$$

For two important reasons the preceding rough result is truly striking. First it is quite close, in fact very close to highly accurate cosmic measurements and observations connected to the famous COBE, WMAP and Type 1a Supernova [33] [39] which was awarded the Nobel Prize in Physics or Cosmology in 2011. These measurements establish the existence of 4.5% ordinary energy density while the expected but missing 95.5% energy density was dubbed dark energy and concluded that it is behind the accelerated rather than previously believed deceleration of cosmic expansion [33] [39]. The second reason for the profundity of our simple estimation is connected to the magnificent theorem of the late, great Ukrainian born legendary mathematician and past President of the Wiseman Institute, I. Dvoretzky [45]-[48]. This theorem states that in a high dimensional manifold almost 96 percent of the volume is at the surface leaving only 4 percent in the bulk. The analogy and connection is obvious. Now we have solved this problem in numerous previous publications and came to a definite answer, namely that E of Einstein may be dissected into two quantum components $E(O)$ of the quantum particle and $E(D)$ of the quantum wave. Within an exact integer solution one finds that [35]-[39]

$$E=E(O)+E(D)=mc^2/22+mc^2(21/22) \tag{7}$$

That means $E(O)$ is not 4% but rather 4.5% while $E(D)$ is not 96% but 95.5% to a very high degree of accuracy and in astounding agreement with measurements [33] [30]. This leads us to the next section where we will attempt to improve our first estimation presented at the beginning of this section.

3. An Almost Exact Integer Solution of the Ordinary and Dark Energy Density Problem Based on the Number of Independent Riemannian Curvature

Our first estimate of $\gamma(O)$ clearly missed the fact that we needed to add $D = 5$ to $R^{(5)} = 50$ and analogously $D = 11$ to $R^{(11)} = 1210$. This is an obvious and trivial embedding problem because $R^{(5)}$ and $R^{(11)}$ are treated as quasi-dimensions estimating the size of our spacetime manifold. Consequently a more accuret $\gamma(O)$ must be [35]-[39] [45]-[48]

$$\gamma(O)=\frac{R^{(5)}+D^{(5)}}{R^{(11)}+D^{(11)}}=\frac{50+5}{1210+11}=\frac{55}{1221}\cong\frac{1}{22.2} \tag{8}$$

This is almost the familiar exact rational (1/22) value as document in my previous papers using different methods. Clearly $\gamma(D)$ is given by the self explanatory values

$$\gamma(D)=1-\gamma(O)\simeq 21.2/22.2 \tag{9}$$

almost exactly as expected.

4. The Exact Integer Value of Ordinary and Dark Energy Density

Although not trivial, it is not difficult to obtain the truly exact formulas of energy density $\gamma(O)=1/22$ and $\gamma(D)=21/22$ using the Riemannian tensor independent components method. The trick is to realize that we have to add not $D^{(5)} = 5$ to $R^{(5)}$ but the full space which embeds the SL(2, 7) Lie symmetry group of the holographic boundary of our universe, *i.e.* $D = 7$ and similarly the vacuum of Witten's $D = 11$ which is the corresponding pure gravity with $D=n(n-3)/2$. For $n = 8$ we have the famous $D = 20$ case but in the case of eleven dimensions we set $n = 11$ and find a 44 degrees of freedom vacuum. Consequently our exact $\gamma(O)$ must be

given by [35]-[39] [45]-[48].

$$\gamma(O)=\frac{R^{(5)}+D^{(7)}}{R^{(11)}+\text{vacuum}}=\frac{50+7}{1210+44} \tag{10}$$

In other words we have [35]-[38] [52]

$$\gamma(O)=\frac{57}{1254}=\frac{1}{22} \tag{11}$$

which is this time the truly exact integer value. For $\gamma(D)$ we have naturally also the exact integer value

$$\gamma(D)=21/22 \tag{12}$$

We may remark on passing that 57 is actually the intrinsic dimension of the fundamental $E(8)$ exceptional group [52] with its famous 248 isometries which gives E8E8 of D. Gross *et al*. heterotic superstring symmetry group, the famous $|E8E8| = (2)(248) = 496$ dimensions [50]-[52].

5. A Short Introduction to the Von Neumann-Connes Theory and Comparison with the Exact "Transfinite" Solution of Ordinary Dark Energy Density

Readers familiar with E-infinity Cantor spacetime theory [4] [8] know that the key to all exact results of this theory, including the ordinary and the dark energy density section of the cosmos, is the deceptively simple dimensional function due to the work of J. von Neumann in his unsung papers and book published posthumously "Continuous Geometry" as well as the work of the creator of noncommutative geometry, the great French pure and applied mathematician A. Connes [34]. This function as is well known is given by [34]

$$D_H = a+b\phi \tag{13}$$

where D_H is the Hausdorff dimension, $a,b\in Z$ and $\phi=\left(\sqrt{5}-1\right)/2$. In E-infinity we made our first move by identifying the zero set as being necessarily be the empty set which we equate physically and mathematically to the pre-quantum wave. Therefore the Hausdorff dimension of the empty set is given by $D(-1)$ and can be found together with all other sets recursively in a Fibonacci-like way as shown below where we start with the two trivial seeds, namely the zero set $D_H(O)=\phi$ and the unity set $D_H(1)=1+0=(1/\phi)^0=1.$ which are indicated in Equation (14) by two small arrows. Proceeding in this way we find [34] [39]

$$\begin{aligned}
&D(-2)=(0-1)+\phi-(-\phi)=\phi^3\\
&D(-1)=(1-0)+(0-\phi)=\phi^2\\
\rightarrow\ &D(0)=0+\phi=(1/\phi)^{-1}=\phi\\
\rightarrow\ &D(1)=1+0=(1/\phi)^0=1\\
&D(2)=1+\phi=(1/\phi)=1+\phi\\
&D(3)=2+\phi=(1/\phi)^2=2+\phi\\
&D(4)=3+2\phi=(1/\phi)^3=4+\phi^3
\end{aligned} \tag{14}$$

From the above we see that the pre-quantum particle is identified by the bi-dimension [47]

$$D_Q(\text{particle})\equiv(0,\phi) \tag{15}$$

while the pre-quantum wave is given by

$$D_Q(\text{wave})\equiv(-1,\phi^2) \tag{16}$$

From all these previous results, it is easily reasoned that the "topological" volume of the pre-particle in $5D$ is given by the obvious multiplication formula [39]

$$\begin{aligned}
&Vol(\text{wave})=(5)\phi^2\\
&\phi^5+5\phi^2=2
\end{aligned} \tag{17}$$

The corresponding additive volume of the pre-quantum wave on the other hand is given by

$$Vol(\text{wave}) = (5)\phi^2 \tag{18}$$

The total volume is thus equivalent to world sheet of string theory [21]-[25]

$$\phi^5 + 5\phi^2 = 2 \tag{19}$$

Inserting mean volume <vol(total)> = 2/2 = 1 in Einstein's formula $E = mc^2$ one finds [35]-[39]

$$E(\text{Einstein}) = \left[\frac{1}{2}(\phi^5) + \frac{1}{2}(5\phi^2)\right]mc^2 \tag{20}$$

That means [35]-[39] [48]-[52]

$$\begin{aligned} E(\text{Einstein}) &= E(O) + E(D) = (\phi^5/2)mc^2 + (5\phi^2/2)mc^2 \\ &= mc^2/22.18033989 + mc^2\frac{21.18033}{22.18033} = mc^2 \end{aligned} \tag{21}$$

This is the exact expression which leads to the integer solution by disregarding $k = 0.18033989$ compared to 21 and 22. We note that this k was interpreted physically as 'tHooft's renormalon hypothetical particle which is equal to $2\phi^5$ where ϕ^5 is hardy's famous quantum probability of two entangled quantum particles which is the exact solution of the corresponding Dirac's equations of the problem. In addition we must stress that ϕ^5 was verified experimentally and found to a very high degree of precision. Thus our theory is well founded theoretically and experimentally on all fundamental levels. The more interesting it must be that one can find the exact integer solution without direct reference to the theory of quantum relativity. In the next section we will look at the same problem using nothing more than our ordinary three dimensional space coupled to a rather familiar fractal curve [53].

6. Solving Dark Energy in a Classical Newtonian Three Space Dimensions

Although we have not invoked in all the preceding analysis any Lorentzian transformations or Einsteinian conception relating to the meaning of simultaneousity [40] nor of course a Schrödinger equations [1]-[9], we did make extensive use of higher dimensionality of spacetime as well as the basic final results of Einstein's special relativity marvel, namely $E = mc^2$. In the following solution all these things will be dispensed of so that the reader may see clearly the main message of the present paper that even a low dimensional fractal is essentially infinite quasi dimensional because of the involved infinite iteration and self similarity and that even a harmless conventional fractal curve in 3 dimensions like the familiar Menger sponge [53] could simulate quantum effects involved in the physics geometry and topology of ordinary and dark energy density of the cosmos [47]-[57]. Thus we draw in our following analysis on the classical three dimensional sponge named after the great Austria-American mathematician Karl Menger [53] who together with the outstanding young Russian mathematician P. Urysohn discovered the inductive dimensional theory which is one of our main tools in erecting E-infinity theory [28] [50]. The Hausdorff dimension in this case is [53]

$$D(\text{Menger sponge}) = \frac{\ell n 20}{\ell n 3} = 2.726833028 \tag{22}$$

This fractal, although it looks like a cubic sponge in 3D is essentially a curve, not a real 3D and possesses in our case the disadvantage of being continuous and could therefore be expected to deliver a good approximation only because continuity violates one of our main E-infinity theory principles, namely being the "pointless" point-set theory as emphasized in the pioneering work of von Neumann's continuous geometry where continuity is not referring to the geometry [34] [39] [47] but to the spectrum of the most important topological invariant of a manifold, namely the dimension. Thus one should not be misled by the word "continuity" with which von Neumann means fractal dimensionality spectrum but at the time, the word fractal was not invented yet by Mandelbrot nor were fractals part of the mathematical science culture [3] [46]. Since the Hausdorff dimension refers here not to the dark non-differentiable lines remaining from the Menger sponge iteration but to the space en-

cased between these 3 dimensional lines, we see that the ratio between D_H = 2.726833028 and D_T = 3 will give us the density of the involved empty set which represents dark energy. Consequently we may write

$$\gamma(D)=\frac{D_H}{D_T}=\frac{\ell n20/\ell n3}{3}=\frac{2.726833028}{3}=0.09089443426 \tag{23}$$

Consequently the ordinary energy density must be

$$\gamma(O)=1-\gamma(D)=1-0.9089443426=0.09105565738 \tag{24}$$

Now, and this is a crucial point, we do not insert $\gamma(O)$ in Einstein's formula $E=\gamma mc^2$ which we used all along because Einstein's formula belongs to D = 4 while the previous analysis is in D = 3. Here we remain truly classical and insert in $E=(1/2)mv^2$ of Newton and take the limit $v\to c$ to find

$$\begin{aligned} E(D)&=\left(\frac{1}{2}\right)(\gamma(O))(m)(v\to c)^2=\frac{0.09105565738}{2}mc^2 \\ &=(0.0455278288)mc^2\cong mc^2/21.964\simeq mc^2/22 \end{aligned} \tag{25}$$

For a basically almost entirely classical analysis this result reinforces our conjectured equation:

$$\text{Q R G}\simeq\text{H D}+\text{F G} \tag{26}$$

and together with the rest of the paper shows beyond reasonable doubt that there is far more than meets the eye to dimensionality of spacetime and fractal Cantorian geometry.

7. Discussion and Conclusion

There are many shortcut derivations and radically different solutions all converging directly or indirectly towards the main thesis of the present work, namely that of measure concentration of volume in a sufficiently high dimensional manifold with fractal-Cantorian features. Thus, we have all three fractal spacetime theories of 'tHooft-Veltman-Wilson dimensional regularization spacetime $D=4-k$ as well as Kaluza-Klein fractal space $D=4+\phi^3$ and Witten's fractal M-theory [55] with the remarkable dimensionality $D=11+\phi^5$ all leading to exactly the same result, namely [35]-[39]

$$\begin{aligned} E&=E(O)+E(D)=(\phi^5/2)mc^2+(5\phi^2/2)mc^2 \\ &=mc^2/(21+k)+mc^2(21+k/22+k) \end{aligned} \tag{27}$$

where $k=\phi^3(1-\phi^3)=2\phi^5=0.18033989$. The "integer" exact value is

$$E=mc^2/22+mc^2(21/22)=mc^2 \tag{28}$$

The analysis is in complete conformity with the result based on pure mathematical theorems such as Dvoretzky's theorem as well as accurate measurements and observations such as COBE, WMAP and Type 1a supernova which is awarded the 2011 Nobel Prize [35]-[39].

From all the above we conclude that higher dimensionality and fractality of spacetime are a reality of the small and large scale structure of spacetime and that our conceptual equation constituting the title of the present paper is far from being esoteric or mathematical abstraction with no tangible content. Hardy's quantum entanglement [35]-[39], the missing dark energy which we find and the observed accelerated cosmic expansion clearly says that our conceptual equation is real. From this fundamental conclusion to the realization that negative probability, phantoms and ghosts in strings and quantum fields are fairly exchangeable concepts lurking behind the empty set dark energy of the quantum wave is only one step [57].

References

[1] M. Tegmark: Our Mathematical Universe. Allen Lane, Penguin Books, London, 2014.

[2] J. Changeux and A. Connes: Conversation on Mind, Matter and Mathematics. Princeton University Press, Princeton, New Jersey, USA, 1989.

[3] R. Penrose: The Road to Reality. J. Cape, London, UK, 2004.

[4] J.-H. He, *et al.*: Transfinite Physics: A Collection of Publications on E-Infinity Cantorian Spacetime Theory. China

Science & Culture Publishing, 2005.

[5] J. Mageuijo: Faster than the Speed of Light. Heinemann, London, UK, 2003.

[6] L. Nottale: Fractal Space-Time and Micro Physics. World Scientific, Singapore, 1993.

[7] S. Vrobel: Fractal Time. World Scientific, Singapore, 2011.

[8] P. Weibel, G. Ord and O. Rössler (Editors): Spacetime Physics and Fractality. Springer, Vienna-New York, 2005.

[9] L. Smolin: The Trouble with Physics. Allen Lane-Penguin, London, 2006.

[10] HRH The Prince of Wales, Tony Juniper and Ian Skelly: Harmony: A New Way of Looking at Our World. Harper Collins Publications, London, UK, 2010. (see in particular page 113).

[11] P. Woit: Not Even Wrong. Jonathan Cape, London, 2006.

[12] L.M. Wapner: The Pea and the Sun. A.K. Peters Ltd., Wellesley, MA, USA, 2005.

[13] H. Diebner, T. Druckrey and P. Weibel (Editors): Science of the Interface. GenistaVerlag, Tübingen, Germany, 2001.

[14] A. Connes, M. Heller, S. Majid, R. Penrose, J. Polkinghorne and A. Taylor: On Space and Time. Cambridge University Press, Cambridge, 2009.

[15] A. Connes, A. Lichnerowicz and M.P. Schutzeuberger: Triangle of Thoughts. American Mathematical Society, Rhode Island, USA, 2001.

[16] P. Cartier, B. Julia, P. Moussa and P. Vanhove (Editors): Frontiers in Number Theory, Physics and Geometry Vol. I. Springer, Berlin, 2006.

[17] L. Smolin: Three Roads to Quantum Gravity. Weindenfeld & Nicolson, London, UK, 2000.

[18] A.B. Balachandran, S. Kürkcüoglu and S. Vaidya: Lectures on Fuzzy and Fuzzy Susy Physics. World Scientific, Singapore, 2007.

[19] M.S. El Naschie, O.E. Rössler and I. Prigogine (Editors): Quantum Mechanics, Diffusion and Chaotic Fractals. Pergamon Press/Elsevier, Oxford, 1995, (see in particular pp. 191-205).

[20] S. Vongehr: Post Modern Physics Description of Relativity. 24 September 2012. www.science20.com/alpha-meme/postmodern-physics-description-Relativity-94362

[21] M. Green, J. Schwarz and E. Witten: Superstring Theory. Vol. II. Cambridge University Press, Cambridge, 1987.

[22] J. Polchinski: String Theory, Vol. II. Cambridge University Press, Cambridge, 1998.

[23] K. Becker, M. Becker and J.H. Schwarz: String Theory and M-Theory. Cambridge University Press, Cambridge, 2007.

[24] M. Kaku: Introduction to Superstrings and M-Theory. Springer, New York, USA, 1999.

[25] P. West: Introduction to Strings and Branes. Cambridge University Press, Cambridge, UK, 2012.

[26] R. Gambini and J. Pulling: Loop Quantum Gravity. Oxford University Press, Oxford, 2011.

[27] C. Rovelli: Quantum Gravity. Cambridge Press, Cambridge, 2004.

[28] M.S. El Naschie: A Review of E-Infinity Theory and the Mass Spectrum of High Energy Particle Physics. Chaos, Solitons & Fractals, 19(1), 2004, pp. 209-236.

[29] M.S. El Naschie: On the Uncertainty of Cantorian Geometry and the Two-Slit Experiment. Chaos, Solitons & Fractals, 19(3), 1998, pp. 517-529.

[30] M.S. El Naschie: On the Unification of Heterotic Strings, M Theory and E (∞) Theory. Chaos, Solitons & Fractals, 11(14), 2000, pp. 2397-2408.

[31] M. Duff (Editor): The World in Eleven Dimensions. IOP Publishing, Bristol, 1999.

[32] G.W. Gibbons and S.W. Hawking: Euclidean Quantum Gravity. World Scientific, Singapore, 1993.

[33] L. Amendola and S. Tsujikawa: Dark Energy: Theory and Observation. Cambridge University Press, Cambridge, UK, 2010.

[34] A. Connes: Noncommutative Geometry. Academic Press, San Diego, USA, 1994.

[35] M.S. El Naschie: From E = mc2 to E = mc2/22—A Short Account of the Most Famous Equation in Physics and Its Hidden Quantum Entangled Origin. Journal of Quantum Information Science, 4, 2014, pp. 284-291.

[36] A. Connes and M. Marcolli: Noncommutative Geometry, Quantum Fields and Motives. American Mathematical Society, Rhode Island, USA, 2008.

[37] A.J. Babchin and M.S. El Naschie: On the Real Einstein Beauty E = kmc^2. World Journal of Condensed Matter Physics, 6(1), 2016, pp. 1-6.

[38] M.S. El Naschie: Einstein-Rosen Bridge (ER), Einstein-Podolski-Rosen Experiment (EPR) and Zero Measure Rindler

KAM Cantorian Spacetime Geometry (ZMG) Are Conceptually Equivalent. Journal of Quantum Information Science, 6, 2016, pp. 1-9.

[39] L. Marek-Crnjac: On El Naschie's Fractal-Cantorian Space-Time and Dark Energy—A Tutorial Review. Natural Science, 7(13), 2015, pp. 581-598.

[40] W. Rindler: Relativity (Special, General and Cosmological). Oxford University Press, Oxford, 2006.

[41] L.B. Okun: Energy and Mass in Relativity Theory. World Scientific, Singapore, 2009.

[42] G.S. Hall: Symmetries and Curvature Structure in General Relativity. World Scientific, Singapore, 2004.

[43] J.L. Martin: General Relativity. Prentice Hall, London, 1995.

[44] S. Sternberg: Curvature in Mathematics and Physics. Dover Publications, New York, USA, 2012.

[45] M.S. El Naschie: Application of Dvoretzky's Theorem of Measure Concentration in Physics and Cosmology. Open Journal of Microphysics, 5, 2015, pp. 11-15.

[46] M.S. El Naschie: The Counterintuitive Increase of Information Due to Extra Spacetime Dimensions of a Black Hole and Dvoretzky's Theorem. Natural Science, 7(10), 2015, pp. 483-487.

[47] M.S. El Naschie: Mathematical Models and Methods in Dark Energy Theory: Dvoretzky's Theorem, Casimir Effect, Mobius Geometry. Problems of Nonlinear Analysis in Engineering Systems, 2(44), 2015, pp. 1-16. University of Kazan Press, Russia. (Published in Russian and English language versions).

[48] M.S. El Naschie: Banach Spacetime-Like Dvoretzky Volume Concentration as Cosmic Holographic Dark Energy. International Journal of High Energy Physics, 2(1), 2015, pp. 13-21.

[49] M.S. El Naschie: If Quantum Wave of the Universe then Quantum Particle of the Universe: A Resolution of the Dark Energy Question and the Black Hole Information Paradox. International Journal of Astronomy and Astrophysics, 5(4), 2015, pp. 249-260.

[50] M.S. El Naschie: The theory of Cantorian Spacetime and High Energy Particle Physics (An Informal Review). Chaos, Solitons & Fractals, 41(5), 2009, pp. 2635-2646.

[51] M.S. El Naschie: The Exceptional Lie Symmetry Groups Hierarchy and the Expected Number of Higgs Bosons. Chaos, Solitons & Fractals, 35(2), 2008, pp. 268-273.

[52] M.S. El Naschie: Exceptional Lie Groups Hierarchy and the Structure of the Micro Universe. International Journal of Nonlinear Sciences and Numerical Simulation, 8(3), 2007, pp. 445-450.

[53] M.S. El Naschie. A Fractal Menger Sponge Spacetime Proposal to Reconcile Measurements and Theoretical Predictions of Cosmic Dark Energy. International Journal of Modern Nonlinear Theory & Application, 2, 2013, pp. 107-121.

[54] M.S. El Naschie: Cosmic Dark Energy Density from Classical Mechanics and Seemingly Redundant Riemannian Finitely Many Tensor Components of Einstein's General Relativity. World Journal of Mechanics, 4(6), 2014, pp. 153-156.

[55] M.S. El Naschie: On a fractal version of Witten's M-Theory. Journal of Astronomy & Astrophysics, 6(2), 2016, pp. 135-144.

[56] M.S. El Naschie: From Witten's 462 Supercharges of 5-D Branes in Eleven Dimensions to the 95.5 Percent Cosmic Dark Energy Density behind the Accelerated Expansion of the Universe. Journal of Quantum Information Science, 6(2), 2016, pp. 57-61.

[57] M.S. El Naschie: Negative Norms in Quantized Strings as Dark Energy Density of the Cosmos. World Journal of Condensed Matter Physics, 6, 2016, pp. 63-67.

Journal of Modern Physics, 2016, 7, 737-759
Published Online April 2016 in SciRes. http://www.scirp.org/journal/jmp
http://dx.doi.org/10.4236/jmp.2016.78070

Spin Forms and Spin Interactions among Higgs Bosons, between Higgs Boson and Graviton

ShaoXu Ren

Institute of Physical Science and Engineering
Tongji University, 200092, Shanghai, China
Corresponding email: shaoxu-ren@hotmail.com

Received 16 March 2016; accepted 25 April 2016; published 29 April 2016

Abstract

This paper offers concrete spin matrix forms of $0\hbar$ spin zero particle, and shows the existent of the spin interactions among $0\hbar$ spin zero particles. It is obviously hoping to approach, on the most comprehensive level, to understand what really Higgs Boson is and what role-play Higgs Boson is acting in particle physics.

As a " particle " of gravitational force, the spin interaction between $0\hbar$ spin zero particle (Higgs Boson) and $2\hbar$ spin particle (Graviton) is given, which maybe a way that people would find Graviton in future.

Keywords

Higgs Boson ; Graviton; Vacuum Bubble Pair ; Spin Topological Space, STS ; Casimir operator; right-hand $0\hbar$ spin zero particle; left-hand $0\hbar$ spin zero particle

1. Introduction

Higgs particle is a fundamental particle predicted by the Standard Model, and confirmed by the Large Hadron Collider at CERN.[1] Higgs particle could explain why the photon has no mass while W and Z Bosons are very heavy in electron-weak theory, and endows Fermions such as electron, muon and tau particle and quarks with their masses. The intrinsic spin angular momentum of Higgs particle is $0\hbar$. In conventional quantum mechanics, the representation of spin zero particle is a zero-matrix of one dimensional space, this means, in fact, Higgs particle has no matrix representation for its spin property in the Standard Model. What a pity ! magical Higgs particle could create masses of the particles in universe, however, failing to write out its own non-trivial spin matrices. Zero is not nothing, zero spin is not non-twirling. From the pointview of **The Third Kind of Particles**, **TKP**, [2] the angular momentum property of spin zero particle *can be expressed by* infinite dimensional non-Hermitian matrices which related to **Vacuum Bubble Pair**, **VBP** ,

How to cite this paper: Ren, S.X. (2016) Spin Forms and Spin Interactions among Higgs Bosons, between Higgs Boson and Graviton. *Journal of Modern Physics*, **7**, 737-759. http://dx.doi.org/10.4236/jmp.2016.78070

these pairs could be excited into $0\hbar$ spin particle form phase transitions of **Vacuum Spin Particle**, **VSP**, whose Casimir Operator is $-\frac{1}{4}\hbar^2 I_0$, *less than zero*. [3] (Casimir Operator of Higgs particle is $0\hbar^2 I_0$, of Graviton is $6\hbar^2 I_0$)

In conventional quantum mechanics, each particle has its own spin space: one spin prticle, one spin space; two spin particles, two spin spaces; .....; *n* spin particles, *n* spin spaces. These spin spaces are independent each other, and expressed by $V = V_1 \otimes V_2 \otimes V_3 \otimes \ldots \otimes V_n$.

This paper gives advice: Since the spin angular momentum constituents of every elementary particle are composed of the common series of math elements that based on the raising operators $\pi_j^+ = \pi_{1;j,k}^+ + i\pi_{2;j,k}^-$ and lowering operators $\pi_k^- = \pi_{1;j,k}^+ - i\pi_{2;j,k}^-$, (which compose **VBP**, **TKP**), then *a new type* of spin space, the so-called **Spin Topological Space**, **STS** , [4] is established. All sorts of spin sparticles are attributed to this spin space, **STS**.

In traditional views, there are no any spin interactions among spin zero particles. However, by means of **STS** concept, on the contrary, it is shown there are the spin interactions. $0\hbar$ Spin zero particle not only possesses spin phenomena but also appears out right-circumrotation and left-circumrotation, such kind of properties may exist in Higgs Boson world of the Standard Model.

Same reason for, there should be spin particle interactions between Higgs Boson and graviton, and spin interactions among gravitons, detecting gravitational force, after the interference effect of gravitational wave is comfirmed. [5]

2. Higgs Boson's Spin angular Momentum matrices $\pi_1(l), \pi_2(l), \pi_3(l)$

The mathematical structure of $\pi_1(l), \pi_2(l), \pi_3(l)$ and $\pi_3^2(l)$, $\pi_1^2(l) + \pi_2^2(l)$ are given in matrix series (1), (2), (3) shown below.

They satisfy angular momentum commutation rules

$$\pi_i(l)\pi_j(l) - \pi_j(l)\pi_i(l) = i\pi_k(l) \qquad (0.1)$$

$$i, j, k = 1, 2, 3 \text{ are circulative}$$

Casimir Operator

$$\pi^2(l) = \pi_1^2(l) + \pi_2^2(l) + \pi_3^2(l) = 0I_0 = 0(0+1)I_0 \qquad (0.2)$$

Using raising operator, lowering operator

$$\pi^+(l) = \pi_1(l) + i\pi_2(l) \quad ; \quad \pi^-(l) = \pi_1(l) - i\pi_2(l) \qquad (0.3)$$

Then (0.1) turns to

$$\pi_3(l)\pi^+(l) - \pi^+(l)\pi_3(l) = +\pi^+(l) \qquad (0.4)$$

$$\pi_3(l)\pi^-(l) - \pi^-(l)\pi_3(l) = -\pi^-(l) \qquad (0.5)$$

$$\pi^+(l)\pi^-(l) - \pi^-(l)\pi^+(l) = 2\pi_3(l) \qquad (0.6)$$

What follows are the explicit spin matrix representations of three generations ($l = 1,2,3$) of $0\hbar$ Boson, (Higgs Boson).

$\pi_1(1) =$ $:\pi^{+,-}_{0,+1}(1):$ $\pi_2(1) =$

$$\frac{1}{2}\begin{bmatrix}
\cdot & \cdot & \cdot & \cdot & \cdot & \cdot & \cdot & \cdot & \cdot & \cdot & \cdot & \cdot & \cdot & \cdot \\
\cdot & 0 & 5 & & & & & & & & & & 0 & \cdot \\
\cdot & -6 & 0 & 4 & & & & & & & & & & \cdot \\
\cdot & & -5 & 0 & 3 & & & & & & & & & \cdot \\
\cdot & & & -4 & 0 & 2 & & & & & & & & \cdot \\
\cdot & & & & -3 & 0 & 1 & & & & & & & \cdot \\
\cdot & & & & & -2 & \underline{0} & \mathbf{0} & & & & & & \cdot \\
\cdot & & & & & & -1 & 0 & -1 & & & & & \cdot \\
\cdot & & & & & & & \mathbf{0} & 0 & -2 & & & & \cdot \\
\cdot & & & & & & & & 1 & 0 & -3 & & & \cdot \\
\cdot & & & & & & & & & 2 & 0 & -4 & & \cdot \\
\cdot & 0 & & & & & & & & & 3 & 0 & & \cdot \\
\cdot & \cdot & \cdot & \cdot & \cdot & \cdot & \cdot & \cdot & \cdot & \cdot & \cdot & \cdot & \cdot & \cdot
\end{bmatrix}, \frac{1}{2}\begin{bmatrix}
\cdot & \cdot & \cdot & \cdot & \cdot & \cdot & \cdot & \cdot & \cdot & \cdot & \cdot & \cdot & \cdot & \cdot \\
\cdot & 0 & -i5 & & & & & & & & & & 0 & \cdot \\
\cdot & -i6 & 0 & -i4 & & & & & & & & & & \cdot \\
\cdot & & -i5 & 0 & -i3 & & & & & & & & & \cdot \\
\cdot & & & -i4 & 0 & -i2 & & & & & & & & \cdot \\
\cdot & & & & -i3 & 0 & -i1 & & & & & & & \cdot \\
\cdot & & & & & -i2 & \underline{0} & \mathbf{0} & & & & & & \cdot \\
\cdot & & & & & & -i1 & 0 & i1 & & & & & \cdot \\
\cdot & & & & & & & \mathbf{0} & 0 & i2 & & & & \cdot \\
\cdot & & & & & & & & i1 & 0 & i3 & & & \cdot \\
\cdot & & & & & & & & & i2 & 0 & i4 & & \cdot \\
\cdot & 0 & & & & & & & & & i3 & 0 & & \cdot \\
\cdot & \cdot & \cdot & \cdot & \cdot & \cdot & \cdot & \cdot & \cdot & \cdot & \cdot & \cdot & \cdot & \cdot
\end{bmatrix}$$

(1.1) (1.2)

$\pi_1(2) =$ $:\pi^{+,-}_{-1,+1}(2):$ $\pi_2(2) =$

$$\frac{1}{4}\begin{bmatrix}
\cdot & \cdot & \cdot & \cdot & \cdot & \cdot & \cdot & \cdot & \cdot & \cdot & \cdot & \cdot & \cdot & \cdot \\
\cdot & 0 & 0 & 4 & & & & & & & & & 0 & \cdot \\
\cdot & 0 & 0 & 0 & 3 & & & & & & & & & \cdot \\
\cdot & -6 & 0 & 0 & 0 & 2 & & & & & & & & \cdot \\
\cdot & & -5 & 0 & 0 & 0 & 1 & & & & & & & \cdot \\
\cdot & & & -4 & 0 & 0 & 0 & \mathbf{0} & & & & & & \cdot \\
\cdot & & & & -3 & 0 & \underline{0} & 0 & -1 & & & & & \cdot \\
\cdot & & & & & -2 & 0 & 0 & 0 & -2 & & & & \cdot \\
\cdot & & & & & & -1 & 0 & 0 & 0 & -3 & & & \cdot \\
\cdot & & & & & & & \mathbf{0} & 0 & 0 & 0 & -4 & & \cdot \\
\cdot & & & & & & & & 1 & 0 & 0 & 0 & & \cdot \\
\cdot & 0 & & & & & & & & 2 & 0 & 0 & & \cdot \\
\cdot & \cdot & \cdot & \cdot & \cdot & \cdot & \cdot & \cdot & \cdot & \cdot & \cdot & \cdot & \cdot & \cdot
\end{bmatrix}, \frac{1}{4}\begin{bmatrix}
\cdot & \cdot & \cdot & \cdot & \cdot & \cdot & \cdot & \cdot & \cdot & \cdot & \cdot & \cdot & \cdot & \cdot \\
\cdot & 0 & 0 & -i4 & & & & & & & & & 0 & \cdot \\
\cdot & 0 & 0 & 0 & -i3 & & & & & & & & & \cdot \\
\cdot & -i6 & 0 & 0 & 0 & -i2 & & & & & & & & \cdot \\
\cdot & & -i5 & 0 & 0 & 0 & -i1 & & & & & & & \cdot \\
\cdot & & & -i4 & 0 & 0 & 0 & \mathbf{0} & & & & & & \cdot \\
\cdot & & & & -i3 & 0 & \underline{0} & 0 & i1 & & & & & \cdot \\
\cdot & & & & & -i2 & 0 & 0 & 0 & i2 & & & & \cdot \\
\cdot & & & & & & -i1 & 0 & 0 & 0 & i3 & & & \cdot \\
\cdot & & & & & & & \mathbf{0} & 0 & 0 & 0 & i4 & & \cdot \\
\cdot & & & & & & & & i1 & 0 & 0 & 0 & & \cdot \\
\cdot & 0 & & & & & & & & i2 & 0 & 0 & & \cdot \\
\cdot & \cdot & \cdot & \cdot & \cdot & \cdot & \cdot & \cdot & \cdot & \cdot & \cdot & \cdot & \cdot & \cdot
\end{bmatrix}$$

(2.1) (2.2)

$\pi_1(3) =$ $:\pi^{+,-}_{-2,+1}(3):$ $\pi_2(3) =$

$$\frac{1}{6}\begin{bmatrix}
\cdot & \cdot & \cdot & \cdot & \cdot & \cdot & \cdot & \cdot & \cdot & \cdot & \cdot & \cdot & \cdot & \cdot \\
\cdot & 0 & 0 & 0 & 3 & & & & & & & & 0 & \cdot \\
\cdot & 0 & 0 & 0 & 0 & 2 & & & & & & & & \cdot \\
\cdot & 0 & 0 & 0 & 0 & 0 & 1 & & & & & & & \cdot \\
\cdot & -6 & 0 & 0 & 0 & 0 & 0 & \mathbf{0} & & & & & & \cdot \\
\cdot & & -5 & 0 & 0 & 0 & 0 & 0 & -1 & & & & & \cdot \\
\cdot & & & -4 & 0 & 0 & \underline{0} & 0 & 0 & -2 & & & & \cdot \\
\cdot & & & & -3 & 0 & 0 & 0 & 0 & 0 & -3 & & & \cdot \\
\cdot & & & & & -2 & 0 & 0 & 0 & 0 & 0 & -4 & & \cdot \\
\cdot & & & & & & -1 & 0 & 0 & 0 & 0 & 0 & & \cdot \\
\cdot & & & & & & & \mathbf{0} & 0 & 0 & 0 & 0 & & \cdot \\
\cdot & 0 & & & & & & & 1 & 0 & 0 & 0 & & \cdot \\
\cdot & \cdot & \cdot & \cdot & \cdot & \cdot & \cdot & \cdot & \cdot & \cdot & \cdot & \cdot & \cdot & \cdot
\end{bmatrix}, \frac{1}{6}\begin{bmatrix}
\cdot & \cdot & \cdot & \cdot & \cdot & \cdot & \cdot & \cdot & \cdot & \cdot & \cdot & \cdot & \cdot & \cdot \\
\cdot & 0 & 0 & 0 & -i3 & & & & & & & & 0 & \cdot \\
\cdot & 0 & 0 & 0 & 0 & -i2 & & & & & & & & \cdot \\
\cdot & 0 & 0 & 0 & 0 & 0 & -i1 & & & & & & & \cdot \\
\cdot & -i6 & 0 & 0 & 0 & 0 & 0 & \mathbf{0} & & & & & & \cdot \\
\cdot & & -i5 & 0 & 0 & 0 & 0 & 0 & i1 & & & & & \cdot \\
\cdot & & & -i4 & 0 & 0 & \underline{0} & 0 & 0 & i2 & & & & \cdot \\
\cdot & & & & -i3 & 0 & 0 & 0 & 0 & 0 & i3 & & & \cdot \\
\cdot & & & & & -i2 & 0 & 0 & 0 & 0 & 0 & i4 & & \cdot \\
\cdot & & & & & & -i1 & 0 & 0 & 0 & 0 & 0 & & \cdot \\
\cdot & & & & & & & \mathbf{0} & 0 & 0 & 0 & 0 & & \cdot \\
\cdot & 0 & & & & & & & i1 & 0 & 0 & 0 & & \cdot \\
\cdot & \cdot & \cdot & \cdot & \cdot & \cdot & \cdot & \cdot & \cdot & \cdot & \cdot & \cdot & \cdot & \cdot
\end{bmatrix}$$

(3.1) (3.2)

$$\pi_3(1) = \quad :\pi^{+-}_{0,+1}(1): \quad \pi^2_3(1) = -\{\pi^2_1(1) + \pi^2_2(1)\} =$$

$$\frac{1}{1}\begin{bmatrix}
\cdot & \cdot & \cdot & \cdot & \cdot & \cdot & \cdot & \cdot & \cdot & \cdot & \cdot & \cdot & \cdot & \cdot \\
\cdot & 6 & & & & & & & & & & & 0 & \cdot \\
\cdot & & 5 & & & & & & & & & & & \cdot \\
\cdot & & & 4 & & & & & & & & & & \cdot \\
\cdot & & & & 3 & & & & & & & & & \cdot \\
\cdot & & & & & 2 & & & & & & & & \cdot \\
\cdot & & & & & & 1 & & & & & & & \cdot \\
\cdot & & & & & & & 0 & & & & & & \cdot \\
\cdot & & & & & & & & -1 & & & & & \cdot \\
\cdot & & & & & & & & & -2 & & & & \cdot \\
\cdot & & & & & & & & & & -3 & & & \cdot \\
\cdot & 0 & & & & & & & & & & & -4 & \cdot \\
\cdot & \cdot & \cdot & \cdot & \cdot & \cdot & \cdot & \cdot & \cdot & \cdot & \cdot & \cdot & \cdot & \cdot
\end{bmatrix}, \frac{1}{1}\begin{bmatrix}
\cdot & \cdot & \cdot & \cdot & \cdot & \cdot & \cdot & \cdot & \cdot & \cdot & \cdot & \cdot & \cdot & \cdot \\
\cdot & 36 & & & & & & & & & & & 0 & \cdot \\
\cdot & & 25 & & & & & & & & & & & \cdot \\
\cdot & & & 16 & & & & & & & & & & \cdot \\
\cdot & & & & 9 & & & & & & & & & \cdot \\
\cdot & & & & & 4 & & & & & & & & \cdot \\
\cdot & & & & & & 1 & & & & & & & \cdot \\
\cdot & & & & & & & 0 & & & & & & \cdot \\
\cdot & & & & & & & & 1 & & & & & \cdot \\
\cdot & & & & & & & & & 4 & & & & \cdot \\
\cdot & & & & & & & & & & 9 & & & \cdot \\
\cdot & 0 & & & & & & & & & & & 16 & \cdot \\
\cdot & \cdot & \cdot & \cdot & \cdot & \cdot & \cdot & \cdot & \cdot & \cdot & \cdot & \cdot & \cdot & \cdot
\end{bmatrix}$$

(1.3) (1.4)

$$\pi_3(2) = \quad :\pi^{--}_{-1,+1}(2): \quad \pi^2_3(2) = -\{\pi^2_1(2) + \pi^2_2(2)\} =$$

$$\frac{1}{2}\begin{bmatrix}
\cdot & \cdot & \cdot & \cdot & \cdot & \cdot & \cdot & \cdot & \cdot & \cdot & \cdot & \cdot & \cdot & \cdot \\
\cdot & 6 & & & & & & & & & & & 0 & \cdot \\
\cdot & & 5 & & & & & & & & & & & \cdot \\
\cdot & & & 4 & & & & & & & & & & \cdot \\
\cdot & & & & 3 & & & & & & & & & \cdot \\
\cdot & & & & & 2 & & & & & & & & \cdot \\
\cdot & & & & & & 1 & & & & & & & \cdot \\
\cdot & & & & & & & 0 & & & & & & \cdot \\
\cdot & & & & & & & & -1 & & & & & \cdot \\
\cdot & & & & & & & & & -2 & & & & \cdot \\
\cdot & & & & & & & & & & -3 & & & \cdot \\
\cdot & 0 & & & & & & & & & & & -4 & \cdot \\
\cdot & \cdot & \cdot & \cdot & \cdot & \cdot & \cdot & \cdot & \cdot & \cdot & \cdot & \cdot & \cdot & \cdot
\end{bmatrix}, \frac{1}{4}\begin{bmatrix}
\cdot & \cdot & \cdot & \cdot & \cdot & \cdot & \cdot & \cdot & \cdot & \cdot & \cdot & \cdot & \cdot & \cdot \\
\cdot & 36 & & & & & & & & & & & 0 & \cdot \\
\cdot & & 25 & & & & & & & & & & & \cdot \\
\cdot & & & 16 & & & & & & & & & & \cdot \\
\cdot & & & & 9 & & & & & & & & & \cdot \\
\cdot & & & & & 4 & & & & & & & & \cdot \\
\cdot & & & & & & 1 & & & & & & & \cdot \\
\cdot & & & & & & & 0 & & & & & & \cdot \\
\cdot & & & & & & & & 1 & & & & & \cdot \\
\cdot & & & & & & & & & 4 & & & & \cdot \\
\cdot & & & & & & & & & & 9 & & & \cdot \\
\cdot & 0 & & & & & & & & & & & 16 & \cdot \\
\cdot & \cdot & \cdot & \cdot & \cdot & \cdot & \cdot & \cdot & \cdot & \cdot & \cdot & \cdot & \cdot & \cdot
\end{bmatrix}$$

(2.3) (2.4)

$$\pi_3(3) = \quad :\pi^{+-}_{-2,+1}(3): \quad \pi^2_3(3) = -\{\pi^2_1(3) + \pi^2_2(3)\} =$$

$$\frac{1}{3}\begin{bmatrix}
\cdot & \cdot & \cdot & \cdot & \cdot & \cdot & \cdot & \cdot & \cdot & \cdot & \cdot & \cdot & \cdot & \cdot \\
\cdot & 6 & & & & & & & & & & & 0 & \cdot \\
\cdot & & 5 & & & & & & & & & & & \cdot \\
\cdot & & & 4 & & & & & & & & & & \cdot \\
\cdot & & & & 3 & & & & & & & & & \cdot \\
\cdot & & & & & 2 & & & & & & & & \cdot \\
\cdot & & & & & & 1 & & & & & & & \cdot \\
\cdot & & & & & & & 0 & & & & & & \cdot \\
\cdot & & & & & & & & -1 & & & & & \cdot \\
\cdot & & & & & & & & & -2 & & & & \cdot \\
\cdot & & & & & & & & & & -3 & & & \cdot \\
\cdot & 0 & & & & & & & & & & & -4 & \cdot \\
\cdot & \cdot & \cdot & \cdot & \cdot & \cdot & \cdot & \cdot & \cdot & \cdot & \cdot & \cdot & \cdot & \cdot
\end{bmatrix}, \frac{1}{9}\begin{bmatrix}
\cdot & \cdot & \cdot & \cdot & \cdot & \cdot & \cdot & \cdot & \cdot & \cdot & \cdot & \cdot & \cdot & \cdot \\
\cdot & 36 & & & & & & & & & & & 0 & \cdot \\
\cdot & & 25 & & & & & & & & & & & \cdot \\
\cdot & & & 16 & & & & & & & & & & \cdot \\
\cdot & & & & 9 & & & & & & & & & \cdot \\
\cdot & & & & & 4 & & & & & & & & \cdot \\
\cdot & & & & & & 1 & & & & & & & \cdot \\
\cdot & & & & & & & 0 & & & & & & \cdot \\
\cdot & & & & & & & & 1 & & & & & \cdot \\
\cdot & & & & & & & & & 4 & & & & \cdot \\
\cdot & & & & & & & & & & 9 & & & \cdot \\
\cdot & 0 & & & & & & & & & & & 16 & \cdot \\
\cdot & \cdot & \cdot & \cdot & \cdot & \cdot & \cdot & \cdot & \cdot & \cdot & \cdot & \cdot & \cdot & \cdot
\end{bmatrix}$$

(3.3) (3.4)

Be brief, in Spin Topological Space, STS , [4], the above spin matrices { (1.1), (1.2), (1.3); (2.1), (2.2), (2.3); (3.1), (3.2), (3.3) } of Higgs Boson can be rewritten in the spin forms of (4.1), (4.2), (4.3)

$$\vec{\pi}_{\,0,+1}(1) = \{ \pi_1(1), \pi_2(1), \pi_3(1) \} \quad (4.1)$$

$$\vec{\pi}_{\,-1,+1}(2) = \{ \pi_1(2), \pi_2(2), \pi_3(2) \} \quad (4.2)$$

$$\vec{\pi}_{\,-2,+1}(3) = \{ \pi_1(3), \pi_2(3), \pi_3(3) \} \quad (4.3)$$

For an example of $\vec{\pi}_{\,0,+1}(1)$, now, (4.1) is denoted by (5.0):

$$\vec{\pi}_{\,0,+1}(1) = \{ \pi_{1;\,0,+1}(1), \pi_{2;\,0,+1}(1), \pi_{3;\,0,+1}(1) \} \quad (5.0)$$

$$\pi_{1;\,0,+1}(1) = \frac{1}{2}(\pi_0^+ + \pi_{+1}^-) = \pi_1(1) \quad (5.1)$$

$$\pi_{2;\,0,+1}(1) = \frac{1}{2\mathrm{i}}(\pi_0^+ - \pi_{+1}^-) = \pi_2(1) \quad (5.2)$$

$$\pi_{3;\,0,+1}(1) = \frac{1}{\mathrm{i}}\{\pi_{1;\,0,+1}(1)\pi_{2;\,0,+1}(1) - \pi_{2;\,0,+1}(1)\pi_{1;\,0,+1}(1)\} = \pi_3(1) \quad (5.3)$$

3. Spin Interactions between Two Higgs Bosons

a) First we deal with two-body system that compose of Higgs Boson a, $\vec{\pi}_a$ and Higgs Boson b, $\vec{\pi}_b$. $\vec{\pi}_a$ and $\vec{\pi}_b$ are their spin angular momentum matrix operators. Then show a case of a spin coupling interaction (6.0) between $\vec{\pi}_a$ and $\vec{\pi}_b$, the scalar products $\mathbb{S}^2(l)$, or Casimir operators of their three generations as follows

$$\mathbb{S}^2(l) = \vec{\mathbb{S}}(l) \cdot \vec{\mathbb{S}}(l) \quad (6.0)$$

Where $$\vec{\mathbb{S}}(l) = \vec{\pi}_a(l) + \vec{\pi}_b(l) \quad (7.0)$$

Or $$\vec{\mathbb{S}}_{\,0,+1\,;\,-2,\,-1}(1) = \vec{\pi}_{\,0,+1}(1) + \vec{\pi}_{-2,\,-1}(1) \quad (7.1)$$

$$\vec{\mathbb{S}}_{-1,+1\,;\,-3,-1}(2) = \vec{\pi}_{-1,+1}(2) + \vec{\pi}_{-3,\,-1}(2) \quad (7.2)$$

$$\vec{\mathbb{S}}_{-2,+1\,;\,-4,-1}(3) = \vec{\pi}_{\,-2,+1}(3) + \vec{\pi}_{-4,\,-1}(3) \quad (7.3)$$

After careful calculation, for $\mathbb{S}^2$ (6.0), we have (8.0)

$$\mathbb{S}^2(l) = \vec{\mathbb{S}}(l) \cdot \vec{\mathbb{S}}(l) = 0I_0 \quad (8.0)$$

Or $$\mathbb{S}^2_{\,0,\,+1\,;\,-2,\,-1}(1) = 0I_0 \quad (8.1)$$

$$\mathbb{S}^2_{-1,+1\,;\,-3,-1}(2) = 0I_0 \quad (8.2)$$

$$\mathbb{S}^2_{-2,+1\,;\,-4,-1}(3) = 0I_0 \quad (8.3)$$

$$I_0 = \mathrm{diag}\,\{..., 1,\ 1,\ 1,\ 1,\ 1,\ \underline{1},\ 1,\ 1,\ 1,\ 1,\ 1, ...\} \quad (9.0)$$

(8.0) and (8.1), (8.2), (8.3) show: there are no any effects of spin coupling bwtween two $0\hbar$ zero spin particles, $\vec{\pi}_a(l)$ and $\vec{\pi}_b(l)$.

b) How can we find no-trivial spin-coupling interaction rather than (8), by using augular momentum operators of $0\hbar$ zero spin particle ?

Actually there are two types of $0\hbar$ zero spin particles, which is a way to overcome the obstacle

Assume $0\hbar$ zero spin particles $\vec{\pi}_{0,+1}(1)$ and $\vec{\pi}_{-2,-1}(1)$ to be thought of as two right-hand spin particles, frmula (7.1) could be written as (10).

$$\overrightarrow{A_R} = \vec{\mathbb{S}}_{0,+1\,;\,-2,-1}(1) = \vec{\pi}_{0,+1}(1) + \vec{\pi}_{-2,-1}(1) \tag{10}$$

Further the formula (8.1) is expressed as (11)

$$\overrightarrow{A_R}\, I_0\, \overrightarrow{A_R} = \mathbb{S}^2_{0,+1\,;\,-2,-1}(1) = 0I_0 \tag{11}$$

On the other side, $\overrightarrow{A_L}^{\odot}$ is marked as the adjoint counter of $\overrightarrow{A_R}$ with metric cofficient operator Ω, then $\vec{\pi}^{\odot}_{0,+1}(1)$ and $\vec{\pi}^{\odot}_{-2,-1}(1)$ are left-hand zero spin particles accordingly. we have

$$\overrightarrow{A_L}^{\odot} = \vec{\mathbb{S}}^{\odot}_{0,+1\,;\,-2,-1}(1) = \vec{\pi}^{\odot}_{0,+1}(1) + \vec{\pi}^{\odot}_{-2,-1}(1) \tag{12}$$

We are now ready to take further our discussion of scalar product of right-hand-to-right-hand, $\overrightarrow{A_R}\, I_0\, \overrightarrow{A_R}$ (11), to psecudo-scalar product of left-hand-to-right-hand, $\overrightarrow{A_L}^{\odot}\, \Omega\, \overrightarrow{A_R}$ (13), as follows

$$\overrightarrow{A_R}\, I_0\, \overrightarrow{A_R} \;\Rightarrow\; \overrightarrow{A_L}^{\odot}\, \Omega\, \overrightarrow{A_R} \tag{13}$$

Here metric cofficient operator Ω is selected as

$$\Omega = \begin{bmatrix} 0 & 1 & 0 \\ 1 & 0 & 0 \\ 0 & 0 & 1 \end{bmatrix} \tag{14}$$

Attention:

right-hand $0\hbar$ zero spin particles $\vec{\pi}_{0,+1}(1)$ and $\vec{\pi}_{-2,-1}(1)$ obey angular momentum commutation rules of right-handed coordinate system;

left-hand $0\hbar$ zero spin particles $\vec{\pi}^{\odot}_{0,+1}(1)$ and $\vec{\pi}^{\odot}_{-2,-1}(1)$ obey angular momentum commutation rules of left-handed coordinate system.

For more concise, the symbols (15) are given in the future discussions

$$\overrightarrow{A_R}(j,k\,;\,r,s) \equiv \vec{\pi}_{j,k}(1) + \vec{\pi}_{r,s}(1), \qquad \pi_3(i,j) \equiv \pi_{3;\,i,j}(1) \tag{15}$$

c) Let us have a look at an example of psecudo-scalar product of left-hand-to-right-hand of spin zero particles, $\overrightarrow{A_L}^{\odot}\ \Omega\ \overrightarrow{A_R}$. After careful calculation, we get two groups of $0\hbar$ spin interactions, Group-A and Group-B.

By way of illustration, we shall refer to the feature B(1) of Group-B:

Formulas (16.1) (16.2) and formulas (17.1), (17.2) are the third compoments of initial state *i* and final state *f* of psecudo-scalar spin interaction of the first generation spin particles (l=1).

Initial state

$$0\hbar \quad \pi_3(\,0\,,\,+1) = \text{diag}\ \{...6,\ 5,\ 4,\ 3,\ 2,\ \underline{1},\ 0,\ -1,\ -2,\ -3,\ -4,...\} \qquad (16.1)$$

$$0\hbar \quad \pi_3(-2,\,-1) = \text{diag}\ \{...4,\ 3,\ 2,\ 1,\ \underline{0},\ \underline{-1},\ -2,\ -3,\ -4,\ -5,\ -6...\} \qquad (16.2)$$

Final state

$$0\hbar \quad \pi_3(\,0\,,\,-1) = \text{diag}\ \{...5,\ 4,\ 3,\ 2,\ 1,\ \underline{0},\ -1,\ -2,\ -3,\ -4,\ -5,...\} \qquad (17.1)$$

$$1\hbar \quad \pi_3(-2,\,+1) = \text{diag}\ \{...5,\ 4,\ 3,\ 2,\ 1,\ \underline{0},\ -1,\ -2,\ -3,\ -4,\ -5,...\} \qquad (17.2)$$

And the conservation of the third compoment of spin angular momentums between initial state *i* and final state *f* is obtained as (18.0)

$$\pi_3(\,0\,,\,+1;\,-2,\,-1) \quad = \quad \pi_3(\,0\,,\,-1;\,-2,\,+1) \qquad (18.0)$$

ininal sum of s.a.m final sum of s.a.m

Where

$$\pi_3(\,0\,,\,+1;\,-2,\,-1) = \pi_3(\,0\,,\,+1) + \pi_3(-2,\,-1) \qquad (18.1)$$

$$\pi_3(\,0\,,\,-1;\,-2,\,+1) = \pi_3(\,0\,,\,-1) + \pi_3(-2,\,+1) \qquad (18.2)$$

And the conservation of psecudo-scalar spin interaction about ininl state *i* and final state *f* is obtained as (19.0)

$$\mathcal{L}_{B,i}\,(1) = \mathcal{L}_{B,f}\,(1) = \mathcal{L}_B \qquad (19.0)$$

Where

$$\mathcal{L}_{B,i}\,(1) = \overrightarrow{B_{L,1}}^{\odot}\,(\,0\,,+1;-2,-1)\ \Omega\ \overrightarrow{B_{R,1}}\,(\,0\,,+1;-2,-1) \qquad (19.1)$$

$$\mathcal{L}_{B,f}\,(1) = \overrightarrow{B_{L,1}}^{\odot}\,(\,0\,,-1;-2,+1)\ \Omega\ \overrightarrow{B_{R,1}}\,(\,0\,,-1;-2,+1) \qquad (19.2)$$

$$\mathcal{L}_B = -2\ \text{diag}\ \{...10^2,\ 8^2,\ 6^2,\ 4^2,\ 2^2,\ \underline{0^2},\ 2^2,\ 4^2,\ 6^2,\ 8^2,\ 10^2,,...\} \qquad (20)$$

What mentioned above is so-called fission of $0\hbar$ zero spin particles, refer to Fig4.

Conservation (18.0) and conservation (19.0) imply that if initial state *i* and final state *f* exchange places, so-called fusion of other spin particles is given, refer to Fig3.

Fig1, Fig2 of Group-A are obtained by the analogy to those of Fig3, Fig4 of Group-B above.

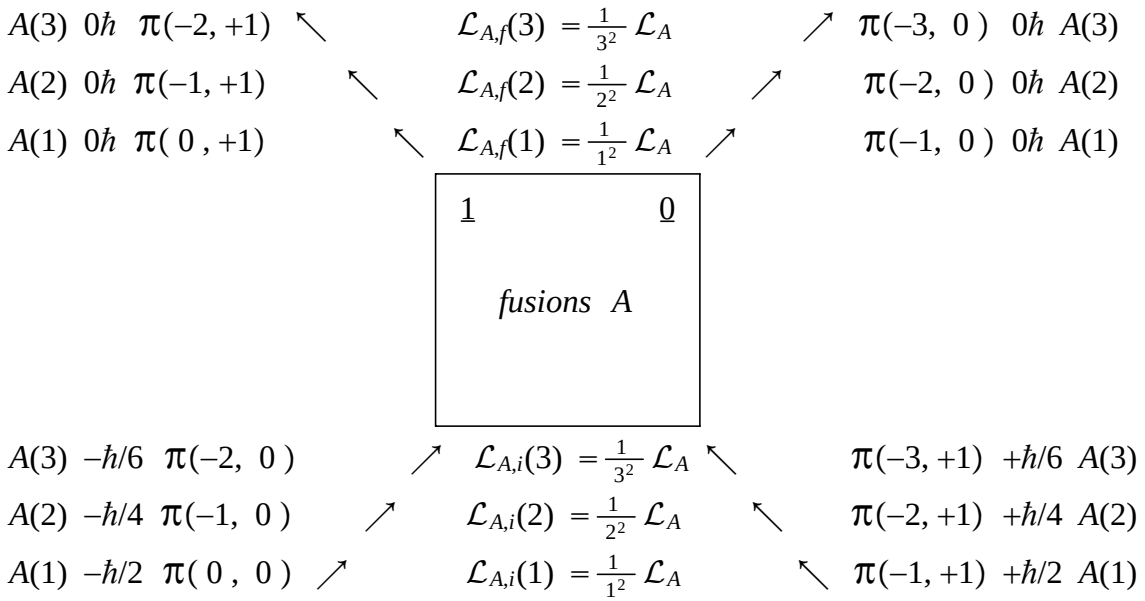

Fig1 zero spin particles are formed by the fusions of other spin particles

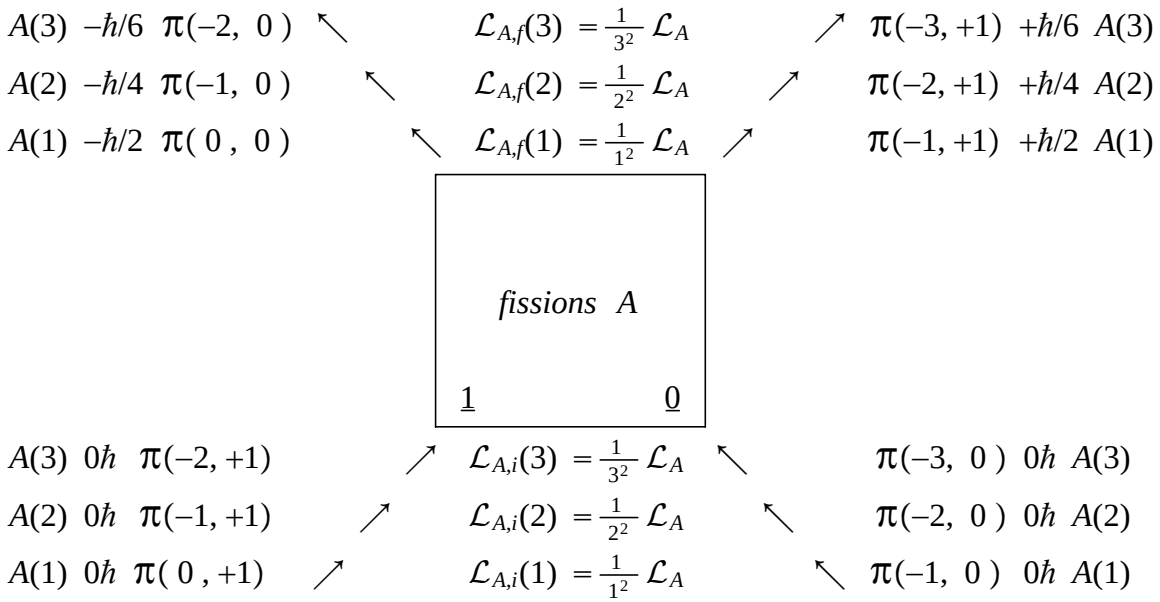

Fig2 other spin particles are released by the fissions of zero spin particles

$$\mathcal{L}_{A,f}(3) \equiv \overrightarrow{A_{L,3}}^{\odot}(-2,\ 0\ ;-3,+1)\ \Omega\ \overrightarrow{A_{R,3}}(-2,-1;-3,+1) \qquad (21.1)$$

$$\mathcal{L}_{A,i}(3) \equiv \overrightarrow{A_{L,3}}^{\odot}(-2,+1;-2,+1)\ \Omega\ \overrightarrow{A_{R,3}}(\ 0,+1;-3,\ 0\ ) \qquad (21.2)$$

$$\mathcal{L}_{A,f}(2) \equiv \overrightarrow{A_{L,2}}^{\odot}(-1,\ 0\ ;-2,+1)\ \Omega\ \overrightarrow{A_{R,2}}(-1,-1;-2,+1) \qquad (22.1)$$

$$\mathcal{L}_{A,i}(2) \equiv \overrightarrow{A_{L,2}}^{\odot}(-1,+1;-1,+1)\ \Omega\ \overrightarrow{A_{R,2}}(-1,+1;-2,\ 0\ ) \qquad (22.2)$$

$$\mathcal{L}_{A,f}(1) \equiv \overrightarrow{A_{L,1}}^{\odot}(\ 0\ ,\ 0\ ;-1,+1)\ \Omega\ \overrightarrow{A_{R,1}}(\ 0\ ,\ 0\ ;-1,+1) \qquad (23.1)$$

$$\mathcal{L}_{A,i}(1) \equiv \overrightarrow{A_{L,1}}^{\odot}(\ 0\ ,+1;-1,\ 0\ )\ \Omega\ \overrightarrow{A_{R,1}}(\ 0\ ,+1;-1,\ 0\ ) \qquad (23.2)$$

$$\mathcal{L}_A = -2\ \mathrm{diag}\ \{...11^2,\ 9^2,\ 7^2,\ 5^2,\ 3^2,\ \underline{1^2},\ 1^2,\ 3^2,\ 5^2,\ 7^2,\ 9^2,...\} \qquad (24)$$

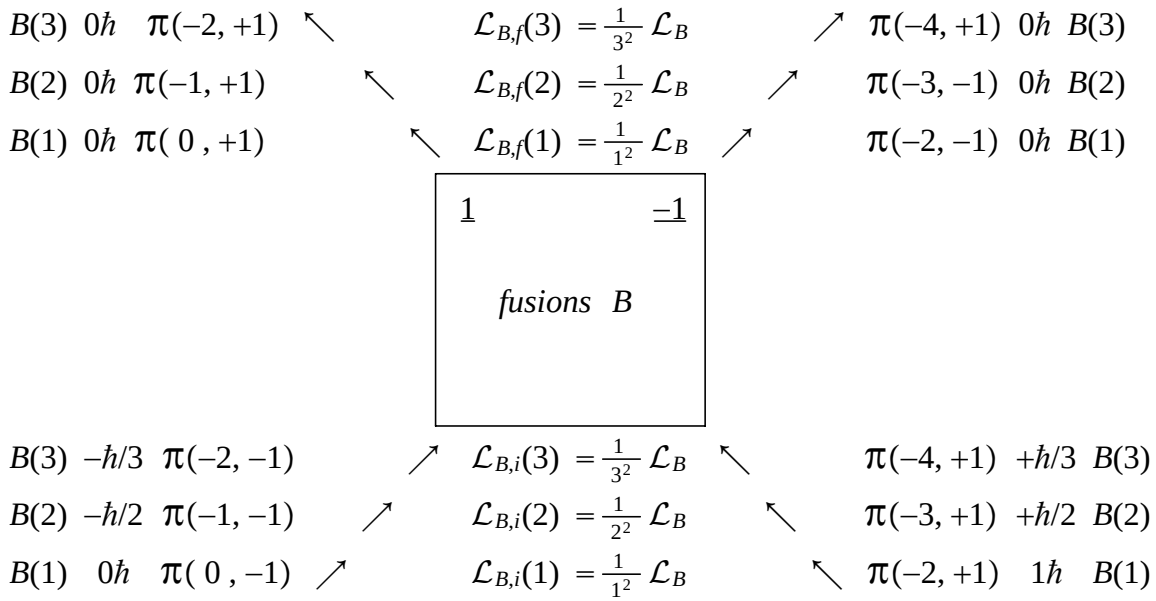

Fig3 zero spin particles are formed by the fusions of other spin particles

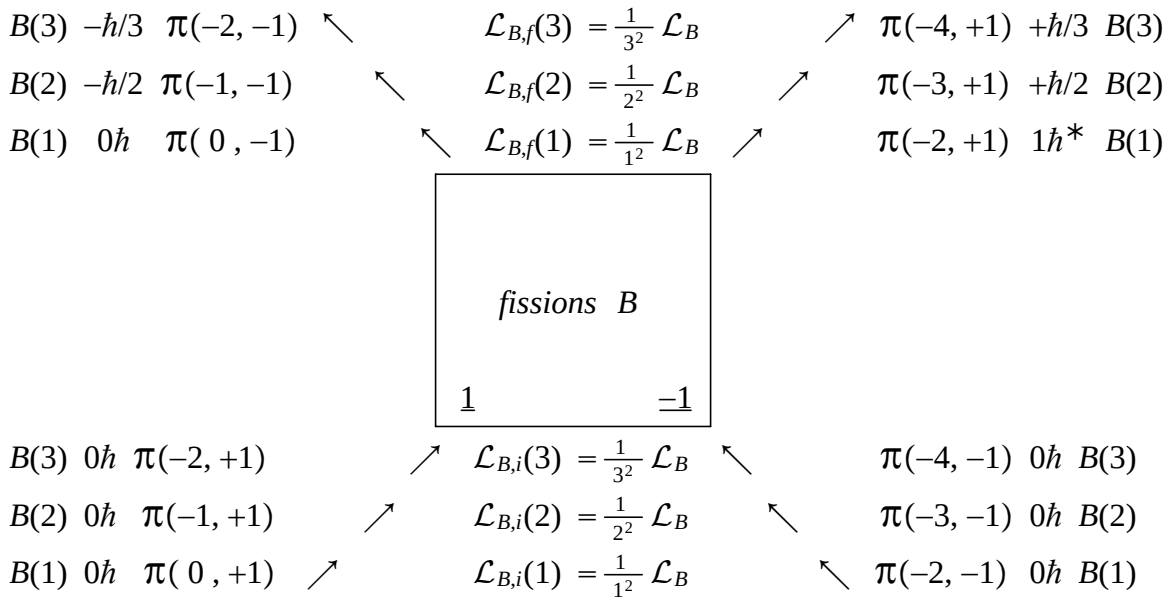

Fig4 other spin particles are released by the fissions of zero spin particles

$$\mathcal{L}_{B,f}(3) \equiv \overrightarrow{B_{L,3}}^{\odot}(-2,-1;-4,+1)\,\Omega\,\overrightarrow{B_{R,3}}(-2,-1;-4,+1) \quad (25.1)$$

$$\mathcal{L}_{B,i}(3) \equiv \overrightarrow{B_{L,3}}^{\odot}(-2,+1;-4,-1)\,\Omega\,\overrightarrow{B_{R,3}}(0,+1;-4,-1) \quad (25.2)$$

$$\mathcal{L}_{B,f}(2) \equiv \overrightarrow{B_{L,2}}^{\odot}(-1,-1;-3,+1)\,\Omega\,\overrightarrow{B_{R,2}}(-1,-1;-3,+1) \quad (26.1)$$

$$\mathcal{L}_{B,i}(2) \equiv \overrightarrow{B_{L,2}}^{\odot}(-1,+1;-3,-1)\,\Omega\,\overrightarrow{B_{R,2}}(-1,+1;-3,-1) \quad (26.2)$$

$$\mathcal{L}_{B,f}(1) \equiv \overrightarrow{B_{L,1}}^{\odot}(0,-1;-2,+1)\,\Omega\,\overrightarrow{B_{R,1}}(0,-1;-2,+1) \quad (27.1)$$

$$\mathcal{L}_{B,i}(1) \equiv \overrightarrow{B_{L,1}}^{\odot}(0,+1;-2,-1)\,\Omega\,\overrightarrow{B_{R,1}}(0,+1;-2,-1) \quad (27.2)$$

$$\mathcal{L}_B = -2\ \mathrm{diag}\ \{...10^2,\ 8^2,\ 6^2,\ 4^2,\ 2^2,\ \underline{0^2},\ 2^2,\ 4^2,\ 6^2,\ 8^2,\ 10^2,...\} \quad (28)$$

4) Spin Interactions between Higgs Bosons and Gravitons

d) To return to the case of scalar product of right-hand-to-right-hand particles, $\overrightarrow{A_R}\, I\, \overrightarrow{A_R}$, because we could get no-trivial spin-coupling interactions between $0\hbar$ zero spin particle and $2\hbar$ spin particle. Here two groups of , Group-C and Group-D. are given. Analogously, illustration by example of the feature D(1) of Group-D as follows：

Formulas (29.1) (29.2) and formulas (30.1), (30.2) are the third compoments of initial state i and final state f of scalar spin interaction of the first generation spin particles (l=1)

Initial state

$0\hbar$ $\pi_3(0, +1) = \text{diag}\ \{...6,\ 5,\ 4,\ 3,\ 2,\ \underline{1},\ 0,\ -1,\ -2,\ -3,\ -4,...\}$ (29.1)

$2\hbar$ $\pi_3(-3, +2) = \text{diag}\ \{...5,\ 4,\ 3,\ 2,\ 1,\ \underline{0},\ -1,\ -2,\ -3,\ -4,\ -5,...\}$ (29.2)

Final state

$1\hbar/2$ $\pi_3(0, +2) = \frac{1}{2}\,\text{diag}\ \{...13,\ 11,\ 9,\ 7,\ 5,\ \underline{3},\ 1,\ -1,\ -3,\ -5,\ -7,...\}$ (30.1)

$3\hbar/2$ $\pi_3(-3, +1) = \frac{1}{2}\,\text{diag}\ \{...9,\ 7,\ 5,\ 3,\ 1,\ \underline{-1},\ -3,\ -5,\ -7,\ -9,\ -11...\}$ (30.2)

And the conservation of the third compoment of spin angular momentums between initial state i and final state f is obtained as (31.0)

$$\underset{\text{ininal sum of s.a.m}}{\pi_3(0, +1; -3, +2)} = \underset{\text{final sum of s.a.m}}{\pi_3(0, +2; -3, +1)} \qquad (31.0)$$

Where

$$\pi_3(0, +1; -3, +2) = \pi_3(0, +1) + \pi_3(-3, +2) \qquad (31.1)$$

$$\pi_3(0, +2; -3, +1) = \pi_3(0, +2) + \pi_3(-3, +1) \qquad (31.2)$$

And the conservation of scalar spin interaction about ininl state i and final state f is obtained as (32.0)

$$\mathcal{L}_{D,i}(1) = \mathcal{L}_{D,f}(1) = \mathcal{L}_D \qquad (32.0)$$

Where

$$\mathcal{L}_{D,i}(1) = \overrightarrow{D_{R,1}}(0, +1; -3, +2)\, I\, \overrightarrow{D_{R,1}}(0, +1; -3, +2) \qquad (32.1)$$

$$\mathcal{L}_{D,f}(1) = \overrightarrow{D_{R,1}}(0, +2; -3, +1)\, I\, \overrightarrow{D_{R,1}}(0, +2; -3, +1) \qquad (32.2)$$

$$\mathcal{L}_D = 8I_0 \qquad (33)$$

What mentioned above is so-called fission of Higgs Boson and Graviton, refer to Fig8.

Conservation (31.0) and conservation (32.0) imply that if initial state i and final state f exchange places, so-called fusion of other spin particles is given, refer to Fig7.

Fig5, Fig6 of Group-C are obtained by the analogy to those of Fig7, Fig8 of Group-D above.

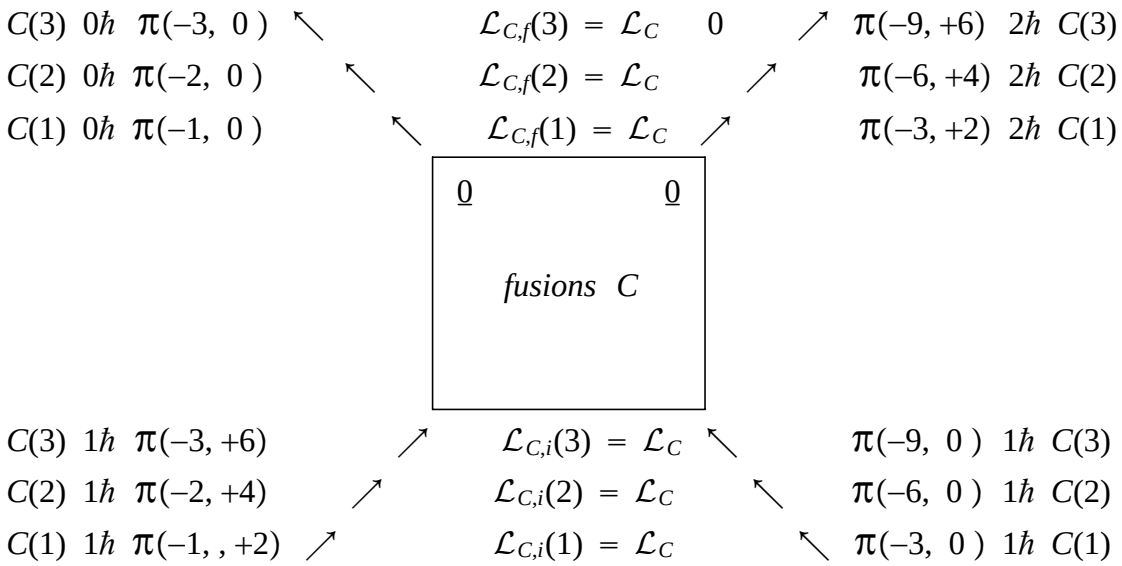

Fig5 Higgs Boson and Graviton are formed by fusions of other spin particles

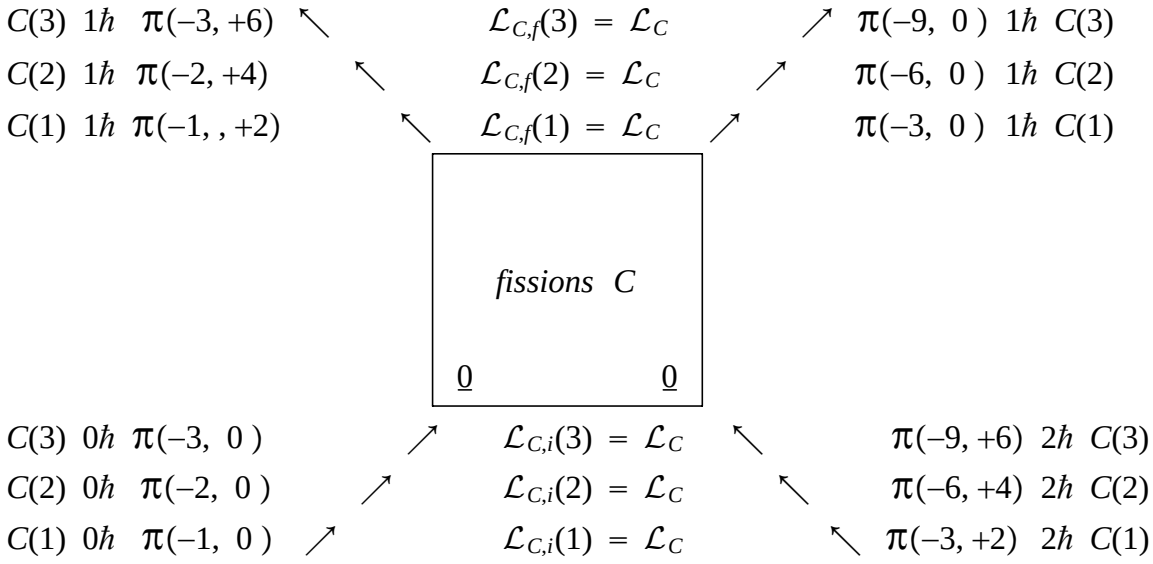

Fig6 other spin particles are released by fissions of Higgs Boson and Graviton

$$\mathcal{L}_{C,f}(3) \equiv \overrightarrow{C_{R,3}}^{\odot}(-3,+6;-9,\ 0)\, I_0\, \overrightarrow{C_{R,3}}(-3,+6;-9,\ 0) \tag{34.1}$$

$$\mathcal{L}_{C,i}(3) \equiv \overrightarrow{C_{R,3}}^{\odot}(-3,\ 0;-9,+6)\, I_0\, \overrightarrow{C_{R,3}}(-3,\ 0;-9,+6) \tag{34.2}$$

$$\mathcal{L}_{C,f}(2) \equiv \overrightarrow{C_{R,2}}^{\odot}(-2,+4;-6,\ 0)\, I_0\, \overrightarrow{C_{R,2}}(-2,+4;-6,\ 0) \tag{35.1}$$

$$\mathcal{L}_{C,i}(2) \equiv \overrightarrow{C_{R,2}}^{\odot}(-2,\ 0;-6,+4)\, I_0\, \overrightarrow{C_{R,2}}(-2,\ 0;-6,+4) \tag{35.2}$$

$$\mathcal{L}_{C,f}(1) \equiv \overrightarrow{C_{R,1}}^{\odot}(-1,+2;-3,\ 0)\, I_0\, \overrightarrow{C_{R,1}}(-1,+2;-3,\ 0) \tag{36.1}$$

$$\mathcal{L}_{C,i}(1) \equiv \overrightarrow{C_{R,1}}^{\odot}(-1,\ 0;-3,+2)\, I_0\, \overrightarrow{C_{R,1}}(-1,\ 0;-3,+2) \tag{36.2}$$

$$\mathcal{L}_C = 8I_0 \tag{37}$$

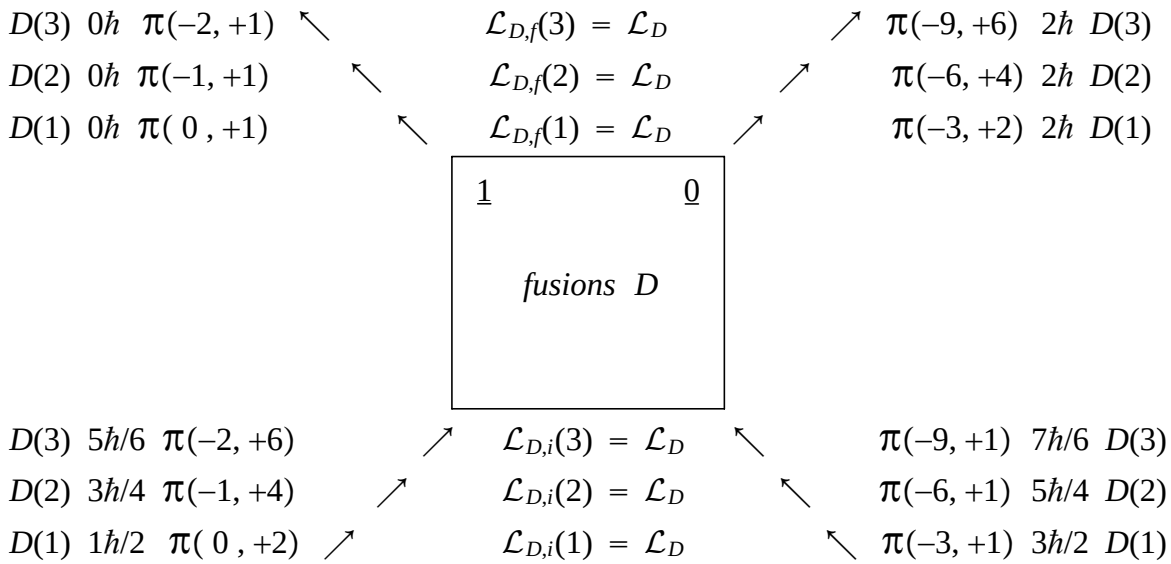

Fig7 Higgs Boson and Graviton are formed by fusions of other spin particles

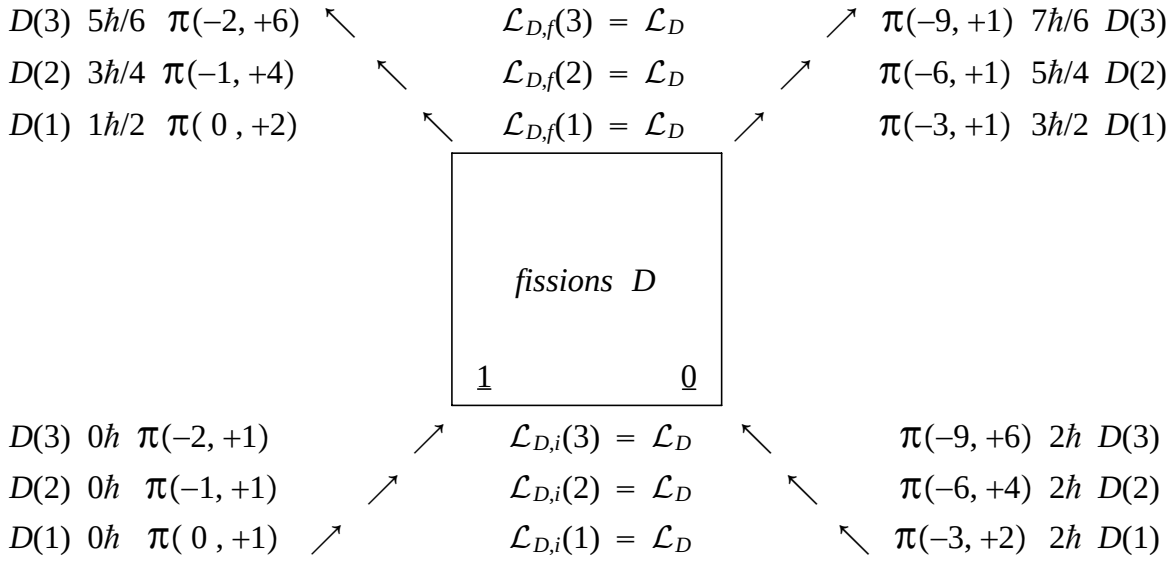

Fig8 other spin particles are released by fissions of Higgs Boson and Graviton

$$\mathcal{L}_{D,f}(3) \equiv \overrightarrow{D_{R,3}}^{\odot}(-2,+6;-9,+1)\, I_0\, \overrightarrow{D_{R,3}}(-2,+6;-9,+1) \tag{38.1}$$

$$\mathcal{L}_{D,i}(3) \equiv \overrightarrow{D_{R,3}}^{\odot}(-2,+1;-9,+6)\, I_0\, \overrightarrow{D_{R,3}}(-2,+1;-9,+6) \tag{38.2}$$

$$\mathcal{L}_{D,f}(2) \equiv \overrightarrow{D_{R,2}}^{\odot}(-1,+4;-6,+1)\; I_0\; \overrightarrow{D_{R,2}}(-1,+4;-6,+1) \tag{39.1}$$

$$\mathcal{L}_{D,i}(2) \equiv \overrightarrow{D_{R,2}}^{\odot}(-1,+1;-6,+4)\; I_0\; \overrightarrow{D_{R,2}}(-1,+1;-6,+4) \tag{39.2}$$

$$\mathcal{L}_{D,f}(1) \equiv \overrightarrow{D_{R,1}}^{\odot}(0,+2;-3,+1)\; I_0\; \overrightarrow{D_{R,1}}(0,+2;-3,+1) \tag{40.1}$$

$$\mathcal{L}_{D,i}(1) \equiv \overrightarrow{D_{R,1}}^{\odot}(0,+1;-3,+2)\; I_0\; \overrightarrow{D_{R,1}}(0,+1;-3,+2) \tag{40.2}$$

$$\mathcal{L}_D = 8I_0 \tag{41}$$

5) Conclusions

$\mathcal{L}_A(l)$ and $\mathcal{L}_B(l)$ in paragraph **3)**, which construct self-actions of zero spin particles, could be thought of as the Lagrangian function of Higgs Boson in quantum quantum field. Further research could show that such kind of mechanism may lead to the change of symmetry breaking in the Standard Model.

$\mathcal{L}_C(l)$ $\mathcal{L}_D(l)$ in paragraph **4)**, which construct creation and annihilation between $0\hbar$ zero spin particles and $2\hbar$ spin particle, may be able to dectect the existent of graviton from the 'particulate' nature of gravitation experimentally, comparative study, wavelike properties of gravitation have been exhibited [5]

References

[1] Higgs, Peter
Broken Symmetries and the Masses of Gauge Bosons Physical Review Letters 13 (16) 508–509

Bibcode:1964 PhRvL..13..508H. doi:10.1103/PhysRevLett. 13.508 (1964)

European particle physics laboratory, CERN, (2012)

[2] ShaoXu Ren
Advanced Non-Euclidean Quantum Mechanics
ISBN 978-7-80703-585-4 (2006)
The Third Kind of Particles
ISBN 978-7-900500-91-5 (2011)
ISBN 978-988-15598-9-0 (2012)
ISBN 988-3-659-17892-4 (2012)
The Third Kind of Particles
Journal of Modern Physics, **5**, 800-869
http:/dx.doi.org/10.4236/jmp.2014.59090

[3] ShaoXu Ren
The Origins Of Spins Of Elementary Particles
ISBN 978-988-13649-7-5 (2014)
The Origins of Bosons and Fermions
Journal of Modern Physics, **5**, 1848-1879
http:/dx.doi.org/10.4236/jmp.2014.517181

[4] ShaoXu Ren
Interaction of the Origins of Spin Angular Momentum
ISBN 978-988-14902-0-9 (2016 2nd edition)

[5] LIGO, LSC (2016)

[6] ShaoXu Ren
Faster Than Velocity Of Light (Infinite Dimensional Lorentz Group Of TKP) ISBN 978-988-12266-2-4 (2013)

6) Appendix: Higgs Boson Wave Differential Equation of First Order and Klein–Gordon Wave Differential Equation

e) Using math elements $\vec{\pi}_{j,k}$ in **STS** [4], the Hamiltonians of the first order and the second order linear wave differential equantions of $0\hbar$ spin zero particles, (Higgs Boson) are written as the following:

$$\mathbb{H}_{j,\,j+l}(l) \;=\; \{\; H_{j,\,j+l}(l) \;+\; \rho_3 m \;\} \qquad \text{(A–1)}$$

$$\mathbb{H}_{j,\,j+l\,;\,k,\,k+l}(l) \;=\; \mathbb{H}_{j,\,j+l}(l)\mathbb{H}_{k,\,k+l}(l) \qquad \text{(A–2)}$$

$H_{j,\,j+l}(l)$ in (A–1) is kinectic energy. There are many combinations in (A–2), which made by various choise of j and k.

For clarity, here $l = 1$ and omitting the mark " (1) " in above expressions. Then, taking $j = k = -1$ in cases of (A–1) and (A–2). getting below:

For (A–1) $$H_{-1,\,0} \;=\; \rho_1 \vec{\pi}_{-1,\,0} \cdot \vec{P} \qquad \text{(A–3)}$$

and first order wave differential equantions of $0\hbar$ spin zero particle

$0\hbar$ $$\{\; i\partial_t \;-\; \rho_1 \vec{\pi}_{-1,\,0} \cdot \vec{P} \;-\; \rho_3 m \;\}\Psi_{-1,\,0} \;=\; 0 \qquad \text{(A–4)}$$

For (A–2) $$\mathbb{H}_{-1,\,0\,;\,-1,\,0} \;=\; H^2_{-1,\,0} \;+\; m^2 \qquad \text{(A–5)}$$

and second order wave differential equantions of $0\hbar$ spin zero particle

$0\hbar$ $$\{\; \partial^2_{tt} \;+\; H^2_{-1,\,0} \;+\; m^2 \;\}\Phi_{-1,\,0} \;=\; 0 \qquad \text{(A–6)}$$

To make it clearer, we consinder the diagonal terms of (A–5) and have:

$$\text{diagonal}\;\{H^2_{-1,\,0}\} \qquad \text{(A–7)}$$

$$= \text{diag}\{,\, -25/2,\, -16/2,\, -9/2,\, -4/2,\, -1/2,\; \underline{0},\; -1/2,\, -4/2,\, -9/2,\, -16/2,\; -25/2,\, \}P_1^2$$
$$+ \text{diag}\{,\, -25/2,\, -16/2,\, -9/2,\, -4/2,\, -1/2,\; \underline{0},\; -1/2,\, -4/2,\, -9/2,\, -16/2,\; -25/2,\, \}P_2^2$$
$$+ \text{diag}\{,\; 25,\; 16,\; 9,\; 4,\; 1,\; \underline{0},\; 1,\; 4,\; 9,\; 16,\; 25,\; \}P_3^2 \qquad \text{(A–8)}$$

$$= \{\; -\tfrac{1}{2}\{P_1^2 \;+\; P_2^2\} \;+\; P_3^2 \;\}\pi_0^2(0) \qquad \text{(A–9)}$$

$$\pi_0^2(0) \;=\; \text{diag}\{,\; 5^2,\; 4^2,\; 3^2,\; 2^2,\; 1^2,\; \underline{0^2},\; 1^2,\; 2^2,\; 3^2,\; 4^2,\; 5^2,\, \} \qquad \text{(A–10)}$$

(A–9) indicates

$$\{\; -\tfrac{1}{2}\{P_1^2 \;+\; P_2^2\} \;+\; P_3^2 \;\} \;\subset\; \text{diagonal}\;\{H^2_{-1,\,0} \;;\; 0\hbar \text{ spin}\} \qquad \text{(A–11)}$$

and

$$\{\; \partial^2_{tt} \;+\; \tfrac{1}{2}\{\partial^2_{xx} \;+\; \partial^2_{yy}\} \;-\; \partial^2_{zz} \;+\; m^2 \;\}\Phi_{\text{diagonal};\,-1,\,0} \;=\; 0 \qquad \text{(A–12)}$$

f) The Hamiltonians of the first order and the second order linear differential equantions of $\hbar/2$ spin Fermion particles are written as following:

$$\mathbb{H}_{j,\,j-2l}(l) = \{\ H_{j,\,j-2l}(l) + \rho_3 m\ \} \tag{A–13}$$

$$\mathbb{H}_{j,\,j-2l;\,k,\,k-2l}(l) = \mathbb{H}_{j,\,j-2l}(l)\mathbb{H}_{k,\,k-2l}(l) \tag{A–14}$$

Accordingly, taking $j = k = 0$ in case of (A–13) and (A–14), we get:

For (A–13) $$H_{0,-2} = 2\rho_1\vec{\pi}_{0,-2}\cdot\vec{P} \tag{A–15}$$

and first order wave differential equantions of $\hbar/2$ spin particle

$\hbar/2$ $$\{\ i\partial_t - 2\rho_1\vec{\pi}_{0,-2}\cdot\vec{P} - \rho_3 m\ \}\Psi_{0,-2} = 0 \tag{A–16}$$

For (A–14) $$\mathbb{H}_{0,-2;\,0,-2} = H^2_{0,-2} + m^2 \tag{A–17}$$

and second order wave differential equantions of $\hbar/2$ spin particle

$\hbar/2$ $$\{\ \partial^2_{tt} + H^2_{0,-2} + m^2\ \}\Phi_{0,-2} = 0 \tag{A–18}$$

Taking out the diagonal terms from (A–17) and have:

$$\text{diagonal}\ \{H^2_{0,-2}\} \tag{A–19}$$

$$\begin{aligned}&= \text{diag}\{, -39, -23, -11, -3, \ \mathbf{1}, \ \underline{\mathbf{1}}, -3, -11, -23, -39, -59, \}P_1^2\\ &+ \text{diag}\{, -39, -23, -11, -3, \ \mathbf{1}, \ \underline{\mathbf{1}}, -3, -11, -23, -39, -59, \}P_2^2\\ &+ \text{diag}\{, \ 81, \ 49, \ 25, \ 9, \ \mathbf{1}, \ \underline{\mathbf{1}}, \ 9, \ 25, \ 49, \ 81, \ 121, \}P_3^2\end{aligned} \tag{A–20}$$

Now, we see the two terms (A–21) in the center part of diagonal $\{H^2_{0,-2}\}$ (A–20), is just the square sum H^2_{Dirac} of kinectic energy of well-known *Dirac equation of second order.*

$$\{H^2_{Dirac}\} = \text{diag}\{..., \ \mathbf{1}, \ \underline{\mathbf{1}}, \ ...\}\{P_1^2 + P_2^2 + P_3^2\} \subset \text{diagonal}\ \{H^2_{0,-2}\} \tag{A–21}$$

Or

$$\{H^2_{Dirac}\} = \{H_{KG}\} = -\nabla^2 \subset \text{diagonal}\ \{H^2_{0,-2}\ ;\ \hbar/2\ \text{spin}\} \tag{A–22}$$

And contrast with (A–11), we get

$$\{H^2_{Dirac}\} = \{H_{KG}\} = -\nabla^2 \subsetneq \text{diagonal}\ \{H^2_{-1,0}\ ;\ 0\hbar\ \text{spin}\} \tag{A–23}$$

Formula (A–22) and (A-23) mean: $-\nabla^2$ is a subset of $H^2_{0,-2}$, *not a set of* $H^2_{-1,0}$. **So** *Klein-Gordon Equation*

$$\{\ \hbar^2\partial^2_{tt} - c^2\hbar^2\nabla^2 + m^2c^4\ \}\Phi_{\mathrm{KG}} = 0 \tag{A–24}$$

$$\{\ \ \Box - \chi^2\ \}\Phi_{\mathrm{KG}} = 0 \tag{A–25}$$

$$\Box = \nabla^2 - \partial^2_{tt}/c^2, \quad \chi = mc/\hbar \tag{A–26}$$

is closer to $\hbar/2$ **spin Fermion particle**, **rather than** $0\hbar$ **spin Boson particle.**

It is more reasonable to use equation (A–4), equation (A–6) to describe zero spin Boson particle (Higgs Boson) than to use Klein Gordon equation.

g) For Vacuum Spin particle, VSP, $-\hbar/2$ negative one-second fermion particle, its Hamiltonians of the first order and the second order linear wave differential equantions are written as the following:

$$\mathbb{H}_{j,j}(l) = \{ H_{j,j}(l) + \rho_3 m \} \tag{A–27}$$

$$\mathbb{H}_{j,j;k,k}(l) = \mathbb{H}_{j,j}(l)\mathbb{H}_{k,k}(l) \tag{A–28}$$

Taking $j = k = 0$ in case of (A–27) and (A–28), we get:

For (A–27) $$H_{0,0} = 2\rho_1 \vec{\pi}_{0,0} \cdot \vec{P} \tag{A–29}$$

and first order wave differential equantions of $-\hbar/2$ spin particle

$-\hbar/2$ $$\{ i\partial_t - 2\rho_1 \vec{\pi}_{0,0} \cdot \vec{P} - \rho_3 m \} \Psi_{0,0;\mathrm{VSP}} = 0 \tag{A–30}$$

For (A–28) $$\mathbb{H}_{0,0;0,0} = H^2_{0,0} + m^2 \tag{A–31}$$

and second order wave differential equantions of $-\hbar/2$ spin particle

$-\hbar/2$ $$\{ \partial^2_{tt} + H^2_{0,0} + m^2 \} \Phi_{0,0;\mathrm{VSP}} = 0 \tag{A–32}$$

Taking out the diagonal terms from (A–31) and have:

$$\text{diagonal } \{H^2_{0,0}\} \tag{A–33}$$

$$\begin{aligned} &= \mathrm{diag}\{, -61, -41, -25, -13, -5, \underline{-1}, \underline{-1}, -5, -13, -25, -41, \} P_1^2 \\ &+ \mathrm{diag}\{, -61, -41, -25, -13, -5, \underline{-1}, \underline{-1}, -5, -13, -25, -41, \} P_2^2 \\ &+ \mathrm{diag}\{, 121, 81, 49, 25, 9, \underline{1}, 1, 9, 25, 49, 81, \} P_3^2 \end{aligned} \tag{A–34}$$

Now turn to the two terms (A–35) in the center part of diagonal $\{H^2_{0,0}\}$

$$\{H_{\mathrm{VSP}}\} = \mathrm{diag}\{..., \underline{1}, 1, ...\}\{-P_1^2 - P_2^2 + P_3^2\} \subset \text{diagonal } \{H^2_{0,0}\} \tag{A–35}$$

and have wave equation of VSP, ($-\hbar/2$ spin fermion particle)

$$\{ \partial^2_{tt} + \partial^2_{xx} + \partial^2_{yy} - \partial^2_{zz} + m^2 \} \Phi_{\mathrm{VSP}} = 0 \tag{A–36}$$

h) Next we shall discuss the solutions $\Psi^0 \equiv \Psi^{m=0}_{j,0}$ of zero mass particle differential equantions of First Order, which are based on free $-\hbar/2$ VSP particle (A–30), free $0\hbar$ zero spin particle (Higgs Boson) (A–4), free $+\hbar/2$ Dirac spin particle (A–16). Which are given as below:

$-\hbar/2$ $$\{ i\partial_t - 2\vec{\pi}_{0,0} \cdot \vec{P} \} \Psi^0_{0,0;\mathrm{VSP}} = 0 \tag{A–37}$$

$0\hbar$ $$\{ i\partial_t - \vec{\pi}_{-1,0} \cdot \vec{P} \} \Psi^0_{-1,0;\,\mathrm{Higgs\ Boson}} = 0 \tag{A–38}$$

$+\hbar/2$ $$\{ i\partial_t - 2\vec{\pi}_{0,-2} \cdot \vec{P} \} \Psi^0_{0,-2;\,\mathrm{Dirac}} = 0 \tag{A–39}$$

Notation:

$$E \;=\; E_{\pm} = \pm\, p \;,\;\; p \;=\; \sqrt{p_1^2 \,+\, p_2^2 \,+\, p_3^2} \qquad \text{(A–40)}$$

h1) For free $-\hbar/2$ VSP zero mass particle (A–37)

$$\Psi^{0}_{0\,,\,0\,;\,\mathrm{VSP}} \;=\; F_{\,0\,,\,0}\;\, e^{-iEt} \qquad \text{(A–41)}$$

Getting

$$F_{+p;\;\;0\,,\,0}\;\, e^{-iE_{+}t} = \begin{bmatrix} -\,(p\,-\,p_3)^5\;/p_{+}^5 \\ +\,(p\,-\,p_3)^4\;/p_{+}^4 \\ -\,(p\,-\,p_3)^3\;/p_{+}^3 \\ +\,(p\,-\,p_3)^2\;/p_{+}^2 \\ -\,(p\,-\,p_3)^1\;/p_{+}^1 \\ +\,(p\,-\,p_3)^0\;/p_{+}^0 \\ +\,(p\,+\,p_3)^0\;/p_{-}^0 \\ -\,(p\,+\,p_3)^1\;/p_{-}^1 \\ +\,(p\,+\,p_3)^2\;/p_{-}^2 \\ -\,(p\,+\,p_3)^3\;/p_{-}^3 \\ +\,(p\,+\,p_3)^4\;/p_{-}^4 \\ -\,(p\,+\,p_3)^5\;/p_{-}^5 \end{bmatrix} e^{-iE_{+}t} \qquad \text{(A–41.1)}$$

$$F_{-p;\;\;0\,,\,0}\;\, e^{-iE_{-}t} = \begin{bmatrix} +\,(p\,+\,p_3)^5\;/p_{+}^5 \\ +\,(p\,+\,p_3)^4\;/p_{+}^4 \\ +\,(p\,+\,p_3)^3\;/p_{+}^3 \\ +\,(p\,+\,p_3)^2\;/p_{+}^2 \\ +\,(p\,+\,p_3)^1\;/p_{+}^1 \\ +\,(p\,+\,p_3)^0\;/p_{+}^0 \\ +\,(p\,-\,p_3)^0\;/p_{-}^0 \\ +\,(p\,-\,p_3)^1\;/p_{-}^1 \\ +\,(p\,-\,p_3)^2\;/p_{-}^2 \\ +\,(p\,-\,p_3)^3\;/p_{-}^3 \\ +\,(p\,-\,p_3)^4\;/p_{-}^4 \\ +\,(p\,-\,p_3)^5\;/p_{-}^5 \end{bmatrix} e^{-iE_{-}t} \qquad \text{(A–41.2)}$$

$$F_{+p;\,\theta>0} = \begin{bmatrix} -\,\tan^5\theta/2\;\, e^{-i5\varphi} \\ +\,\tan^4\theta/2\;\, e^{-i4\varphi} \\ -\,\tan^3\theta/2\;\, e^{-i3\varphi} \\ +\,\tan^2\theta/2\;\, e^{-i2\varphi} \\ -\,\tan^1\theta/2\;\, e^{-i\varphi} \\ +\qquad\quad e^{+i0\varphi} \end{bmatrix} \qquad F_{-p;\,\theta>0} = \begin{bmatrix} +\,\cot^5\theta/2\;\, e^{-i5\varphi} \\ +\,\cot^4\theta/2\;\, e^{-i4\varphi} \\ +\,\cot^3\theta/2\;\, e^{-i3\varphi} \\ +\,\cot^2\theta/2\;\, e^{-i2\varphi} \\ +\,\cot^1\theta/2\;\, e^{-i\varphi} \\ +\qquad\quad e^{+i0\varphi} \end{bmatrix}$$

$$F_{+p;\,\theta<0} = \begin{bmatrix} +\qquad\quad e^{+i0\varphi} \\ -\,\cot^1\theta/2\;\, e^{+i\varphi} \\ +\,\cot^2\theta/2\;\, e^{+i2\varphi} \\ -\,\cot^3\theta/2\;\, e^{+i3\varphi} \\ +\,\cot^4\theta/2\;\, e^{+i4\varphi} \\ -\,\cot^5\theta/2\;\, e^{+i5\varphi} \end{bmatrix} \qquad F_{-p;\,\theta<0} = \begin{bmatrix} +\qquad\quad e^{+i0\varphi} \\ +\,\tan^1\theta/2\;\, e^{+i\varphi} \\ +\,\tan^2\theta/2\;\, e^{+i2\varphi} \\ +\,\tan^3\theta/2\;\, e^{+i3\varphi} \\ +\,\tan^4\theta/2\;\, e^{+i4\varphi} \\ +\,\tan^5\theta/2\;\, e^{+i5\varphi} \end{bmatrix}$$

(A–41.3) (A–41.4)

VSP particle $F_{+p;\;\;0\,,\,0} \;=\; F_{+p;\,\theta>0} \;+\; F_{+p;\,\theta<0}$ (A–41.5)

$F_{-p;\;\;0\,,\,0} \;=\; F_{-p;\,\theta>0} \;+\; F_{-p;\,\theta<0}$ (A–41.6)

h2) For free $0\hbar$ zero spin zero mass particle (Higgs Boson) (A–38)

$$\Psi^{0}_{-1\,,\,0\,;\,\mathrm{HB}} \;=\; F_{-1\,,\,0}\;\; e^{-iEt} \tag{A–42}$$

Getting

$$\Psi^{0}_{+p\;;\;-1\,,\,0\,;\,\mathrm{HB}} = \begin{bmatrix} -\,(p\,-\,p_3)^4\;\; p/p^5_{+} \\ +\,(p\,-\,p_3)^3\;\; p/p^4_{+} \\ -\,(p\,-\,p_3)^2\;\; p/p^3_{+} \\ +\,(p\,-\,p_3)^1\;\; p/p^2_{+} \\ -\,(p\,-\,p_3)^0\;\; p/p^1_{+} \\ +\,(p\,\mp\,p_3)^0\; p^0/p^0_{\pm} \\ -\,(p\,+\,p_3)^0\;\; p/p^1_{-} \\ +\,(p\,+\,p_3)^1\;\; p/p^2_{-} \\ -\,(p\,+\,p_3)^2\;\; p/p^3_{-} \\ +\,(p\,+\,p_3)^3\;\; p/p^4_{-} \\ -\,(p\,+\,p_3)^4\;\; p/p^5_{-} \end{bmatrix} e^{-iE_{+}t} \tag{A–42.1}$$

$$\Psi^{0}_{-p\;;\;-1\,,\,0\,;\,\mathrm{HB}} = \begin{bmatrix} +\,(p\,+\,p_3)^4\;\; p/p^5_{+} \\ +\,(p\,+\,p_3)^3\;\; p/p^4_{+} \\ +\,(p\,+\,p_3)^2\;\; p/p^3_{+} \\ +\,(p\,+\,p_3)^1\;\; p/p^2_{+} \\ +\,(p\,+\,p_3)^0\;\; p/p^1_{+} \\ +\,(p\,\pm\,p_3)^0\; p^0/p^0_{\pm} \\ +\,(p\,-\,p_3)^0\;\; p/p^1_{-} \\ +\,(p\,-\,p_3)^1\;\; p/p^2_{-} \\ +\,(p\,-\,p_3)^2\;\; p/p^3_{-} \\ +\,(p\,-\,p_3)^3\;\; p/p^4_{-} \\ +\,(p\,-\,p_3)^4\;\; p/p^5_{-} \end{bmatrix} e^{-iE_{-}t} \tag{A–42.2}$$

$$= \begin{bmatrix} -\,\tan^4\theta/2\;\; e^{-i5\varphi} \\ +\,\tan^3\theta/2\;\; e^{-i4\varphi} \\ -\,\tan^2\theta/2\;\; e^{-i3\varphi} \\ +\,\tan^1\theta/2\;\; e^{-i2\varphi} \\ -\qquad\quad e^{-i\varphi} \\ \qquad\sin\theta \\ -\qquad\quad e^{+i\varphi} \\ +\,\cot\theta^1/2\;\; e^{+i2\varphi} \\ -\,\cot\theta^2/2\;\; e^{+i3\varphi} \\ +\,\cot\theta^3/2\;\; e^{+i4\varphi} \\ -\,\cot\theta^4/2\;\; e^{+i5\varphi} \end{bmatrix} e^{-iE_{+}t} \tag{A–42.3}$$

$$= \begin{bmatrix} +\,\cot^4\theta/2\;\; e^{-i5\varphi} \\ +\,\cot^3\theta/2\;\; e^{-i4\varphi} \\ +\,\cot^2\theta/2\;\; e^{-i3\varphi} \\ +\,\cot^1\theta/2\;\; e^{-i2\varphi} \\ +\qquad\quad e^{-i\varphi} \\ \qquad\sin\theta \\ \qquad\quad e^{+i\varphi} \\ +\,\tan\theta^1/2\;\; e^{+i2\varphi} \\ +\,\tan\theta^2/2\;\; e^{+i3\varphi} \\ +\,\tan\theta^3/2\;\; e^{+i4\varphi} \\ +\,\tan\theta^4/2\;\; e^{+i5\varphi} \end{bmatrix} e^{-iE_{-}t} \tag{A–42.4}$$

There are two singularities at $\theta = 0,$ and π in the above two expressions. Obviously, some uncertainties of choise of free $0\hbar$ zero spin zero mass wavefunction should be addressed. Here (A–42.3) and (A–42.4) are only an investigation.

h3) For free $+\hbar/2$ Dirac spin zero mass particle (A–39)

$$\Psi^{0}_{0\,,\,-2\,;\,\mathrm{Dirac}} \;=\; F_{0\,,\,-2}\;\; e^{-iEt} \qquad \text{(A–43)}$$

Getting

$$\Psi^{0}_{+p\;;\;\;0\,,\,-2\,;\,\mathrm{Dirac}} = \begin{bmatrix} \cdots\cdots \\ +\,(p\,+\,p_3)^4 / p_+^4 \\ +\,(p\,+\,p_3)^3 / p_+^3 \\ +\,(p\,+\,p_3)^2 / p_+^2 \\ +\,(p\,+\,p_3)^1 / p_+^1 \\ +\,(p\,\pm\,p_3)^0 \;/p_\pm^0 \\ +\,(p\,-\,p_3)^1 / p_-^1 \\ +\,(p\,-\,p_3)^2 / p_-^2 \\ +\,(p\,-\,p_3)^3 / p_-^3 \\ +\,(p\,-\,p_3)^4 / p_-^4 \\ +\,(p\,-\,p_3)^5 / p_-^5 \\ \cdots\cdots \end{bmatrix} e^{-iE_+t} \quad , \qquad \text{(A–43.1)}$$

$$= \begin{bmatrix} \cdots\cdots \\ -\,(p\,-\,p_3)^5 / p_+^5 \\ +\,(p\,-\,p_3)^4 / p_+^4 \\ -\,(p\,-\,p_3)^3 / p_+^3 \\ +\,(p\,-\,p_3)^2 / p_+^2 \\ -\,(p\,-\,p_3)^1 / p_+^1 \\ +\,(p\,\mp\,p_3)^0 / p_\pm^0 \\ -\,(p\,+\,p_3)^1 / p_-^1 \\ +\,(p\,+\,p_3)^2 / p_-^2 \\ -\,(p\,+\,p_3)^3 / p_-^3 \\ +\,(p\,+\,p_3)^4 / p_-^4 \\ \cdots\cdots \end{bmatrix} e^{-iE_-t} \qquad \text{(A–43.2)}$$

$$= \begin{bmatrix} \cdots\cdots \\ \cot^4\theta/2\;\cos\theta/2\;e^{-i4\varphi} \\ \cot^3\theta/2\;\cos\theta/2\;e^{-i3\varphi} \\ \cot^2\theta/2\;\cos\theta/2\;e^{-i2\varphi} \\ \cot^1\theta/2\;\cos\theta/2\;\;e^{-i\varphi} \\ \cos\theta/2 \\ \sin\theta/2\;\;e^{+i\varphi} \\ \tan^1\theta/2\;\sin\theta/2\;e^{+i2\varphi} \\ \tan^2\theta/2\;\sin\theta/2\;e^{+i3\varphi} \\ \tan^3\theta/2\;\sin\theta/2\;e^{+i4\varphi} \\ \tan^4\theta/2\;\sin\theta/2\;e^{+i5\varphi} \\ \cdots\cdots \end{bmatrix} e^{-iE_+t} \quad , \qquad \text{(A–43.3)}$$

$$= \begin{bmatrix} \cdots\cdots \\ -\,\tan^4\theta/2\;\sin\theta/2\;e^{-i5\varphi} \\ +\,\tan^3\theta/2\;\sin\theta/2\;e^{-i4\varphi} \\ -\,\tan^2\theta/2\;\sin\theta/2\;e^{-i3\varphi} \\ +\,\tan^1\theta/2\;\sin\theta/2\;e^{-i2\varphi} \\ -\qquad\sin\theta/2\;\;e^{-i\varphi} \\ \cos\theta/2 \\ -\,\cot^1\theta/2\;\cos\theta/2\;\;e^{+i\varphi} \\ +\,\cot^2\theta/2\;\cos\theta/2\;e^{+i2\varphi} \\ -\,\cot^3\theta/2\;\cos\theta/2\;e^{+i3\varphi} \\ +\,\cot^4\theta/2\;\cos\theta/2\;e^{+i4\varphi} \\ \cdots\cdots \end{bmatrix} e^{-iE_-t} \qquad \text{(A–43.4)}$$

The two elements in the centers of the above expressions are just the spin wavefunction representation of operator $\vec{\sigma}\cdot\vec{n}$ of $\hbar/2$ Dirac spin in two dimensional spin space in traditional quantum machenics.

$$\Psi^{0}_{+p\;;\;\mathrm{Dirac}} = \begin{bmatrix} \cos\theta/2 \\ \sin\theta/2\;\;e^{+i\varphi} \end{bmatrix} , \qquad \text{(A–43.5)}$$

$$\Psi^{0}_{-p\;;\;\mathrm{Dirac}} = \begin{bmatrix} -\sin\theta/2\;\;e^{-i\varphi} \\ \cos\theta/2 \end{bmatrix} \qquad \text{(A–43.6)}$$

i) Finally we digress slightly, to tackle the situations of the velocity of light, because light speed is related to spin angular momentum in STS.

i1) The special case of $P_1 = P_1 = 0$ for non-zero mass particle Second Order differential equantions $-\hbar/2$ (A-32), **VSP** particle, zero spin particle (Higgs Boson) (A-6), $+\hbar/2$ Dirac spin particle (A–18) are given below：

$$-\hbar/2 \qquad \{ E^2 + \alpha^2_{0,0}\partial^2_{zz} - m^2 \}\, \Phi_{0,0;\,\mathrm{VSP}} = 0 \qquad \text{(A–44)}$$

$$\alpha^2_{0,0} = \mathrm{diag}\{,\ 121,\ 81,\ 49,\ 25,\ 9,\ \underline{\mathbf{1}},\ \mathbf{1},\ 9,\ 25,\ 49,\ 81,\ \}$$

$$0\hbar \qquad \{ E^2 + \alpha^2_{-1,0}\partial^2_{zz} - m^2 \}\, \Phi_{-1,0;\,\mathrm{Higgs\ Boson}} = 0 \qquad \text{(A–45)}$$

$$\alpha^2_{-1,0} = \mathrm{diag}\{,\ 25,\ 16,\ 9,\ 4,\ \mathbf{1},\ \underline{0},\ \mathbf{1},\ 4,\ 9,\ 16,\ 25,\ \}$$

$$+\hbar/2 \qquad \{ E^2 + \alpha^2_{0,-2}\partial^2_{zz} - m^2 \}\, \Phi_{0,-2;\,\mathrm{Dirac}} = 0 \qquad \text{(A–46)}$$

$$\alpha^2_{0,-2} = \mathrm{diag}\{,\ 81,\ 49,\ 25,\ 9,\ \mathbf{1},\ \underline{\mathbf{1}},\ 9,\ 25,\ 49,\ 81,\ 121,\ \}$$

getting [2]

$$E^{\pm}_{S=|j-k|} = \pm\sqrt{m^2c^4 + \alpha^2_{i,j}c^2P^2_3} \geq \sqrt{m^2c^4 + c^2P^2_3} \qquad \text{(A–47)}$$

Photon velocity in multi-level universes world is quantized：the limiting speed of particle with zero mass $m = 0$, could be greater than c

$$C_{S=|j-k|} = \alpha_{i,j}\, c = 1c, 2c, 3c, 4c, \ldots \text{ or } 1c, 3c, 5c, 7c, \ldots \geq c, \qquad \text{(A–48)}$$

i2) Lorentz Group Operators are constructed by six 4×4 dimensional matrices : J_1, J_2, J_3 and K_1, K_2, K_3

$$J_1 = \begin{bmatrix} 0 & 0 & 0 & 0 \\ 0 & 0 & 0 & 0 \\ 0 & 0 & 0 & -i \\ 0 & 0 & i & 0 \end{bmatrix},\quad J_2 = \begin{bmatrix} 0 & 0 & 0 & 0 \\ 0 & 0 & 0 & i \\ 0 & 0 & 0 & 0 \\ 0 & -i & 0 & 0 \end{bmatrix},\quad J_3 = \begin{bmatrix} 0 & 0 & 0 & 0 \\ 0 & 0 & -i & 0 \\ 0 & i & 0 & 0 \\ 0 & 0 & 0 & 0 \end{bmatrix} \qquad \text{(A–49)}$$

$$K_1 = \begin{bmatrix} 0 & i & 0 & 0 \\ i & 0 & 0 & 0 \\ 0 & 0 & 0 & 0 \\ 0 & 0 & 0 & 0 \end{bmatrix},\quad K_2 = \begin{bmatrix} 0 & 0 & i & 0 \\ 0 & 0 & 0 & 0 \\ i & 0 & 0 & 0 \\ 0 & 0 & 0 & 0 \end{bmatrix},\quad K_3 = \begin{bmatrix} 0 & 0 & 0 & i \\ 0 & 0 & 0 & 0 \\ 0 & 0 & 0 & 0 \\ i & 0 & 0 & 0 \end{bmatrix} \qquad \text{(A–50)}$$

$$K_3 = i\frac{\partial}{\partial\eta_3}L_3(\eta)|_{\eta=\eta_3=0} = i\frac{\partial}{\partial\eta_3}\begin{bmatrix} Ch\,\eta & 0 & 0 & Sh\,\eta \\ 0 & 1 & 0 & 0 \\ 0 & 0 & 1 & 0 \\ Sh\,\eta & 0 & 0 & Ch\,\eta \end{bmatrix}|_{\eta=\eta_3=0} \qquad \text{(A–51)}$$

$L_3(\eta)$ is the familiar expression of Einstein special relativity.

Using infinite dimensional spin augular momentum operators $\vec{\pi}_{-2,1}$ $(\pi_{1:-2,1}, \pi_{2:-2,1}, \pi_{3:-2,1})$ of $1\hbar$ spin boson particle, we could get six infinite dimensional matrices $\mathbb{J}_1, \mathbb{J}_2, \mathbb{J}_3$ and $\mathbb{K}_1, \mathbb{K}_2, \mathbb{K}_3$ of Lorentz Group Operators. Among them, matrix $\mathbb{K}_3$ is shown below

$$K_3 \Rightarrow \mathbb{K}_3 = \begin{bmatrix}
\cdot & \cdot & \cdot & \cdot & \cdot & \cdot & \cdot & \cdot & \cdot & \cdot & \cdot & \cdot & \cdot & \cdot & \cdot \\
\cdot & 0 & 0 & 0 & 0 & & & & & & & & & 5i & \cdot \\
\cdot & 0 & 0 & 0 & 0 & & & & & & & & 4i & & \cdot \\
\cdot & 0 & 0 & 0 & 0 & & & & & & & 3i & & & \cdot \\
\cdot & 0 & 0 & 0 & 0 & & & & & & 2i & & & & \cdot \\
\cdot & & & & & 0 & 0 & 0 & i & & & & & & \cdot \\
\cdot & & & & & 0 & 0 & 0 & 0 & & & & & & \cdot \\
\cdot & & & & & 0 & 0 & 0 & 0 & & & & & & \cdot \\
\cdot & & & & & i & 0 & 0 & 0 & & & & & & \cdot \\
\cdot & & & & 2i & & & & & 0 & 0 & 0 & 0 & & \cdot \\
\cdot & & & 3i & & & & & & 0 & 0 & 0 & 0 & & \cdot \\
\cdot & & 4i & & & & & & & 0 & 0 & 0 & 0 & & \cdot \\
\cdot & 5i & & & & & & & & 0 & 0 & 0 & 0 & & \cdot \\
\cdot & \cdot & \cdot & \cdot & \cdot & \cdot & \cdot & \cdot & \cdot & \cdot & \cdot & \cdot & \cdot & \cdot & \cdot
\end{bmatrix} \qquad \text{(A–52)}$$

Or

$$K_3 \Rightarrow \mathbb{K}_3 = \begin{bmatrix}
\cdot & \cdot & \cdot & \cdot & \cdot & \cdot & \cdot & \cdot & \cdot & \cdot & \cdot & \cdot & \cdot & \cdot & \cdot \\
\cdot & 0 & 0 & 0 & 0 & & & & & & & & & 5 & \cdot \\
\cdot & 0 & 0 & 0 & 0 & & & & & & & & 4 & & \cdot \\
\cdot & 0 & 0 & 0 & 0 & & & & & & & 3 & & & \cdot \\
\cdot & 0 & 0 & 0 & 0 & & & & & & 2 & & & & \cdot \\
\cdot & & & & & 0 & 0 & 0 & 1 & & & & & & \cdot \\
\cdot & & & & & 0 & 0 & 0 & 0 & & & & & & \cdot \\
\cdot & & & & & 0 & 0 & 0 & 0 & & & & & & \cdot \\
\cdot & & & & & -1 & 0 & 0 & 0 & & & & & & \cdot \\
\cdot & & & & -2 & & & & & 0 & 0 & 0 & 0 & & \cdot \\
\cdot & & & -3 & & & & & & 0 & 0 & 0 & 0 & & \cdot \\
\cdot & & -4 & & & & & & & 0 & 0 & 0 & 0 & & \cdot \\
\cdot & -5 & & & & & & & & 0 & 0 & 0 & 0 & & \cdot \\
\cdot & \cdot & \cdot & \cdot & \cdot & \cdot & \cdot & \cdot & \cdot & \cdot & \cdot & \cdot & \cdot & \cdot & \cdot
\end{bmatrix} \qquad \text{(A–53)}$$

Take note of (A–52) and (A–53), they are two different types of Non-Hermitian operators, antisymmetrical matrices, base on them, proceed as follows

$$L_3(\eta) \Rightarrow \mathbb{L}_3(\eta) \qquad \text{(A–54)}$$

From (A–57), some curious spectacles that similar to (A–48) are emerged [6] :

For (A–52) , For (A–53)

$$\mathbb{L}_3^{00}(\lambda) = \begin{bmatrix} Ch\,\lambda & Sh\,\lambda \\ Sh\,\lambda & Ch\,\lambda \end{bmatrix} \quad , \quad \mathbb{L}_3^{00}(\lambda) = \begin{bmatrix} Sech\,\lambda & -Th\,\lambda \\ Th\,\lambda & Sech\,\lambda \end{bmatrix}$$

$$\mathbb{L}_3^{01}(\lambda) = \begin{bmatrix} Ch\,2\lambda & Sh\,2\lambda \\ Sh\,2\lambda & Ch\,2\lambda \end{bmatrix} \quad , \quad \mathbb{L}_3^{01}(\lambda) = \begin{bmatrix} Sech\,2\lambda & -Th\,2\lambda \\ Th\,2\lambda & Sech\,2\lambda \end{bmatrix}$$

$$\mathbb{L}_3^{02}(\lambda) = \begin{bmatrix} Ch\,3\lambda & Sh\,3\lambda \\ Sh\,3\lambda & Ch\,3\lambda \end{bmatrix} \quad , \quad \mathbb{L}_3^{02}(\lambda) = \begin{bmatrix} Sech\,3\lambda & -Th\,3\lambda \\ Th\,3\lambda & Sech\,3\lambda \end{bmatrix}$$

..... = ... = ...

(A–55) (A–56)

Then, Einstein Special Relativity is extended to the following so-called :

Worm Hole Special Relativity in Multi-Level Universes World: [6]

$$\begin{bmatrix} x'_{0,j} \\ x'_{3,j} \end{bmatrix} = \mathbb{L}_3^{0,j}(\eta) \begin{bmatrix} x_{0,j} \\ x_{3,j} \end{bmatrix} \qquad (A–57)$$

For (A–55), have: , For (A–56), have

$$x'_0 = Ch\,\eta\; x_0 + Sh\,\eta\; x_3 \quad , \quad x'_0 = Sech\,\eta\; x_0 - Th\,\eta\; x_3$$

$$x'_3 = Sh\,\eta\; x_0 + Ch\,\eta\; x_3 \quad , \quad x'_3 = Th\,\eta\; x_0 + Sech\,\eta\; x_3$$

$$\eta = \lambda, 2\lambda, 3\lambda, \ldots \quad , \quad \eta = \lambda, 2\lambda, 3\lambda, \ldots$$

(A–58) (A–59)

and

$$Sh\,\eta = \beta\gamma \quad (A–58.1) \quad , \quad Th\,\eta = \beta\gamma \quad (A–59.1)$$

$$Ch\,\eta = \gamma \quad (A–58.2) \quad , \quad Sech\,\eta = \gamma \quad (A–59.2)$$

$$Th\,\eta = \beta \quad (A–58.3) \quad , \quad Sh\,\eta = \beta \quad (A–59.3)$$

$$Ch^2\,\eta - Sh^2\,\eta = 1 \quad (A–58.4) \quad , \quad Sech^2\,\eta + Th^2\,\eta = 1 \quad (A–59.4)$$

j) Spin Topological Space STS is the space that could discribe and help people understand how the transitions of particle spins, between various types of spin particles, are happening. Before this, the concepts of physics and math about these transitions were indistinct and blurred.

To appreciate the beauty and subtlety of STS, the FIG. below is essential.

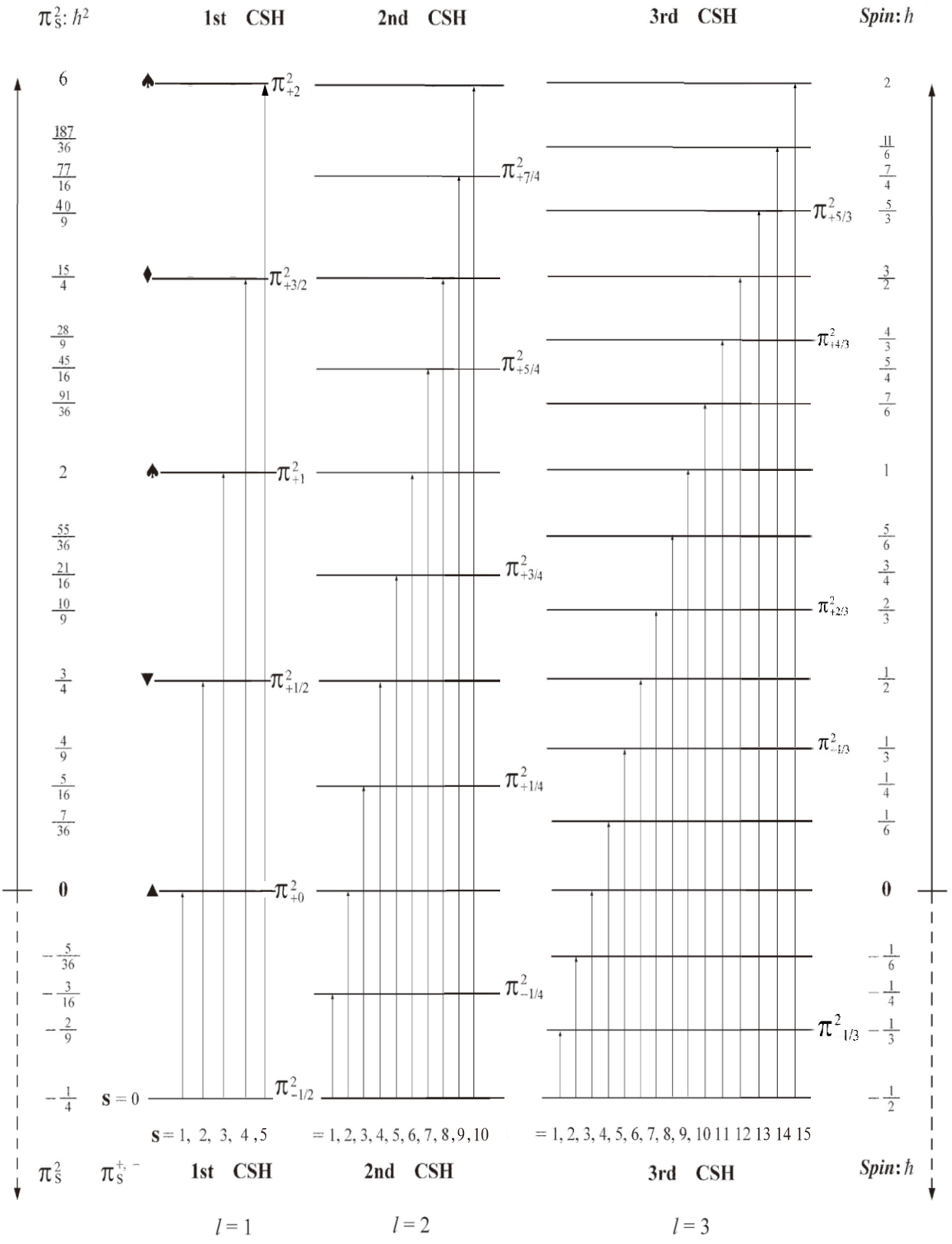

FIG. Phase transitions of Vacuum Bubble Pair $\pi^{+,-}_{s=|i-j|}(l)$ from the sea floor one-fourth $-\frac{1}{4}\hbar^2$ deep in **SAMV** ocean (not to scale) in Spin topological space, **STS**, [4]

Journal of Modern Physics, 2016, 7, 760-773
Published Online April 2016 in SciRes. http://www.scirp.org/journal/jmp
http://dx.doi.org/10.4236/jmp.2016.78071

Scientific Research Publishing

Thermodynamics of Criticality: Percolation Loci, Mesophases and a Critical Dividing Line in Binary-Liquid and Liquid-Gas Equilibria

Leslie V. Woodcock

Department of Physics, University of Algarve, Faro, Portugal
Email: lvwoodcock@ualg.pt

Received 25 February 2016; accepted 26 April 2016; published 29 April 2016

Abstract

High-temperature and pressure boundaries of the liquid and gas states have not been defined thermodynamically. Standard liquid-state physics texts use either critical isotherms or isobars as *ad hoc* boundaries in phase diagrams. Here we report that percolation transition loci can define liquid and gas states, extending from super-critical temperatures or pressures to "ideal gas" states. Using computational methodology described previously we present results for the thermodynamic states at which clusters of excluded volume (V_E) and pockets of available volume (V_A), for a spherical molecule diameter σ, percolate the whole volume ($V = V_E + V_A$) of the ideal gas. The molecular-reduced temperature (T)/pressure(p) ratios ($T^* = k_B T / p\sigma^3$) for the percolation transitions are T^*_{PE} = 1.495 ± 0.015 and T^*_{PA} = 1.100 ± 0.015. Further MD computations of percolation loci, for the Widom-Rowlinson (W-R) model of a partially miscible binary liquid (A-B), show the connection between the ideal gas percolation transitions and the 1st-order phase-separation transition. A phase diagram for the penetrable cohesive sphere (PCS) model of a one-component liquid-gas is then obtained by analytic transcription of the W-R model thermodynamic properties. The PCS percolation loci extend from a critical coexistence of gas plus liquid to the low-density limit ideal gas. Extended percolation loci for argon, determined from literature equation-of-state measurements exhibit similar phenomena. When percolation loci define phase bounds, the liquid phase spans the whole density range, whereas the gas phase is confined by its percolation boundary within an area of low T and p on the density surface. This is contrary to a general perception and opens a debate on the definitions of gaseous and liquid states.

Keywords

Thermodynamics, Criticality, Percolation Transition, Ideal Gas: Liquid State

How to cite this paper: Woodcock, L.V. (2016) Thermodynamics of Criticality: Percolation Loci, Mesophases and a Critical Dividing Line in Binary-Liquid and Liquid-Gas Equilibria. *Journal of Modern Physics*, **7**, 760-773.
http://dx.doi.org/10.4236/jmp.2016.78071

1. Introduction

Almost 40 years ago, in their classic review on the status of liquid state theory [1], Barker and Henderson began with the words "Liquids exist in a relatively small part of the enormous range of temperatures and pressures existing in the universe". The tiny liquid area, in the T-p projection of Gibbs density surface, was defined within either a critical isotherm, or isobar, and a triple point. Above a critical temperature (or pressure) and below the triple-point, the liquid state did not exist. Not everyone agreed with these *ad hoc* bounds, however. For example, recent research on percolation transition loci on Gibbs thermodynamic surfaces [2] shows that J. D. Bernal may have been closer to the truth. Besides noting that the liquid state, albeit metastable, should extend down to absolute zero using random close packing as a starting point, Bernal also argued that the liquid state should extend to supercritical temperatures and pressures, where it is bounded from the gas phase by a "hypercritical" line of discontinuity.

Here, we report results for ideal gas properties, which, alongside real experimental p-V-T properties of a typical real fluid (argon), comprise compelling evidence that the liquid state is not bounded, by either the critical isotherm or isobar. Liquid and gas phases are terminated by percolation loci along any isotherm. Moreover, we find that percolation loci extend all the way from critical coexistence to low density states with ideal gas properties.

The equation-of-state of a real gas with finite molecular size (diameter σ) behaving ideally within a low-density limit, is simply

$$p^* = \rho^* \tag{1}$$

where p^* is a molecular-reduced pressure ($p\sigma^3/k_BT$), T is temperature (K), k_B is Boltzmann's constant, ρ^* is a reduced density ($\rho^* = N\sigma^d/L^d$), where L^d is length (L, $d = 1$), area (A, $d = 2$) or volume (V, $d = 3$). Equation (1) has an abiding role in the description of thermodynamic properties of real molecular fluids. Pressure is everywhere continuous; second and all higher derivatives of $p(\rho)$ are zero. Because of this simplicity, all state functions are exactly known for any d. Equation (1) is a universal scaling law that spans the dimensions.

Within the ideal gas limit of obedience to Equation (1), real fluids with finite size, *i.e.* $\sigma > 0$, however, exhibit various properties that cannot scale with d, linear transport coefficients, for example. Percolation transitions, not unrelated to the transport coefficients, are also strongly dimension dependent in form, and are known to determine thermodynamic phase changes in model lattice gases [3]. Percolation transitions of the available volume (V_A) and excluded volume (V_E) for the insertion of one more molecule of a finite diameter are properties relating to Gibbs energies that effect phase transitions.

For hard-core fluids,

$$V = V_A + V_E \tag{2}$$

then, the ensemble averages $\langle V_A \rangle$ and $\langle V_E \rangle$ equate with chemical potential (μ_i) of species i

$$\mu_i = -k_BT \log_e \left(\langle V_A \rangle / V \right) \tag{3}$$

Equation (3), with Equation (2), defines $\langle V_A \rangle$ and $\langle V_E \rangle$ for real fluids.

For the ideal gas, percolation of V_E is defined as a density above, or temperature below which, the overlapping exclusion spheres of radius σ/2 from a point in a uniformly random distribution of N points, form clusters that can span the whole of V. V_A comprises a distribution in configuration space of accessible pockets in which there are no ideal gas point molecules within one sphere diameter anywhere in the pocket. The percolation transition for V_A is the density above, or temperature below which, the empty pockets coalesce to span the system. For temperatures above percolation, V_A comprises a network of connecting pathways to the whole system accessible to a diffusing sphere in the static ideal gas equilibrium configuration.

2. Percolation Transitions

For an ideal gas the exclusion sphere diameter defines $T^* = k_BT / p\sigma^3 = 1/\rho^*$. Experimental coexistence data on binary liquid phase diagrams is generally obtained at constant pressure (1 atm.) and presented with temperature (T) the dependent variable as a function of mole fraction (X_B), hence at this stage, with binary liquids in

mind, we choose T^* as the state variable. (note: for an ideal gas $T^* = 1/p^* = V^* = 1/\rho^*$) We designate the percolation transition reduced temperatures as T^*_{PE} and T^*_{PA} respectively. Relationships between dimensionality and percolation transitions can be summarized:

d = 1 no percolation

d = 2 PE and PA coincide $T^*_{PE} = T^*_{PA}$ and $\rho^*_{PE} = \rho^*_{PA}$

d = 3 there is an inequality $T^*_{PE} > T^*_{PA}$ and $\rho^*_{PE} < \rho^*_{PA}$

There is a fundamental difference between 2 and 3 dimensions. For d = 2, there are two regions, "gas-like" $T^* > T^*_{PE}$ and "liquid-like" $T^* < T^*_{PE}$, whereas for d = 3 there are three regions, gas-like $T^* > T_{PA}$, liquid-like $T^* < T_{PA}$ and a mesophase, $T^*_{PA} > T^* > T^*_{PE}$. In the mesophase, both the pockets of availability and clusters of exclusion sites percolate the system. The mesophase is both gas-like and liquid-like.

PE both for d = 2 and 3 has been investigated by a number of authors for the present and related systems [4]-[11] Rough estimates of PE for d = 2 and 3 ideal gases can be gleaned from **Figure 3** and **Figure 4** of the paper by Bug *et al.* [4]. Extrapolating their data points, when their attraction parameter $\varepsilon = 0$, to zero density one obtains for d = 2 $\Phi_{PE} \sim 1.2$ and for d = 3 $\Phi_{PE} \sim 0.35$, where Φ is the excluded volume fraction ($=\pi\rho\sigma^3/6$). Heyes and coworkers [5]-[8] report related investigations of PE for various models by MC and MD simulations. From an interpolation to zero density of the hard-sphere fluid variable-exclusion shell percolation threshold Heyes *et al.* [7] obtain $\Phi_{PE} = 0.346$ (d = 3). The most accurate values for both the d = 2 (PE and PA) percolation transition are probably those of Ziff and coworkers: the values for ρ^* are 1.275 (d = 2) and 0.653 (d = 3). An extensive study of ideal-gas PE transitions for exclusion squares, cubes, and other geometric shapes has also been reported [11].

Educational insight, and estimates of $\rho^*_{PE/PA}$ for d = 2 can easily be obtained pictorially in just a few minutes using an EXCEL spreadsheet. **Figure 1** shows a typical configuration, 2000 random numbers from a uniform distribution 0 - 1, *i.e.* an ideal gas (N = 1000) in the vicinity of the percolation transition. Disc diameters do not vary when the square area is expanded or contracted on the display. Fixing the diameter at 5 mm, percolation occurs at L ~ 14.0 cm hence $\rho^*_{PE/PA} = 1.28$ or $T^*_{PE/PA} = 0.77$, *i.e.* in close proximity to reference [9]. Computation of PA for the ideal gas d = 3 has not previously been reported.

There are no reports of PA (d = 3) having been previously investigated or determined for the ideal gas, although the transition density ρ^*_{PA} is known to be 0.537 ± 0.05 for the hard-sphere fluid [12]. Here, we use the same methods, and criteria for percolation, as described previously for the hard-sphere fluid. Both T^*_{PE} and T^*_{PA} have been computed for a range of finite size systems; the results are summarized in **Figure 2**. Thermodynamic limiting values ($N \rightarrow \infty$) are obtained from the linear trendlines.

Every configuration either has a percolating cluster or it does not. Clearly, for small finite systems, there will be configurations that percolate, and some that do not, in the vicinity of PE. The percolation threshold in the computations of Heyes *et al.* [5]-[8] was defined when 50% of configurations have a percolating cluster, with details described by Seaton *et al.* [13]. Here, we define PE using an ensemble average definition of a percolation

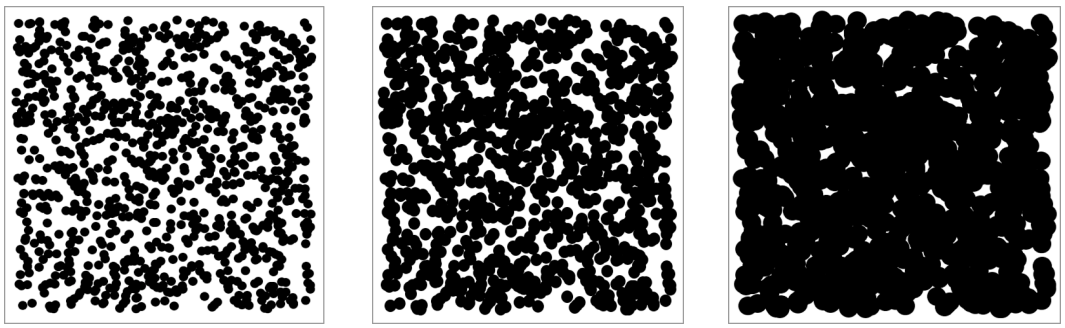

(a) (b) (c)

Figure 1. Excluded and accessible areas (black and white respectively) for a configuration of a two-dimensional ideal gas: (a) "gas-like" density below the percolation transition (b) close to the percolation transition and (c) "liquid-like" density above the percolation transition.

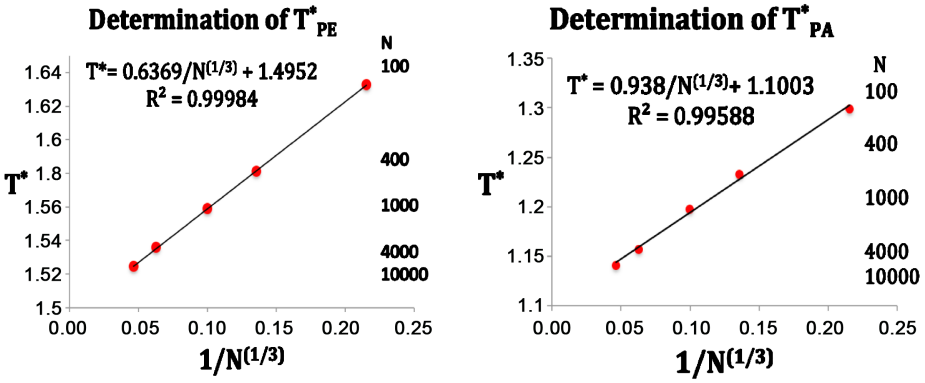

(a) (b)

Figure 2. (a) Ideal gas PE transition (T^*_{PE}) from the mean cluster size distribution saddle-point method [12] for a range of finite systems: (b) Ideal gas PA transition (T^*_{PA}) from zero-diffusivity limit method [12].

density [12]; *i.e.* ρ^*_{PE} is the saddle-point density above which the cluster size probability distribution $P(n)$ is bimodal. This is the normalized probability of a site belonging to a cluster of size n. Above T^*_{PE}, $P(n)$ is a monotonic gas-like distribution, for all PE below T^*_{PE} it is bimodal. Plotting the saddle-point definition of $T^*_{PE}(N)$ against $1/N^{1/3}$ (**Figure 2(a)**) gives a linear trendline that interpolates to the result $T^*_{PE}(N\to\infty)=1.495\pm0.01$ ($\rho^*_{PE}=0.668$).

Our method for determining T^*_{PA} is essentially that described previously for hard spheres [12], except that it is easier for the ideal gas. Here we use N-V-T MD for non-additive binary spheres that can simulate the Widom-Rowlinson (W-R) model fluid [14] [15]. This belongs to the general class of symmetric binary non-additive hard-sphere fluid mixtures defined by collision diameters

$$\sigma_{AA}=\sigma_{BB}=(1+\delta)\sigma_{AB}$$

where δ is a dimensionless non-additivity, that varies from −1, for the W-R penetrable-sphere model binary fluid, via zero for one-component hard spheres, to infinity. Positive δ relates to ionic liquids and ionic crystal structures when mole fraction $X_B = 0.5$.

The MD program solves equations of motion of a binary mixture $N_A + N_B$. The results for the PA values in **Figure 2(b)** are obtained by the mean-squared displacements of B average over many frozen random configurations of ideal gas A. As the B particles do not interact with themselves, we average over all N_B in the same MD simulation run. All the values in **Figure 2(b)** were obtained for equimolar systems. Plotting the point of zero diffusivity, $D_i(\rho, N) \to 0$, against N (N_A in MD run) gives a linear trendline with the result $T^*_{PA}(N\to\infty)=1.100\pm0.01$ ($\rho^*_{PA}=0.908$).

3. W-R Model Binary Liquid

3.1. MD Simulation Results

We have determined T^*_{PE} along isopleths of the binary W-R model fluid; T^* is defined as $T^* = 1/p^*$ and $p^* = p\sigma^3/k_BT$. MD simulations have some advantages over Grand Canonical Monte Carlo [15] (GCMC). Not least is the direct extraction of transport properties for determination of T^*_{PA} loci. These are obtainable by "freezing" component A whilst allowing B to diffuse. The cluster distributions that determine T^*_{PE} also yield accurate values for coexisting X_B by integrating the solute cluster probability distribution $P(n)$ which decreases monotonically, from a maximum at $n = 1$, to zero for clusters of B in solution of A, or vice-verser. Accurate MD pressures are calculated from A-B collision frequencies.

What is the effect on the percolation transitions of increasing the mole fraction of B from the ideal gas limit ($X_B = 0$)? For the isopleth at $X_B = 0.1$, and for $N = 10{,}000$, the reduced pressures at which the two transitions oc-

cur, *i.e.* p^*_{PE} and p^*_{PA} are 0.715 and 0.923 respectively. We find, up to X_B = 0.1 and beyond, both percolation pressures increase with X_B, PE more so than PA, roughly according to

$$p^*_{PE}\left(\rho^*_B\right) \sim p^*_{PE}(0)\left[1+\rho^*_B\right]$$

$$p^*_{PA}\left(\rho^*_B\right) \sim p^*_{PA}(0)\left[1+\rho^*_B/2\right]$$

where $\rho^*_B = \rho^* X_B$. The percolation transition pressures increase with ρ^*_B because, as B are added at constant T, the system expands with both V_A and V_E increasing, but V_E increases more than V_A; adding B causes A-sites to cluster more, whilst creating more spherical B-pockets. The pressures of percolation transitions for finite X_B appear to be coincident with higher-order discontinuities (**Figure 3**) in the supercritical region. Weak thermodynamic discontinuities have been both predicted theoretically for real systems [16], and reportedly seen experimentally [17]. Changes in pressure slopes are evident from the MD excess pressures defined relative to the ideal gas.

$$p^*_{ex} = p^* - \rho^* \tag{4}$$

Figure 3(a) shows the isopleth X_B = 0.1 has four distinct regions. At high density, in the two-phase region, the MD pressures averaged over 100 million A-B collisions still show fairly large uncertainties. The maximum pressure along any isopleth coincides with the first-order mixing-demixing transition. This reflects the thermodynamic equilibrium condition of minimal Gibbs energy (G) (since $\mathrm{d}G_T = \rho^{-1}\mathrm{d}p$) for equilibrium on either side of the transition. At the mole fraction X_B = 0.1 in the mesophase region pressure increases linearly with density. In the one-phase region, the MD data is sufficient to observe that the percolation loci appear to be associated

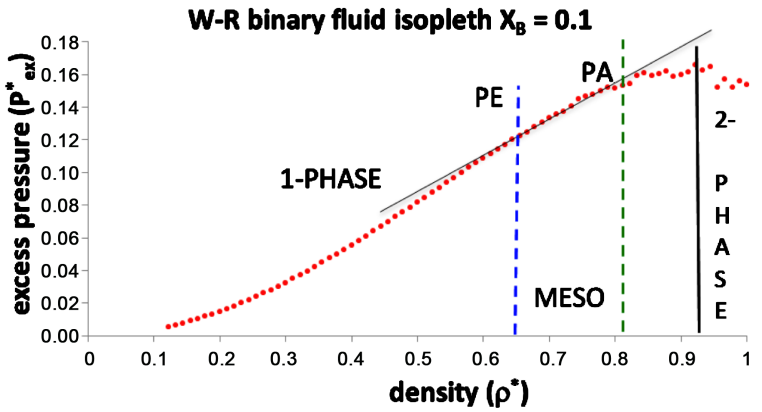

(a)

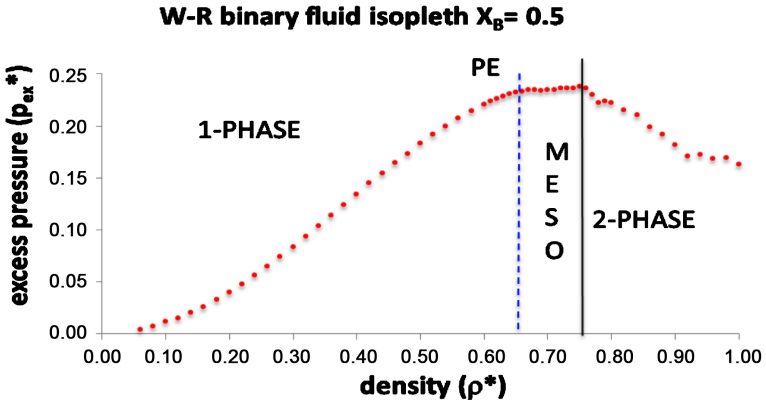

(b)

Figure 3. Excess pressures of the Widom-Rowlinson binary fluid mixture: (a) along the isopleth X_B = 0.1 (N = 10,000); (b) along the equimolarisopleth X_B = 0.5 (N = 8000).

with changes in slope that could reflect higher-order thermodynamic phase transitions, but presently not sufficiently accurate to establish the order or strength of discontinuities.

The vertical dashed lines in **Figure 3** correspond to the percolation transition densities computed explicitly by the methods described in the text and referenced [5]: they coincide with changes in the slope of the excess pressure. The MD results for $X_B = 0.5$ show three regions; there is no PA, just the PE transition at the density 0.65. The change in the slope of p^*_{ex}, and hence also p^*, is more pronounced. The rigidity function $(\mathrm{d}p/\mathrm{d}\rho)_T$ is again constant in the mesophase, close to zero as evidenced by a very slight slope.

3.2. Demixing Phase Transition

In all previous investigations of the W-R fluid, the existence of a critical point singularity at the UCST has invariable been assumed at the outset [14] [15]. The connection between percolation loci and phase transitions is now well-established. Equation (3) of this paper exactly relates V_A or V_E to chemical potentials, which determine equilibrium between phases. The essential new result here, is for the percolation of V_A *i.e.* T^*_{PA} in 3d (**Figure 2(b)**) which ~35% greater than the already known T^*_{PE}. Between these transition temperatures both V_E and V_A percolate, hence the mesophase only exists in real 3d liquid-liquid or liquid gas fluids. This result for the ideal gas enables the connection between percolation loci and the demixing transition to be determined.

As solute concentration (X_B) increases in the W-R fluid, the two percolation temperatures become closer and then coincide. From thermodynamic considerations, this intersection triggers a first-order phase transition, with the two different phases having the same T, p and chemical potential. It is this fundamental property of percolation in 3d that does not exist in 2d that vitiates the hypothetical concept of universality, and confirms the new science of criticality for both liquid-gas [2], and now also liquid-liquid coexistence.

Along any isopleth, the pressure is a maximum at the two-phase boundary to comply with the thermodynamic requirement of minimum Gibbs energy as shown in **Figure 3**. However, we have also determined the coexistence line directly from the results for the $X_B = 0.5$ equimolar isopleth by a more accurate method than GEMC [15], by integrating the cluster distribution, obtained from all MD runs, up to the hiatus in 2-phase region. **Figure 4** shows some plots of the cluster distributions and the integrated mole fractions. The distribution is bimodal in the mesophase and monomodal in the one-phase region. In the two-phase region it is bimodal with a hiatus.

Reference [15] provides an estimate of the coexistence density and pressure for several X_B well away from the critical coexisting compositions. For $X_B = 0.1$, $\rho^* \sim 0.86$. Because of the symmetry of the W-R model the mean of the two coexisting compositions at the upper critical consolute composition must be at $X_B = 0.5$. Our results show that there is no "critical point". Thus in **Figure 3(b)** the onset of the two-phase region is at the mean criti-

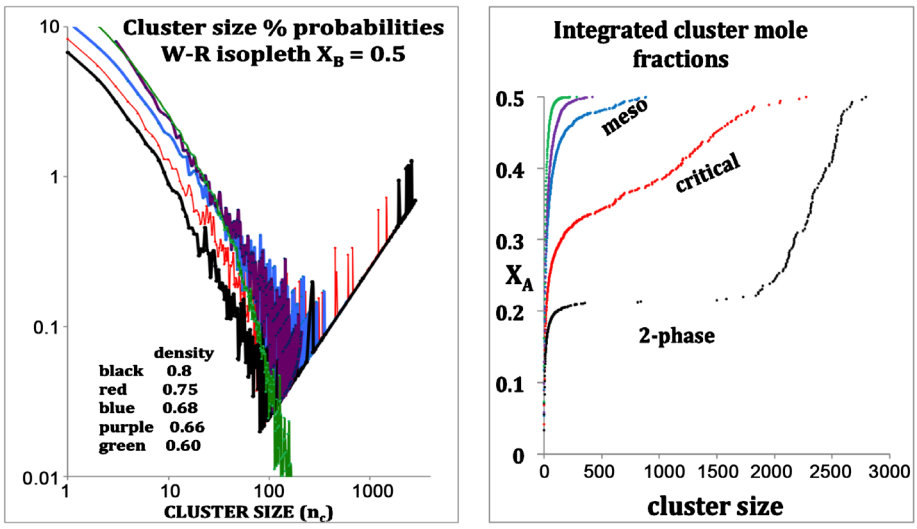

(a) (b)

Figure 4. (a) Cluster size distributions for W-R binary fluid; (b) integrated mole fractions for state points in 4a showing how the coexistence mole fraction is obtained in the 2-phase region, e.g. at the density 0.8 (black points) $X_A = 0.214 \pm 0.01$.

cal density; there is a flattish pressure vs. density mesophase up to the phase separation followed at higher densities by a steady fall of pressure in the two-phase region. The vertical line is at $\rho^* \sim 0.75$ is close to the previously estimated demixing density $\rho^*(T) = 0.749$ of de Miguel *et al.* [15].

The percolation loci on the T^*-X_B surface (**Figure 5**), to within the uncertainty of the data, decrease with X_B an intersection occurs when $T^* = 1.00 \pm 0.01$ with the uncertainty estimated from the combined regressions. At this intersection the fluid phase separates as solutions of A in B and B in A have the same T, p, and μ of both species (chemical potential). Solving for X_B when $T^*_{PE} = T^*_{PA}$ gives $X_B = 0.339$ for the critical coexistence mole fraction. From the coexistence pressures, and direct computations of PA and PE, we are able to construct a phase diagram for the W-R binary fluid. The temperature loci of the percolation transitions fit the trendlines (dashed lines in **Figure 5**)

$$T^*_{PE} = 1.495 - 0.750 X_B$$

$$T^*_{PA} = 1.100 + 0.045 X_B - 1.004 X_B^2$$

showing the connection between percolation and the demixing phase transition. Note the perfect symmetry about the isopleth $X_B = 0.5$.

The present results show a dividing line at T^*_c, rather than an Ising-like singular critical point. The evidence for higher-order discontinuities at PE and PA loci may invalidate some mean-field theoretical approaches.

The W-R binary fluid is essentially a simple model of partially miscible liquids, e.g. cyclohexane and methanol**.** The high-density fluid states at low temperatures are immiscible ideal gases. Here we have an example of what could arguably be described as "liquid states" of the ideal gas. Within the respective uncertainties, the present results agree with de Miguel *et al.* [15]. Our phase diagram could just as easily be presented as p^*, ρ^* or V^*, it would not change the science. We choose T^* to identify directly with real binary-liquid experimental phase diagrams that exhibit a similar UCST (**Figure 6**).

3.3. Experimental Evidence

Many mixtures of dissimilar liquids, just as seen here for the W-R fluid, separate into two coexisting phases over a lower temperature range. On heating, compositions of the two phases become more and more similar and at a critical temperature there is a single phase. This is the UCST. At higher temperature there is just one liquid phase. It is possible to define various percolation thresholds for clusters of solute molecules in the single liquid phase by analogy with clusters of molecules in a gas phase. The present evidence suggest that they these percolation loci that delimit the solution will give rise to a mesophase and a coexistence line the UCST [17].

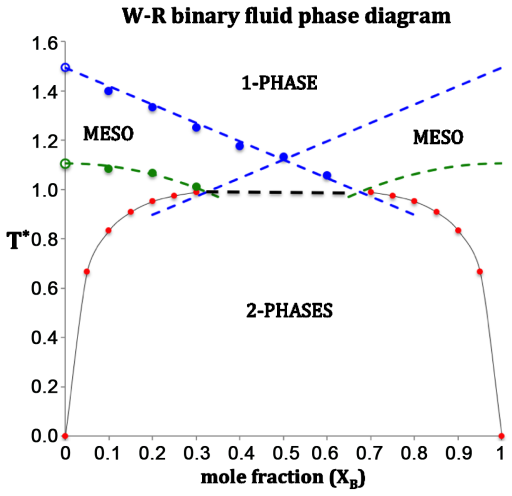

Figure 5. Phase diagram of the Widom-Rowlinson binary fluid; T^*_{PE} and T^*_{PA} loci blue and green respectively; percolation transitions of the ideal gas open circles at $X_B = 0$; computed 2-phase coexistence state points are the red circles.

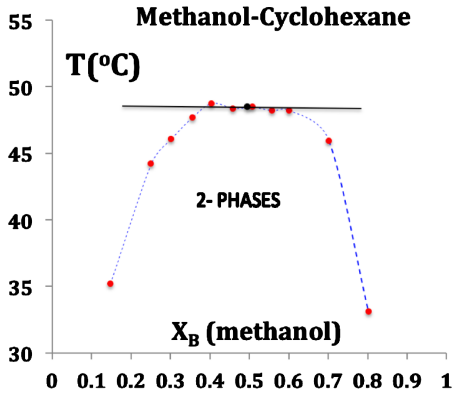

Figure 6. Typical experimental data points for the 2-phase coexistence of a partially miscible liquid-liquid mixture showing a UCST at horizontal line within the uncertainty: data from [19] [19] The black dot is a hypothetical "critical point".

Experimental critical parameters for a range of partially miscible binary liquids are tabulated in Kaye and Laby [19]. The critical compositions are actually mean compositions of the maximum observable coexisting compositions, defined and obtained using the law of rectilinear diameters in the vicinity of T_c., usually in conjunction with a cubic equation-of-state, or similar [19] [20]. This also applies to the critical densities of computer models using Gibbs ensemble Monte Carlo methods [15], just as for liquid-gas coexistence in square-well model fluids [21]-[24]. Likewise, within the uncertainties of experimental measurements of liquid-liquid UCST (**Figure 6**), the coexistence envelopes at T_c are flat on top. The hypothetical "critical point" has been obtained using *a priori* hypothesis of existence, and is defined only by a numerical parameterization.

The simulation results we present for the W-R mixture suggest that the phase diagram of real liquids will be determined by the intersection of percolation loci. These results for the W-R mixture should stimulate further laboratory experimental research into the percolation loci. The critical "point" in **Figure 6** is defined only by a numerical parameterization using a theoretical functional form that presumes its existence.

4. PCS Liquid-Gas Model

Probably the simplest 3D model Hamiltonian of a molecular fluid, which is continuous in phase space, and exhibits liquid-gas criticality and two-phase gas-liquid coexistence, is the penetrable cohesive sphere (PCS) fluid [14] [15]. The internal energy (U) is simply

$$U = 3Nk_BT/2 + \varepsilon\left(\left\langle V_E/v_0\right\rangle - N\right) \tag{5}$$

where k_B is Boltzmann's constant and T is temperature (K); the angular brackets denote a configurational average. Equation (5) defines an attractive molecular energy (ε) complementary to the volume of overlapping clusters, *i.e.* V_E as defined above for an ideal gas, of a configuration of N penetrable spheres, and v_0 ($=4\pi\sigma^3/3$) is the volume of a sphere. At low temperatures, this model exhibits the exact properties of an ideal gas in both the low-density (gas phase) and high-density (liquid-phase) limits. Here again, there is a liquid-like state with the properties of the ideal gas. Both W-R and PCS models, therefore raise a curious conundrum. Could a supercritical fluid with the properties of an ideal gas be described as "liquid"?

Experimental thermodynamic liquid-gas coexistence phase diagrams [21] [23] have traditionally been obtained along isotherms by measurements of coexistence pressures. Hence, we prefer to maintain the connection with experimental data of gas-liquid thermodynamic equilibrium measurements established over a period of 150 years by plotting $p(\rho)_T$ isotherms (note the contrast with [15]). A more detailed analysis of the connection of percolation loci with experimental isotherms is recently published [18].

Every state of the PCS fluid corresponds to a transcribed state of the W-R binary model fluid. The equations for the transcription from the W-R binary percolation and coexistence pressures (**Figure 7(a)**) to the PCS one-component gas-liquid pressure can be derived, for example, from an analysis of the respective grand partition functions as described by de Miguel *et al.* [15]. The transcription equations we need here are

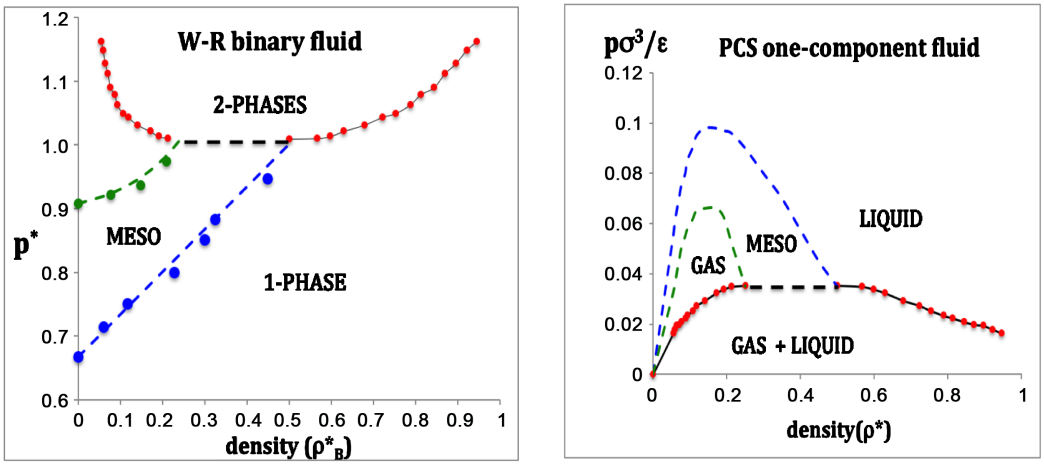

(a) (b)

Figure 7. (a) Phase diagram of the W-R binary fluid in the pressure-density projection: p^*_{PE} and p^*_{PA} loci are dashed blue and green respectively; coexistence data points are red circles; (b) phase diagram of the PCS liquid-gas system obtained by transcription of W-R pressures in 7a.

$$\text{pressure} \quad [\text{PCS}]\, p\sigma^3/\varepsilon = [\text{W-R}]\left(p^* - Z^*_A/v_o\right)k_BT/\varepsilon \tag{6}$$

$$\text{density} \quad [\text{PCS}]\, p\sigma^3 = [\text{W-R}]\,\rho^*_B \tag{7}$$

where Z^*_A is the thermodynamic activity of a component defined as $\ln Z^* = \mu/k_BT$ and μ is Gibbs chemical potential relative to the ideal gas at the same T, p. Gibbs energy change, hence Z^*, can be obtained by integrating the excess pressure loci at constant T, with respect to density.

$$\mu/k_BT = \int \left(p - p_{id}\right) \mathrm{d}\log_e\left(\rho_B\right) \tag{8}$$

For the one-component isomorphism of W-R fluid, pressure is the natural variable so the p^* vs. ρ^* representation along isotherms relates directly to experimental results and phase diagrams. We plot the values of the pressure at coexistence vs. ρ^* which we plot in **Figure 7(b)**. Itshows that the simplest imaginable continuous Hamiltonian model to exhibit liquid-gas coexistence and a critical temperature has a coexistence line at the intersection percolation loci as observed for square-well and Lennard-Jones model fluids and many real fluids [24]-[28]. There is a liquid-gas critical dividing line between 2-phase coexistence and a supercritical mesophase. The liquid state extends to an ideal gas zero density and pressure limit. This raises the question: could there exist a high temperature limit of the percolation transition loci in real fluids at very low density in the region of obedience to the ideal gas law?

The evidence suggests this is indeed the case, provided we re-interpret the experimental thermodynamic properties of real fluids in the light of our knowledge of percolation transitions. For 80 important gases or liquids, including the simplest real liquid argon, in the NIST "Thermophysical Properties of Fluid Systems" data bank [23], equation-of-state p-V-T data with 6-figure accuracies are obtainable. These $p(\rho)_T$ supercritical isotherms have been formulated, however, using a large number of parameters and an assumption of a supercritical continuity of liquid and gas. If there were to be no continuity of liquid and gas, there would need to exist three different equations-of-state to describe the gas and liquid phases, bounded by percolation loci, and the mesophase region in between. Present findings suggest theory-based equations-of-state with far fewer parameters, and with scientifically correct functional forms should eventually replace the NIST equations. Present observations indicate a virial expansion for the gas phase, perhaps a free-volume expansion for the liquid, and a linear combination for the mesophase.

5. Real Fluids

Although lacking a molecular-level definition, for any real fluid, for which an exact Hamiltonian is generally

unknown, the percolation loci can be defined and obtained phenomenologically along any thermodynamic equilibrium isotherm by the rigidity inequalities [18]. In the case of real fluids with attractive potentials, the percolation transition bounding the gas phase, *i.e.* the counterpart of PE for impenetrable spheres, has been designated PB, as it is a percolation of bonded clusters.

Rigidity (ω_T) is the work required to isothermally increase the density of a fluid; with dimensions of molar energy and is plotted for a range of isotherms for CO_2 in **Figure 8**. The symmetry of the rigidity in both the subcritical and supercritical regions is the subject of a recent paper [18]. We note from **Figure 8** that the percolation loci PB and PA appear to be converging at the Boyle rigidity in the case of CO_2.

The rigidity state function relates directly to the change in Gibbs energy (G) with density at constant T according to

$$w_T = \left(\mathrm{d}p/\mathrm{d}\rho\right)_T = \rho\left(\mathrm{d}G/\mathrm{d}\rho\right)_T \tag{9}$$

The following inequalities (10)-(12) are presently empirical, but do have a molecular-level explanation in terms of the number density fluctuations of gas and liquid respectively [18]

$$\text{gas} \quad \rho < \rho_{PB} \quad \left(\mathrm{d}\omega/\mathrm{d}\rho\right)_T < 0 \tag{10}$$

$$\text{meso} \quad \rho_{PB} > \rho > \rho_{PA} \quad \left(\mathrm{d}\omega/\mathrm{d}\rho\right)_T = 0 \tag{11}$$

$$\text{liquid} \quad \rho > \rho_{PA} \quad \left(\mathrm{d}\omega/\mathrm{d}\rho\right)_T > 0 \tag{12}$$

It is clear from Equation (9) that $\omega \geq 0$, *i.e.* rigidity must always be positive: Gibbs energy cannot decrease with pressure when T is constant. By these definitions, moreover, not only can there be no "continuity" of gas and liquid, but the gas and liquid states are fundamentally different in their thermodynamic description. Rigidity is determined by number density fluctuations at the molecular level, which have different density dependencies in either phase. The gas phase comprises one large void with many small clusters, which determine fluctuations, whereas the liquid phase comprises one large cluster and with many vacant pockets, which determine density fluctuations. Since the properties of a hole or an occupied site are statistically equivalent, this give rise to a symmetry of supercritical properties between gas and liquid phases [18].

Experimental argon isotherms [21]-[23] from the critical temperature (T_c = 151K) to 500K are plotted in **Figure 9.** All the isotherms below a temperature around 400K show that there is a flat meso region, *i.e.* $(\mathrm{d}\omega/\mathrm{d}\rho)_T$ = 0. In this narrow range, for each supercritical isotherm, to within the uncertainty of the original experimental data, the rigidity is constant. A value can be obtained by a linear fit over a finite density range with a linear trendline regression between 0.999999 and 1.0 for all the supercritical isotherms in **Figure 9**. An accurate equation-of-state for the meso region is thus obtained

$$p\left(meso\right) = \omega_T \rho + p_0 \tag{13}$$

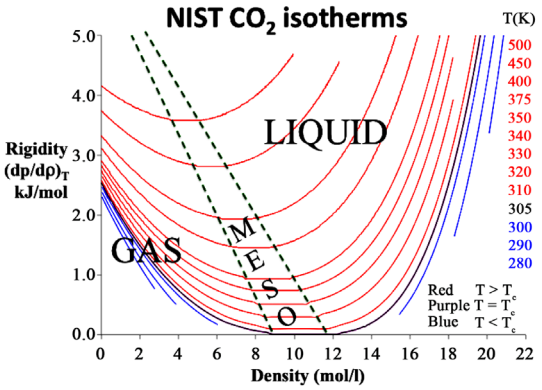

Figure 8. Supercritical isotherms of carbon dioxide: the rigidity is obtained from NIST thermophysical tables with 4-figure accuracy [23]: loci of PB and PA that bound gas and liquid respectively are the dashed lines. The percolation loci appear to be converging at ρ = 0; the Boyle temperature for CO_2 is 715K corresponding to a rigidity of 5.945 KJ/mol.

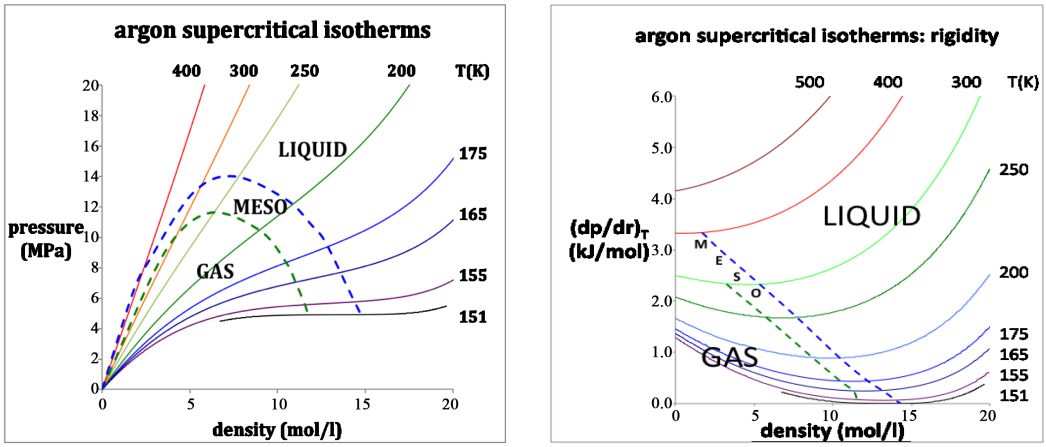

(a) (b)

Figure 9. Supercritical isotherms of fluid argon from NIST Thermophysical Property Tables [23]: loci of PB and PA are green and blue respectively (a) pressure isotherms; (b) rigidity isotherms.

where ω_T is the rigidity along any isotherm T(K) and p_0 is a pressure constant. The percolation loci densities can be estimated by observing the differences p(gas) − p(meso), and p(liquid)–p(meso), both decrease quadratically with density, and interpolate to zero at the percolation loci densities ρ_{PB} and ρ_{PA}.

The initial slope of the percolation loci in the pressure plot (**Figure 9(a)**) corresponds to an intercept temperature obtained from percolation loci in **Figure 9(b)** at zero density, as $\omega(\rho \to 0) = Nk_BT$ for an ideal gas. All molecular gases exhibit a characteristic temperature at which the second virial coefficient changes sign. This corresponds to a low-density limit of the percolation transition loci that may converge together at or below this temperature. The Boyle temperature of argon is 407 K [23] corresponding to a rigidity of 3.38 KJ/mol.

6. What Defines "Liquid Phase"?

6.1. Phase Diagram

The results presented here for the percolation transition loci comparing both real and model fluids reaffirm previous observations [24]-[28] that there is no critical point singularity on Gibbs density surface for gas-liquid condensation. Rather, there is a coexistence boundary line at the critical temperature, above which there exists a mesohase between the percolation loci that bound the liquid and gas phases. From the present W-R results, we can further infer that partially miscible liquid-liquid mixtures will also show an upper critical consolute temperature with a dividing line separating one- and two-phase regions. Above this critical divide, there will be a mesophase bounded by the percolation loci that may extend to the ideal dilute solution limits. Experimental studies of liquid-liquid UCST phenomena, however, are limited, being generally at ambient pressures and terminate at the boiling temperatures.

Returning to the question about universality and dimensionality dependence of the description of criticality, we observe for $d = 2$, since PE = PA for all densities (or concentration X_B), the phase behavior and criticality will be quite different; there can be no mesophase in 2-dimensions. We conjecture, therefore, that the percolation locus intersects the equimolarisopleth with a critical singularity at $X_B = 0.5$ for the $d = 2$ W-R model. Another consequence of the absence of a $d = 2$ mesophase would be no metastability beyond the first-order phase boundaries, and, unlike $d = 3$, no metastability and hence no spinodals within the subcritical bimodals. The existence of a mesophase is a property only of $d = 3$ systems. This difference in the description of liquid-gas criticality between 2 and 3 dimensions vitiates the hypothetical "universality" concept as applied to liquid-gas, and binary-liquid, criticality.

The present results for various percolation loci suggest that all real atomic and molecular fluids will have a liquid state that is bounded only by a percolation transition at high temperature and its equilibrium freezing transition at low temperature along any isotherm. The boundary may be defined phenomenologically by inequality (12). The locus of this liquid-state boundary is seen to extend all the way from the liquid critical temperature and pressure, to an ideal gas at limiting low density. On the basis of these observations, it is the "gas phase", *i.e.* de-

fined by the inequality (10) that exists in a limited area of the universal T-p plane.

We note, however, that there can be no zero of density/pressure for a real fluid, as they become logarithmic to high vacuum levels. The truly ideal gas cannot exist in reality; the sign of the second virial coefficient determines the designation "gas" or "liquid", by the rigidity criterion and in this limit. The liquid area of existence extends to infinite pressure and temperature; whereas the gas phase extends to infinite vacuum, but only below a certain temperature. It appears the liquid phase will extend upwards in temperature, for all pressures to perhaps continuously become plasma (**Figure 10**). This is contrary to what is hitherto generally believed to be liquid state [1].

6.2. Ideal Gas Connection

The symmetry similarity between gas and liquid opens the way to an alternative definition of liquid state, which is usually regarded just as the high density portion of the fluid phase below the critical temperature, *i.e.* defined *ad hoc* as being bound by the critical isotherm, or sometimes the critical isobar. Here we advocate a thermodynamic definition. A "liquid" phase can be identified as the region at density higher than the available volume percolation transition.

On examination of the loci of two percolation transition densities in real gases at high dilution, we note that these lines do not have any thermodynamic signature in the equilibrium properties of the ideal gas. The "ideal gas" is a fictitious concept that cannot exist in reality. In any real gas, the density cannot go to zero. It is logarithmic; for all real gases behaving ideally, thermodynamic properties everywhere depend upon a distance scale. In the W-R binary-liquid and PCS fluid it is the penetrable sphere diameter. For real gases, the percolation transitions are present in the low-density region of obedience to the ideal gas law, *i.e.* when $p \sim \rho kT$ and extend to the Boyle temperature. Thus, in the low-density limit, the boundary between gas and "liquid" phases according the criteria of Equations (10)-(12) becomes the sign of the second virial coefficient (b_2), as defined in the expansion of pressure in powers of density along any isotherm

$$p = \rho k_B T\left(1 + b_2(T)\rho + \cdots + b_n(T)\rho^{(n-1)} + \cdots\right) \tag{13}$$

In the gas region of the phase diagram $b_2(T)$ is negative, whereas in a region of a liquid phase it is positive; at the Boyle temperature b_2 is zero.

A definition of liquid state based on the existence of percolation lines has implication for the thermodynamics of the system for the following reason. When the two supercritical percolation lines that bound the existence of liquid and gas phases intersect on the Gibbs density surface the respective phases have the same temperature and pressure but different densities, and therefore also the same Gibbs chemical potential, and hence coexist at a first-order phase transition. These new results for the percolation transitions of an ideal gas and loci for model fluids, are valuable contributions to the literature as they lead to an alternative more plausible interpretation of the phase behavior of the W-R model binary liquid and the one-component liquid gas fluid. The possible alternative operative description of "liquid" phase is a corollary of these findings.

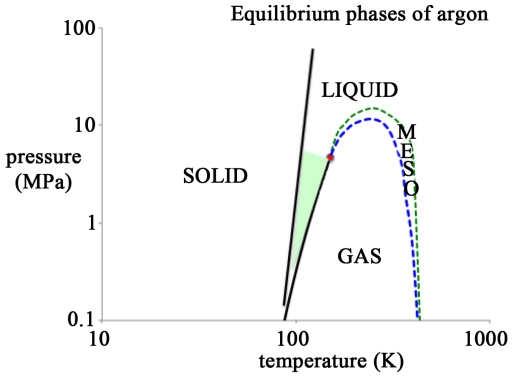

Figure 10. Phase diagram for argon showing the percolation loci that bound the liquid and gas states and mesophase: the tiny shaded area is generally referred to as "liquid": the red circle is the critical point on the p-T projection [1].

7. Conclusions

In Section 2 we have presented a new result for the penetrable sphere available volume percolation transition temperature (T_{PA}^*) of an ideal gas and found that $T_{PA}^*/T_{PE}^* = 1.36$. We conclude that the $d = 3$ ideal gas has three regions liquid-like, gas-like, and a meso-region wherein both V_E and V_A percolate. The connection to the coexistence envelope of a W-R fluid is the ultimate compelling evidence for the absence of any van der Waals singularity on the density surface of liquid-gas equilibrium or on composition surface of the partially miscible binary liquid at the critical temperature or pressure.

In Section 3 we have reported the direct determination of both percolation loci T_{PA}^* and T_{PE}^* along several isopleths of the W-R fluid. We find that both percolation loci decrease with composition X_B (or X_A) and, around $T^* \sim 1$, and intersect with two phases then having the same temperature, pressure and minimal chemical potential at the known critical temperature. It is wholly consistent with previous results for the intersection of percolation loci in the p-T plane at the critical temperatures for model square-well fluids [23], Lennard-Jones fluids [24], and real fluids including argon [26] [26] and water [27]. To suggest that percolation transitions are unrelated to thermodynamic properties would imply that the intersection of percolation loci at p_c-T_c, in all these systems, would have to be a series of incredible coincidences. This is quite implausible.

The phase behavior (Section 4) for the model penetrable sphere fluid obtained by transcription of the W-R fluid properties, therefore, is further compelling evidence that there is no critical point on Gibbs density surface for liquid-gas equilibria. This simple model liquid-gas Hamiltonian shows a critical dividing line between a maximum coexisting gas density and a minimum coexisting liquid density, above which exists a supercritical mesophase.

We have also shown that the thermodynamic state function rigidity, $(\mathrm{d}p/\mathrm{d}\rho)_T$, can define a distinction between gas and liquid. For any one-phase system rigidity is everywhere positive; in any two-phase region $\omega = 0$. Rigidity decreases with density for a gas and increases with density for a liquid. For temperatures above critical coexistence the rigidity has a constant value in the mesophase that separates the percolation loci, which bound the limits of existence of liquid and gas phases in the supercritical region.

We have compared the results for the ideal gas percolation ratios with the high-temperature, low pressure and density, limits of argon. The results from the modern NIST thermophysical property tables [23] indicate that the supercritical mesophase, at least in the case of simple fluids, extends all the way to a dilute gas behaving ideally. This reopens the debate "What is liquid?" [1].

Finally, we have presented results that show there cannot be "universality" in the description of criticality between 2- and 3-dimensional systems. The mesophase is a fundamental property of complementary excluded and available volume percolation loci only in 3d, which does not exist in 2d. Hence, there can be a critical point singularity on the density surface of 2d fluids, whereas it is a critical dividing line for real 3d liquid-gas thermodynamic systems.

Acknowledgements

We acknowledge this paper is written by invitation of Guest-Editor Prof. Chan Kwong-Yu of the University of Hong Kong in honor of distinguished liquid-state physicist Dr. Yiping Tang. This version has benefited from some referees comments. We remain heartened, however, that there is nothing to vitiate this new science of criticality in any previous referee reports, including those contrived by Molecular Physics editor G. Jackson to reject this new science of liquid-gas criticality. These reviews and rebuttals, together with an acknowledged list of known contributors to this debate, will be published elsewhere.
https://www.researchgate.net/profile/Leslie_Woodcock

References

[1] Barker, J.A. and Henderson, D. (1976) *Reviews of Modern Physics*, **48**, 587-625. http://dx.doi.org/10.1103/RevModPhys.48.587

[2] Finney, J.L. and Woodcock, L.V. (2014) *Journal of Physics*: *Condensed Matter*, **26**, 463102.

[3] Stauffer, D. and Aharony, A. (1994) Introduction to Percolation Theory. 2nd Edition, Chapter 7: Percolation and Thermal Phase Transitions. Taylor and Francis, London.

[4] Bug, A.L.R., Safran, S.A., Grest, G.S. and Webman, I. (1985) *Physical Review Letters*, **55**, 1896-1899. http://dx.doi.org/10.1103/PhysRevLett.55.1896

[5] Heyes, D.M. and Melrose, J.R. (1988) *Journal of Physics A*: *Mathematical and General*, **21**, 4075-4085. http://dx.doi.org/10.1088/0305-4470/21/21/015

[6] Heyes, D.M. (1990) *Journal of Physics*: *Condensed Matter*, **2**, 2241-2249. http://dx.doi.org/10.1088/0953-8984/2/9/013

[7] Heyes, D.M., Cass, M. and Branka, A.C. (2006) *Molecular Physics*, **104**, 3137-3146. http://dx.doi.org/10.1080/00268970600997721

[8] Heyes, D.M. and Okumura, H. (2006) *The Journal of Chemical Physics*, **124**, 164507. http://dx.doi.org/10.1063/1.2176675

[9] Quintanilla, S., Torquato, R.M. and Ziff, J. (2000) *Journal of Physics A*: *Mathematical and General*, **23**, 399-407. http://dx.doi.org/10.1088/0305-4470/33/42/104

[10] Lorentz, C.D. and Ziff, R.M. (2001) *The Journal of Chemical Physics*, **114**, 3659-3661. http://dx.doi.org/10.1063/1.1338506

[11] Baker, D.R., Paul, G., Sreenivisen, S. and Stanley, H.E. (2002) *Physical Review E*, **66**, Article ID: 046136. http://dx.doi.org/10.1103/PhysRevE.66.046136

[12] Woodcock, L.V. (2011) *AIChE Journal*, **58**, 1610-1618. http://dx.doi.org/10.1002/aic.12666

[13] Seaton, N.A. and Glandt, E.D. (1987) *The Journal of Chemical Physics*, **86**, 4668-4677. http://dx.doi.org/10.1063/1.452707

[14] Widom, B. and Rowlinson, J.S. (1970) *The Journal of Chemical Physics*, **52**, 1670-1679. http://dx.doi.org/10.1063/1.1673203

[15] de Miguel, E., Almarza, N.G. and Jackson, G. (2007) *The Journal of Chemical Physics*, **127**, Article ID: 034707. http://dx.doi.org/10.1063/1.2751153

[16] Ma, T. and Wang, S. (2011) *AIP Advances*, **1**, Article ID: 042101. http://dx.doi.org/10.1063/1.3650703

[17] Nishikawa, K. and Morita, T. (1998) *The Journal of Supercritical Fluids*, **13**, 143-148. http://dx.doi.org/10.1016/S0896-8446(98)00045-X

[18] Woodcock, L.V. (2016) *International Journal of Thermophysics*, **37**, 24-33. http://link.springer.com/article/10.1007/s10765-015-2031-z http://dx.doi.org/10.1007/s10765-015-2031-z

[19] Kaye and Laby (2008) Tables of Physical & Chemical Constants: Online Version 1.1. www.kayelaby.npl.co.uk

[20] Trejo, A., Yañez, P. and Eustaquio-Rincón, R. (2006) *Journal of Chemical & Engineering Data*, **51**, 1070-1075. http://dx.doi.org/10.1021/je0505321

[21] Stewart, R.B. and Jacobsen, R.T. (1989) *Journal of Physical and Chemical Reference Data*, **18**, 639-798. http://dx.doi.org/10.1063/1.555829

[22] Tegeler, C., Span, R. and Wagner, W. (1999) *Journal of Physical and Chemical Reference Data*, **28**, 779-850. http://dx.doi.org/10.1063/1.556037

[23] US National Institute of Standards and Technology (NIST) (2016) Thermophysical Properties of Fluid Systems. http://webbook.nist.gov/chemistry/fluid/

[24] Woodcock, L.V. (2013) *Fluid Phase Equilibria*, **351**, 25-33. http://dx.doi.org/10.1016/j.fluid.2012.08.029

[25] Heyes, D.M. and Woodcock, L.V. (2013) *Fluid Phase Equilibria*, **356**, 301-308. http://dx.doi.org/10.1016/j.fluid.2013.07.056

[26] Woodcock, L.V. (2014) *International Journal of Thermophysics*, **35**, 1770-1784. http://dx.doi.org/10.1007/s10765-013-1411-5

[27] Woodcock, L.V. (2013) *Natural Science*, **5**, 194-206. http://dx.doi.org/10.4236/ns.2013.52030

[28] Woodcock, L.V. (2014) *Natural Science*, **6**, 411-432. http://dx.doi.org/10.4236/ns.2014.66041

Journal of Modern Physics, 2016, 7, 774-789
Published Online April 2016 in SciRes. http://www.scirp.org/journal/jmp
http://dx.doi.org/10.4236/jmp.2016.78072

Scientific Research Publishing

Tetraquark and Pentaquark Systems in Lattice QCD

Fumiko Okiharu[1], Takumi Doi[2], Hiroko Ichie[3], Hideaki Iida[4], Noriyoshi Ishii[5], Makoto Oka[3], Hideo Suganuma[6], Toru T. Takahashi[7]

[1]Faculty of Education, Niigata University, Niigata, Japan
[2]Theoretical Research Division, Nishina Center, RIKEN, Wako, Japan
[3]Department of Physics, Tokyo Institute of Technology, Tokyo, Japan
[4]Research and Education Center for Natural Sciences, Keio University, Kanagawa, Japan
[5]Research Center for Nuclear Physics (RCNP), Osaka University, Ibaraki, Japan
[6]Department of Physics, Graduate School of Science, Kyoto University, Kyoto, Japan
[7]Gunma National College of Technology, Maebashi, Japan
Email: suganuma@scphys.kyoto-u.ac.jp

Received 12 February 2016; accepted 26 April 2016; published 29 April 2016

Abstract

We study multi-quark systems in lattice QCD. First, we revisit and summarize our accurate mass measurements of low-lying 5Q states with $J = 1/2$ and $I = 0$ in both positive- and negative-parity channels in anisotropic lattice QCD. The lowest positive-parity 5Q state is found to have a large mass of about 2.24 GeV after the chiral extrapolation. To single out the compact 5Q state from NK scattering states, we use the hybrid boundary condition (HBC), and find no evidence of the compact 5Q state below 1.75 GeV in the negative-parity channel. Second, we study the multi-quark potential in lattice QCD to clarify the inter-quark interaction in multi-quark systems. The 5Q potential V_{5Q} for the QQ-$\bar{Q}$-QQ system is found to be well described by the "OGE Coulomb plus multi-Y Ansatz": The sum of the one-gluon-exchange (OGE) Coulomb term and the multi-Y-type linear term based on the flux-tube picture. The 4Q potential V_{4Q} for the QQ-$\bar{Q}\bar{Q}$ system is also described by the OGE Coulomb plus multi-Y Ansatz, when QQ and $\bar{Q}\bar{Q}$ are well separated. The 4Q system is described as a "two-meson" state with disconnected flux tubes, when the nearest quark and antiquark pair are spatially close. We observe a lattice-QCD evidence for the "flip-flop", *i.e.*, the fluxtube recombination between the connected 4Q state and the "two-meson" state. On the confinement mechanism, the lattice QCD results indicate the flux-tube-type linear confinement in multi-quark hadrons. Finally, we propose a proper quark-model Hamiltonian based on the lattice QCD results.

Keywords

Lattice QCD, Multi-Quarks, Quark Confinement, Exotic Hadrons

How to cite this paper: Okiharu, F., Doi, T., Ichie, H., Iida, H., Ishii, N., Oka, M., Suganuma, H. and Takahashi, T.T. (2016) Tetraquark and Pentaquark Systems in Lattice QCD. *Journal of Modern Physics*, **7**, 774-789.
http://dx.doi.org/10.4236/jmp.2016.78072

1. Introduction

The Multi-quark physics is one of the new interesting fields in the hadron physics. So far, several new particles have been experimentally reported as the candidates of multi-quark hadrons.

At first, the candidates of pentaquark (5Q) baryons were reported: a narrow peak identified as the $\Theta^+(1540)$ was found at SPring-8 [1], ITEP, JLab and ELSA [2]-[4]. The $\Theta^+(1540)$ has the baryon number $B=1$ and the strangeness $S=+1$, and hence it is a manifestly exotic baryon and is considered to be a pentaquark ($\mathrm{uudd\bar{s}}$) in the valence-quark picture. Other pentaquark candidate, the $\Xi^{--}(1862)$ ($\mathrm{ddss\bar{u}}$), was reported at CERN [5], and also a charmed pentaquark, the $\Theta_c(3099)$ ($\mathrm{uudd\bar{c}}$), was reported at HERA [6]. However, after high-energy experimental groups reported no evidence of the $\Theta^+(1540)$ [7]-[9], these pentaquark candidates are no more credible experimentally at present. (For the recent experimental status of the $\Theta^+(1540)$, see, e.g., Refs. [10] [11]). Nevertheless, the very $\Theta^+(1540)$ gave an important trigger to open the new area of the multi-quark physics.

As the next important stage, the candidates of tetraquark (4Q) mesons were experimentally observed. The X(3872) [12]-[15] was found in the process of $\mathrm{B}^+ \to \mathrm{K}^+ + \mathrm{X}(3872) \to \mathrm{K}^+ + \pi^-\pi^+ J/\psi$ at KEK [12]. The X(3872) is much heavier than the J/ψ, and its mass is close to the threshold of $\mathrm{D}^0(\mathrm{c\bar{u}})$ and $\bar{\mathrm{D}}^{0*}(\mathrm{u\bar{c}})$. However, its decay width is very narrow as $\Gamma < 2.3\,\mathrm{MeV}$ (90% C.L.). These features indicate the X(3872) to be a tetraquark, e.g., a bound state of D^0 and $\bar{\mathrm{D}}^{0*}$. Similarly, the $\mathrm{D}_s(2317)$ [16] [17] is expected to be a tetraquark candidate. Also, quite recently, the LHCb experimental group has reported two candidates of the *charmed pantaquark* ($\mathrm{uudc\bar{c}}$), $\mathrm{P}_c^+(4380)$ and $\mathrm{P}_c^+(4450)$ [18], from a careful analysis of the decay product in the high-energy process, and this news has activated the multi-quark physics again. In any case, these discoveries of multi-quark hadrons are expected to reveal hidden aspects of hadron physics.

In the theoretical side, the quark model is one of the most popular models to describe hadrons. In the quark model, mesons and baryons are usually described as $q\bar{q}$ and $3q$ composite particles, respectively. In more microscopic viewpoint, quantum chromodynamics (QCD) is the fundamental theory to describe the strong interaction. In terms of QCD, not only ordinary $q\bar{q}$ mesons and $3q$ baryons, but also exotic hadrons, such as multi-quark hadrons ($q\bar{q}q\bar{q}, qqqq\bar{q}, \cdots$), hybrid mesons ($q\bar{q}g, \cdots$), hybrid baryons ($qqqg, \cdots$) and glueballs ($gg, ggg, \cdots$) are expected to appear. We here aim to study these multi-quark hadrons directly based on QCD. Even at present, however, it is rather difficult to deal with the low-energy region analytically in QCD owing to its strong-coupling nature. As an alternative way, the lattice QCD Monte Carlo simulation is established as the powerful method to treat non-perturbative nature of low-lying hadrons including exotic hadrons. In this paper, we perform the following two lattice QCD studies to clarify the properties of multi-quark systems.

First, we investigate the mass and the parity of the 5Q system in lattice QCD. As for the parity assignment of the lowest-lying pentaquark, little agreement is achieved even in the theoretical side: the positive-parity assignment is supported by the chiral soliton model [19] and the diquark model [20], while the negative-parity assignment is supported by the nonrelativistic quark model [21], the QCD sum rule [22] and so on. For the exotic hadrons, most investigations have been done with model calculations, but these models were originally constructed only for ordinary hadrons. In fact, it is nontrivial that these models can describe the multi-quark system beyond the ordinary hadrons. To get solid information for the multi-quark systems, we study their properties directly from QCD by the lattice QCD simulation [23] [24], which is the first-principle calculation and model independent.

Second, we study the inter-quark interaction in multi-quark systems in lattice QCD. The inter-quark force is one of the most important elementary quantities in hadron physics. Nevertheless, for instance, no body knows the exact form of the confinement force in the multi-quark systems directly from QCD. In fact, some hypothetical forms of the inter-quark potential have been used in almost all quark model calculations so far. Then, the lattice QCD study of the inter-quark interaction is quite desired for the study of the multi-quark systems. It presents the proper Hamiltonian in multi-quark systems and leads to a guideline to construct the QCD-based quark model. In this paper, to clarify the inter-quark force in the multi-quark system, we study the

static multi-quark potential systematically in lattice QCD using the multi-quark Wilson loop. We investigate the three-quark (3Q) potential [25]-[28], which is responsible to baryon properties, and perform the lattice-QCD study for the multi-quark potential, the tetraquark (4Q) and the pentaquark (5Q) potentials [29]-[33].

We show in **Figure 1** our global strategy to understand the hadron properties from QCD. One way is the direct lattice QCD calculations for the low-lying hadron masses and simple hadron matrix elements, although the wave function is unknown and the practically calculable quantities are severely limited. The other way is to construct the quark model from QCD. From the analysis of the inter-quark forces in lattice QCD, we extract the quark-model Hamiltonian. Through the quark model calculation, one can obtain the quark wave-function of hadrons and more complicated properties of hadrons including properties of excited hadrons.

This paper is organized as follows. In Section 2, we present an accurate mass calculation of low-lying 5Q systems in anisotropic lattice QCD [34] [34]. In Section 3, we perform the systematic study of the inter-quark interaction in multi-quark systems [28]-[33]. Section 4 is devoted for the summary and concluding remarks.

2. Lattice QCD Study for Multi-Quark Hadrons

There have been many theoretical studies for multi-quark systems in the context of X(3872) and $\Theta^+(1540)$ [36] [37]. As for the $\Theta^+(1540)$, however, its existence as a low-lying pentaquark resonance is not credible experimentally. In fact, high-energy experimental groups reported no evidence of the $\Theta^+(1540)$ [7]-[9].

Also in lattice QCD, there is no consensus on the existence and the parity assignment of the lowest-lying pentaquark system. Two early works supported the negative-parity state for the $\Theta^+(1540)$ [38] [39], while one early work supported the positive-parity state [39]. We and another group indicated no evidence for the low-lying pentaquark narrow resonance [34] [41], and one study suggested a negative-parity pentaquark state in more highly-excited region around 1.8 GeV [42].

In this section, we perform the accurate mass measurement of the 5Q system in anisotropic lattice QCD, and apply hybrid boundary condition [34] [43] to distinguish a compact resonance and a scattering state.

2.1. Strategy for High Precession Measurements in Lattice QCD

As a difficulty on the lattice study of multi-quarks, even if a compact multi-quark resonance state exists, there appears a mixture with several multi-hadron scattering states, even at the quenched level. For instance, in the channel of Θ^+, several NK scattering states appears. In this paper, we use the term of the Θ^+ only for the compact 5Q resonance to distinguish it from the NK scattering state. In order to examine whether the low-lying 5Q state appears as a compact resonance Θ^+, we perform the accurate lattice QCD calculations with adopting the following three advanced methods [34].

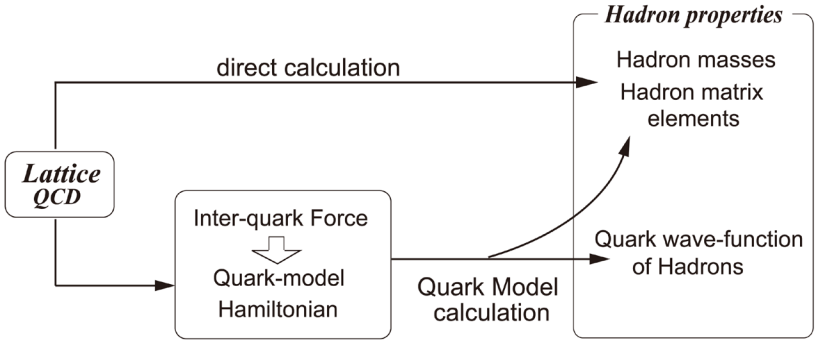

Figure 1. Our global strategy to understand the hadron properties from QCD. One way is the direct lattice QCD calculations for the low-lying hadron masses and simple hadron matrix elements, although the wave function is unknown and the practically calculable quantities are severely limited. The other way is to construct the quark model from QCD. From the analysis of the inter-quark forces in lattice QCD, we extract the quark-model Hamiltonian. Through the quark model calculation, one can obtain the quark wave-function of hadrons and more complicated properties of hadrons including properties of excited hadrons.

2.1.1. Usage of Anisotropic Lattice QCD

We use the anisotropic lattice, where the temporal lattice spacing a_t is much finer than the spatial one a_s as shown in **Figure 2**. In lattice QCD, hadron masses are calculated from the asymptotic temporal behavior of the hadron correlators. On the anisotropic lattice, we can get the detailed information on the temporal behavior of the 5Q correlator, and hence we can perform accurate mass measurements for the low-lying 5Q system.

2.1.2. Usage of the Non-NK-Type Interpolating Field Operator

We use a non-NK-type interpolating field to extract the $\Theta^+(1540)$ state. This choice of the interpolating field would be important and effective. For instance, in Ref. [41], the authors used the NK-type interpolating field and only obtained the NK scattering state instead of the compact 5Q state. However, their null result may be merely due to a small amount of the compact 5Q component in the NK-type interpolating field, because their calculation suffers from a large contamination of NK scattering states.

We adopt the non-NK-type interpolating field [22],

$$O_\alpha \equiv \epsilon_{abc}\epsilon_{ade}\epsilon_{bfg}\left(u_d^T C\gamma_5 d_e\right)\left(u_f^T C d_g\right)\left(C\bar{s}_c^T\right)_\alpha, \tag{1}$$

for the 5Q state with spin $J=1/2$ and isospin $I=0$. Here α denotes the Dirac index, and roman indices *a*-*g* are color indices. $C\equiv\gamma_4\gamma_2$ denotes the charge conjugation matrix. Note that the non-NK-type operator in Equation (1) cannot be decomposed into N and K in the nonrelativistic limit and its coupling to the NK state is rather weak. Hence, the 5Q resonance state Θ^+ can be singled out as much as possible in the present calculation, and the results are less biased by the contamination from NK scattering states.

2.1.3. Application of the Hybrid Boundary Condition Method

To distinguish compact resonances from scattering states, we have proposed a useful method with the "hybrid boundary condition" (HBC) [34] [43] instead of the ordinary periodic boundary condition. In the HBC, we impose the it anti-periodic boundary condition for u, d quarks, and the periodic boundary condition for s-quarks, as shown in **Table 1**. By applying the HBC on a finite-volume lattice, the NK threshold is raised up, while the mass of a compact 5Q resonance Θ^+ is almost unchanged. Therefore, we can distinguish a compact 5Q state Θ^+ from an NK scattering state by comparing between the HBC and the standard periodic boundary condition.

In lattice QCD with the finite spatial volume L^3, the spatial momenta are quantized as $p_i = 2n_i\pi/L$ ($n_i \in \mathbf{Z}$) under the periodic boundary condition and $p_i = (2n_i+1)\pi/L$ under the anti-periodic boundary condition. In the periodic boundary condition, N and K can have zero momenta $|\mathbf{p}_{\min}|=0$ in the s-wave NK scattering state. The HBC imposes the anti-periodic boundary condition for u and d quarks and periodic boundary condition for s quark, while the periodic boundary condition is usually employed for all u, d, s quarks. In the HBC, the net boundary conditions of both N(uud,udd) and K($u\bar{s}$, $d\bar{s}$) are anti-periodic. Then, under the HBC, N and K have minimum momenta $p_i = \sqrt{3}\pi/L$ in a finite box with L^3, and the threshold of the s-wave NK scattering state is raised up as $\sqrt{m_N^2+\mathbf{p}_{\min}^2}+\sqrt{m_K^2+\mathbf{p}_{\min}^2}$. In contrast to N and K, the compact 5Q resonance Θ^+ ($uudd\bar{s}$) contains even number of u and d quarks, and hence its mass does not shift in the HBC (see **Table 2**).

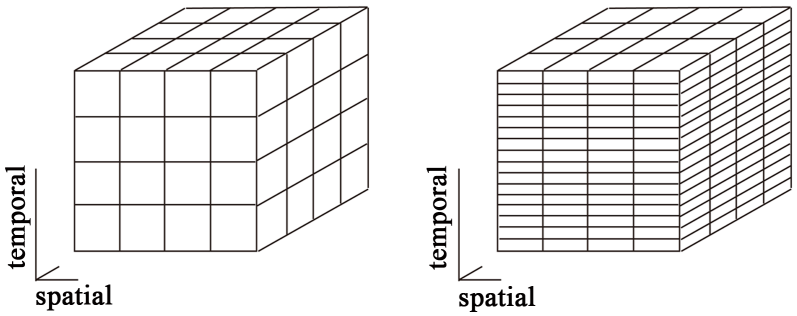

Figure 2. Schematic figures of the isotropic lattice (left) and the anisotropic lattice (right). On the anisotropic lattice, the temporal lattice spacing a_t is taken to be smaller than the spatial one a_s.

Table 1. The *hybrid boundary condition* (*HBC*) to distinguish a compact multi-quark resonance and an two-hadron scattering state for the $uudd\bar{s}$ system. The standard boundary condition (BC) is also shown for comparison.

	u quark	d quark	s quark
HBC	anti-periodic	anti-periodic	periodic
standard BC	periodic	periodic	periodic

Table 2. The net boundary condition for Θ^+ ($uudd\bar{s}$), N (uud or udd) and K ($d\bar{s}$ or $u\bar{s}$) in the hybrid boundary condition (HBC) and in the standard boundary condition (BC).

	Θ^+ ($uudd\bar{s}$)	N (uud or udd)	K ($d\bar{s}$ or $u\bar{s}$)
HBC	periodic	anti-periodic	anti-periodic
standard BC	periodic	periodic	periodic

2.2. Lattice QCD Setup for the Pentaquark Mass

To generate gluon configurations, we use the standard plaquette action on the anisotropic lattice as [34]

$$S_{\mathrm{G}} = \frac{\beta}{N_c}\frac{1}{\gamma_{\mathrm{G}}}\sum_{s,i<j\leq 3}\mathrm{Re}\,\mathrm{Tr}\left\{1-P_{ij}(s)\right\} + \frac{\beta}{N_c}\gamma_{\mathrm{G}}\sum_{s,i\leq 3}\mathrm{Re}\,\mathrm{Tr}\left\{1-P_{i4}(s)\right\}, \tag{2}$$

with $\beta \equiv 2N_c/g^2$, the plaquette $P_{\mu\nu}(s)$ and the bare anisotropy γ_{G}.

For the quark part, we adopt the $O(a)$-improved Wilson (clover) fermion action on the anisotropic lattice,

$$S_{\mathrm{F}} \equiv \sum_{x,y}\bar{\psi}(x)K(x,y)\psi(y), \tag{3}$$

with the quark kernel $K(x,y)$ as

$$\begin{aligned} K(x,y) \equiv{}& \delta_{x,y} - \kappa_t\left\{(1-\gamma_4)U_4(x)\delta_{x+\hat{4},y} + (1+\gamma_4)U_4^{\dagger}\left(x-\hat{4}\right)\delta_{x-\hat{4},y}\right\} \\ & - \kappa_s\sum_i\left\{(r-\gamma_i)U_i(x)\delta_{x+\hat{i},y} + (r+\gamma_i)U_i^{\dagger}\left(x-\hat{i}\right)\delta_{x-\hat{i},y}\right\} \\ & - \kappa_s c_E\sum_i\sigma_{i4}G_{i4}\delta_{x,y} - r\kappa_s c_B\sum_{i<j}\sigma_{ij}G_{ij}\delta_{x,y}, \end{aligned} \tag{4}$$

where κ_s and κ_t denote the spatial and temporal hopping parameters, respectively. $G_{\mu\nu}$ denotes the field strength, which is defined through the standard clover-leaf-type construction. The Wilson parameter r and the clover coefficients, c_E and c_B, are fixed by the tadpole-improved tree-level values as $r = 1/\xi$, $c_E = 1/\left(u_s u_t^2\right)$ and $C_B = 1/u_s^3$, where u_s and u_t denote the mean-field values of the spatial and the temporal link-variables, respectively.

For the lattice QCD simulation, we use $\beta = 5.75$ and $12^3\times 96$ with the renormalized anisotropy $a_s/a_t = 4$, which corresponds to $\gamma_{\mathrm{G}} = 3.2552$. In this calculation, the lattice spacing is found to be $a_s \simeq 0.18\ \mathrm{fm} \simeq (1.1\ \mathrm{GeV})^{-1}$ and $a_t \simeq 0.045\ \mathrm{fm} \simeq (4.4\ \mathrm{GeV})^{-1}$. We adopt four values of the hopping parameter as $\kappa = 0.1210\,(0.0010)\,0.1240$ for u and d quarks, and use $\kappa_{\text{s-quark}} = 0.1240$ for the s quark. We calculate typical hadron masses at each κ as shown in **Table 3**, and find $\kappa_{\text{phys.}} \simeq 0.1261$ corresponding to the physical situation of $m_\pi \simeq 0.14\ \mathrm{GeV}$.

2.3. Lattice QCD Results for the $\Theta^+(1540)$

Now, using anisotropic lattice QCD, we perform the accurate mass measurement of the low-lying 5Q states with

Table 3. The lattice QCD results for the masses of π, ρ, K and N at each hopping parameter κ in the physical unit of GeV [43]. The $\kappa_{\text{phys.}} \simeq 0.1261$ corresponds to the physical situation of $m_\pi \simeq 0.14\,\text{GeV}$.

κ	0.1210	0.1220	0.1230	0.1240	$\kappa_{\text{phys.}}$
m_π	1.005 (2)	0.898 (2)	0.784 (2)	0.656 (3)	0.140
m_ρ	1.240 (3)	1.161 (3)	1.085 (4)	1.011 (5)	0.850 (7)
m_K	0.845 (2)	0.785 (2)	0.723 (2)	0.656 (3)	0.530 (4)
m_N	1.878 (5)	1.744 (5)	1.604 (5)	1.460 (6)	1.173 (9)

$J = 1/2$ and $I = 0$ in both positive- and negative-parity channels from the correlator of the non-NK-type 5Q operator with parity projection [34].

In **Figure 3**, we show the lattice QCD results [34] for the masses of lowest positive- and negative-parity 5Q states under the standard periodic boundary condition. After the chiral extrapolation, the lowest positive-parity 5Q state is found to be rather heavy as $m_{5Q}\left(J^\pi = \frac{1}{2}^+\right) \simeq 2.24\,\text{GeV}$, which seems to be too heavy to be identified as the $\Theta^+(1540)$.

On the other hand, we get a lower mass for the negative-parity 5Q state as $m_{5Q}\left(J^\pi = \frac{1}{2}^-\right) \simeq 1.75\,\text{GeV}$ after the chiral extrapolation. This value $m_{5Q} \simeq 1.75\,\text{GeV}$ seems to be closer to the experimental result of $m_{\Theta^+} \simeq 1.54\,\text{GeV}$. At this stage, however, this lowest negative-parity 5Q state may be merely an NK scattering state, although the non-NK-type 5Q operator used in this calculation includes only a small amount of the NK component.

To clarify whether the observed low-lying 5Q state is a compact 5Q resonance Θ^+ or an NK scattering state, we use the hybrid boundary condition (HBC) method, and compare the lattice results with the HBC and those with the standard periodic boundary condition (BC). Recall that, in the HBC, the NK threshold is largely raised up, while the mass of the compact 5Q resonance ($uudd\bar{s}$) is to be almost unchanged, as was mentioned in Section 2.1.3.

In **Figure 4**, we show the mass of the lowest-lying negative-parity 5Q state in lattice QCD with the standard periodic BC and the HBC at each κ [34]. The symbols denote the lattice QCD results for the 5Q state and the lines denote the NK threshold at each κ. The left and right figures show the results with the standard periodic BC and the hybrid boundary condition (HBC), respectively. Note that the NK threshold is estimated to be raised up about 200 - 250 MeV in the HBC.

As a lattice QCD result, the mass of the 5Q state is largely raised in the HBC in accordance with the NK threshold, which indicates that the lowest 5Q state observed on the lattice is merely an s-wave NK scattering state. In other words, if there exists a compact 5Q resonance Θ^+ below 1.75 GeV, it should be observed in this lattice calculation with the non-NK-type operator, and its mass should be almost unchanged also in the HBC. However, there is no such a 5Q state observed in the lattice calculation, which means absence of the compact 5Q resonance Θ^+ below 1.75 GeV.

To conclude, our lattice QCD calculation at the quenched level indicates absence of the low-lying compact 5Q resonance Θ^+ with $J = 1/2$ and $I = 0$ near 1.54 GeV [34].

2.4. Discussion on Null Result of $\Theta^+(1540)$ in Lattice QCD

Now, let us consider the physical consequence of the present null result on the low-lying 5Q resonance Θ^+ in lattice QCD. One plausible answer is absence of the pentaquark resonance $\Theta^+(1540)$, as was indicated by several experiments [7]-[11]. However, there may be some loopholes in the lattice calculation.

First, the present lattice simulation has been done at the quenched level, where dynamical quark effects are suppressed. This quenching effect is not clear and then it may cause the 5Q resonance Θ^+ to be heavier as an unknown effect.

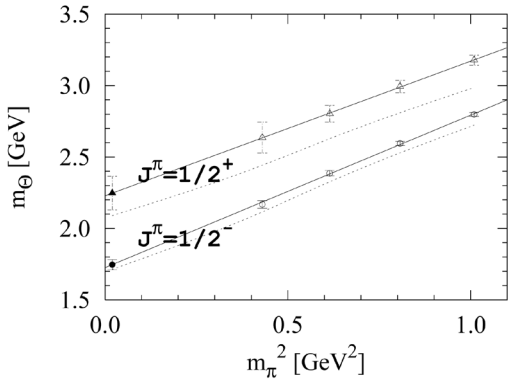

Figure 3. The lowest mass m_{5Q} of the positive- and negative-parity 5Q states plotted against m_π^2, taken from Ref. [34]. The open symbols denote the direct lattice QCD data for positive-parity (triangles) and negative-parity (circles). The solid symbols denote the results of the chiral extrapolation. The dotted lines indicate the NK thresholds for p-wave (upper) and s-wave (lower) cases.

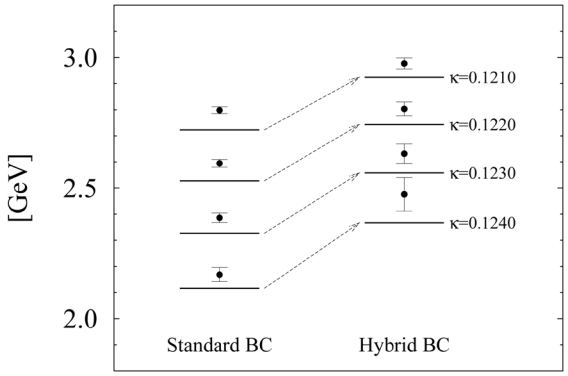

Figure 4. Comparison between the standard periodic boundary condition (Standard BC) and the Hybrid Boundary Condition (HBC) for the lowest mass of the negative-parity 5Q system, taken from Ref. [34]. At each κ, the lattice QCD result (the solid symbol) is raised up in accordance with the corresponding NK threshold (the solid line). This behavior indicates that the low-lying negative-parity 5Q state observed in lattice QCD is an NK scattering state rather than a compact 5Q resonance Θ^+.

Second, we investigated the 5Q state with spin $J=1/2$ and isoscalar $I=0$ in this paper. However, the $\Theta^+(1540)$ may have other quantum numbers [44]-[46], e.g., spin $J=3/2$, isovector $I=1$ or isotensor $I=2$. Considering such a possibility, our group investigated the 5Q system with higher spin $J=3/2$ in lattice QCD, and found no low-lying pentaquark also in this channel [43].

Third, we have used a localized 5Q interpolating field in this lattice QCD calculation. However, the actual $\Theta^+(1540)$ may have more complicated structure beyond the localized interpolating field. Such a possibility has been pointed out in the theoretical side. For instance, Karliner and Lipkin [47] proposed the diquark-triquark (qq-$qq\bar{q}$) picture for the Θ, and Bicudo *et al.* [48] pointed out the possibility of the heptaquark picture, where the Θ^+ is described as a bound state of π, K and N. If the $\Theta^+(1540)$ has such a complicated structure, we have to use the corresponding nonlocal interpolating field to get its proper information.

2.5. Necessity of the Wave Function of Multi-Quarks

So far, we have performed the direct mass measurement of 5Q states in lattice QCD, where the path integral over arbitrary states is numerically calculated on a supercomputer. In the path-integral formalism, however, it is rather difficult to extract the state information, such as the wave-function of the multi-quark state, and therefore

only limited simple information can be obtained in the direct lattice-QCD calculation.

Actually, to distinguish the compact 5Q resonance Θ^+ from NK scattering states was rather difficult in lattice QCD, and hence we had to develop a new method with the hybrid boundary condition (HBC). In this respect, if the wave function is obtained, one easily finds out whether it is a compact resonance state Θ^+ or not.

Indeed, to get the wave function is very important to clarify the further various properties of the multi-quark state such as the underlying structure and the decay width, which cannot be obtained practically only with the direct lattice-QCD calculation.

Then, apart from the direct lattice-QCD calculation, we have to seek the way to obtain the proper wave function of the multi-quark state. To do so, we need a proper Hamiltonian for the multi-quark system based on QCD. One possible way in this direction is to construct the quark model from QCD, as was mentioned in Section 1. In the next section, we study the inter-quark interaction in multi-quark systems directly from QCD, and aim to construct the QCD-based quark-model Hamiltonian.

3. Inter-Quark Interaction in Multi-Quark Systems in Lattice QCD

In this section, we study the inter-quark interaction in multi-quark systems using lattice QCD [29]-[33], and seek for the QCD-based quark-model Hamiltonian to describe multi-quark hadrons. The quark-model Hamiltonian consists of the kinetic term and the potential term, which is not known form QCD in multi-quark systems.

As for the potential at short distances, the perturbative one-gluon-exchange (OGE) potential would be appropriate, due to the asymptotic nature of QCD. For the long-range part, however, there appears the confinement potential as a typical non-perturbative property of QCD, and its form is highly nontrivial in the multi-quark system.

In fact, to clarify the confinement force in multi-quark systems is one of the essential points for the construction of the QCD-based quark-model Hamiltonian. Then, in this paper, we investigate the multi-quark potential in lattice QCD, with paying attention to the confinement force in multi-quark hadrons.

3.1. The Three-Quark Potential in Lattice QCD

So far, only for the simplest case of static $\mathrm{Q\bar{Q}}$ systems, detailed lattice QCD studies have been done, and the $\mathrm{Q\bar{Q}}$ potential $V_{\mathrm{Q\bar{Q}}}$ is known to be well described by the Coulomb plus linear potential as [23]-[26] [49]

$$V_{\mathrm{Q\bar{Q}}}(r) = -\frac{A_{\mathrm{Q\bar{Q}}}}{r} + \sigma_{\mathrm{Q\bar{Q}}} r + C_{\mathrm{Q\bar{Q}}} \tag{5}$$

with r being the inter-quark distance.

To begin with, we study three-quark (3Q) systems in lattice QCD to understand the structure of baryons at the quark-gluon level. Similar to the derivation of the $\mathrm{Q\bar{Q}}$ potential from the Wilson loop, we calculate the 3Q potential $V_{3\mathrm{Q}}$ from the 3Q Wilson loop $W_{3\mathrm{Q}}$ in SU(3) lattice QCD with ($\beta = 5.7$, $12^3 \times 24$), ($\beta = 5.8$, $16^3 \times 32$), ($\beta = 6.0$, $16^3 \times 32$) and ($\beta = 6.2$, 24^4) at the quenched level. For more than 300 different patterns of spatially-fixed 3Q systems, we perform accurate and detailed calculations for the 3Q potential [25]-[28] [31] [33], and find that the lattice QCD data of the 3Q potential $V_{3\mathrm{Q}}$ are well described by the Coulomb plus Y-type linear potential, *i.e.*, Y-Ansatz,

$$V_{3\mathrm{Q}} = -A_{3\mathrm{Q}} \sum_{i<j} \frac{1}{|\mathbf{r}_i - \mathbf{r}_j|} + \sigma_{3\mathrm{Q}} L_{\min}^{3\mathrm{Q}} + C_{3\mathrm{Q}}, \tag{6}$$

within 1%-level deviation [25]-[28] [31] [33]. Here, $L_{\min}^{3\mathrm{Q}}$ is the minimal total length of the color flux tube, which is Y-shaped for the 3Q system.

To demonstrate the validity of the Y-Ansatz, we show in **Figure 5** the lattice QCD data of the 3Q confinement potential $V_{3\mathrm{Q}}^{\mathrm{conf}}$, *i.e.*, 3Q potential subtracted by the Coulomb part, plotted against Y-shaped flux-tube length $L_{\min}^{3\mathrm{Q}}$ [30]. For each β, clear linear correspondence is found between 3Q confinement potential $V_{3\mathrm{Q}}^{\mathrm{conf}}$

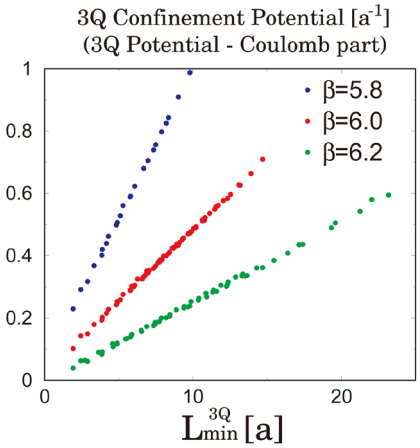

Figure 5. The lattice QCD result for the 3Q confinement potential V_{3Q}^{conf}, *i.e.*, the 3Q potential subtracted by its Coulomb part, plotted against Y-shaped flux-tube length L_{min}^{3Q} at $\beta = 5.8$, 6.0 and 6.2 in the lattice unit, taken from Ref. [30]. The clear linear correspondence between 3Q confinement potential V_{3Q}^{conf} and L_{min}^{3Q} indicates the Y-Ansatz for the 3Q potential.

and L_{min}^{3Q}, which indicates the Y-Ansatz for the 3Q potential [30] [31] [33].

Here, we consider the physical meaning of the Y-Ansatz. Apart from an irrelevant constant, the Y-Ansatz, Equation (6), consists of the Coulomb term and the Y-type linear potential, which play the dominant role at short and long distances, respectively. The Coulomb term would originate from the one-gluon-exchange (OGE) process. In fact, at short distances, perturbative QCD is applicable, and therefore the inter-quark potential is expressed as the sum of the two-body one-gluon-exchange (OGE) Coulomb potential.

The appearance of the Y-type linear potential supports the flux-tube picture [50]-[53] at long distances, where there appears the color flux tube linking quarks inside hadrons with its length minimized. In particular, the confinement force in baryons corresponds to the Y-shaped flux tube, which implies existence of the three-body interaction in baryons.

In usual many-body systems, the main interaction is described by a two-body interaction and the three-body interaction is a higher-order contribution. In contrast, as is clarified by our lattice-QCD study, the quark confinement force in baryons is a genuinely three-body interaction [25] [26], which is one of significant features of QCD. In fact, the appearance of the Y-type junction and the three-body confinement force reflect the SU(3) group structure in QCD, e.g., the number of color, $N_c = 3$, and is peculiar to QCD [25] [26]. In this sense, the study of the 3Q system is very important to get a deeper insight of the QCD physics.

In lattice QCD, a clear Y-type flux-tube formation is actually observed for spatially-fixed 3Q systems [31] [33] [54]. Thus, together with several other analytical and numerical studies [55]-[57], the Y-Ansatz seems to be confirmed as the correct functional form of the static 3Q potential. This result indicates the color-flux-tube picture for baryons.

3.2. The OGE Coulomb Plus Multi-Y Ansatz

Now, we proceed to multi-quark systems. We first consider the theoretical form of the multi-quark potential, since we will have to analyze the lattice QCD data by comparing them with some theoretical Ansatz.

By generalizing the lattice QCD result of the Y-Ansatz for the three-quark potential, we propose the one-gluon-exchange (OGE) Coulomb plus multi-Y Ansatz [29]-[33],

$$V = \frac{g^2}{4\pi}\sum_{i<j}\frac{T_i^a T_j^a}{|\mathbf{r}_i - \mathbf{r}_j|} + \sigma L_{min} + C, \tag{7}$$

for the potential form of the multi-quark system. Here, the confinement potential is proportional to the minimal total length L_{min} of the color flux tube linking the quarks, which is multi-Y shaped in most cases.

In the following, we study the inter-quark interaction in multi-quark systems in lattice QCD, and compare the

lattice QCD data with the theoretical form in Equation (7). Note here that the lattice QCD data are meaningful as primary data on the multi-quark system directly based on QCD, and do not depend on any theoretical Ansatz.

3.3. Formalism of the Multi-Quark Wilson Loop

Next, we formulate the multi-quark Wilson loop to obtain the multi-quark potential in lattice QCD [29]-[33].

Similar to the derivation of the $\mathrm{Q\bar{Q}}$ potential from the Wilson loop, the static multi-quark potential can be derived from the corresponding multi-quark Wilson loop. We construct the tetraquark Wilson loop $W_{4\mathrm{Q}}$ [30] and the pentaquark Wilson loop $W_{5\mathrm{Q}}$ [29] in a gauge invariant manner as shown in **Figure 6(a)** and **Figure 6(b)**, respectively.

The tetraquark Wilson loop $W_{4\mathrm{Q}}$ and the pentaquark Wilson loop $W_{5\mathrm{Q}}$ are defined by

$$\begin{aligned} W_{4\mathrm{Q}} &\equiv \frac{1}{3}\mathrm{tr}\left(\tilde{M}_1\tilde{R}_{12}\tilde{M}_2\tilde{L}_{12}\right), \\ W_{5\mathrm{Q}} &\equiv \frac{1}{3!}\epsilon^{abc}\epsilon^{a'b'c'}M^{aa'}\left(\tilde{R}_3\tilde{R}_{12}\tilde{R}_4\right)^{bb'}\left(\tilde{L}_3\tilde{L}_{12}\tilde{L}_4\right)^{cc'}, \end{aligned} \tag{8}$$

where $\tilde{M}$, $\tilde{M}_i$, $\tilde{L}_j$ and $\tilde{R}_j$ (i = 1, 2, j = 1, 2, 3, 4) are given by

$$\tilde{M},\tilde{M}_i,\tilde{R}_j,\tilde{L}_j \equiv P\exp\left\{ig\int_{M,M_i,R_j,L_j}\mathrm{d}x^\mu A_\mu(x)\right\} \in \mathrm{SU}(3)_\mathrm{c}. \tag{9}$$

Here, $\tilde{R}_{12}$ and $\tilde{L}_{12}$ are defined by

$$\tilde{R}_{12}^{a'a} \equiv \frac{1}{2}\epsilon^{abc}\epsilon^{a'b'c'}R_1^{bb'}R_2^{cc'}, \quad \tilde{L}_{12}^{a'a} \equiv \frac{1}{2}\epsilon^{abc}\epsilon^{a'b'c'}L_1^{bb'}L_2^{cc'}. \tag{10}$$

The multi-quark Wilson loop physically means that a gauge-invariant multi-quark state is generated at $t=0$ and annihilated at $t=T$ with quarks being spatially fixed in $\mathbf{R}^3$ for $0<t<T$.

The multi-quark potential is obtained from the vacuum expectation value of the multi-quark Wilson loop:

$$V_{4\mathrm{Q}} = -\lim_{T\to\infty}\frac{1}{T}\ln\langle W_{4\mathrm{Q}}\rangle, \quad V_{5\mathrm{Q}} = -\lim_{T\to\infty}\frac{1}{T}\ln\langle W_{5\mathrm{Q}}\rangle. \tag{11}$$

3.4. Lattice QCD Setup for the Multi-Quark Potential

Here, we briefly summarize the lattice QCD setup in this calculation. For the study of the multi-quark potential, the SU(3) lattice QCD simulation is done with the standard plaquette action at $\beta = 6.0$ on the $16^3\times 32$ lattice at the quenched level. (The calculation for large-size multi-quark configurations are performed by identifying $16^3\times 32$ as the spatial size.)

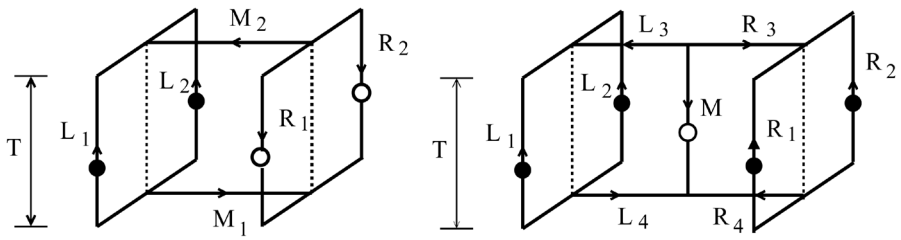

Figure 6. (a) The tetraquark Wilson loop $W_{4\mathrm{Q}}$ [30]. (b) The pentaquark Wilson loop $W_{5\mathrm{Q}}$ [29]. The contours $M,M_i,R_j,L_j\,(i=1,2,j=3,4)$ are line-like and $R_j,L_j\,(j=1,2)$ are staple-like. The multi-quark Wilson loop physically means that a gauge-invariant multi-quark state is generated at $t=0$ and annihilated at $t=T$ with quarks being spatially fixed in $\mathbf{R}^3$ for $0<t<T$.

In this calculation, the lattice spacing a is estimated as $a \simeq 0.104$ fm, which leads to the string tension $\sigma_{Q\bar{Q}} = (427\ \text{MeV})^2$ in the $Q\bar{Q}$ potential [31]. We use 150 gauge configurations for the 5Q potential simulation and 300 gauge configurations for the 4Q potential simulation. The smearing method is used for the enhancement of the ground-state component. We here adopt $\alpha = 2.3$ and the iteration number $N_{\text{smr}} = 40$, which lead to a large enhancement of the ground-state component [29]-[33].

3.5. Lattice QCD Result of the Pentaquark Potential

We study the pentaquark potential V_{5Q} in lattice QCD for 56 different patterns of QQ-$\bar{Q}$-QQ type pentaquark configurations, as shown in **Figure 7**. As the conclusion, the lattice QCD data of V_{5Q} are found to be well described by the OGE Coulomb plus multi-Y Ansatz, *i.e.*, the sum of the OGE Coulomb term and the multi-Y-type linear term based on the flux-tube picture [29] [31]-[33].

We show in **Figure 8** the lattice QCD results of the 5Q potential V_{5Q} [29] for symmetric planar 5Q configurations as shown in **Figure 7**, where each 5Q system is labeled by $d \equiv \overline{Q_1Q_2}/2$ and $h \equiv \overline{Q_1Q_3}$.

In **Figure 8**, we add the theoretical curves of the OGE Coulomb plus multi-Y Ansatz, where the coefficients (A_{5Q}, σ_{5Q}) are set to be (A_{3Q}, σ_{3Q}) obtained from the 3Q potential [26]. (Note that there is no adjustable parameter in the theoretical Ansatz apart from an irrelevant constant.) In **Figure 8**, one finds a good agreement between the lattice QCD data of V_{5Q} and the theoretical curves of the OGE Coulomb plus multi-Y Ansatz.

In this way, the pentaquark potential V_{5Q} is found to be well described by the OGE Coulomb plus multi-Y Ansatz as [29] [31]-[33].

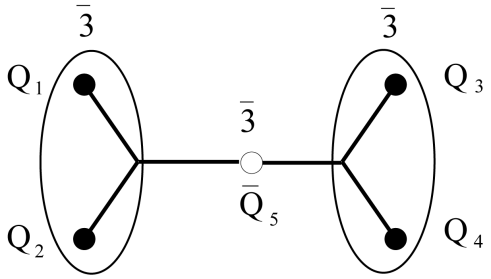

Figure 7. A QQ-$\bar{Q}$-QQ type pentaquark configuration [29]. In the 5Q system, (Q_1, Q_2) and (Q_3, Q_4) form 3 representation of SU(3) color, respectively. The lattice QCD results indicate the multi-Y-shaped flux-tube formation in the QQ-$\bar{Q}$-QQ system.

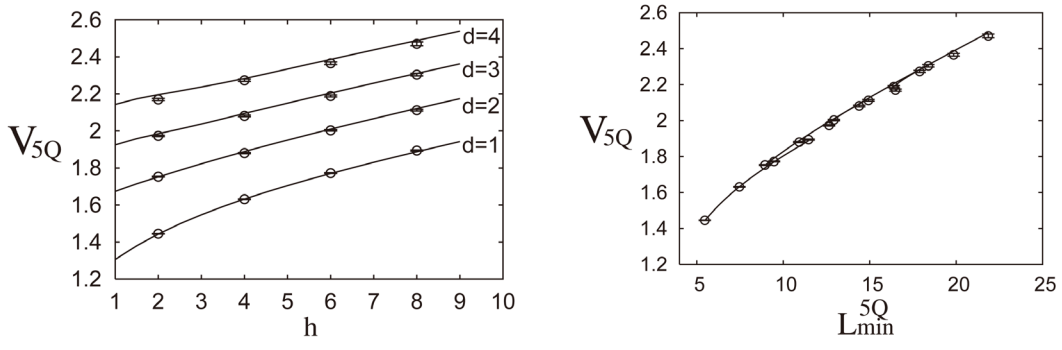

Figure 8. Lattice QCD results of the pentaquark potential V_{5Q} for symmetric planar 5Q configurations in the lattice unit: (a) V_{5Q} v.s. (d,h) and (b) V_{5Q} v.s. L^{5Q}_{min}, taken from Ref. [29]. The symbols denote the lattice QCD data, and the curves the theoretical form of the OGE plus multi-Y Ansatz.

$$V_{5Q} = -A_{5Q}\left\{\left(\frac{1}{r_{12}}+\frac{1}{r_{34}}\right)+\frac{1}{2}\left(\frac{1}{r_{15}}+\frac{1}{r_{25}}+\frac{1}{r_{35}}+\frac{1}{r_{45}}\right)+\frac{1}{4}\left(\frac{1}{r_{13}}+\frac{1}{r_{14}}+\frac{1}{r_{23}}+\frac{1}{r_{24}}\right)\right\}+\sigma_{5Q}L_{\min}^{5Q}+C_{5Q}, \quad (12)$$

where r_{ij} is the distance between Q_i and Q_j. Here, $L_{\min}^{5Q}$ is the minimal total length of the flux tube, which is multi-Y-shaped as shown in **Figure 7**. This lattice result supports the flux-tube picture for the 5Q system.

3.6. Tetraquark Potential and Flip-Flop in Lattice QCD

We study the tetraquark potential V_{4Q} in lattice QCD for about 200 different patterns of QQ-$\bar{\mathrm{Q}}\bar{\mathrm{Q}}$ configurations, and find the following results [30]-[32].

1. When QQ and $\bar{\mathrm{Q}}\bar{\mathrm{Q}}$ are well separated, the 4Q potential V_{4Q} is well described by the OGE Coulomb plus multi-Y Ansatz, which indicates the multi-Y-shaped flux-tube formation as shown in **Figure 9(a)**.
2. When the nearest quark and antiquark pair is spatially close, the 4Q potential V_{4Q} is well described by the sum of two $\mathrm{Q}\bar{\mathrm{Q}}$ potentials, which indicates a "two-meson" state as shown in **Figure 9(b)**.

We show in **Figure 10** the lattice QCD results of the 4Q potential V_{4Q} [30] for symmetric planar 4Q configurations as shown in **Figure 9**, where each 4Q system is labeled by $d \equiv \overline{\mathrm{Q}_1\mathrm{Q}_2}/2$ and $h \equiv \overline{\mathrm{Q}_1\mathrm{Q}_3}$.

For large value of *h* compared with *d*, the lattice data seem to coincide with the solid curve of the OGE Coulomb plus multi-Y Ansatz,

$$V_{4Q} = -A_{4Q}\left\{\left(\frac{1}{r_{12}}+\frac{1}{r_{34}}\right)+\frac{1}{2}\left(\frac{1}{r_{13}}+\frac{1}{r_{14}}+\frac{1}{r_{23}}+\frac{1}{r_{24}}\right)\right\}+\sigma_{4Q}L_{\min}^{4Q}+C_{4Q},$$

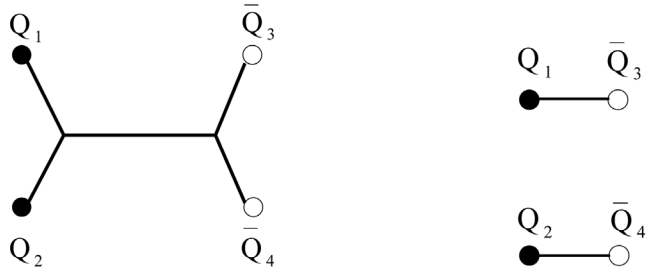

(a) (b)

Figure 9. (a) A connected tetraquark (QQ-$\bar{\mathrm{Q}}\bar{\mathrm{Q}}$) configuration and (b) A "two-meson" configuration [30]. The lattice QCD results indicate the multi-Y-shaped flux-tube formation for the connected 4Q system.

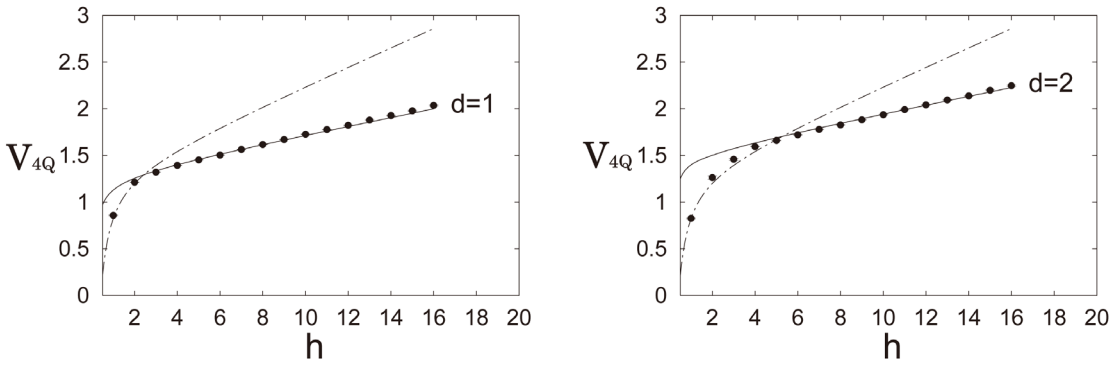

(a) (b)

Figure 10. Lattice QCD results of the tetraquark potential V_{4Q} for symmetric planar 4Q configurations in the lattice unit, taken from Ref. [30]. The symbols denote the lattice QCD data. The solid curve denotes the OGE plus multi-Y Ansatz, and the dotted-dashed curve the two-meson Ansatz.

where $L_{\min}^{4Q}$ is the minimal total length of the flux tube, which is multi-Y-shaped as shown in **Figure 9(a)**. Here, the coefficients $\left(A_{4Q},\sigma_{4Q}\right)$ are set to be $\left(A_{3Q},\sigma_{3Q}\right)$ obtained from the 3Q potential [26].

For small *h*, the lattice data tend to agree with the dotted-dashed curve of the "two-meson" Ansatz, where the 4Q potential is described by the sum of two $Q\bar{Q}$ potentials as $V_{Q\bar{Q}}\left(r_{13}\right)+V_{Q\bar{Q}}\left(r_{24}\right)=2V_{Q\bar{Q}}\left(h\right)$.

Thus, the tetraquark potential V_{4Q} is found to take the smaller energy of the connected 4Q state or the two-meson state. In other words, we observe a clear lattice QCD evidence of the "flip-flop", *i.e.*, the flux-tube recombination between the connected 4Q state and the two-meson state. This lattice result also supports the flux-tube picture for the 4Q system.

3.7. Proper Quark-Model Hamiltonian for Multi-Quarks

From a series of our lattice QCD studies [25]-[33] on the inter-quark potentials, the inter-quark potential is clarified to consist of the one-gluon-exchange (OGE) Coulomb part and the flux-tube-type linear confinement part in $Q\bar{Q}$-mesons, 3Q-baryons and multi-quark (4Q, 5Q) hadrons.

Furthermore, from the comparison among the $Q\bar{Q}$, 3Q, 4Q and 5Q potentials in lattice QCD, we find the universality of the string tension σ,

$$\sigma_{Q\bar{Q}} \simeq \sigma_{3Q} \simeq \sigma_{4Q} \simeq \sigma_{5Q}, \tag{13}$$

and the OGE result of the Coulomb coefficient *A* as

$$\frac{1}{2}A_{Q\bar{Q}} \simeq A_{3Q} \simeq A_{4Q} \simeq A_{5Q} \tag{14}$$

in Equations (5), (6), (12) and (13).

Here, the OGE Coulomb term is considered to originate from the OGE process, which plays the dominant role at short distances, where perturbative QCD is applicable. The flux-tube-type linear confinement would be physically interpreted by the flux-tube picture, where quarks and antiquarks are linked by the one-dimensional squeezed color-electric flux tube with the string tension σ.

To conclude, the inter-quark interaction would be generally described by the sum of the short-distance two-body OGE part and the long-distance flux-tube-type linear confinement part with the universal string tension $\sigma \simeq 0.89\ \mathrm{GeV/fm}$.

Thus, based on the lattice QCD results, we propose the proper quark-model Hamiltonian $\hat{H}$ for multi-quark hadrons as

$$\hat{H}=\sum_i \sqrt{\hat{\mathbf{p}}_i^2+M_i^2}+\sum_{i<j}V_{\mathrm{OGE}}^{ij}+\sigma L_{\min}, \tag{15}$$

where $L_{\min}$ is the minimal total length of the flux tube linking quarks. V_{OGE}^{ij} denotes the OGE potential between *i*th and *j*th quarks, which becomes the OGE Coulomb potential in Equation (7) in the static case. M_i denotes the constituent quark mass. The semi-relativistic treatment would be necessary for light quark systems.

It is desired to investigate various properties of multi-quark hadrons with this QCD-based quark model Hamiltonian $\hat{H}$.

4. Summary and Concluding Remarks

We have studied tetraquark and pentaquark systems in lattice QCD Monte Carlo simulations, motivated by the experimental discoveries of multi-quark candidates.

First, we have performed accurate mass calculations of low-lying 5Q states with $J=1/2$ and $I=0$ in both positive- and negative-parity channels in anisotropic lattice QCD. We have found that the lowest positive-parity 5Q state has a large mass of about 2.24 GeV after the chiral extrapolation. To single out the compact 5Q state from NK scattering states, we have used the hybrid boundary condition (HBC) method, and have found no evidence of the compact 5Q state below 1.75 GeV in the negative-parity channel.

Second, we have studied the multi-quark potential in lattice QCD to clarify the inter-quark interaction in

multi-quark systems. We have found that the 5Q potential V_{5Q} for the QQ-$\bar{Q}$-QQ system is well described by the "OGE Coulomb plus multi-Y Ansatz": the sum of the one-gluon-exchange (OGE) Coulomb term and the multi-Y-type linear term based on the flux-tube picture. The 4Q potential V_{4Q} for the QQ-$\bar{Q}\bar{Q}$ system is also described by the OGE Coulomb plus multi-Y Ansatz, when QQ and $\bar{Q}\bar{Q}$ are well separated. On the other hand, the 4Q system is described as a "two-meson" state with disconnected flux tubes, when the nearest quark and antiquark pair is spatially close. We have observed a lattice-QCD evidence for the "flip-flop", *i.e.*, the flux-tube recombination between the connected 4Q state and the "two-meson" state. On the confinement mechanism, we have clarified the flux-tube-type linear confinement in multi-quark hadrons. Finally, we have proposed the proper quark-model Hamiltonian based on the lattice QCD results.

Acknowledgements

This paper is based on the unpublished proceeding (hep-ph/0507187, talk by F.O.) at International Workshop on Quark Nuclear Physics, 22-24 Feb 2005. Phoenix Park, Korea. The lattice QCD Monte Carlo calculations were performed on supercomputers at Osaka University and at KEK.

References

[1] Nakano, T., *et al.*, LEPS Collaboration (2003) *Physical Review Letters*, **91**, Article ID: 012002. http://dx.doi.org/10.1103/PhysRevLett.91.012002

[2] Barmin, V.V., *et al.*, DIANA Collaboration (2003) *Physics of Atomic Nuclei*, **66**, 1715. http://dx.doi.org/10.1134/1.1611587

[3] Stephanyan, S., *et al.*, CLAS Collaboration (2003) *Physical Review Letters*, **91**, Article ID: 252001. http://dx.doi.org/10.1103/PhysRevLett.91.252001

[4] Barth, J., *et al.*, SAPHIR Collaboration (2003) *Physics Letters*, **B572**, 127. http://dx.doi.org/10.1016/j.physletb.2003.08.019

[5] Alt, C., *et al.*, NA49 Collaboration (2004) *Physical Review Letters*, **92**, Article ID: 042003. http://dx.doi.org/10.1103/PhysRevLett.92.042003

[6] Aktas, A., *et al.*, H1 Collaboration (2004) *Physics Letters*, **B588**, 17. http://dx.doi.org/10.1016/j.physletb.2004.03.012

[7] Schael, S., *et al.*, ALEPH Collaboration (2004) *Physics Letters*, **B599**, 1. http://dx.doi.org/10.1016/j.physletb.2004.08.021

[8] Bai, J.X., *et al.*, BES Collabolation (2004) *Physical Review*, **D70**, Article ID: 012004. http://dx.doi.org/10.1103/PhysRevD.70.012004

[9] Abt, I., *et al.*, HERA-B Collaboration (2004) *Physical Review Letters*, **93**, Article ID: 212003. http://dx.doi.org/10.1103/PhysRevLett.93.212003

[10] Naruki, M. (2009) *Lecture Notes in Physics*, **781**, 139, and Its References. http://dx.doi.org/10.1007/978-3-642-00961-7_6

[11] Moritsu, M., *et al.*, J-PARC E19 Collaboration (2014) *Physical Review C*, **90**, Article ID: 035205. http://dx.doi.org/10.1103/PhysRevC.90.035205

[12] Choi, S.K., *et al.*, Belle Collaboration (2003) *Physical Review Letters*, **91**, Article ID: 262001. http://dx.doi.org/10.1103/PhysRevLett.91.262001

[13] Acosta, D., *et al.*, CDF II Collaboration (2004) *Physical Review Letters*, **93**, Article ID: 072001. http://dx.doi.org/10.1103/PhysRevLett.93.072001

[14] Abazov, V.M., *et al.*, D0 Collaboration (2004) *Physical Review Letters*, **93**, Article ID: 162002. http://dx.doi.org/10.1103/PhysRevLett.93.162002

[15] Aubert, B., *et al.*, BABAR Collaboration (2004) *Physical Review Letters*, **93**, Article ID: 041801. http://dx.doi.org/10.1103/PhysRevLett.93.041801

[16] Aubert, B., *et al.*, BABAR Collaboration (2003) *Physical Review Letters*, **90**, Article ID: 242001. http://dx.doi.org/10.1103/PhysRevLett.90.242001

[17] Krokovny, P., *et al.*, Belle Collaboration (2003) *Physical Review Letters*, **91**, Article ID: 262002. http://dx.doi.org/10.1103/PhysRevLett.91.262002

[18] Aaij, R., *et al.*, LHCb Collaboration (2015) *Physical Review Letters*, **115**, Article ID: 072001.

http://dx.doi.org/10.1103/PhysRevLett.115.072001

[19] Diakonov, D., Petrov, V. and Polyakov, M.V. (1997) *Zeitschrift für Physik A Hadrons and Nuclei*, **359**, 305-314. http://dx.doi.org/10.1103/PhysRevLett.115.072001

[20] Jaffe, R.L. and Wilczek, F. (2003) *Physical Review Letters*, **91**, Article ID: 232003. http://dx.doi.org/10.1103/PhysRevLett.91.232003

[21] Stancu, F. and Riska, D.O. (2003) *Physics Letters B*, **575**, 242-248. http://dx.doi.org/10.1016/j.physletb.2003.09.061

[22] Sugiyama, J., Doi, T. and Oka, M. (2004) *Physics Letters B*, **581**, 167-174. http://dx.doi.org/10.1016/j.physletb.2003.12.018

[23] Creutz, M. (1979) *Physical Review Letters*, **43**, 553-556. http://dx.doi.org/10.1103/PhysRevLett.43.553
Creutz, M. (1980) *Physical Review D*, **21**, 2308-2315. http://dx.doi.org/10.1103/PhysRevD.21.2308

[24] Rothe, H.J. (2012) Lattice Gauge Theories. 4th Edition, World Scientific, Singapore. http://dx.doi.org/10.1142/8229

[25] Takahashi, T.T., Matsufuru, H., Nemoto, Y. and Suganuma, H. (2001) *Physical Review Letters*, **86**, 18-21. http://dx.doi.org/10.1103/PhysRevLett.86.18

[26] Takahashi, T.T., Suganuma, H., Nemoto, Y. and Matsufuru, H. (2002) *Physical Review D*, **65**, Article ID: 114509. http://dx.doi.org/10.1103/PhysRevD.65.114509

[27] Takahashi, T.T. and Suganuma, H. (2003) *Physical Review Letters*, **90**, Article ID: 182001. http://dx.doi.org/10.1103/PhysRevLett.90.182001
Takahashi, T.T. and Suganuma, H. (2004) *Physical Review D*, **70**, Article ID: 074506. http://dx.doi.org/10.1103/PhysRevD.70.074506

[28] Sakumichi, N. and Suganuma, H. (2015) *Physical Review D*, **92**, Article ID: 034511. http://dx.doi.org/10.1103/PhysRevD.92.034511

[29] Okiharu, F., Suganuma, H. and Takahashi, T.T. (2005) *Physical Review Letters*, **94**, Article ID: 192001. http://dx.doi.org/10.1103/PhysRevLett.94.192001

[30] Okiharu, F., Suganuma, H. and Takahashi, T.T. (2005) *Physical Review D*, **72**, Article ID: 014505. http://dx.doi.org/10.1103/PhysRevD.72.014505

[31] Suganuma, H., Takahashi, T.T., Okiharu, F. and Ichie, H. (2005) *AIP Conference Proceedings*, **756**, 123. http://dx.doi.org/10.1063/1.1920939
Suganuma, H., Takahashi, T.T., Okiharu, F. and Ichie, H. (2005) *Nuclear Physics B—Proceedings Supplements*, **141**, 92-98. http://dx.doi.org/10.1016/j.nuclphysbps.2004.12.015

[32] Okiharu, F., Suganuma, H. and Takahashi, T.T. (2005) The Static Pentaquark Potential in Lattice QCD. *Proceedings of the International Workshop on Pentaquark* 04, SPring-8, Hyogo, 20-23 July 2004, 339-343.

[33] Suganuma, H., Okiharu, F., Takahashi, T.T. and Ichie, H. (2005) *Nuclear Physics A*, **755**, 399-402. http://dx.doi.org/10.1016/j.nuclphysa.2005.03.098

[34] Ishii, N., Doi, T., Iida, H., Oka, M., Okiharu, F. and Suganuma, H. (2005) *Physical Review D*, **71**, Article ID: 034001. http://dx.doi.org/10.1103/PhysRevD.71.034001

[35] Ishii, N., Doi, T., Iida, H., Oka, M., Okiharu, F. and Suganuma, H. (2005) *Nuclear Physics A*, **755**, 467-470. http://dx.doi.org/10.1016/j.nuclphysa.2005.03.057

[36] Zhu, S.L. (2004) *International Journal of Modern Physics A*, **19**, 3439-3469. http://dx.doi.org/10.1142/S0217751X04019676

[37] Oka, M. (2004) *Progress of Theoretical Physics*, **112**, 1-19. http://dx.doi.org/10.1143/PTP.112.1

[38] Csikor, F., Fodor, Z., Katz, S.D. and Kovacs, T.G. (2003) *Journal of High Energy Physics*, **2003**, 070.

[39] Sasaki, S. (2004) *Physical Review Letters*, **93**, Article ID: 152001. http://dx.doi.org/10.1103/PhysRevLett.93.152001

[40] Chiu, T.W. and Hsieh, T.H. (2005) *Physical Review D*, **72**, Article ID: 034505. http://dx.doi.org/10.1103/PhysRevD.72.034505

[41] Mathur, N., Lee, F.X., Alexandru, A., Bennhold, C., Chen, Y., Dong, S.J., Draper, T., Horváth, I., Liu, K.F., Tamhankar, S. and Zang, J.B. (2004) *Physical Review D*, **70**, Article ID: 074508. http://dx.doi.org/10.1103/PhysRevD.70.074508

[42] Takahashi, T.T., Umeda, T., Onogi, T. and Kunihiro, T. (2005) *Physical Review D*, **71**, Article ID: 114509. http://dx.doi.org/10.1103/PhysRevD.71.114509

[43] Ishii, N., Doi, T., Nemoto, Y., Oka, M. and Suganuma, H. (2005) *Physical Review D*, **72**, Article ID: 074503. http://dx.doi.org/10.1103/PhysRevD.72.074503

[44] Capstick, S., Page, P.R. and Roberts, W. (2003) *Physics Letters B*, **570**, 185-190.

http://dx.doi.org/10.1016/j.physletb.2003.08.010

[45] Hosaka, A. (2003) *Physics Letters B*, **571**, 55-60. http://dx.doi.org/10.1016/j.physletb.2003.07.067

[46] Kanada-Enyo, Y., Morimatsu, O. and Nishikawa, T. (2005) *Physical Review C*, **71**, Article ID: 045202. http://dx.doi.org/10.1103/PhysRevC.71.045202

[47] Karliner, M. and Lipkin, H.J. (2003) *Physics Letters B*, **575**, 249-255. http://dx.doi.org/10.1016/j.physletb.2003.09.062

[48] Bicudo, P. and Marques, G.M. (2004) *Physical Review D*, **69**, Article ID: 011503. http://dx.doi.org/10.1103/PhysRevD.69.011503

[49] Sakumichi, N. and Suganuma, H. (2014) *Physical Review D*, **90**, Article ID: 111501(R). http://dx.doi.org/10.1103/PhysRevD.90.111501

[50] Nambu, Y. (1974) *Physical Review D*, **10**, 4262-4268. http://dx.doi.org/10.1103/PhysRevD.10.4262

[51] Kogut, J. and Susskind, L. (1975) *Physical Review D*, **11**, 395-408. http://dx.doi.org/10.1103/PhysRevD.11.395

[52] Casher, A., Neuberger, H. and Nussinov, S. (1979) *Physical Review D*, **20**, 179-188. http://dx.doi.org/10.1103/PhysRevD.20.179

[53] Carlson, J., Kogut, J.B. and Pandharipande, V.R. (1983) *Physical Review D*, **27**, 233-243. http://dx.doi.org/10.1103/PhysRevD.27.233
Carlson, J., Kogut, J.B. and Pandharipande, V.R. (1983) *Physical Review D*, **28**, 2807-2817. http://dx.doi.org/10.1103/PhysRevD.28.2807

[54] Ichie, H., Bornyakov, V., Streuer, T. and Schierholz, G. (2003) *Nuclear Physics A*, **721**, C899-C902. http://dx.doi.org/10.1016/S0375-9474(03)01238-7

[55] Kuzmenko, D.S. and Simonov, Y.A. (2003) *Physics of Atomic Nuclei*, **66**, 950-954. http://dx.doi.org/10.1134/1.1577917

[56] Bowman, P.O. and Szczepaniak, A.P. (2004) *Physical Review D*, **70**, Article ID: 016002. http://dx.doi.org/10.1103/PhysRevD.70.016002

[57] Cornwall, J.M. (2004) *Physical Review D*, **69**, Article ID: 065013. http://dx.doi.org/10.1103/PhysRevD.69.065013
Cornwall, J.M. (2005) *Physical Review D*, **71**, Article ID: 056002. http://dx.doi.org/10.1103/PhysRevD.71.056002

Journal of Modern Physics, 2016, 7, 790-805
Published Online April 2016 in SciRes. http://www.scirp.org/journal/jmp
http://dx.doi.org/10.4236/jmp.2016.78073

Non-Perturbative Analysis of Various Mass Generation by Gluonic Dressing Effect with the Schwinger-Dyson Formalism in QCD

Shotaro Imai[1], Hideo Suganuma[2]

[1]Institute for the Advancement of Higher Education, Hokkaido University, Sapporo, Japan
[2]Department of Physics, Graduate School of Science, Kyoto University, Kyoto, Japan
Email: imai@nucl.sci.hokudai.ac.jp, suganuma@scphys.kyoto-u.ac.jp

Received 15 February 2016; accepted 26 April 2016; published 29 April 2016

Abstract

As a topic of "quantum color dynamics", we study various mass generation of colored particles and gluonic dressing effect in a non-perturbative manner, using the Schwinger-Dyson (SD) formalism in (scalar) QCD. First, we review dynamical quark-mass generation in QCD in the SD approach as a typical fermion-mass generation via spontaneous chiral-symmetry breaking. Second, using the SD formalism for scalar QCD, we investigate the scalar diquark, a bound-state-like object of two quarks, and its mass generation, which is clearly non-chiral-origin. Here, the scalar diquark is treated as an extended colored scalar field, like a meson in effective hadron models, and its effective size R is introduced as a form factor. As a diagrammatical difference, the SD equation for the scalar diquark has an additional 4-point interaction term, in comparison with the single quark case. The diquark size R is taken to be smaller than a hadron, $R \sim 1$ fm, and larger than a constituent quark, $R \sim 0.3$ fm. We find that the compact diquark with $R \sim 0.3$ fm has a large effective mass of about 900 MeV, and therefore such a compact diquark is not acceptable in effective models for hadrons. We also consider the artificial removal of 3- and 4-point interaction, respectively, to see the role of each term, and find that the 4-point interaction plays the dominant role of the diquark self-energy. From the above two different cases, quarks and diquarks, we guess that the mass generation of colored particles is a general result of non-perturbative gluonic dressing effect.

Keywords

Dynamical Mass Generation, Diquarks, Schwinger-Dyson Formalism, QCD

1. Introduction

Quantum chromodynamics (QCD) is the fundamental gauge theory of the strong interaction, and it is a long

How to cite this paper: Imai, S. and Suganuma, H. (2016) Non-Perturbative Analysis of Various Mass Generation by Gluonic Dressing Effect with the Schwinger-Dyson Formalism in QCD. *Journal of Modern Physics*, **7**, 790-805.
http://dx.doi.org/10.4236/jmp.2016.78073

important problem to describe hadron structure and properties based on QCD. Quarks and gluons, the basic ingredients of QCD, strongly interact with each other in an infrared region, and they are confined in hadrons. Then, due to their non-perturbative properties, it is fairly difficult to describe hadrons directly from QCD. Also, the non-perturbative dynamics in QCD directly relates to the other important physical subject of "mass generation."

The origin of mass is one of the most fundamental issues in physics. One famous category of mass generation is the Yukawa interaction with the Higgs field. However, even besides the dark sector, the Higgs-origin mass is only about 1% of the total mass in our universe, where dominant massive particles are nuclei (u,d quarks) and electrons. Actually, the Higgs interaction only gives the electron mass (about 0.5MeV) and a small current quark mass (a few MeV) for u,d quarks [1]. In contrast, about 99% of mass of matter in our universe are created by the strong interaction, apart from the dark sector. In fact, a large constituent quark mass of $M_q = (300\text{ - }400)\,\mathrm{MeV}$ arises from non-perturbative dynamics in QCD. Thus, QCD gives another category of mass generation.

Such a dynamical fermion-mass generation in the strong interaction was first pointed out by Y. Nambu *et al.* [2] in 1961 in the context of spontaneous chiral-symmetry breaking. The QCD-based quantitative analysis of dynamical fermion mass generation was performed by Higashijima and Miransky in 1980's [3] [4] using the Schwinger-Dyson formalism. Thus, light u,d-quarks are considered to acquire a large constituent quark mass of about 300 - 400 MeV, in accordance with spontaneous chiral-symmetry breaking.

Even without chiral symmetry breaking, however, it is likely that QCD has several dynamical mass generation mechanism. For example, while the charm quark has no chiral symmetry, some difference seems to appear between current and constituent masses for charm quarks: the current mass is $m_c \simeq 1.2$ GeV at renormalization point $\mu = 2$ GeV [1], and the constituent charm quark mass is $M_c \simeq 1.6$ GeV in the quark model. The gluon is more drastic case. While the gluon mass is zero in perturbation QCD, the non-perturbative effect of the self-interaction of gluons seems to generate a large effective mass of 0.6 GeV [5]-[7], and the lowest glueball mass is about 1.6GeV [8] [9]. Furthermore, the dynamical mass generation for scalar-quark have been studied in the lattice scalar-QCD calculation [10]. Thus, we deduce that "quantum color dynamics" generally accompanies a large mass generation, due to the strong interaction.

Next, let us consider compositeness of hadrons in terms of quarks. As an infrared effective theory, the constituent quark model has been successful for the description of the hadron spectroscopy. The constituent quark belongs to the fundamental representation $\mathbf{3}_c$ in the $\mathrm{SU}(3)$ color group, and many hadrons can be classified as the color-singlet ($\mathbf{1}_c$) bound states of some quarks and antiquarks. In this picture, ordinary mesons and baryons are identified as quark-antiquark and three-quark systems, respectively. However, besides the ordinary baryons and mesons, QCD allows the existence of other color-singlet states, such as glueballs, hybrids and multi-quark states, called exotic hadrons. Recent experiments have reported the candidates for these exotic states [1]. The heavy hadrons, which includes one or more heavy (anti)quarks, are also recent hot topics in hadron physics [1] [11] [12]. For example, very recently, LHCb has reported the discovery of *two charmed pentaquarks*, P_c^+ (4380) and P_c^+ (4450), from a careful analysis of the decay product in the high-energy process, and this report seems to activate the multi-quark physics again [13].

In the theoretical study of these states, the diquark picture [14] [15] has been discussed as an important effective degree of freedom. The diquark is composed of two quarks with strong correlation, where the one-gluon-exchange interaction between two quarks is attractive in the color anti-triplet $\bar{\mathbf{3}}_c$ channel [16] [17], of which color is the same as an anti-quark. In $\mathrm{SU}(3)$ flavor case, the flavor-antisymmetric and spin-singlet with even parity is the most attractive channel in diquark, which is called scalar diquark. If the diquark correlation is developed in a hadron, this scalar diquark channel would be favored. The diquark correlation in a hadron is discussed in various situations, such as tetra-quarks, heavy baryons and other exotic states [18] [19]. The tetra-quark states as the bound state of the diquark/antidiquark is suggested in early day [20], and X(3872) [21] and X(1576) [22] are considered as tetra-quark states. Light flavor mesons as tetra-quark [23]-[32] and mixing with $q\bar{q}$ state [33]-[35] are discussed. There are various studies the heavy baryons focused on diquark [36]-[40], e.g., single heavy quark/light diquark (Qqq) picture [41]-[45]. The other exotic states including heavy quark(s) are studied [46]-[52]. The ordinary baryon properties focused on the diquarks have been also discussed [53]-[57]. The diquark correlation is found in the lattice QCD simulation [58]-[61]. It is also considered that the diquark condensation is occurred in an extremely high density system, called the color superconductivity [62].

We note that diquark properties strongly depend on the color number N_c. If we consider the two-color QCD, the diquarks compose the color singlet (baryons). The strength of correlation between two quarks is same as quark/antiquark channel, and the (diquark-)baryons correspond to the mesons. This fact is known as the Pauli-Gürsey symmetry. The quark-hadron matter in two-color system is investigated [63]-[69]. For the $N_c = 4$ case, the diquarks belong to $\mathbf{6}_c$ or $\mathbf{10}_c$. As an interesting fact for the case, the diquark contents must be different between baryons and tetra-quarks. In fact, the diquark qq in an $N_c = 4$ baryon $qqqq$ belongs to $\mathbf{6}_c$, which is self-adjoint. On the other hand, the diquark in a tetra-quark $qq\overline{qq}$ belongs to $\mathbf{10}_c$. From this viewpoint, the $N_c = 3$ case is rather special, because the diquarks belong to the same color $\overline{\mathbf{3}}_c$ in both cases of baryon qqq and tetra-quark $qq\overline{qq}$.

The properties of diquarks such as the mass and size are not understood well, although the diquarks have been discussed as important object of hadron physics. While the diquark is made by two quarks with gluonic interaction, it still strongly interacts with gluons additionally because of its non-zero color charge. Therefore, such dressing effect of gluons for diquark should be considered in a non-perturbative way. The dynamics of diquark and gluons may affect the structure of hadrons. In the quark-hadron physics, the Schwinger-Dyson (SD) formalism is often used to evaluate the non-perturbative effect based on QCD [3] [4] [70]-[78]. In this paper, we apply the SD formalism to scalar diquark to investigate the effective mass of scalar diquark, which reflects a non-perturbative dressing effect by gluons. The scalar diquark is treated as an extended field like a meson in effective hadron models, and interacts with the gluons [10] [42].

For the argument of the scalar diquark, it would be important to consider its effective size. For, point scalar particles generally have large radiative corrections even in the perturbation theory [79] [80]. As an example, in the framework of the grand unified theory (GUT), the Higgs scalar field suffers from a large radiative correction of the GUT energy scale, and therefore severe "fine-tuning" is inevitably required to realize the low-lying Higgs mass of about 126 GeV [81], which leads to the notorious hierarchy problem [79] [80]. The Higgs propagator with radiative correction has been investigated by setting the mass renormalization condition to reproduce 126 GeV [82]-[84]. A similar large radiative correction also appears for point-like scalar-quarks, which correspond to compact scalar diquarks, in scalar lattice QCD calculations [10]. In fact, the point-like scalar-quark interacting with gluons acquires a large extra mass of about 1.5 GeV at the cutoff $a^{-1} \simeq 1\,\mathrm{GeV}$, where a is the lattice spacing. Such a large-mass acquirement would be problematic in describing hadrons with scalar diquarks. However, since it is a bound-state-like object inside a hadron, the diquark must have an effective size. This effect gives a natural UV cutoff of the theory, and reduces the large radiative correction. Then, we take account of the effective size and investigate the mass of the scalar diquark inside a hadron within the SD formalism.

This paper is organized as follows. In Section 2, we review the SD formalism for the light quark, as the typical fermion mass generation in QCD. In Section 3, we investigate the SD equation for the scalar diquark, where a simple form factor is introduced for the possible size of diquark. In Section 4, we present the numerical result of the diquark self-energy with the dependence of the bare mass and size of diquark, and briefly discuss the dynamical mass generation for the scalar diquark in the SD formalism. Section 5 is devoted to conclusion and discussion.

2. Dynamical Mass Generation of Quarks in QCD

The chiral symmetry is a fundamental symmetry in the light-quark sector of QCD, and it is an exact global symmetry in the chiral limit. In the low-energy region of QCD, spontaneous chiral-symmetry breaking takes place, which generates a large effective mass of light quarks. Actually, in the theoretical analysis with the Schwinger-Dyson (SD) formalism in QCD, a large self-energy generation of quarks is demonstrated in an infrared region, which breaks the chiral symmetry in the physically stable vacuum [3] [4]. In this section, as the standard fermionic mass generation in QCD, we briefly review the quark mass generation in the SD formalism for QCD in the Landau gauge, which is frequently used. This review part gives a important basis for the non-perturbative QCD physics, and is also useful to set up the formalism for the scalar diquark case in Section 3.

As a merit of the Lorentz-covariant gauge like the Landau gauge, the dressed quark propagator is generally described as $S(p^2) = iZ(p^2)\left(\not{p} - \Sigma_q(p^2)\right)^{-1}$ with the wave function renormalization $Z(p^2)$ and the

self-energy of quark $\Sigma_q\left(p^2\right)$. The general and exact SD equation for the quark propagation is diagrammatically expressed in **Figure 1**. In principle, the quark propagator is exactly obtained by solving this equation, if the exact form of the gluon propagator and the quark-gluon vertex are given. Here, the kernel in the SD equation depicted in **Figure 1** is expressed by the product of the quark-gluon vertex $\Gamma_a^\mu\left(p,k\right)$ and the gluon dressing function $Z_g\left(\left(p-k\right)^2\right)$ [85],

$$\frac{g^2}{4\pi}Z_g\left(\left(p-k\right)^2\right)\gamma^\mu T_a\Gamma_b^\nu\left(p,k\right), \tag{1}$$

where T_a ($a=1,2,\cdots,N_c^2-1$) denotes the generator of the SU(N_c) color group.

In the most SD studies for quarks, one takes the rainbow-ladder approximation with the renormalization-group improvement of the quark-gluon vertex at the one-loop level. Note that, owing to the iterative structure of the SD equation, a simplified full-order treatment on the coupling α_s can be achieved, even with the use of the one-loop level vertex and so on. In actual, by the diagrammatical expansion, one can easily confirm the inclusion of infinite order of the coupling α_s, and the non-perturbative effect of gluons is thus included in this formalism. Recall that any nontrivial vacuum cannot be expressed by the perturbation theory.

Here, we briefly mention the treatment of quark confinement in the SD approach. In most works of the SD approach, the confinement effect is ignored, which seems problematic for the study of QCD. On this point, several recent studies, both analytical works [86] and lattice QCD simulations [87], have suggested that chiral symmetry breaking and quark confinement are not directly correlated in QCD. If this is the case, even without confinement, one may be able to discuss chiral symmetry breaking in QCD, as is the SD approach.

At the one-loop level of renormalization-group improvement, the SD kernel is approximated as

$$\frac{g^2}{4\pi}Z_g\left(\left(p-k\right)^2\right)\gamma^\mu T_a\Gamma_b^\nu\left(p,k\right)\to\alpha_s\left(\left(p-k\right)^2\right)\gamma^\mu T_a\gamma^\nu T_b, \tag{2}$$

and the Landau-gauge gluon propagator is given as

$$D_{\mu\nu}^{ab}\left(p^2\right)=\frac{-1}{p^2}\left(g_{\mu\nu}-\frac{p_\mu p_\nu}{p^2}\right)\delta^{ab}. \tag{3}$$

Then, by taking Dirac trace or the trace after multiplying $\not{p}$, the SD equation for the quark is expressed by the coupled integral equations:

$$\frac{\Sigma_q\left(p^2\right)}{Z\left(p^2\right)}=m_q+\frac{3iC_2\left(\mathbf{3}\right)}{4\pi^3}\int\mathrm{d}^4k\frac{\alpha_s\left(\left(p-k\right)^2\right)Z\left(k^2\right)\Sigma_q\left(k^2\right)}{\left(k^2-\Sigma_q^2\left(k^2\right)\right)\left(p-k\right)^2}, \tag{4}$$

$$\frac{1}{Z\left(p^2\right)}=1+\frac{iC_2\left(\mathbf{3}\right)}{4\pi^3p^2}\int\mathrm{d}^4k\frac{\alpha_s\left(\left(p-k\right)^2\right)Z\left(k^2\right)}{k^2-\Sigma_q^2\left(k^2\right)}\left(\frac{3p\cdot k}{\left(p-k\right)^2}+\frac{2\left(p\cdot k\right)^2}{\left(p-k\right)^4}-\frac{2p^2k^2}{\left(p-k\right)^4}\right), \tag{5}$$

with the bare quark mass m_q and the Casimir operator $C_2\left(\mathbf{3}\right)=\sum_{a=1}^8T^aT^a=4/3$ in the SU(3) color case.

We use one-loop level renormalization-group-improved coupling in the case of $N_c=3$ and $N_f=3$,

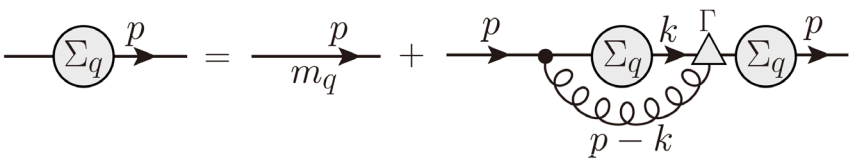

Figure 1. The Schwinger-Dyson equation for the quark field. The shaded blob denotes the self-energy of the quark $\Sigma_q\left(p^2\right)$, the black dot the bare quark-gluon vertex, the shaded triangle the dressed vertex $\Gamma_a^\mu\left(p,k\right)$, the solid line the quark propagator and the curly line the gluon propagator.

$$\alpha_s\left(p_E^2\right)=\frac{g^2\left(p_E^2\right)}{4\pi}=\frac{12\pi}{11N_c-2N_f}\begin{cases}\dfrac{1}{\ln\left(p_E^2/\Lambda_{\mathrm{QCD}}^2\right)} & \left(p_E^2\geq p_{\mathrm{IR}}^2\right)\\ \dfrac{1}{\ln\left(p_{\mathrm{IR}}^2/\Lambda_{\mathrm{QCD}}^2\right)} & \left(p_E^2\leq p_{\mathrm{IR}}^2\right)\end{cases}, \tag{6}$$

with an infrared regularization of a simple cut at $p_{\mathrm{IR}}\simeq 640\ \mathrm{MeV}$ which leads to $\ln\left(p_{\mathrm{IR}}^2/\Lambda_{\mathrm{QCD}}^2\right)=1/2$, and the QCD scale parameter $\Lambda_{\mathrm{QCD}}=500\ \mathrm{MeV}$ [4] [73] [77]. The subscript E, such as p_E, denotes the value in Euclidean space. The infrared regularization has been introduced to avoid the divergent pole at $p=\Lambda_{\mathrm{QCD}}$. The behavior of the coupling is shown in **Figure 2** in the Euclidean space. All the figures for the numerical results will be in the Euclidean space.

The Higashijima-Miransky approximation is to take the larger value of the argument (Euclidean momenta) in the coupling as $\alpha_s\left(\left(p_E-k_E\right)^2\right)\approx\alpha_s\left(\max\left(p_E^2,k_E^2\right)\right)$, and this approximation is also frequently used in the SD approach for quarks, because $Z\left(p_E^2\right)=1$ is analytically obtained in the Landau gauge and the computation becomes quite simplified for the quark self-energy $\Sigma_q\left(p_E^2\right)$:

$$\Sigma_q\left(p_E^2\right)=m_q+\frac{2\alpha_s\left(p_E^2\right)}{\pi p_E^2}\int_0^{p_E}\mathrm{d}k_E\,\frac{k_E^3\Sigma_q\left(k_E^2\right)}{k_E^2+\Sigma_q^2\left(p_E^2\right)}+\frac{2}{\pi}\int_{p_E}^{\Lambda_{\mathrm{UV}}}\mathrm{d}k_E\,\frac{k_E\alpha_s\left(k_E^2\right)\Sigma_q\left(k_E^2\right)}{k_E^2+\Sigma_q^2\left(k_E^2\right)}, \tag{7}$$

where the Wick rotation has been taken. (For the detail, see, e.g., Appendix in Ref. [73].) The result of the SD equation is shown in **Figure 3** in the chiral limit $m_q=0$. There is a small cusp structure at p_{IR} due to the coupling behavior Equation (6). The ultraviolet cutoff Λ_{UV} is taken as 5 GeV. The self-energy $\Sigma_q\left(p_E^2\right)$ is

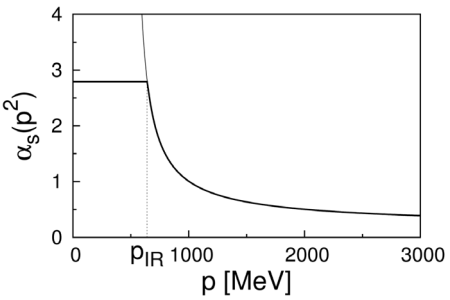

Figure 2. The behavior of the running coupling of our model $\alpha_s\left(p^2\right)$ as a function of the momentum p in the Euclidean space. The thin line is the one-loop renormalization group improved running coupling. We introduce a simple cut at p_{IR} as an infrared regularization.

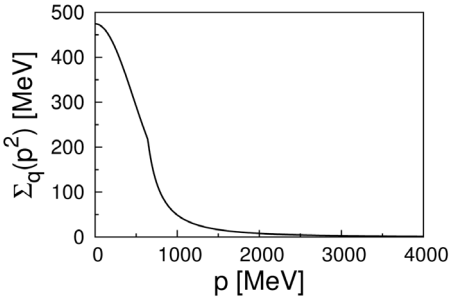

Figure 3. The quark self-energy $\Sigma_q\left(p^2\right)$ as a function of the momentum p in the chiral limit. The self-energy is large in the low momentum region and goes to zero monotonously with the momentum.

unchanged even the cutoff is taken 10 GeV. The quark mass is large at the infrared region and monotonously goes to zero with the momentum, which reflects spontaneous chiral-symmetry breaking [2]-[4] [88].

The scale parameter Λ_{QCD} is chosen to reproduce chiral properties for quarks in the SD formalism with the Higashijima-Miransky approximation in the Landau gauge, while the ordinary QCD scale parameter is around $\Lambda_{\mathrm{QCD}} \sim 200$ - 300 MeV. The self-energy leads to the pion decay constant with the Pagels-Stokar approximation [89]:

$$f_\pi^2 = \frac{N_c}{2\pi^2}\int_0^\infty \mathrm{d}k_E \frac{k_E^3 \Sigma_q\left(k_E^2\right)}{\left[k_E^2+\Sigma_q^2\left(k_E^2\right)\right]^2}\left(\Sigma_q\left(k_E^2\right)-\frac{k_E}{4}\frac{\mathrm{d}}{\mathrm{d}k_E}\Sigma_q\left(k_E^2\right)\right), \tag{8}$$

and the (unrenormalized) chiral condensate:

$$\left\langle \bar{q}q\right\rangle_{\Lambda_{\mathrm{UV}}} = -\frac{N_c}{2\pi^2}\int_0^{\Lambda_{\mathrm{UV}}} \mathrm{d}k_E \frac{k_E^3 \Sigma_q\left(k_E^2\right)}{k_E^2+\Sigma_q^2\left(k_E^2\right)}. \tag{9}$$

Since the pion decay constant is a physical value, its renormalization is not required and it does not depend on the ultraviolet cutoff Λ_{UV}. Hence, the upper limit of the integration has been taken as $\Lambda_{\mathrm{UV}} \to \infty$. On the other hand, the chiral condensate depends on the renormalization point. We adopt a standard renormalization point $\mu = 2$ GeV [1], and consider the chiral condensate $\left\langle \bar{q}q\right\rangle_{\mu=2\ \mathrm{GeV}}$ according to the renormalization-group formula [73] [74] [77]:

$$\left\langle \bar{q}q\right\rangle_{\mu=2\ \mathrm{GeV}} = \left(\frac{\alpha_s\left(\Lambda^2\right)}{\alpha_s\left(\mu^2\right)}\right)^{\frac{3C_2\left(N_c\right)}{16\pi^2\beta_0}} \left\langle \bar{q}q\right\rangle_{\Lambda_{\mathrm{UV}}}, \tag{10}$$

with $\frac{3C_2\left(N_c\right)}{16\pi^2\beta_0} = 4/9$ and $\beta_0 = \frac{11N_c - 2N_f}{48\pi^2}$ corresponding to the lowest coefficient of the β function of the renormalization group. Taking the scale parameter Λ_{QCD} as 500 MeV and the ultraviolet cutoff Λ_{UV} as 5 GeV, the pion decay constant and the chiral condensate are fixed as $f_\pi \simeq 90$ MeV and $-\left\langle \bar{q}q\right\rangle_{\mu=2\ \mathrm{GeV}}^{1/3} \simeq 242$ MeV, respectively. We have numerically checked that they are stable against the variation of the ultraviolet cutoff Λ_{UV}. The SD formalism with the approximations in the Landau gauge reproduces these chiral properties well.

3. The Schwinger-Dyson Equation for the Scalar Diquark

In this section, we investigate the scalar diquark, *i.e.*, an extended colored scalar object, and its mass generation, using the Schwinger-Dyson (SD) formalism.

Diquark is a bound-state-like object of two quarks and decomposed into color anti-triplet $\bar{\mathbf{3}}_c$ and sextet $\mathbf{6}_c$ and flavor anti-triplet $\bar{\mathbf{3}}_f$ and sextet $\mathbf{6}_f$ in SU(3) flavor case. The most attractive channel for diquark is the color and flavor anti-triplet $\bar{\mathbf{3}}_{c,f}$ and spin singlet with even parity 0^+ by one gluon exchange [16] [17] and by instanton interactions [90] [91], which is called scalar diquark. If the diquark correlation is developed in a hadron such as a heavy baryon (Qqq), this scalar diquark channel would be favored. We consider the scalar diquark as an effective degree of freedom with a peculiar size, assuming it to be an extended scalar field $\phi(x)$ [10] [42] like a meson in the effective hadron models. The scalar diquark is composed of two quarks with the gluonic interaction, and still affected by non-perturbative gluonic effects since it has non-zero color charge as shown **Figure 4**. The dynamics of the scalar diquark field ϕ is expected to be described by the gauge-invariant scalar-QCD-type Lagrangian:

$$\mathcal{L} = \left[\left(\partial^\mu + igA_a^\mu T^a\right)\phi\right]^\dagger \left[\left(\partial_\mu + igA_{\mu b}T^b\right)\phi\right] - m_\phi^2\,\phi^\dagger\phi, \tag{11}$$

where the bare diquark mass m_ϕ and the gauge field A_a^μ (gluon) with the generator T^a have been introduc-

(a) (b)

Figure 4. The two types of gluonic interaction for a diquark: (a) inter-two-quarks gluonic interaction to form a diquark and (b) gluonic dressing for the diquark due to its non-zero color charge. The single line denotes a quark, the double line a diquark and the curly line a gluon.

ed. We note that the scalar diquark has the 4-point interaction term of $|\phi|^2 A^2$ type, which is different from the quark. In general, such gauged scalar fields accompany the 4-point interaction [79] [82]-[84] [92].

Since the diquark is a bound-state-like object confined in a hadron, it must have an effective size and its size should be smaller than the hadron. In order to include the size effect of diquark, we introduce a simple "form factor" in the four-dimensional Euclidean space as

$$f_\Lambda\left(p_E^2\right)=\left(\frac{\Lambda^2}{p_E^2+\Lambda^2}\right)^\nu, \tag{12}$$

where the momentum cutoff Λ corresponds to the inverse of the diquark size R. In this paper, we set $R\equiv\Lambda^{-1}$. Since the radiative correction for the scalar particle is generally large, this form factor has also a role of the convergence factor. As for the form factor $f_\Lambda\left(p_E^2\right)$, it has the roles of introducing an effective size and convergence of the SD equation, so one can use arbitrary function such as the step function $\theta\left(\Lambda^2-p_E^2\right)$, the exponential function $\exp\left(-p_E^2/\Lambda^2\right)$ and so on. In this study, we take Equation (12) with $\nu=2$ to simple analysis and the convergence of the SD equation. The size effect of the diquark can be included in the vertex as $\alpha_s\left(p^2\right)\to\alpha_s\left(p^2\right)f_\Lambda\left(p^2\right)$.

While the scalar QCD Lagrangian (11) is renormalizable, this theory is an effective cutoff theory with an UV cutoff parameter Λ, which corresponds to the inverse size of the scalar diquark. Here, the scalar diquark cannot be observed as an isolated object, and has no characteristic symmetry, such as the chiral symmetry, so that it is difficult to set the renormalization condition. Instead, we introduce an effective size $R=\Lambda^{-1}$ of the diquark, which leads to a natural UV cutoff in the theory. As we will see later, the effective size of diquark will play an important role for the convergent of loop integrations, and therefore we will not take the limit of $\Lambda\to\infty$ ($R\to 0$). In fact, the extended diquark is treated as the effective degrees of freedom appearing in the QCD system of quarks and gluons, and hence, also for the scalar diquark, we basically use the same framework as the single quark case, presented in the previous section. For instance, we will use the same running coupling $\alpha_s\left(p_E^2\right)$ in Equation (6) for the argument of diquarks.

We now describe the SD equation for the scalar diquark, as shown in **Figure 5**. For the self-energy diagram, we include the first order of the coupling α_s at the one-loop level, like the improved ladder QCD [3] [4] [73] [74]. Note however that, due to the iterative calculation, this formalism includes infinite order of the coupling α_s and describes non-perturbative effects. It is also notable that the same form of the running coupling for the quark/gluon coupling can be used even for the scalar diquark/gluon [93] [94]. (In particular, in the heavy mass limit of colored particles, the QCD interaction depends only on their color.) Since the scalar diquark corresponds to an antiquark in terms of the color representation, we may use the same form of the running coupling even for the scalar diquark case. Then, the SD equation for the scalar diquark is diagrammatically expressed as **Figure 5** and is written by

$$\begin{aligned}\Sigma^2\left(p_E^2\right)=m_\phi^2&+\frac{3C_2(\mathbf{3})}{2\pi^3}\int_0^{\Lambda_{\mathrm{UV}}}\mathrm{d}^4k_E\,\frac{\alpha_s\left(k_E^2\right)f_\Lambda\left(k_E^2\right)}{k_E^2}\\&-\frac{C_2(\mathbf{3})}{\pi^3}\int_0^{\Lambda_{\mathrm{UV}}}\mathrm{d}^4k_E\,\frac{\alpha_s\left(\left(p_E-k_E\right)^2\right)f_\Lambda\left(\left(p_E-k_E\right)^2\right)}{k_E^2+\Sigma^2\left(k_E^2\right)}\frac{p_E^2k_E^2-\left(p_E\cdot k_E\right)^2}{\left(p_E-k_E\right)^4}.\end{aligned} \tag{13}$$

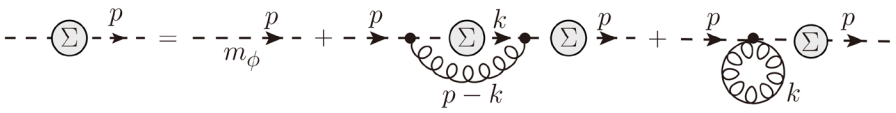

Figure 5. The Schwinger-Dyson equation for the scalar diquark. The shaded blob is the self-energy $\Sigma\left(p^2\right)$, the dashed line denotes the scalar diquark propagator and the curly line the gluon propagator. The last term arisig from 4-point interaction is the peculiar term in gauged scalar theories, and it does not appear in the single quark case in QCD.

In the right-hand side of Equation (13), the second term arises from the 4-point vertex and the third term is lead from the 3-point vertex, as shown in **Figure 5**. Here, we do not consider the wave functional renormalization, as is often assumed for the quark field in the Landau gauge. Similarly in the single quark case, we adopt the Higashijima-Miransky approximation $\alpha_s\left(\left(p_E-k_E\right)^2\right)\approx\alpha_s\left(\max\left(p_E^2,k_E^2\right)\right)$ for the 3-point vertex, and finally obtain the SD equation for the self-energy $\Sigma^2\left(p_E^2\right)$ of the scalar diquark:

$$\Sigma^2\left(p_E^2\right)=m_\phi^2+\frac{4}{\pi}\int_0^{\Lambda_{\mathrm{UV}}}\mathrm{d}k_E k_E\alpha_s\left(k_E^2\right)f_\Lambda\left(k_E^2\right)-\frac{2\alpha_s\left(p_E^2\right)f_\Lambda\left(p_E^2\right)}{\pi p_E^2}\int_0^{p_E}\mathrm{d}k_E\frac{k_E^5}{k_E^2+\Sigma^2\left(k_E^2\right)}$$
$$-\frac{2p_E^2}{\pi}\int_{p_E}^{\Lambda_{\mathrm{UV}}}\mathrm{d}k_E\frac{\alpha_s\left(k_E^2\right)f_\Lambda\left(k_E^2\right)k_E}{k_E^2+\Sigma^2\left(k_E^2\right)}. \tag{14}$$

4. Numerical Results and Discussion

4.1. The Parameter Setting

The bare mass m_ϕ and cutoff Λ (inverse of the size *R*) are free parameters of the diquark theory. In this subsection, we consider the possible range of these parameters from the physical viewpoint.

The diquark is originally made of two consistent quarks, and the color-Coulomb interaction is one of the main attractive forces. We here estimate the color-Coulomb interaction between the two massive quarks from the three-quark (3Q) potential [99], or generally from the mult-quark potential such as 4Q($\mathrm{QQ\bar{Q}\bar{Q}}$) and 5Q($\mathrm{4Q\bar{Q}}$) potentials [100]. In SU(3) lattice QCD, the 3Q potential among the three quarks located at $r_i\left(i=1,2,3\right)$ is well reproduced by

$$V_{3\mathrm{Q}}=-\sum_{i<j}\frac{A_{3\mathrm{Q}}}{\left|\mathbf{r}_i-\mathbf{r}_j\right|}+\sigma L_{\min}, \tag{15}$$

with the color-Coulomb coefficient $A_{3\mathrm{Q}}\simeq A_{\mathrm{Q\bar{Q}}}/2\simeq 0.12(1)$, the string tension $\sigma\simeq 0.89\,\mathrm{GeV/fm}$ and the minimal flux-tube length $L_{\min}$ [99]. Since the color-Coulomb potential energy between two quarks is $A_{3\mathrm{Q}}/R$ for the inter-quark distance *R*, the potential energy is estimated as $A_{3\mathrm{Q}}/R\simeq 24\text{ - }80\ \mathrm{MeV}$ for the typical range of $R=0.3\text{ - }1\ \mathrm{fm}$, and its value is not so large in comparison with the two-quark mass of about 600 MeV. [Note also that similar estimation also leads to a small value of the diquark-diquark interaction, which gives a reason of the absence of $\left(\phi^\dagger\phi\right)^2$ in the diquark Lagrangian (11).] The same result can be obtained from the multi-quark potential [100], because the color-Coulomb coefficient is the same for two quarks in the diquark, *i.e.*, $A_{n\mathrm{Q}}\simeq A_{\mathrm{Q\bar{Q}}}/2\simeq 0.12(1)$ for *n* = 3, 4, 5. Therefore, the bare mass of diquark is expected to be simply considered as the twice of the quark mass.

In this paper, we consider two cases of the bare diquark mass. One is twice of constituent quark mass, *i.e.*, $m_\phi=600\ \mathrm{MeV}$. The other is twice of the running quark self-energy, *i.e.*, $m_\phi\left(p_E^2\right)=2\Sigma_q\left(p_E^2\right)$, where $\Sigma_q\left(p_E^2\right)$ is determined by the SD equation for single quark Equation (7). This means that the diquark is constructed by

the two dressing quarks. The constant bare mass case is based on the constituent quark model like picture and the running bare mass case is the SD formalism with omitting the effect of the gluonic attraction force between two quarks. The diquark should be dressed by gluon furthermore because of its non-zero color charge.

The cutoff Λ corresponds to the diquark size in a hadron, R, *i.e.*, $\Lambda \equiv R^{-1}$, so the diquark should be smaller than the hadron. We also consider two cases of the size. One is the typical size of a baryon, $R = 1\,\text{fm}$, *i.e.*, $\Lambda = 200\,\text{MeV}$, which gives the upper limit of the size (the lower limit of the cutoff). The diquark covers the baryon in this case. The second is the typical size of a constituent quark, $R \simeq 0.3\,\text{fm}$, *i.e.*, $\Lambda = 600\,\text{MeV}$, which gives the lower limit of the size (the upper limit of the cutoff).

4.2. The Constant Bare Mass Case

We first show in **Figure 6** the case of the constant bare mass $m_\phi = 600\,\text{MeV}$ with dependence on the cutoff Λ. The diquark self-energy $\Sigma(p^2)$ is always larger than the bare mass m_ϕ and almost constant except for a small bump structure in an infrared region. The value of the self-energy is strongly depends on the cutoff Λ, e.g., the "compact diquark" with $R \simeq 0.3\,\text{fm}$ has a large mass.

The scalar QCD includes both 3-point and 4-point interactions, and the existence of 4-point interaction is diagrammatically different from the ordinary QCD. To see the role of each interaction, we consider the calculation of the artificial removal of 3-point interaction and 4-point interaction, respectively. In fact, we investigate the two cases: (a) removal of 4-point interaction and (b) removal of 3-point interaction. The result is shown in **Figure 7** in the case of $\Lambda = 200\,\text{MeV}$. The bump structure appears in the case without the 4-point interaction term as shown in **Figure 7(a)**. Although the diagrammatic expression of the SD equation for the scalar

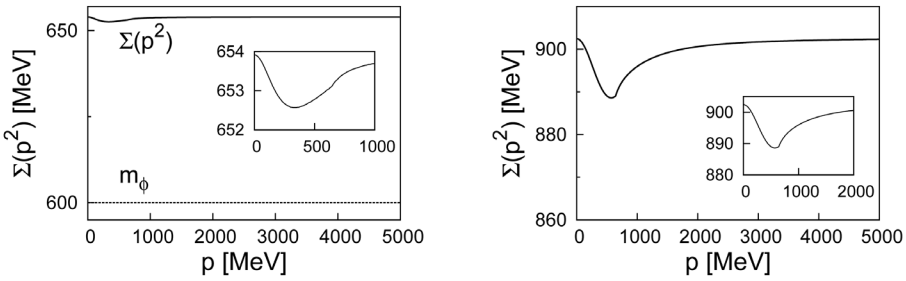

(a) (b)

Figure 6. The scalar diquark self-energy $\Sigma(p^2)$ as a function of the momentum p in the constant bare mass case of $m_\phi = 600\,\text{MeV}$ with (a) $\Lambda = 200\,\text{MeV}$, i.e., $R = 1\,\text{fm}$ and (b) $\Lambda = 600\,\text{MeV}$, i.e., $R \simeq 0.3\,\text{fm}$. In both cases, there appears a small bump structure, which is displayed in the small window. In the left figure, the original bare mass m_ϕ is plotted for comparison.

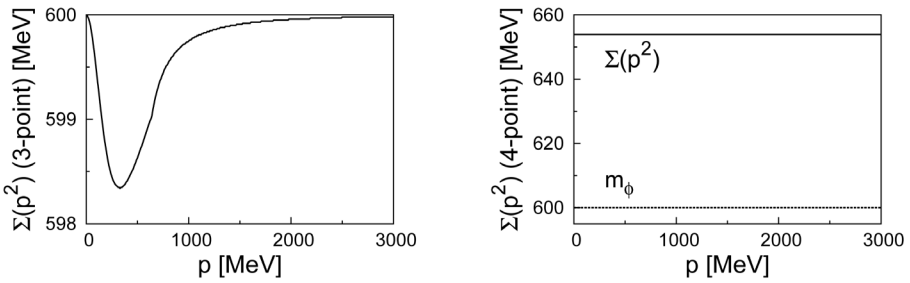

(a) (b)

Figure 7. The self-energy $\Sigma(p^2)$ in the case of (a) without 4-point interaction and (b) without 3-point interaction as the function of the momentum p. Here, $\Lambda = 200\,\text{MeV}$ is taken. In the right figure, the original bare mass m_ϕ is plotted for comparison.

diquark without 4-point interaction term is analogous to the quark SD equation, the behavior is completely different from the quark case. The diquark self-energy $\Sigma\left(p_E^2\right)$ starts from the bare mass $m_\phi = 600$ MeV at zero momentum, then decreases at low momentum and rises up to the original value 600 MeV. On the other hand, the quark self-energy $\Sigma_q\left(p_E^2\right)$ starts from a large value and goes to zero monotonously with the momentum. The SD equation without 3-point interaction just rises the self-energy and keeps constant. The strong dependence of the cutoff Λ (or the size R) mainly comes from the 4-point interaction term.

4.3. The Running Bare Mass Case

We show in **Figure 8** the case of the running bare mass $m_\phi\left(p_E^2\right) = 2\Sigma_q\left(p_E^2\right)$ with dependence on the cutoff Λ. The diquark self-energy $\Sigma\left(p_E^2\right)$ also strongly depends on the cutoff Λ. In the low-momentum region, the behavior of $\Sigma\left(p_E^2\right)$ reflects the running property of the bare mass, especially in the $\Lambda = 200$ MeV case, the gluonic effect seems to be small, because of $\Sigma\left(p_E^2\right) \approx 2\Sigma_q\left(p_E^2\right)$. In the high-momentum region, the diquark self-energy keeps a large value, while the bare mass $m_\phi\left(p_E^2\right)$ goes to zero. This suggests the mass generation of the scalar diquark by gluonic radiative correction.

4.4. Discussion on the Scalar Diquark Property

In this subsection, we discuss the mass and the size of the scalar diquark, with comparing to the chiral quark. One of the most important properties of single quark SD equation (7) is the existence of the trivial solution $\Sigma_q = 0$ in the chiral limit $m_q \to 0$. In fact, the quark mass remains to be zero due to the chiral symmetry in the perturbative treatment, and the quark mass generation, *i.e.*, chiral symmetry breaking, is realized by the non-perturbative gluonic interaction [3] [4]. Such arguments can be done even in the limit of $\Lambda_{\mathrm{UV}} \to \infty$, which is consistent with the point quark as an elementary particle.

On the other hand, the SD equation (13) for scalar diquark has no trivial solution and is a highly non-linear equation, even in the zero bare mass limit $m_\phi \to 0$. For example, the 4-point interaction term gives a strong dependence of the UV cutoff Λ. This is similar to the framework of GUT, where the Higgs scalar field suffers from a large radiative correction of the GUT energy scale.

Actually, the scalar diquark self-energy $\Sigma\left(p^2\right)$ strongly depends on the diquark size $R \equiv \Lambda^{-1}$ in both cases of the bare mass. In an extreme case of the point-like limit $R \to 0$, *i.e.*, $\Lambda \to \infty$, the diquark effective mass diverges. This suggests that the simple treatment of point-like diquarks is somehow dangerous in hadron models and the diquark must have an effective size.

As a quantitative argument, our calculations show that the "compact diquark" with $R \simeq 0.3$ fm has a large effective mass in both cases, and does not seem to be acceptable in effective models for hadrons. In fact, the appropriate diquark is not so compact as $R \simeq 0.3$ fm but is fairly extended as $R \sim 1$ fm.

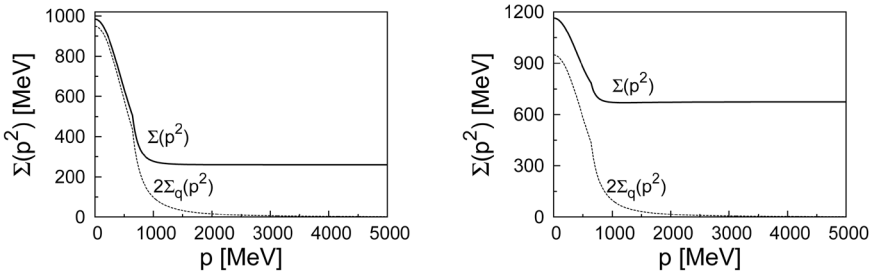

Figure 8. The scalar diquark self-energy $\Sigma\left(p^2\right)$ as a function of the momentum p in the running bare mass case with (a) $\Lambda = 200$ MeV ($R = 1$ fm) and (b) $\Lambda = 600$ MeV ($R \simeq 0.3$ fm). The bare mass $m_\phi(p) = 2\Sigma_q(p)$ is also plotted with the dotted line for comparison.

4.5. Mass Generation for Colored Scalar Particle

Finally, we consider the zero bare-mass case of diquark, $m_\phi \equiv 0$. Even for a finite mass of quark, the bare mass of diquark can be zero, if the attraction between two quarks extremely strong. The result is shown in **Figure 9** for the two cases: (a) $\Lambda = 200$ MeV and (b) $\Lambda = 600$ MeV on the cutoff. The self-energy $\Sigma\left(p_E^2\right)$ is always finite and takes a large value even for $m_\phi \equiv 0$. The mass generation mechanism in QCD is usually considered in the context of spontaneous chiral-symmetry breaking. On the other hand, our scalar diquark theory is composed of an effective scalar diquark field $\phi(x)$ and does not have the chiral symmetry explicitly, although the original diquark is constructed by two chiral quarks. Nevertheless, the effective mass of diquark emerges by the non-perturbative gluonic effect. In fact, the mechanism of dynamical mass generation seems to work in the scalar diquark theory, even without chiral symmetry breaking. If we take $\Lambda = 1$ GeV, the diquark self-energy is $\Sigma \sim 950$ MeV. This result seems to be consistent with the lattice QCD result on the colored scalar particle [10].

5. Conclusion and Discussion

We have studied various mass generation of colored particles and gluonic dressing effect in a non-perturbative manner, using the Schwinger-Dyson (SD) formalism in QCD. First, we have briefly reviewed dynamical quark-mass generation in QCD in the SD approach as a typical fermion-mass generation via spontaneous chiral-symmetry breaking. Second, using the SD formalism for scalar QCD, we have investigated the scalar diquark, a bound-state-like object of two quarks, and its mass generation, which is clearly non-chiral-origin. Considering the possible size of the diquark inside a hadron, the effect of diquark size R is introduced as a cutoff parameter $\Lambda = R^{-1}$ in the form factor, as is used in effective theories.

The basic technology of scalar SD formalism is imported from the single quark case, such as the running coupling, the approximations and so on. Since the diquark is located in and construct of a hadron, the size should be smaller than the hadron ($R \sim 1$ fm) and larger than the constituent quark ($R \sim 0.3$ fm). The size (cutoff) dependence of self-energy have been investigated. We have considered the two cases of the constant bare mass $m_\phi = 600$ MeV and the running bare mass $m_\phi\left(p_E^2\right) = 2\Sigma_q\left(p_E^2\right)$. The diquark self-energy strongly depends on the size $R = \Lambda^{-1}$ in both cases, especially the small diquark ($R \simeq 0.3$ fm) has a large effective mass by the gluonic dressing effect.

We find that the effective diquark mass is finite and large even for the zero bare-mass case, and the value strongly depends on the size R, which is an example of dynamical mass generation by the gluonic effect, without chiral symmetry breaking. The mass difference between current and constituent charm quark mass and the large glueball mass are also examples of this type of mass generation. In this sense, spontaneous chiral-symmetry breaking may be a special case of massless (or small mass) fermion. As was conjectured in Ref. [10], it would be a general property of strong interacting theory that all colored particles acquire a large effective mass by the dressing effect, as shown in **Figure 10**.

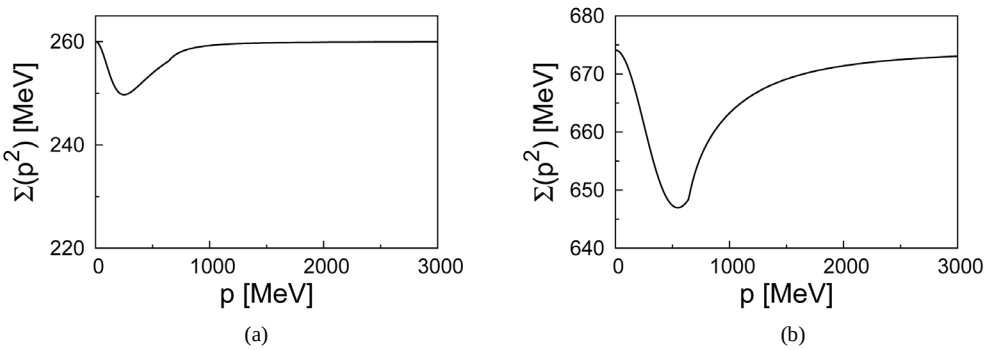

Figure 9. The scalar diquark self-energy $\Sigma\left(p^2\right)$ as a function of the momentum p in the massless case of $m_\phi = 0$: (a) $\Lambda = 200$ MeV ($R = 1$ fm) and (b) $\Lambda = 600$ MeV ($R \simeq 0.3$ fm). The self-energy $\Sigma\left(p^2\right)$ is finite in both cases.

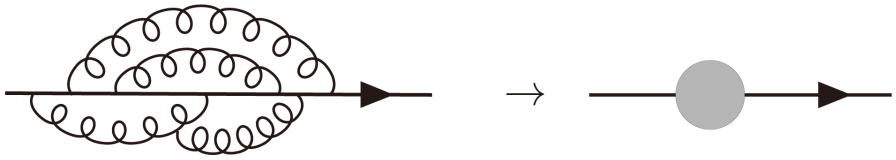

Figure 10. The schematic picture for dynamical mass generation of the colored particle. The colored particle (solid line) interacting with the gluons (curly line). The effective mass emerges by the non-perturbative interaction even without the chiral symmetry.

In this study, we have mainly investigated the diquark properties, and have not calculated physical quantities. It is however desired to describe the color-singlet states such as heavy baryon Qqq based on the scalar theory. One of description of diquark based on QCD is the Bethe-Salpeter (BS) formalism for two quarks [95]-[98]. However, the treatment of the scalar diquark as an explicit degree of freedom $\phi(x)$ is a good approximation for the structure of the heavy baryons. The constituent scalar-quark(diquark)/quark picture in the scalar lattice QCD [10] and the structure of Λ_h ($h = s, c, b$ quarks) with explicit diquark degree of freedom using QCD sum rule [42] have been discussed. The description of the heavy baryon as heavy quark/diquark ($Q\phi$) using the BS equation will be investigated as our future work.

The tetra-quark states $qq\overline{qq}$ may include diquark/antidiquark components. Although the two mesons molecular states may dominate in the tetra-quark due to the strong correlation between quark and antiquark, the diquark/antidiquark would be also important components [21]-[25]. The tetra-quark states would be described as the linear combination of two mesons and diquark/antidiquark states based on the BS formalism. The structure of sigma meson (light scalar mesons) is also applicable subject. The sigma meson is considered as a chiral partner of the pion in the context of the chiral symmetry, which structure is quark/antiquark bound state. The possibility of the light scalar mesons as four-quark states have been discussed [20] [23]-[35]. The structure of the sigma meson (light scalar mesons) can be described as the linear combination of quark/antiquark, diquark/antidiquark and two mesons in the context of the BS formalism.

Acknowledgements

S.I. thanks T.M. Doi, H. Iida and N. Yamanaka for useful discussion and comments. This work is in part supported by the Grant for Scientific Research [Priority Areas “New Hadrons” (E01:21105006), (C) No.23540306, No.15K05076] from the Ministry of Education, Culture, Science and Technology of Japan.

References

[1] Olive, K.A., *et al.*, Particle Data Group (2014) *Chinese Physics*, **C38**, Article ID: 090001.

[2] Nambu, Y. and Jona-Lasinio, G. (1961) *Physical Review*, **122**, 345. http://dx.doi.org/10.1103/PhysRev.122.345

Nambu, Y. and Jona-Lasinio, G. (1961) *Physical Review*, **124**, 246. http://dx.doi.org/10.1103/PhysRev.124.246

[3] Miransky, V.A. (1983) *Soviet Journal of Nuclear Physics*, **38**, 280.

Miransky, V.A. (1994) Dynamical Symmetry Breaking in Quantum Field Theories. World Sicentific, Singapore.

[4] Higashijima, K. (1984) *Physical Review*, **D29**, 1228. http://dx.doi.org/10.1103/PhysRevD.29.1228

Higashijima, K. (1991) *Progress of Theoretical Physics Supplement*, **104**, 1. http://dx.doi.org/10.1143/PTPS.104.1

[5] Iritani, T., Suganuma, H. and Iida, H. (2009) *Physical Review*, **D80**, Article ID: 114505. http://dx.doi.org/10.1103/PhysRevD.80.114505

[6] Mandula, J. and Ogilvie, M. (1987) *Physics Letters*, **B185**, 127. http://dx.doi.org/10.1016/0370-2693(87)91541-3

[7] Amemiya, K. and Suganuma, H. (1999) *Physical Review*, **D60**, Article ID: 114509. http://dx.doi.org/10.1103/PhysRevD.60.114509

Gongyo, S. and Suganuma, H. (2013) *Physical Review*, **D87**, Article ID: 074506. http://dx.doi.org/10.1103/PhysRevD.87.074506

Gongyo, S., Iritani, T. and Suganuma, H. (2012) *Physical Review*, **D86**, Article ID: 094018. http://dx.doi.org/10.1103/PhysRevD.86.094018

[8] Morningstar, C.J. and Peardon, M.J. (1999) *Physical Review*, **D60**, Article ID: 034509. http://dx.doi.org/10.1103/PhysRevD.60.034509

[9] Ishii, N., Suganuma, H. and Matsufuru, H. (2002) *Physical Review*, **D66**, Article ID: 094506. http://dx.doi.org/10.1103/PhysRevD.66.094506

[10] Iida, H., Suganuma, H. and Takahashi, T.T. (2007) *Physical Review*, **D75**, Article ID: 114503 http://dx.doi.org/10.1103/PhysRevD.75.114503

Iida, H., Suganuma, H. and Takahashi, T.T. (2007) *Modern Physics Letters*, **A23**, 2344

Iida, H., Suganuma, H. and Takahashi, T.T. (2008) *AIP Conference Proceedings*, **915**, 256. http://dx.doi.org/10.1063/1.2750775

[11] Brambilla, N., *et al.* (2011) *The European Physical Journal C*, **71**, 1534. http://dx.doi.org/10.1140/epjc/s10052-010-1534-9

[12] Cho, S., *et al.*, ExHIC Collaboration (2011) *Physical Review Letters*, **106**, Article ID: 212001. http://dx.doi.org/10.1103/PhysRevLett.106.212001

[13] Aaij, R., *et al.*, LHCb Collaboration (2015) *Physical Review Letters*, **115**, Article ID: 072001. http://dx.doi.org/10.1103/PhysRevLett.115.072001

[14] Lichtenberg, D. and Tassie, L. (1967) *Physical Review*, **155**, 1601. http://dx.doi.org/10.1103/PhysRev.155.1601

[15] Ida, M. and Kobayashi, R. (1966) *Progress of Theoretical Physics*, **36**, 846-847. http://dx.doi.org/10.1143/PTP.36.846

[16] De Rujula, A., Georgi, H. and Glashow, S. (1975) *Physical Review D*, **12**, 147. http://dx.doi.org/10.1103/PhysRevD.12.147

[17] DeGrand, T.A., Jaffe, R., Johnson, K. and Kiskis, J. (1975) *Physical Review D*, **12**, 2060. http://dx.doi.org/10.1103/PhysRevD.12.2060

[18] Jaffe, R. (2005) *Physics Reports*, **409**, 1-45, http://dx.doi.org/10.1016/j.physrep.2004.11.005

Jaffe, R. (2005) *Nuclear Physics B-Proceedings Supplements* **142**, 343-355. http://dx.doi.org/10.1016/j.nuclphysbps.2005.01.058

[19] Close, F. (2005) *International Journal of Modern Physics A*, **20**, 5156. http://dx.doi.org/10.1142/S0217751X05028661

[20] Jaffe, R.L. (1977) *Physical Review D*, **15**, 267. http://dx.doi.org/10.1103/PhysRevD.15.267

[21] Maiani, L., Piccinini, F., Polosa, A. and Riquer, V. (2005) *Physical Review D*, **71**, Article ID: 014028. http://dx.doi.org/10.1103/PhysRevD.71.014028

[22] Ding, G.-J. and Yan, M.-L. (2006) *Physics Letters B*, **643**, 33-40. http://dx.doi.org/10.1016/j.physletb.2006.10.022

[23] Zhang, A., Huang, T. and Steele, T. (2007) *Physical Review D*, **76**, Article ID: 036004. http://dx.doi.org/10.1103/PhysRevD.76.036004

[24] Lee, H.-J. (2006) *The European Physical Journal A*, **30**, 423-426. http://dx.doi.org/10.1140/epja/i2006-10104-y

[25] Heupel, W., Eichmann, G. and Fischer, C.S. (2012) *Physics Letters B*, **718**, 545-549. http://dx.doi.org/10.1016/j.physletb.2012.11.009

[26] Alford, M.G. and Jaffe, R. (2000) *Nuclear Physics B*, **578**, 367-382. http://dx.doi.org/10.1016/S0550-3213(00)00155-3

[27] Suganuma, H., Tsumura, K., Ishii, N. and Okiharu, F. (2007) *Progress of Theoretical Physics Supplement*, **168**, 168-172. http://dx.doi.org/10.1143/PTPS.168.168

[28] Prelovsek, S., Draper, T., Lang, C.B., Limmer, M., Liu, K.-F., Mathur, N. and Mohler, D. (2010) *Physical Review D*, **82**, Article ID: 094507. http://dx.doi.org/10.1103/PhysRevD.82.094507

[29] Wakayama, M., *et al.*, SCALAR Collaboration (2015) *Physical Review D*, **91**, Article ID: 094508. http://dx.doi.org/10.1103/PhysRevD.91.094508

[30] Alexandrou, C., Daldrop, J.O., Brida, M.D., Gravina, M., Scorzato, L., Urbach, C. and Wagner, M. (2013) *Journal of High Energy Physics*, **1304**, 137. http://dx.doi.org/10.1007/JHEP04(2013)137

[31] Chen, H.-X., Hosaka, A. and Zhu, S.-L. (2007) *Physical Review D*, **76**, Article ID: 094025. http://dx.doi.org/10.1103/PhysRevD.76.094025

Chen, H.-X., Hosaka, A. and Zhu, S.-L. (2007) *Physics Letters B*, **650**, 369-372. http://dx.doi.org/10.1016/j.physletb.2007.05.031

Chen, H.-X., Hosaka, A. and Zhu, S.-L. (2006) *Physical Review D*, **74**, Article ID: 054001. http://dx.doi.org/10.1103/PhysRevD.74.054001

[32] Chen, H.-X., Hosaka, A., Toki, H. and Zhu, S.-L. (2010) *Physical Review D*, **81**, Article ID: 114034. http://dx.doi.org/10.1103/PhysRevD.81.114034

[33] Sugiyama, J., Nakamura, T., Ishii, N., Nishikawa, T. and Oka, M. (2007) *Physical Review D*, **76**, Article ID: 114010. http://dx.doi.org/10.1103/PhysRevD.76.114010

[34] Fariborz, A.H., Jora, R. and Schechter, J. (2008) *Physical Review D*, **77**, Article ID: 094004. http://dx.doi.org/10.1103/PhysRevD.77.094004

[35] 't Hooft, G., Isidori, G., Maiani, L., Polosa, A. and Riquer, V. (2008) *Physics Letters B*, **662**, 424-430. http://dx.doi.org/10.1016/j.physletb.2008.03.036

[36] Rosner, J.L. (2007) *Physical Review D*, **75**, Article ID: 013009. http://dx.doi.org/10.1103/PhysRevD.75.013009

[37] Guo, X.-H., Thomas, A.W. and Williams, A.G. (1999) *Physical Review D*, **59**, Article ID: 116007. http://dx.doi.org/10.1103/PhysRevD.59.116007

[38] Weng, M.-H., Guo, X.-H. and Thomas, A. (2011) *Physical Review D*, **83**, Article ID: 056006. http://dx.doi.org/10.1103/PhysRevD.83.056006

[39] Mehen, T. and Tiburzi, B.C. (2006) *Physical Review D*, **74**, Article ID: 054505. http://dx.doi.org/10.1103/PhysRevD.74.054505

[40] Selem, A. and Wilczek, F. (2005) Hadron Systematics and Emergent Diquarks. *Proceedings of Ringberg Workshop on New Trends in HERA Physics*, Ringberg Castle, Tegernsee, Germany, 2-7 Oct 2005. arXiv:hep-ph/0602128 http://inspirehep.net/record/710535

[41] Hernandez, E., Nieves, J. and Verde-Velasco, J. (2008) *Physics Letters B*, **666**, 150-154. http://dx.doi.org/10.1016/j.physletb.2008.07.007

[42] Kim, K., Jido, D. and Lee, S.H. (2011) *Physical Review C*, **84**, Article ID: 025204. http://dx.doi.org/10.1103/PhysRevC.84.025204

Kim, K., Jido, D. and Lee, S.H. (2013) *Few-Body Systems*, **54**, 271-274. http://dx.doi.org/10.1007/s00601-012-0343-0

[43] Martynenko, A. and Saleev, V. (1996) *Physics Letters B*, **385**, 297-303. http://dx.doi.org/10.1016/0370-2693(96)00848-9

[44] Gomshi Nobary, M. and Sepahvand, R. (2007) *Physical Review D*, **76**, Article ID: 114006. http://dx.doi.org/10.1103/PhysRevD.76.114006

[45] Ebert, D., Feldmann, T., Kettner, C. and Reinhardt, H. (1998) *International Journal of Modern Physics A*, **13**, 1091. http://dx.doi.org/10.1142/S0217751X98000482

Ebert, D., Faustov, R. and Galkin, V. (2011) *Physical Review D*, **84**, Article ID: 014025. http://dx.doi.org/10.1103/PhysRevD.84.014025

[46] Jaffe, R.L. and Wilczek, F. (2003) *Physical Review Letters*, **91**, Article ID: 232003. http://dx.doi.org/10.1103/PhysRevLett.91.232003

[47] Lee, S.H. and Yasui, S. (2009) *The European Physical Journal C*, **64**, 283. http://dx.doi.org/10.1140/epjc/s10052-009-1140-x

Lee, S.H., Yasui, S., Liu, W. and Ko, C.M. (2008) *The European Physical Journal C*, **54**, 259-265. http://dx.doi.org/10.1140/epjc/s10052-007-0516-z

[48] Shuryak, E. and Zahed, I. (2004) *Physics Letters B*, **589**, 21-27. http://dx.doi.org/10.1016/j.physletb.2004.03.019

[49] Hong, D.K., Sohn, Y.J. and Zahed, I. (2004) *Physics Letters B*, **596**, 191-199. http://dx.doi.org/10.1016/j.physletb.2004.06.073

[50] Karliner, M. and Lipkin, H.J. (2003) *Physics Letters B*, **575**, 249-255. http://dx.doi.org/10.1016/j.physletb.2003.09.062

[51] Hyodo, T., Liu, Y.-R., Oka, M., Sudoh, K. and Yasui, S. (2013) *Physics Letters B*, **721**, 56-60. http://dx.doi.org/10.1016/j.physletb.2013.02.045

[52] Yasui, S. and Oka, M. (2007) *Physical Review D*, **76**, Article ID: 034009. http://dx.doi.org/10.1103/PhysRevD.76.034009

[53] Bacchetta, A., Conti, F. and Radici, M. (2008) *Physical Review D*, **78**, Article ID: 074010. http://dx.doi.org/10.1103/PhysRevD.78.074010

[54] Lichtenberg, D., Namgung, W., Predazzi, E. and Wills, J. (1982) *Physical Review Letters*, **48**, 1653. http://dx.doi.org/10.1103/PhysRevLett.48.1653

[55] Ferretti, J., Vassallo, A. and Santopinto, E. (2011) *Physical Review C*, **83**, Article ID: 065204. http://dx.doi.org/10.1103/PhysRevC.83.065204

[56] Nagata, K. and Hosaka, A. (2004) *Progress of Theoretical Physics*, **111**, 857-870. http://dx.doi.org/10.1143/PTP.111.857

[57] Fredriksson, S., Jandel, M. and Larsson, T. (1982) *Zeitschrift für Physik C Particles and Fields*, **14**, 35-39. http://dx.doi.org/10.1007/BF01547961

[58] Alexandrou, C., de Forcrand, P. and Lucini, B. (2006) *Physical Review Letters*, **97**, Article ID: 222002.

http://dx.doi.org/10.1103/PhysRevLett.97.222002

[59] Babich, R., Garron, N., Hoelbling, C., Howard, J., Lellouch, L. and Rebbi, C. (2007) *Physical Review D*, **76**, Article ID: 074021. http://dx.doi.org/10.1103/PhysRevD.76.074021

[60] DeGrand, T., Liu, Z. and Schaefer, S. (2008) *Physical Review D*, **77**, Article ID: 034505. http://dx.doi.org/10.1103/PhysRevD.77.034505

[61] Hess, M., Karsch, F., Laermann, E. and Wetzorke, I. (1998) *Physical Review D*, **58**, Article ID: 111502. http://dx.doi.org/10.1103/PhysRevD.58.111502

[62] Alford, M.G., Schmitt, A., Rajagopal, K. and Schäfer, T. (2008) *Reviews of Modern Physics*, **80**, 1455. http://dx.doi.org/10.1103/RevModPhys.80.1455

[63] Imai, S., Toki, H. and Weise, W. (2013) *Nuclear Physics A*, **913**, 71-102. http://dx.doi.org/10.1016/j.nuclphysa.2013.06.001

[64] Ratti, C. and Weise, W. (2004) *Physical Review D*, **70**, Article ID: 054013. http://dx.doi.org/10.1103/PhysRevD.70.054013

[65] Harada, M., Nonaka, C. and Yamaoka, T. (2010) *Physical Review D*, **81**, Article ID: 096003. http://dx.doi.org/10.1103/PhysRevD.81.096003

[66] Splittorff, K., Toublan, D. and Verbaarschot, J. (2002) *Nuclear Physics B*, **620**, 290-314. http://dx.doi.org/10.1016/S0550-3213(01)00536-3

[67] Hands, S., Kim, S. and Skullerud, J.-I. (2007) *The European Physical Journal A*, **31**, 787-789. http://dx.doi.org/10.1140/epja/i2006-10173-x

[68] Kogut, J.B., Toublan, D. and Sinclair, D.K. (2001) *Physics Letters B*, **514**, 77-87. http://dx.doi.org/10.1016/S0370-2693(01)00586-X

[69] Strodthoff. N., Schaefer. B.-J. and von Smekal, L. (2012) *Physical Review D*, **85**, Article ID: 074007. http://dx.doi.org/10.1103/PhysRevD.85.074007

[70] Alkofer, R. and von Smekal, L. (2001) *Physics Reports*, **353**, 281-465. http://dx.doi.org/10.1016/S0370-1573(01)00010-2

[71] Maris, P. and Roberts, C.D. (2003) *International Journal of Modern Physics E*, **12**, 297. http://dx.doi.org/10.1142/S0218301303001326

[72] Roberts, C.D. and Williams, A.G. (1994) *Progress in Particle and Nuclear Physics*, **33**, 477-575. http://dx.doi.org/10.1016/0146-6410(94)90049-3

[73] Aoki, K.-I., Bando, M., Kugo, T., Mitchard, M.G. and Nakatani, H. (1990) *Progress of Theoretical Physics*, **84**, 683-701. http://dx.doi.org/10.1143/ptp/84.4.683

[74] Kugo, T. and Mitchard, M.G. (1992) *Physics Letters B*, **286**, 355-364. http://dx.doi.org/10.1016/0370-2693(92)91787-A

[75] Fischer, C.S. (2006) *Journal of Physics G*: *Nuclear and Particle Physics*, **32**, R253. http://dx.doi.org/10.1088/0954-3899/32/8/R02

[76] Munczek, H. (1995) *Physical Review D*, **52**, 4736. http://dx.doi.org/10.1103/PhysRevD.52.4736

[77] Yamanaka, N., Doi, T.M., Imai, S. and Suganuma, H. (2013), *Physical Review D*, **88**, Article ID: 074036. http://dx.doi.org/10.1103/PhysRevD.88.074036

Yamanaka, N., Imai, S., Doi, T.M. and Suganuma, H. (2014) *Physical Review*, *D*, **89**, Article ID: 074017. http://dx.doi.org/10.1103/PhysRevD.89.074017

[78] Imai, S. and Suganuma, H. (2013) A Non-Perturbative Effect of Gluons for Scalar Diquark in the Schwinger-Dyson Formalism. *Proceedings of XV International Conference on Hadron Spectroscopy*. arXiv:1401.3099 [hep-ph] http://inspirehep.net/record/1277087

[79] Cheng, T.-P. and Li, L.-F. (1988) Gauge Theory of Elementary Particle Physics. Oxford University Press, Oxford.

[80] Peskin, M.E. and Schroeder, D.V. (1995) An Introduction to Quantum Field Theory (Frontiers in Physics). Westview Press, Boulder.

[81] Aad, G. *et al.*, ATLAS Collaboration (2012) *Physics Letters B*, **716**, 1-29. http://dx.doi.org/10.1016/j.physletb.2012.08.020

[82] Maas, A. (2011) *The European Physical Journal C*, **71**, 1548. http://dx.doi.org/10.1140/epjc/s10052-011-1548-y

Maas, A. and Mufti, T. (2014) *Journal of High Energy Physics*, **1404**, 006.

[83] Macher, V., Maas, A. and Alkofer, R. (2012) *International Journal of Modern Physics A*, **27**, Article ID: 1250098. http://dx.doi.org/10.1142/S0217751X12500984

[84] Hopfer, M. and Alkofer, R. (2013) *Acta Physica Polonica B Proceedings Supplement*, **6**, 929.

[85] Iida, H., Oka, M. and Suganuma, H. (2005) *The European Physical Journal A*, **23**, 305-315. http://dx.doi.org/10.1140/epja/i2004-10082-0

[86] Doi, T.M., Suganuma, H. and Iritani, T. (2014) *Physical Review D*, **90**, Article ID: 094505. http://dx.doi.org/10.1103/PhysRevD.90.094505

Doi, T.M., Redlich, K., Sasaki, C. and Suganuma, H. (2015) *Physical Review D*, **92**, Article ID: 094004. http://dx.doi.org/10.1103/PhysRevD.92.094004

Suganuma, H., Doi, T.M. and Iritani, T. (2016) *Progress of Theoretical and Experimental Physics*, **2016**, Article ID: 013B06. http://ptep.oxfordjournals.org/content/2016/1/013B06

[87] Iritani, T. and Suganuma, H. (2014) *Progress of Theoretical and Experimental Physics*, **2014**, Article ID: 033B03.

Gongyo, S., Iritani, T. and Suganuma, H. (2012) *Physical Review D*, **86**, Article ID: 034510. http://dx.doi.org/10.1103/PhysRevD.86.034510

[88] Hatsuda, T. and Kunihiro, T. (1994) *Physics Reports*, **247**, 221-367. http://dx.doi.org/10.1016/0370-1573(94)90022-1

[89] Pagel, H. and Stokar, S. (1979) *Physical Review D*, **20**, 2947. http://dx.doi.org/10.1103/PhysRevD.20.2947

[90] 't Hooft, G. (1976) *Physical Review D*, **14**, 3432. http://dx.doi.org/10.1103/PhysRevD.14.3432

[91] Schäfer, T. and Shuryak, E.V. (1998) *Reviews of Modern Physics*, **70**, 323. http://dx.doi.org/10.1103/RevModPhys.70.323

[92] Itzykson, C. and Zuber, J.-B. (2006) Quantum Field Theory. Dover Publications, Mineola.

[93] Marinho, J., Gambin, E. and Frederico, T. (2007) *AIP Conference Proceedings*, **884**, 378. http://dx.doi.org/10.1063/1.2710608

[94] Salam, A. and Strathdee, J. (1978) *Physical Review D*, **18**, 4713. http://dx.doi.org/10.1103/PhysRevD.18.4713

[95] Bender, A., Roberts, C.D. and Von Smekal, L. (1996) *Physics Letters B*, **380**, 7-12. http://dx.doi.org/10.1016/0370-2693(96)00372-3

[96] Cahill, R., Roberts, C.D. and Praschifka, J. (1987) *Physical Review D*, **36**, 2804. http://dx.doi.org/10.1103/PhysRevD.36.2804

[97] Wang, Z., Wan, S. and Yang, W. (2007) *Communications in Theoretical Physics*, **47**, 287. http://dx.doi.org/10.1088/0253-6102/47/2/020

[98] Bloch, J.C., Roberts, C.D., Schmidt, S., Bender, A. and Frank, M. (1999) *Physical Review C*, **60**, Article ID: 062201. http://dx.doi.org/10.1103/PhysRevC.60.062201

Bloch, J.C., Roberts, C.D. and Schmidt, S. (1999) *Physical Review C*, **60**, Article ID: 065208. http://dx.doi.org/10.1103/PhysRevC.60.065208

[99] Takahashi, T.T., Matsufuru, H., Nemoto, Y. and Suganuma, H. (2001) *Physical Review Letters*, **86**, 18. http://dx.doi.org/10.1103/PhysRevLett.86.18

Takahashi, T.T., Suganuma, H., Nemoto, Y. and Matsufuru, H. (2002) *Physical Review D*, **65**, Article ID: 114509. http://dx.doi.org/10.1103/PhysRevD.65.114509

Sakumichi, N. and Suganuma, H. (2015) *Physical Review D*, **92**, Article ID: 034511. http://dx.doi.org/10.1103/PhysRevD.92.034511

[100] Okiharu, F., Suganuma, H. and Takahashi, T.T. (2005) *Physical Review Letters*, **94**, Article ID: 192001. http://dx.doi.org/10.1103/PhysRevLett.94.192001

Okiharu, F., Suganuma, H. and Takahashi, T.T. (2005) *Physical Review D*, **72**, Article ID: 014505. http://dx.doi.org/10.1103/PhysRevD.72.014505

Journal of Modern Physics, 2016, 7, 806-818
Published Online April 2016 in SciRes. http://www.scirp.org/journal/jmp
http://dx.doi.org/10.4236/jmp.2016.78074

An Electroscalar Energy of the Sun: Observation and Research

Oleg Antonovich Zaimidoroga

Joint Institute for Nuclear Research, Dubna, Russia
Email: Zaimidoroga@jinr.ru

Received 3 February 2016; accepted 26 April 2016; published 29 April 2016

Abstract

The observation of an electroscalar signal during the eclipse of the Sun by the Moon in 2008 was a starting point for the development and creation of the electroscalar field theory. This observation shows that such radiation has a long wavelength, and is longitudinal and extremely penetrating. The properties of the electroscalar and electromagnetic dynamics of a massive charged particle have been studied. An analogy between the linear theory of elasticity and Maxwell electrodynamics is made. The observed spectrum of radiation clarifying peculiar properties. Real sources of electroscalar radiation are determined. In accordance with the principle of least action, the Lagrangian of the electroscalar field and the field force acting on the particle are defined. The spectral expansion of the electroscalar field allowed us to establish that the field is longitudinal and aligned with the wave vector. At the heart of the electroscalar theory, which is compliant with the experimental data, is the four-dimensional scalar potential that describes radial vibrations of the electroscalar field source. The four-vector Maxwell electromagnetic potential and four-scalar potential neither form a single object in the Minkowski space nor interfere and, as a consequence, prove to be independent and unrelated differential relations. Moreover, a strong correlation between the spatial position of the particle and the field components allows and demonstrates a new degree of freedom in the electrodynamics of charged particles.

Keywords

Four-Scalar Potential of Electroscalar Field, Solar Electroscalar Field, Transport of Coulomb Field

1. Introduction

Registration of electroscalar radiation was made with a system of spherical electro-sensors (four copper spheres) placed in a metallic box during an eclipse of the Sun by the Moon which took place on 1 August 2008. The centers of the four spheres were connected to each other with a copper wire [1]. Data taking was done by an

How to cite this paper: Zaimidoroga, O.A. (2016) An Electroscalar Energy of the Sun: Observation and Research. *Journal of Modern Physics*, **7**, 806-818. http://dx.doi.org/10.4236/jmp.2016.78074

amplitude-digital analyser. In the proposed theory, physical fields are of two types: vortex electric and magnetic as well as potential electric and three-scalar [2] [3]. The fields of the first type can propagate in vacuum as transverse electromagnetic waves, and the fields of the second type as longitudinal electroscalar waves where the electric field vector vibrates along the propagation direction. It is precisely the longitudinal electroscalar mode that performs relativistic transport of the Coulomb field which is absent in the classical Maxwell theory. The absence of wave transport of the Coulomb field brings about certain obstacles in the canonical quantization of the Maxwell theory [4]-[9] and the violation of the causality principle. In frames of the vector formalism the presence of the longitudinal wave mode leads to the loss of gauge invariance in the theory and to the observability of electrodynamic potentials [10]-[14]. The loss of gauge invariance, in its turn, entails problems related to electric charge conservation. An analogy between the theory of elasticity and electrodynamics is made. The longitudinal electroscalar mode in the proposed theory is a consequence of continuum compressibility, while the Maxwell theory describes the wave dynamics of absolutely incompressible continuum. The electroscalar radiation has a long wavelength, is extremely penetrating, and propagates as a plane wave. In the electroscalar field, the particle energy assumes a negative value to the mechanical energy of the particle. The equation of the electromagnetic field contains displacement current, and the electroscalar field contains displacement charge. The electroscalar field has an ability to convey energy and information in any medium. Constructively, this hypothesis is expressed through the introduction of a four-scalar potential along with the four-vector one. These two four-dimensional fields are not connected with each other by any differential or any other correlations. The above circumstance permits to preserve gauge invariance for transverse fields and avoid difficulties pertaining to the law of electric charge conservation. The experimental proofs of the longitudinal electroscalar mode contain evidence for its presence [15]-[17].

2. An Analogy with the Theory of Elasticity

It should be pointed out that the elastic continuum supports propagation of both longitudinal and transverse waves; therefore, an analogy with the elasticity theory will give us a constructive indication of how the equations of generalized electrodynamics should look like. The basic equation of the linear elasticity theory is the Love equation which takes the following form in the absence of any outside forces [18] [19]:

$$-\ddot{\mathbf{u}} + c_l^2 \nabla \mathrm{div}\mathbf{u} - c_t^2 \mathbf{rotrotu} = 0,$$

where the vector $\mathbf{u}$ represents the vector of displacements in an elastic medium; c_l and c_t are the velocities of propagation of the longitudinal and transverse waves, correspondingly. The displacement vector is the main variable in the linear elasticity theory although not directly observable. Physically observable quantities in this theory are first-order derivatives of $\mathbf{u}$, *i.e.* $\dot{\mathbf{u}}$ is the velocity of elastic displacements and $\sigma_{ij} = \chi \mathrm{div}\mathbf{u} + 2\mu u_{ij}$ is the stress tensor, where χ and μ are the elastic constants of the medium and $u_{ij} = 1/2\left(\partial u_i / \partial x_j + \partial u_j / \partial x_i\right)$ is the elastic deformation tensor. With these variables the Love equation looks as follows:

$$-\frac{\partial^2 u_i}{\partial t^2} + \frac{\partial \sigma_{ik}}{\partial x_k} = 0,$$

but here the wave processes are not arranged into transverse and longitudinal elastic waves. In order to separate the wave processes explicitly, the following designations are introduced [20]:

$$\mathbf{E} = -\dot{\mathbf{u}}, \quad \mathbf{H} = c_t \mathbf{rotu}, \quad \mathrm{W} = c_l \mathrm{div}\mathbf{u}, \tag{1}$$

In this case, the Love equation takes the form:

$$\dot{\mathbf{E}} + c_l \nabla \mathrm{W} - c_t \mathbf{rotH} = 0.$$

Now, let us apply the rotor and divergence operations to the vector $\mathbf{E}$:

$$\mathbf{rotE} = -\mathbf{rot}\dot{\mathbf{u}} = -\frac{1}{c_t}\dot{\mathbf{H}},$$

$$\mathrm{div}\mathbf{E} = -\mathrm{div}\dot{\mathbf{u}} = -\frac{1}{c_l}\dot{\mathrm{W}}.$$

Thus, the following system of equations can be obtained from the Love equation for the introduced field denotations:

$$\dot{\vec{\mathbf{E}}} + c_l \nabla \vec{W} - c_t \mathbf{rot} \vec{\mathbf{H}} = 0, \tag{2}$$

$$\frac{1}{c_t} \dot{\mathbf{H}} + \mathbf{rotE} = 0,$$

$$\frac{1}{c_l} \dot{\mathrm{W}} + \mathrm{div}\mathbf{E} = 0, \tag{3}$$

$$\mathrm{div}\mathbf{H} = 0,$$

which, in the event of $\mathrm{W} = c_l \mathrm{div}\mathbf{u} = 0$ corresponding to the incompressible elastic continuum, coincides with the system of Maxwell equations in vacuum:

$$\dot{\mathbf{E}} - c_t \mathbf{rotH} = 0, \tag{4}$$

$$\frac{1}{c_t} \dot{\mathbf{H}} + \mathbf{rotE} = 0. \tag{5}$$

If the continuous medium does not support rotating motion, for which $\mathbf{rotu} = 0$ (e.g. liquid or gas), then compressible system takes the form:

$$\dot{\mathbf{E}} + c_l \nabla \mathrm{W} = 0, \tag{6}$$

$$\frac{1}{c_l} \dot{\mathrm{W}} + \mathrm{div}\mathbf{E} = 0. \tag{7}$$

This system describes the propagation of longitudinal waves in a continuous medium. Because the transverse and longitudinal waves propagate in the elastic continuum with different velocities, c_t for the transverse and c_l for the longitudinal waves, the fields $\mathbf{E}_\perp$ and $\mathbf{E}_\parallel$ can be deemed as independent. Eventually, the following field definitions are introduced:

$$\begin{aligned} &\mathbf{E}_\perp = -\nabla\varphi - \frac{1}{c}\frac{\partial \mathbf{A}}{\partial t}, \quad \mathbf{H} = \mathbf{rotA} \\ &\mathbf{E}_\parallel = \nabla\lambda, \quad \mathrm{W} = -\frac{1}{c}\frac{\partial \lambda}{\partial t}, \end{aligned} \tag{8}$$

where φ and $\mathbf{A}$ are the time and space parts of the electromagnetic four-potential. It should be noted that by their definitions the fields $\mathbf{E}_\parallel$ and W are the components of a four-vector in the Minkowski space-time. Definitions (8) permit to obtain from Equations (5) and (7) two systems of equations, one for the fields $\mathbf{E}_\perp$ and $\mathbf{H}$

$$-\frac{1}{c}\frac{\partial \mathbf{E}_\perp}{\partial t} + \mathbf{rotH} = 0,$$

$$\frac{1}{c}\frac{\partial \mathbf{H}}{\partial t} + \mathbf{rotE}_\perp = 0, \tag{9}$$

$$\mathrm{div}\mathbf{H} = 0,$$

and another for the fields $\mathbf{E}_\parallel$ and W:

$$\frac{1}{c}\frac{\partial \mathbf{E}_\parallel}{\partial t} + \nabla \mathrm{W} = 0,$$

$$\frac{1}{c}\frac{\partial \mathrm{W}}{\partial t} + \mathrm{div}\mathbf{E}_\parallel = 0, \tag{10}$$

$$\mathbf{rotE}_\parallel = 0.$$

In that event, system (9) describes the propagation of strictly transverse waves, and system (10), of longitudinal waves. Now, let us consider the solution of this system in the form of plane waves $\mathbf{E}_{\parallel} = \mathbf{E}_0 \exp\left[i\left(\omega t + \mathbf{kr}\right)\right]$, $\mathrm{W} = \mathrm{W}_0 \exp\left[i\left(\omega t + \mathbf{kr}\right)\right]$, where $\mathbf{E}_0$ and W_0 are the amplitudes, and $\mathbf{k}$ is the wave vector which determines the direction of propagation of a wave with the frequency ω. Then, from (10) the following is obtained:

$$\frac{\omega}{c}\mathbf{E}_0 + \mathbf{k}\mathrm{W}_0 = 0, \quad \frac{\omega}{c}\mathrm{W}_0 + \left(\mathbf{k}\mathbf{E}_0\right) = 0, \quad \mathbf{k}\times\mathbf{E}_0 = 0,$$

i.e. the vector of the electric field vibrates along the direction of wave propagation. The dispersion relation for this wave has the form $\omega = kc$.

3. Sources of the Electroscalar Wavefield

The electroscalar field is produced by the time-dependent, inhomogeneous density of an electric charge or part of the transfer current density with non-zero divergence. This source can be well illustrated by the radial oscillations of electron gas in a spherically symmetric metallic particle.

In **Figure 1**, the arrows correspond to the radial currents in the electron gas (electron convection current); the left part reflects the process of expansion of the electron gas, while the right part demonstrates compression. Due to the spherical symmetry, the magnetic field of the fluctuating radial transfer current equals zero; therefore, the electromagnetic flux is absent. Thus, the radiation losses in this system may be realized at the expense of the longitudinal electroscalar wave radiation. Let us consider the radial motions in the electron gas which are excited by light in a metallic nanoparticle. Here radial motions are such macroscopic motions of the electron gas for which divergence of the transfer current is non-zero and the electron density determines the drift velocity. An example of radial motions in conductive media are plasmons which, from the macroscopic viewpoint, present a collective wave process, *i.e.* compression and expansion waves in the electron gas which are accompanied by the irrotational vector potential A $\left(H = rotA = 0\right)$. The electroscalar waves can be also produced as electrically charged particles slow down in matter (braking electroscalar radiation). The scheme of such a source is given in the following **Figure 2**.

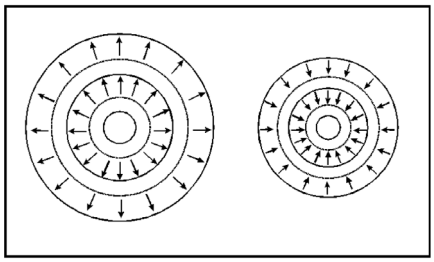

Figure 1. Radial currents in a spherical particle.

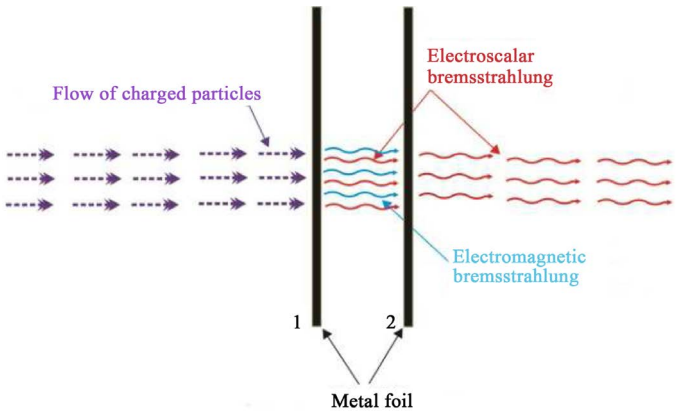

Figure 2. A source of braking electroscalar radiation.

In the case we consider, the charged particles of a pulsed beam (a high-current electron beam or focused ion beam) stopping in metallic foil 1 serve as a source of braking electromagnetic and electroscalar radiation. The electromagnetic radiation is absorbed by foil 2 (the thickness of foil 2 must exceed the respective thickness of the skin-layer for the braking electromagnetic radiation), and the electroscalar radiation can be registered, due to its greater penetrating power, behind foil 2 in which partial absorption of the electroscalar waves will certainly occur.

4. The Scalar Field in Presence of Charges and Currents

Let us consider the interaction of fields with charges and currents supposing that the time component of the four-potential $A^0 = \varphi$ equals zero, and the three-vector $\mathbf{A}$ satisfies the Coulomb condition $\mathrm{div}\mathbf{A} = 0$. Then, the Maxwell electric field becomes a vortex one:

$$\mathbf{E}_{\perp i} = -\frac{1}{c}\frac{\partial \mathbf{A}_{\perp i}}{\partial t} \qquad i = 0,1,2,3.$$

The vacuum equations for the potentials are:

$$\begin{aligned} -\frac{1}{c^2}\frac{\partial^2 \mathbf{A}}{\partial t^2} + \Delta \mathbf{A} = 0, \\ -\frac{1}{c^2}\frac{\partial^2 \lambda}{\partial t^2} + \Delta \lambda = 0. \end{aligned} \tag{11}$$

In order to derive potential equations for the case with presence of charges, the Lagrangian formalism will be used. Three-dimensional Lagrangians corresponding to (11) have the form:

$$\begin{aligned} L_{EH} = \frac{\mathbf{E}_{\perp}^2 - \mathbf{H}^2}{8\pi} = \frac{1}{8\pi}\left(\frac{1}{c}\frac{\partial \mathbf{A}}{\partial t}\right)^2 - \frac{1}{8\pi}(\mathbf{rotA})^2, \\ L_{EW} = \frac{\mathrm{W}^2 - \mathbf{E}_{\parallel}^2}{8\pi} = \frac{1}{8\pi}\left(\frac{1}{c}\frac{\partial \lambda}{\partial t}\right)^2 - \frac{1}{8\pi}(\nabla\lambda)^2. \end{aligned} \tag{12}$$

If we introduce the interactions $(\mathbf{Aj})/c$ for L_{EH} and $\rho\lambda$ for L_{EW}:

$$\begin{aligned} L_{EH} = \frac{\mathbf{E}_{\perp}^2 - \mathbf{H}^2}{8\pi} = \frac{1}{8\pi}\left(\frac{1}{c}\frac{\partial \mathbf{A}}{\partial t}\right)^2 - \frac{1}{8\pi}(\mathbf{rotA})^2 + \frac{1}{c}\mathbf{Aj}, \\ L_{EW} = \frac{\mathrm{W}^2 - \mathbf{E}_{\parallel}^2}{8\pi} = \frac{1}{8\pi}\left(\frac{1}{c}\frac{\partial \lambda}{\partial t}\right)^2 - \frac{1}{8\pi}(\nabla\lambda)^2 + \rho\lambda, \end{aligned}$$

then system (11) takes the form:

$$-\frac{1}{c^2}\frac{\partial^2 \mathbf{A}}{\partial t^2} + \Delta \mathbf{A} = -\frac{4\pi}{c}\mathbf{j}, \tag{13}$$

$$-\frac{1}{c^2}\frac{\partial^2 \lambda}{\partial t^2} + \Delta \lambda = -4\pi\rho, \tag{14}$$

where ρ and $\mathbf{j}$ are the charge and current densities. Since the vector potential $\mathbf{A}$ satisfies the Coulomb condition, only the vortex part of the transport current will be included, *i.e.* $\mathrm{div}\mathbf{j} = 0$. Thus, the continuity equation

$$\frac{\partial \rho}{\partial t} + \mathrm{div}\mathbf{j} = 0 \tag{15}$$

does not impose any constraints on the potentials $\mathbf{A}$ and λ. Substitution in (9) of the definitions of the fields (8) gives:

$$-\frac{1}{c}\frac{\partial \mathbf{E}_{\perp}}{\partial t}+\mathbf{rotH}=\frac{4\pi}{c}\mathbf{j},$$

$$\frac{1}{c}\frac{\partial \mathbf{H}}{\partial t}+\mathbf{rotE}_{\perp}=0, \tag{16}$$

$$\mathrm{div}\mathbf{H}=0,$$

and

$$\frac{1}{c}\frac{\partial \mathbf{E}_{\parallel}}{\partial t}+\nabla \mathrm{W}=0,$$

$$\frac{1}{c}\frac{\partial \mathrm{W}}{\partial t}+\mathrm{div}\mathbf{E}_{\parallel}=-4\pi\rho, \tag{17}$$

$$\mathbf{rotE}_{\parallel}=0.$$

It is seen from the above equation that the electrostatics equation, $\mathrm{div}\mathbf{E}_{\parallel}=-4\pi\rho$, follows from system (17) and the magnetostatics equation, $\mathbf{rotH}=4\pi\mathbf{j}/c$, from (16). These two systems of Equations (16) and (17) can be rewritten in the form of wave equations for the fields:

$$-\frac{1}{c^2}\frac{\partial^2 \mathbf{E}_{\perp}}{\partial t^2}+\Delta\mathbf{E}_{\perp}=\frac{4\pi}{c^2}\frac{\partial \mathbf{j}}{\partial t}, \qquad \mathrm{div}\mathbf{E}_{\perp}=0,$$

$$-\frac{1}{c^2}\frac{\partial^2 \mathbf{H}}{\partial t^2}+\Delta\mathbf{H}=-\frac{4\pi}{c^2}\mathbf{rotj}, \qquad \mathrm{div}\mathbf{H}_{\perp}=0; \tag{18}$$

and

$$-\frac{1}{c^2}\frac{\partial^2 \mathbf{E}_{\parallel}}{\partial t^2}+\Delta\mathbf{E}_{\parallel}=-4\pi\nabla\rho, \qquad \mathbf{rotE}_{\parallel}=0, \tag{19}$$

$$-\frac{1}{c^2}\frac{\partial^2 \mathrm{W}}{\partial t^2}+\Delta\mathrm{W}=\frac{4\pi}{c}\frac{\partial \rho}{\partial t}. \tag{20}$$

The identity $\Delta\equiv-\mathbf{rotrot}+\nabla\mathrm{div}$ was used while deriving these equations. It is seen from these equations that the time-varying current with a rotor different from zero is the source of transverse waves, while the time-dependent non-uniform charge density serves as the source of longitudinal waves. Here, taking into account continuity Equation (15) the later Equation (19) can be presented in the form:

$$-\frac{1}{c^2}\frac{\partial^2 \mathrm{W}}{\partial t^2}+\Delta\mathrm{W}=-\frac{4\pi}{c}\mathrm{div}\mathbf{j}.$$

It is obvious from (17) and (19) that longitudinal electroscalar waves respond to the transport of the Coulomb field.

The energy conservation laws for (16) and (17) have the form:

$$\frac{\partial}{\partial t}\int\epsilon_{EH}\mathrm{d}V+\oint\mathbf{s}_{EH}\mathrm{d}\sigma=-\int\left(\mathbf{jE}_{\perp}\right)\mathrm{d}V, \tag{21}$$

$$\frac{\partial}{\partial t}\int\epsilon_{EW}\mathrm{d}V+\oint\mathbf{s}_{EW}\mathrm{d}\sigma=-c\int\left(\rho\mathrm{W}\right)\mathrm{d}V, \tag{22}$$

where ϵ_{EW} and $\mathbf{s}_{EW}$ are the energy density and the flow vector of the electroscalar field, respectively. The electromagnetic energy density ϵ_{EH} and the flux vector $\mathbf{s}_{EH}$ have the form:

$$\epsilon_{EW}=\frac{\mathbf{E}_{\parallel}^2+\mathrm{W}^2}{8\pi}, \qquad \mathbf{s}_{EW}=\frac{c}{4\pi}\mathbf{E}_{\parallel}\mathrm{W}, \tag{23}$$

$$\epsilon_{EH} = \frac{\mathbf{E}_{\perp}^2 + \mathbf{H}}{8\pi}, \qquad \mathbf{s}_{EH} = \frac{c}{4\pi}\left[\mathbf{E}_{\perp} \times \mathbf{H}\right].$$

The quantities on the right sides of 21 and (22) determine the energy dissipation of the fields per unit time as they interact with charges and currents. Of particular interest is the integrand $\rho \mathrm{W}$ in the right side of (22). Using the definition $\mathrm{W} = -\partial\lambda/\partial(ct)$ and continuity Equation (15) this expression can be brought to the following form:

$$\rho \mathrm{W} = -\rho \frac{1}{c}\frac{\partial \lambda}{\partial t} = -\frac{\partial}{\partial t}\left(\frac{1}{c}\lambda\rho\right) + \frac{1}{c}\lambda\frac{\partial \rho}{\partial t} = -\frac{\partial}{\partial t}\left(\frac{1}{c}\lambda\rho\right) - \mathrm{div}\left(\frac{1}{c}\lambda\mathbf{j}\right) + \frac{1}{c}\mathbf{j}\nabla\lambda. \tag{24}$$

Owing to the field definition $\mathbf{E}_{\|} = \nabla\lambda$, (22) can be represented as:

$$\frac{\partial}{\partial t}\int\left(\epsilon_{EW} - \rho\lambda\right)\mathrm{d}V + \oint\left(\mathbf{s}_{EW} - \lambda\mathbf{j}\right)\mathrm{d}\sigma = -\int\left(\mathbf{j}\mathbf{E}_{\|}\right)\mathrm{d}V. \tag{25}$$

The first integral is the total energy of the system of fields $\mathbf{E}_{\|}$ and W interacting with charges. The summand $\lambda\mathbf{j}$ is added to the surface integral and can be interpreted as energy transfer at the expense of the motion of charges. Now, taking into account that $\mathbf{j} = \rho\mathbf{v}$, one obtains $\lambda\mathbf{j} = (\rho\lambda)\mathbf{v}$. In other words, the total flux consists of two components. The first one is responsible for the energy transfer by means of electroscalar radiation and the other, for the (mechanical) reemission of charges from the area limited by the integration surface.

5. The Continuity Equation of the Electroscalar Field

The equation of continuity determines the variation in the quantity of charges in a volume per unit time both leaving and entering this volume through the surface that limits such volume during the propagation of the electroscalar field. From the equation for the electroscalar field it follows that:

$$\mathrm{div}\mathbf{E}_{\|} = -4\pi\rho_{\|} - \frac{1}{c}\frac{\partial \mathrm{W}}{\partial t}.$$

The electroscalar field is determined both by charged particles and variation of the scalar charge in time:

$$\varrho_{\|} = \rho_{\|} + \frac{1}{4\pi}\frac{1}{c}\rho_0,$$

where $\frac{\partial \mathrm{W}}{\partial t} = \rho_0$ is the charge displacement owing to:

$$\mathrm{div}\mathbf{E}_{\|} = -4\pi\varrho_{\|}.$$

It should be noted that the displacement of scalar charge has a wave nature and, therefore, this term should be averaged in time. Thus, the total number of charges in a volume which pass through the surface S limiting such volume is $\varrho_{\|}v\mathrm{d}S$:

$$\frac{\partial}{\partial t}\int_a^b \varrho_{\|}\mathrm{d}V = -\int_S\left(4\pi\rho_{\|}v + \rho_0 v\right)\mathrm{d}S.$$

Further, using the generalized Gauss theorem the continuity equation of the electroscalar field acquires the form:

$$\frac{\partial}{\partial t}\int_a^b \varrho_{\|}\mathrm{d}V = -\int_a^b\left(4\pi\mathrm{div}\mathrm{j} + \mathrm{div}v\right)\mathrm{d}V,$$

where the second term is the wave component at the expense of charge displacement. Finally:

$$\frac{\partial \varrho_{\|}}{\partial t} = -4\pi\mathrm{div}\mathrm{j} - \mathrm{div}v.$$

Note that in the absence of charged currents in vacuum the scalar term (of charge displacement) does not vanish and allows the electroscalar waves to travel in vacuum due to the reproduction of the charges and their fields during the propagation.

6. The Superposition Principle of the Electroscalar Field

The longitudinality of the wave imposes certain requirements on the action of the field, particularly, on such a property of the field as the superposition principle. The equations for the electromagnetic field (Maxwell equations) contain only the equations for the full charge conservation (equations of continuity) but not the equations of motion for the field producing charges. In the case of the electromagnetic field, the distribution and motion of charges can be specified arbitrarily provided that the full charge is conserved. The character of the charges' distribution is determined then by solving the Maxwell equations using the field produced by the charges. As experience shows, the electromagnetic field obeys this principle which implies that if a charge produces a field, and another charge produces another field, then the total field is a result of superposition of these fields. Such a superposition principle will be referred to as the method of transverse summation of fields. The equations of motion of the electroscalar field contain not only the equations of continuity and full charge conservation, which cannot be determined arbitrarily. But the field itself and the charges' motion must be determined concurrently with the field of the produced charges' field. The principle of superposition of the electroscalar field is longitudinal as summation of the fields' charges occurs only for those located along the line between the charges. This means that the strengths of the resultant electroscalar fields at each point are equal to a sum of the strengths of all the longitudinal fields at this point. Any solution of equations for these fields is a field that can be realized in nature and, consequently, must obey the electroscalar field equations. In the electroscalar field the distribution of charges and their motion must be defined by solving field equations with given initial conditions for the longitudinal superposition of charges. Thus, while radiation is propagating, both the charges and their fields are reproduced in compliance with the electroscalar field laws, and the field potentials and strengths are enhanced due to the linear law of summation of the charges' fields. We will now consider how an electroscalar wave propagates between two charges (for example, of electrons). In this case, the field's electrical component is responsible for the local deviation of the electron density from the equilibrium one, whereas compression of the electric vacuum takes place under the action of the field's scalar component. The passage of the electroscalar radiation through two charges leads to a standing wave with a knot at the charge. Further, the wave passes in this manner all the charges located along the line of its propagation. The increased amplitude of the charges' density and field strength gives rise to a chain of compression and expansion waves up to the arrival at the target. The photo displays the structure of the compression and expansion zones in an electroscalar wave in the atmosphere [21] presents on **Figure 3**.

Figure 3. Expansion and compression zones in the atmosphere.

7. An Observation of Solar Electroscalar Radiation

The most favourable conditions for the registration of longitudinal electroscalar waves are realized during a solar eclipse. During the eclipse, the Moon shields most of the flux of the transverse electromagnetic solar waves, while the longitudinal electroscalar waves having a greater penetration power do reach the Earth's surface. The incident solar radiation may lead to self-excited radial oscillations of the valence electrons in matter which are, in their turn, a source of electroscalar radiation. With this in view, metallic spheres were used to register such radiation. The result of measurements is displayed in **Figure 4**.

The horizontal axis shows the eclipse time with the start at 1p.m. on 1 August 2008. Along the vertical axis, the volt value of the detected signal is plotted. The results of measurements indicate the absence of transverse polarization of the incident solar radiation which passed through the Moon, the independence of the radiation amplitude from the position of the registration system outside or inside the copper box, as well as the large penetration ability of the electroscalar radiation (the thickness of the copper box walls was 5 mm). The maximal signal was registered at 2.38 p.m. and amounted to 1.04 DC volt. The peak obtained in the measurements apparently attests that in this experiment one more signal was detected in addition to the electroscalar one. This can be explained by the following: in the case of a purely electroscalar signal one can expect a dip in the curve instead of a peak because the dip in the curve should depend on the depth of absorption of the electroscalar waves by the Moon. The most reasonable explanation for the registered peak is that scalar gravitational waves were detected together with the electroscalar waves. This assumption is grounded on the fact that the tidal gravitational forces from the Moon and the Sun during a solar eclipse are summed together, with the resulting force reaching its maximum. So, it is the unified electroscalar and scalar-gravitational field that was detected in this experiment. If the hypothesis for the existence of a unified field is confirmed, new perspectives will open up for the measurement of gravitational effects.

The above conclusion is substantiated by another example of using the unified electroscalar and scalar-gravitational interaction. The large amplification of the unified signal is expected during the regular motion of the Moon in its neomenia phase when the Moon is between the Earth and the Sun. **Figure 5** shows the signal values versus the time of the New Moon.

The amplitude of the signal was 0.45 volt and its duration was 10 - 13 hours. The motion of any body equipped with an electroscalar field detector will produce an electric signal due to the combined fields of the Sun and the Moon.

The four copper spheres placed in a metallic screen were used to collect data on the solar radiation. The centers of the four spheres were connected to each other with a copper wire. The detector had a splitter for

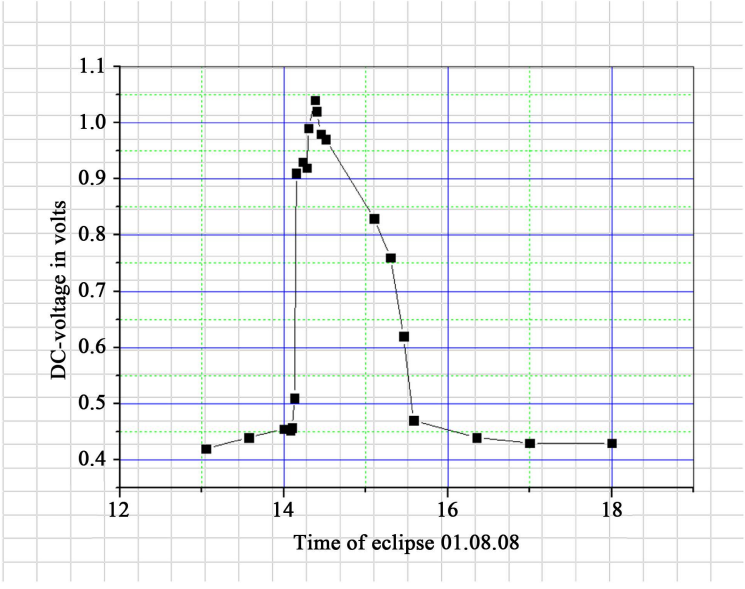

Figure 4. The detected signal from the sun.

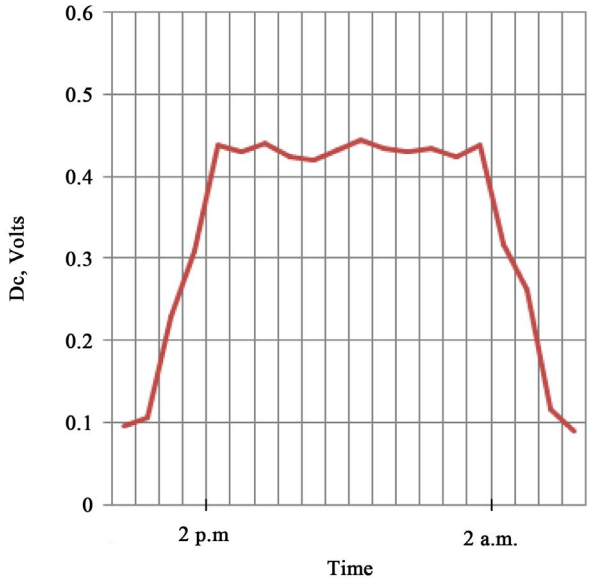

Figure 5. The unified signal during the New Moon.

signals and a system of amplitude-digital analyzers. This detector was able to register only electroscalar radiation. The electroscalar radiation is produced by the structures of solar plasma providing a spectrum having a discrete character with a sign-alternating amplitude of order of 20 millivolt and a frequency (by Fourier) up to 500 Hertz. The averaged value of the spectrum is negative and equals minus 2 - 5 millivolt, with a positive-amplitude signal coming on every millisecond and a negative-amplitude signal following after an interval. The frequency analysis of the spectrum shows that this radiation has a long wavelength and a practically constant amplitude. A single radiation signal has an exceedingly small value of raising time of electrical signal of front and drop of the order of fractions of a picosecond.

The spectrum of the solar electroscalar radiation is shown in **Figure 6**.

8. Spectral Expansion of the Electroscalar Field

The electroscalar field produced by charges may be expanded into a Fourier integral. If we present the electroscalar field as a superposition of plane waves, then the "frequency" of these waves will have a zero value and this field will not be time dependent while the wave vectors will be distinct from zero. The potential of this field is determined using the equation:

$$\Delta\lambda = -4\pi\left(\rho_{\|} + \frac{1}{4\pi}\frac{1}{c}\rho_0\right).$$

We will now expand the electroscalar field potential λ into the Fourier space integral:

$$\lambda = \int_{-\infty}^{+\infty} \exp(ikr)\lambda_k \mathrm{d}^3k.$$

We find next the Laplacian for the left-hand side:

$$\Delta\lambda = -\int_{-\infty}^{+\infty} k^2 \exp(ikr)\lambda_k \mathrm{d}^3k,$$

and the Fourier k-component is: $\Delta\lambda_k = -k^2\lambda_k$. By defining the Fourier component from the right-hand side, we get:

$$\Delta\lambda_k = -k^2\left(\frac{\rho_{\|}}{2\pi^2} + \frac{\rho_0}{c2\pi^3}\right).$$

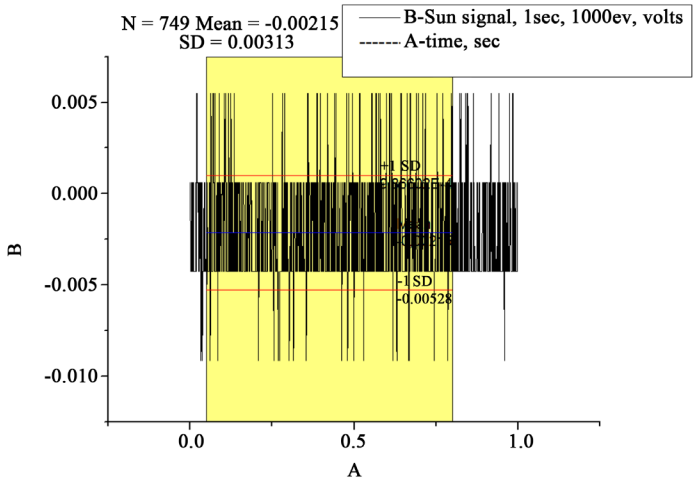

Figure 6. Spectrum of the solar electroscalar radiaton.

Then, we obtain by comparing both sides:

$$\lambda_k = \frac{\rho_{\|}}{2\pi^2} + \frac{\rho_0}{2\pi^3 c}.$$

Similarly to the field potential, the electroscalar field strength may be expanded as follows:

$$\mathbf{E}_{\|} = \nabla \int_{-\infty}^{+\infty} \exp(ikr)\lambda_k \, \mathrm{d}^3 k.$$

We now insert λ_k and have:

$$\vec{\mathbf{E}}_{\|} = i\vec{\mathbf{k}}\left(\frac{\rho_{\|}}{2\pi^2} + \frac{\rho_0}{2\pi^3 c}\right).$$

One may see from this expression that the electroscalar field is directed along the wave vector and its waves are longitudinal.

9. The Degree of Freedom of a Charged Particle

A peculiarity of the electrodynamics of electromagnetic and electroscalar fields is that the different characteristics are caused by changing in the behavior of a heavy charged particle. Due to this a strong correlation between the spatial position of the particle and the electric components of the fields can be possible [22]. It is known that the function of Lagrange remains invariant when the total derivative of any function is added [23]. Thus, we have: $L_1 + L_2 = 0$ and $L_2 = \frac{e}{c}\int \frac{\mathrm{d}}{\mathrm{d}t}[\lambda \mathrm{d}s]$, where $\mathrm{d}s = \sqrt{-\mathrm{d}x_i^2}$ and $i = 1, 2, 3, 4$.

So, we obtain for the action:

$$\mathbf{S} = \left(-mc\mathrm{d}s + \frac{e}{c}A_i \mathrm{d}x_i\right) - \frac{e}{c}\lambda \mathrm{d}s\Big|_a^b = 0.$$

In the case when the upper limit is not equal zero, therefore the variation in action becomes:

$$\delta\mathbf{S} = \delta\int\left(mcu_i\delta\mathrm{d}x_i + \frac{e}{c}A_i\delta\mathrm{d}x_i + \frac{e}{c}\delta A_i \mathrm{d}x_i\right) - \frac{e}{c}\delta\lambda\mathrm{d}s - \frac{e}{c}\lambda\delta\mathrm{d}s = 0. \tag{26}$$

Let us integrate the first, second and fifth terms by parts: finally we have following :

$$\left(mcu_i\left(1 + \frac{e\lambda}{mc^2}\right) + \frac{e}{c}A_i\right)\Big|_a^b = 0, \tag{27}$$

$$\frac{\mathrm{d}u_i}{\mathrm{d}s} = -\frac{e}{c}\mathbf{Z_{ik}}u_k + \frac{e}{c}\mathbf{F_{ik}}u_k. \tag{28}$$

where the equation for the particles' motion content the second-order tensor Z_{ik} of the electroscalar field and the F_{ik} electromagnetic tensor of second-order.

So, the electroscalar and electromagnetic tensors are:

$$\mathbf{Z_{ik}} = \left(\frac{\partial\lambda}{\partial x_i}u_k - \frac{\partial\lambda}{\partial x_k}u_i\right)$$

$$\mathbf{F_{ik}} = \left(\frac{\partial A_i}{\partial x_k} - \frac{\partial A_k}{\partial x_i}\right)$$

Note that the electroscalar force has a negative sign with respect to the electromagnetic one. The Lagranges' method allows one to establish a strong correlation between the spatial position of the particle and the field components. The trajectories of propagation of the electromagnetic photon and electroscalar "scaphon" radiation may be different.This correlation directly points to a new degree of freedom in the electrodynamics of the charged particle, it providing uncontroversial proof that the electroscalar dynamics exists alongside with the electromagnetic one. It should be noted that in the course of transformations of the electromagnetic field into the electroscalar one and vice versa the particle may travel considerable distances and its trajectories may be spaced apart. The transformation of the electromagnetic field into the electroscalar one can also take place in the spheres and cavities of solid bodies that are different in type.

10. Conclusions

As follows from the theoretical and experimental studies, the electroscalar radiation has a long wavelength, is longitudinal and extremely penetrating. Basically, the following conclusions can be made:

1. The detection of the electroscalar radiation from the Sun was done using spherical electroreceptors in an eclipse of the Sun and during the regular motion of the Moon.
2. An analogy with the elasticity equation was made, and due to this the equation for the Maxwell electromagnetic field was derived from the transcendental component of the displacement vector, and an equation for the electroscalar field, from the longitudinal component of the displacement vector.
3. The longitudinal electroscalar wave performs transport of the Coulomb field, which is absent in the electromagnetic field.
4. The registered spectrum of the electroscalar radiation can be described by the law of propagation of the plane wave. The ratio of both components and their directionality are dependent on the type of medium. In vacuum both vectors are directed along the Pointing vector, while in the solid state the electric vector is directed against the motion, and the scalar one, along the wave motion.
5. The continuity equation of the electromagnetic field contains displacement of current, and the electroscalar field contains displacement of charge.
6. The spectral expansion of the electroscalar field testifies that the field is longitudinal since the electric vector is collinear to the vector of propagation.
7. The transfer of energy and information can take place either in vacuum or in any medium.
8. The degree of freedom of a massive charged particle due to the correlation between the space position of the particle and the field component gives the transformation of the electromagnetic field into the electroscalar field (and backwards) which occurs at the expense of the rotation of the transcendental electric vector round the magnetic field vector.
9. In the equation for the particle motion in the electroscalar field, the particle mass changes at the expense of the field energy, and the particle energy in the electroscalar field assumes a negative value to the sign of mechanical energy of motion.
10. An electrically charged particle displays dual properties which are revealed in its behavior as a wave and as a particle. The electromagnetic field of the particle shows wave properties during the interaction, and the electroscalar field acts as a particle due to the large value of the longitudinal force.

One remarkable characteristic of the electrodynamics of electroscalar and electromagnetic fields is the

manifestation of different properties by a charged particle. This points to a possibility that the changes entailed by the new electroscalar dynamics are of profound nature and do not come into contradiction with those properties of electromagnetic dynamics which make it convincing and, consequently, such properties can be included into the electrodynamics as a second dynamics of charge motion.

Acknowledgements

I thank the Editor and the referee for their comments. I would like to thank Dr. D.V. Podgainy for his contribution and participation at the early stage of research. I am deeply obliged to Dr. Irina Molodtsova for assistanse in figure drawing.

References

[1] Zaimidoroga, O.A. and Podgainy, D.V. (2010) Observation of Electroscalar Radiation during an Eclipse of the Sun. *Proceedings of International Conference of the Astroparticle and Cosmic Rays Physics*, Como.

[2] Podgainy, D.V. and Zaimidoroga, O.A. Nonrelativistic Theory of Electroscalar Field and Maxwell Electrodynamics. arXiv:1005.3130.

[3] Podgainy, D.V. and Zaimidoroga, O.A. Relativistic Dynamics of a Charged Particle in an Electroscalar Field. arXiv:1203.2490.

[4] Dirac, P.A.M. (2002) Scientific Papers Collection. V. II. Quantum Theory (Scientific Articles 1924-1947). In: Sukhanov, A.D., Ed., M.: FIZMATLIT (Classics of Science).

[5] Fock, V. and Podolsky, B. (1932) *Sowiet Physical Journal*, **1**, 801.
Fock, V. (1964) The Theory of Space, Time and Gravitation. 2nd Revised Edition, Oxford, London, Paris.

[6] Polubarinov, I.V. (2003) *Physics of Elementary Particles and Atomic Nuclei*, **34**, 738.
Ogievezky, V.I. and Polubarinov, I.V. (1965) *Journal of Nuclear Physics*, **4**, 216.

[7] van Vlaenderen, K.J. and Waser, A. (2001) *Hadronic Journal*, **24**, 609.

[8] van Vlaenderen, K.J. A Generalisation of Classical Electrodynamics for the Prediction of Scalar Field Effects. arXiv:physics/0305098v1 [physics.class-ph].

[9] Khvorostenko, N.P. (1992) *Russian Physics Journal*, **35**, 24-29 (Translated from Izvestiya Vysshikh Uchebnykh Zavedenii, Fizika, No. 3, 24-29, March 1992).

[10] Rousseaux, G. (2005) *Europhysics Letters*, **71**, 15-20. http://dx.doi.org/10.1209/epl/i2005-10059-5

[11] Rousseaux, G., Kofman, R. and Minazzoli, O. (2008) *The European Physical Journal D*, **49**, 249-256.

[12] Dirac, P.A.M. (1932) *Proceedings of the Royal Society*, **A136**, 453.

[13] Podolsky, B. and Fock, V. (1932) *Sowiet Physical Journal*, **2**, 275-277.

[14] Bogoliubov, N.N. and Shirkov, D.V. (1984) Introduction to the Theory of Quantum Fields. Nauka, Moscow.

[15] Monstein, C. and Wesley, J.P. (2002) *Europhysics Letters*, **59**, 514. http://dx.doi.org/10.1209/epl/i2002-00136-9

[16] Ignatiev, G.F. and Leus, V.A. (1999) On a Superluminal Transmission at the Phase Velocities. In: Chubykalo, A.E., Pope, V. and Smirnov-Rueda, R., Eds., *Instantaneous Action at a Distance*, *Modern Physics*: *Pro and Contra*, Nova Science Pub Inc., 203.

[17] Johansson, L. (1999) Longitudinal Electrodynamic Forces and Their Possible Technological Applications. Master of Science Thesis, CODEN:LUTEDX/(TEAT-5027)/1-55/(1996).
http://www.df.lth.se/snorkelf/Longitudinal/Slutdok.html and Contra, p. 203 (1999)

[18] Love, A.E.H. (1927) A Treatise on the Mathematical Theory of Elasticity. Cambridge University Press, Cambridge.

[19] Landau, L.D. and Lifshitz, E.M. (1986) Theory of Elasticity, Vol. 7. 3rd Edition, Butterworth-Heinemann.

[20] Dubrovskii, V.A. (1985) An Elastic Model of the Physical Vacuum. Akademiia Nauk SSSR, Doklady, Vol. 282, No. 1, 83-88.

[21] Zalikhanov, B.Zh. (2016) *Physics of Elementary Particles and Atomic Nuclei*, **1**, Dubna.

[22] Bell, J. (1966) *Review of Modern Physics*, **38**, 447.

[23] Landau, L.D. and Lifshitz, E.M. (1987) Mechanics. Publishing Group, Nauka.

Journal of Modern Physics, 2016, 7, 819-826
Published Online April 2016 in SciRes. http://www.scirp.org/journal/jmp
http://dx.doi.org/10.4236/jmp.2016.78075

Contrast Optimization for an Animal Model of Prostate Cancer MRI at 3T

Christopher Brian Abraham[1,2], Boguslaw Tomanek[1,3], Laura Curiel[1,2]

[1]Thunder Bay Regional Research Institute, Thunder Bay, Canada
[2]Lakehead University, Thunder Bay, Canada
[3]Department of Oncology, University of Alberta, Edmonton, Canada
Email: cabraham@lakeheadu.ca, lcuriel@lakeheadu.ca, tomanek@ualberta.ca

Received 10 March 2016; accepted 26 April 2016; published 29 April 2016

Abstract

Purpose: To optimize contrast to noise ratio (CNR) in magnetic resonance imaging (MRI) of prostate cancer using at 3T. Methods: CNR was expressed as a difference in MR signals of two samples. Amulti-echo spin-echo (MESE) pulse sequence was used. The theoretical value of the maximum CNR was obtained using the derivative of CNR with echo time (TE) as a variable. The T_1 relaxation time was ignored as repetition time (TR) was assumed to be very long (TR >> T_1). The theoretical calculations were confirmed with *in vitro* and *in vivo* experiments. For *in vitro* experiments we used samples with different T_2 values using various concentrations of super paramagnetic iron oxide (SPIO) and for *in vivo* experiments we used an animal model of prostate cancer. Results: CNR was maximized by selecting the optimum TE for a multi-echo spin-echo (MESE) pulse sequence based on theoretical predictions. MR images of prostate cancer at 3T were obtained and showed maximum CNR at the predicted TE. Conclusions: It was possible to maximize CNR of prostate tumour by selecting the optimal TE based on simple theoretical calculations. The proposed method can be applied to other pulse sequences and tissues. It can be applied to any MRI system at any magnetic field. However the method requires knowledge of T_2 relaxation times.

Keywords

MRI, Tissue Contrast, Prostate Cancer, Spin Echo

1. Introduction

Magnetic Resonance Imaging (MRI) has high spatial resolution and the best soft tissue contrast among *in vivo* imaging modalities [1], [2]. However, contrast to noise ratio (CNR) of some cancerous tissues is still often insufficient for accurate diagnosis [3]. Normal and diseased tissues are difficult to differentiate in standard T_1 or

How to cite this paper: Abraham, C.B., Tomanek, B. and Curiel, L. (2016) Contrast Optimization for an Animal Model of Prostate Cancer MRI at 3T. *Journal of Modern Physics*, **7**, 819-826. http://dx.doi.org/10.4236/jmp.2016.78075

T_2-weighted MRI, [4] in particular when tissues have similar relaxation times, such as prostate tumours and surrounding tissue [1], [5]. This poor differentiation between healthy and malignant tissue often leads to over-treatment degrading future quality of life of cancer patients [6]. To rectify this problem, contrast agents are used. However their multiple application can lead to unwanted side effects [7]. Therefore, the purpose of this work was to find out the optimal echo time (TE) that provides the maximum CNR using a spin-echo pulse sequence for MRI of prostate cancer at 3T.

MR signal of a tissue is a function of its spin density and relaxation times [8]. It can be controlled by the pulse sequence parameters, such as echo time (TE), repetition time (TR) or flip angle of a radiofrequency (rf) pulse. As the contrast depends on a difference in signals generated by two samples it can be maximized by selecting optimum parameters of the pulse sequence.

Optimization of MRI pulse sequence parameters has been a field of interest since the beginning of MRI [9]-[11]. The presented solution is different from previous methods by providing a simplistic but effective solution to obtain the maximum CNR between tissues, specifically for prostate cancer. An early study used a method known as Eigen image Filtering to optimize MRI protocols and pulse sequence parameters. This study was able to reduce imaging time for eigen image filtering of brain studies by up to 75% however approximation of tissue parameters from literature was needed, otherwise further tissue parametrization would be needed [9]. Another study used sequence simulations to predict optimal parameters for imaging, however simulated images failed to match the corresponding measured image in areas where tissues or substances moved during the course of measurement. The phenomena of flow could not be feasibly incorporated into the equations [10]. A study in 1987 compared the ability if different T_1, T_2 and proton density (PD) weighted imaging would increase or decrease CNR for hepatic lesions among patients. They concluded that although short-TE T_1-weighted pulse sequences with multiple excitations has the best signal to noise ratio and anatomic resolution at 0.6T, their described technique is limited by relatively inferior contrast discrimination and artifact suppression at 1.5T resulting in a necessary change in imaging strategy when performing hepatic MR imaging at 1.5T [11]. Specifically, for prostate cancer, many studies have incorporated the use of diffusion weighted imaging (DWI) and apparent diffusion coefficient maps (ADC) to increase detection of prostate cancer. However, these methods are only viable with MRI above 1.5T as lower fields do not have the SNR required to create quality DWI and ADC maps [4], [12]. These studies have increased the differentiability of prostate cancer from healthy prostate tissue but require more intensive image processing. Our work follows a similar derivation proposed in [8] but used a solution for spin echo imaging instead of gradient echo and we have optimized CNR for tissues with small differences in T_2. Furthermore, the method does not require absolute values of proton density. Instead we worked with relative values of proton densities between tissues with a method suggested by [13]. A similar method using derivatives is used to determine the concentration of contrast agent needed to optimize the Ernst angle in T_1-weighted spoiled gradient echo imaging [14] and optimal TE to determine maximum $\mathrm{SNR}_{\mathrm{efficiency}}$ for MR-guided interventional procedures [15].

The solution presented in this work maximizes CNR by optimizing TE in the spin-echo pulse sequence. Using a formula for MR signal obtained with the spin-echo pulse sequence and knowing T_2s of the samples we calculated $\mathrm{TE}^{\max}$ that provided the maximum CNR for *in vitro* phantoms and *in vivo* for prostate and surrounding tissues at 3T.

2. Methods

For the calculations of CNR we used an equation providing a relationship between CNR and pulse parameters. We have assumed T_2 relaxation times are known and T_1relaxation can be neglected. Nine samples with different T_2 relaxation times were made using different water concentrations of superparamagnetic iron oxide (SPIO). CNR as a function of TE was calculated for all sample pairs. The theoretical results were compared to the MRI experiments *in vitro* and *in vivo* using the animal model of prostate cancer at 3T.

2.1. Theory

Contrast in MR imaging can be defined as the difference in signals from two samples [8], [16], [17].

$$\mathrm{CNR} = \mathrm{SNR}_1 - \mathrm{SNR}_2 \tag{1}$$

where SNR_1 and SNR_2 are the signal to noise ratios of two samples.

The MR signals from two samples (S_1 and S_2) using spin-echo pulse sequence can be described as: [8], [16]

$$S_1 = \kappa_1 \rho_1 \left[1 - e^{\left(-\frac{TR}{T_1^1}\right)}\right] e^{\left(-\frac{TE}{T_2^1}\right)} \quad (2)$$

$$S_2 = \kappa_2 \rho_2 \left[1 - e^{\left(-\frac{TR}{T_1^2}\right)}\right] e^{\left(-\frac{TE}{T_2^2}\right)} \quad (3)$$

where κ_1, κ_2 are the proportionality constants, ρ_1, ρ_2 are the spin densities, T_1^1, T_1^2 and T_2^1, T_2^2 are the longitudinal and transversal relaxation times of the sample 1 and 2 respectively; TR is the repetition time and TE is the echo time. Each signal for samples is divided by the standard deviation, σ, in the image to obtain SNR.

Subtracting (2) from (3) we obtain CNR for the samples 1 and 2:

$$\mathrm{CNR}(\mathrm{TE}) = \kappa_1 \rho_1 \left[1 - e^{\left(-\frac{TR}{T_1^1}\right)}\right] e^{\left(-\frac{TE}{T_2^1}\right)} \Big/ \sigma - \kappa_2 \rho_2 \left[1 - e^{\left(-\frac{TR}{T_1^2}\right)}\right] e^{\left(-\frac{TE}{T_2^2}\right)} \Big/ \sigma \quad (4)$$

Assuming TR is sufficiently long ($\mathrm{TR} \gg T_1$), and taking the derivative of Equation (4) with respect to TE, the maximum for CNR can be obtained at:

$$\mathrm{TE}^{\max} = \frac{T_2^1 T_2^2}{T_2^2 - T_2^1} \ln\left(\frac{\kappa_1 \rho_1}{\kappa_2 \rho_2} \frac{T_2^2}{T_2^1}\right) \quad (5)$$

As seen from Equation (5), $\mathrm{TE}^{\max}$ depends only on the T_2 relaxation times of the samples thus it can be calculated to provide the maximum CNR if only T_2s are known.

The results of the calculation for different samples pairs are presented in **Table 2** where each sample has a T_2 value and each sample pair has a corresponding $\mathrm{TE}^{\max}$.

2.2. *In Vitro* Experiments

2.2.1. Sample Preparation *in Vitro*

Molday ION Rhodamine Carboxyl, a commonly used SPIO, (MIRB, Cat #: CL-50Q02-6C-50, BioPAL, Inc, Worcester, MA, USA) was diluted in de-ionized water to prepare nine samples (0.0019, 0.0022, 0.0029, 0.0042, 0.0061, 0.0071, 0.0083, 0.0121, and 0.0263 μg/μL).The samples were placed in standard 5-mm NMR tubes (Wilmad NMR tubes, Cat#: Z566411-5EA, Sigma Aldrich, St. Louis, MO, USA) and arranged in a grid pattern to allow simultaneous imaging of all samples.

2.2.2. MR Imaging and T_2 Calculations

MR imaging was performed using a 3T MRI scanner (Achieva, Philips, The Netherlands). Data was acquired using an 8-channel head RF coil. The spin echo pulse sequence with the following parameters was used: 32 echoes, ΔTE = 20 ms, TR = 5000 ms, FOV = 100 mm × 100 mm, 3 mm slice thickness, 224 × 224 matrix size, NEX = 4. The images were transferred to an external workstation and processed with custom MATLAB scripts (MATLAB and Statistics Toolbox Release R2012a, The MathWorks, Inc., Natick, Massachusetts, United States). A region of interest (ROI) was automatically selected for each sample as a circular area within the sample for *in vitro* data. The ROI was determined by a mask with a pre-determined threshold in order to make ROIs determination quick and without human error.Single exponential fitting of the echo train was used to calculate T_Ts according to the formula:

$$M_z(\mathrm{TE}) = A + Be^{-\mathrm{TE}/T_2} \quad (6)$$

where M_z is the signal intensity at the echo time TE; A, B and T_2 are the fitting parameters.8

2.3. *In Vitro* Experiments

2.3.1. Animal Model

To induce prostate tumours, 5 × 106 LNcaP cells suspended in 100 μL of PBS were subcutaneously injected in

the flank of 8 male athymic nude mice (Charles River, Wilmington, MA, USA). The mice were anesthetized with isoflurane (Baxter International Inc., Deerfield, IL, USA) during MR imaging and euthanized immediately after.MR imaging of mice was performed once tumours reached a diameter of 5mmusing calipers according to our approved protocol (Lakehead University Animal Care Committee).

2.3.2. MR Imaging and T_2 Calculations

Data was acquired using the MESE pulse sequence with an 8-channel wrist RF coil with the following parameters: 30 echoes, ΔTE = 8 ms, TR = 1396 ms, FOV = 240 mm × 240 mm, slice thickness = 3 mm, 156 × 156 matrix, NEX = 4. Processing was performed similarly to *in vitro* experiments but ROIs were manually determined for the tumour, muscle, and kidney.

2.4. CNR Calculations

CNR was calculated from the MESE image sets for various echo times. Signal intensity of each sample was normalized to the signal intensity of the first echo for each sample for *in vitro* data and we assumed $\kappa_1\rho_1 = \kappa_2\rho_2$. For CNR calculations *in vivo*, ρ and κ constants were found using the method described by Tofts *et al*. [13] where the values of each κ, ρ for each sample were extrapolated putting TE = 0 in Equation (2) and (3) for MESE images. The method used yields a relative κ, ρ for each tissue compared to other tissues. This is then used to find the ratio of κ, ρ between samples which is then used in Equation (5).

A series of CNR curves as a function of TE were calculated and drawn for all the sample pairs using Equation (5) and cross correlation was used to determine the similarity between the theoretical and the experimental CNR curves.

In order to compare the theoretical and the experimental results of CNR, two parameters were defined. The first parameter ΔTE_{thex} described deviation between theoretical and experimental echo time for maximum CNR and was defined as

$$\Delta TE_{thex} = \left| \frac{TE_{Exp} - TE_{Th}}{TE_{Exp}} \right| \times 100\% \tag{7}$$

where TE_{Exp} is the experimental TE value at which the maximum CNR occurred and TE_{Th} is the theoretical TE value at which the maximum CNR was predicted to occur.

The second parameter ΔCNR_{thex} indicated differences in predictions from theoretical and experimental results of measured CNR

$$\Delta CNR_{thex} = \left| \frac{\mathrm{Max}\left(CNR_{Exp}\right) - CNR_{Exp}\left[TE_{Th}\right]}{\mathrm{Max}\left(CNR_{Exp}\right)} \right| \times 100\% \tag{8}$$

where $\mathrm{Max}\left(CNR_{Exp}\right)$ is the maximum CNR observed experimentally. TETh is the theoretical calculated value of TE (Equation 6) at which CNR is maximum.

3. Results

3.1. *In Vitro*

T_2-weighted MR image of the 9 samples used for analysis is shown in **Figure 1**. Their calculated T_2 values are shown in **Table 1**.

The calculated TE values providing maximum CNR for each sample pair are shown in **Table 2**.

Figure 2 shows four examples of CNR as a function of TE for different sample pairs; T_2 = 96 and 26 ms, 193 and 53 ms, 193 and 123 ms, and 679 and 86 ms. The corresponding TE^{max} values are 46.6, 60.2, 133.4 and 146.6 ms respectively.

The theoretical curves for these samples are superimposed on the experimental results. The mean cross correlation value between the experimental and theoretical curves was r = 0.98 ± 0.02.

The mean percent difference between the theoretical and experimental TEs at which the maximum (ΔTE_{thex}) occurred was 5.1% ± 5.3%. The mean percent difference for maximum CNR (ΔCNR_{thex}) was.32% ± 0.71%.

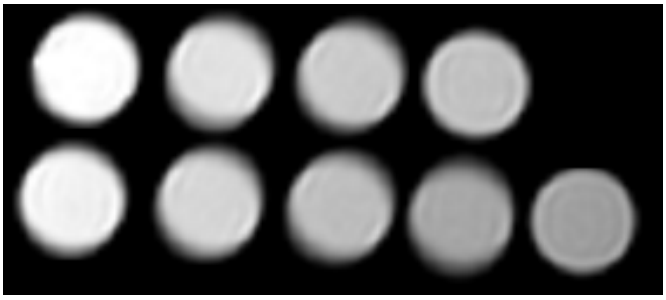

Figure 1. T_2-weighted (TE = 40 ms) *in vitro* MR image. Longest T_2 is at the top left and the shortest T_2 is at the bottom right.

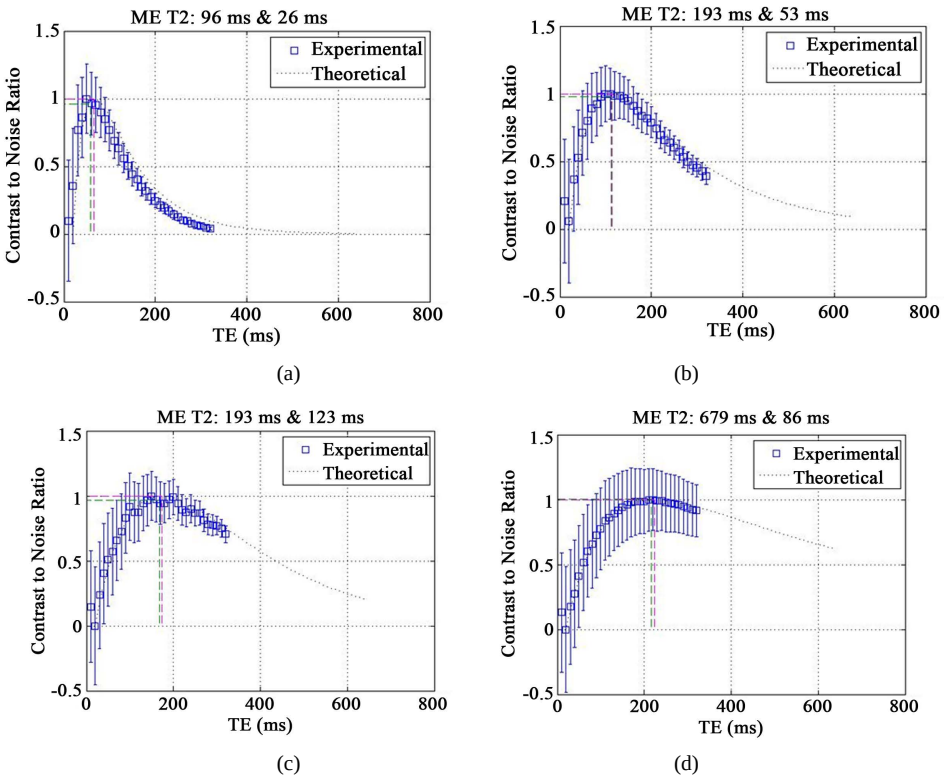

Figure 2. CNR as a function of TE based on theoretical calculations and experimental data: (a) sample 6 (T_2 = 96 ms) vs sample 9 (T_2 = 26 ms); (b) sample 4 (T_2 = 193 ms) vs sample 8 (T_2 = 53 ms); (c) sample 4 (T_2 = 193 ms) vs sample 5 (T_2 = 123 ms); and (d) sample 1 (T_2 = 679 ms) vs sample 7 (T_2 = 86 ms).

Table 1. T_2 values of *in vitro* samples.

Sample	Table column subhead
1	679 ± 32
2	363 ± 28
3	268 ± 23
4	193 ± 10
5	123 ± 6
6	96 ± 4
7	86 ± 5
8	53 ± 3
9	26 ± 1

Table 2. TE values providing maximum CNR for two samples. The top row and the left columns indicate the T_2 values of the sample pair. For example: maximum CNR for a sample pair with T_2 123 ms and 53 ms is obtained at a TE of 51.2 ms.

T_2 (ms) of Samples	Predicted TE value at which maximum CNR would occur for samples							
	679	363	268	193	123	96	86	53
363	488.4	411.6	339.2	256.6	218.7	203.5	146.6	88.2
268		310.7	260.3	201.3	173.6	162.3	119.4	73.8
193			226.4	177.1	153.6	143.9	107.1	67.2
123				152.8	133.4	125.4	94.4	60.2
96					108.4	102.3	78.4	51.2
86						90.8	70.3	46.6
53							66.9	44.6
26								36.3

3.2. *In Vivo*

Figure 3 shows sagittal MR images of the mouse torso at TE values of 56 ms and 96 ms. T_2 of the tumor and normal tissue was found to be 55.8 ± 8.8 ms and 32.9 ± 2.4 ms for all 8 mice respectively. Based on the calculations maximum CNR between muscle and tumour tissue was found to occur at 55.2 ms. Typical T_2-weighted images of human prostate cancer use an echo time of around 96 ms [12]. The images at TE = 56 ms (**Figure 3(b)**) showed CNR increase of 125% compared to an image at TE = 96 ms (**Figure 3(a)**). Mean correlation values, ΔTE_{thex} and ΔCNR_{thex} were 0.94 ± 0.01, 21.2% ± 19.4% and 7.83% ± 7.45% respectively.

Figure 4 shows CNR as a function of TE for muscle, kidney and tumour tissue. A visible CNR maximum appears between tumour and muscle at TE of 56 ms. *In vivo* experimental curves had high cross correlation values of r = 0.98 ± 0.01 and were able to attain maximum CNR based on predictions showing good agreement between the theory and the experiment.

4. Discussion

The results have shown that it was possible to maximize CNR by selecting the proper TE for SE pulse sequences when T_2 relaxation times of the samples are known. The experiments showed that the theory indeed provides the parameters allowing maximum CNR. The cross correlation function showed the theoretical values closely emulated experimental data.

For *in vitro* calculations we assumed $\kappa_2\rho_2 = \kappa_1\rho_1$. This is only valid if we consider the proton density to be the same for each sample. In these experiments it was deemed valid since all the samples were contained distilled water with only negligible amounts of MIRB added.

As it can be seen in **Figure 4** the predicted maximum of CNR between the cancerous tissue and the kidney is at TE = 131.6 ms. However, higher CNR values are also observed for TEs shorter than ~50 ms. This may be caused by differences in proton densities or differences in short T_2 component. In this case where tissues have large differences in proton densities, acquiring a proton density image at short TE could result in an image of higher CNR. This may require the use of very short TE which may not be feasible with some current MRI hardware [17].

One deficiency of Equation (5) is the possibility of resulting in a negative value of the optimal TE. In some cases, where T_2 values are close and there are large differences in proton density, assuming κ is the same, the equation results in a negative TE value. For example, if the T_2 values are 32.9 and 55.8 ms for tumour and muscle tissue respectively, and ρ_1 is half of ρ_2, the resulting optimal TE^{max} is −13.2 ms. This result has no physical meaning so for these cases choosing the smallest TE value possible should result in the best possible CNR.

The experimental values showed CNR can be maximized between prostate cancer and muscle tissues when their T_2 values differed by about 15 ms. However, in clinical practice, the difference in MRI parameters between malignant prostate cancer and healthy prostate tissue is much lower [4]. Therefore although the proposed me-

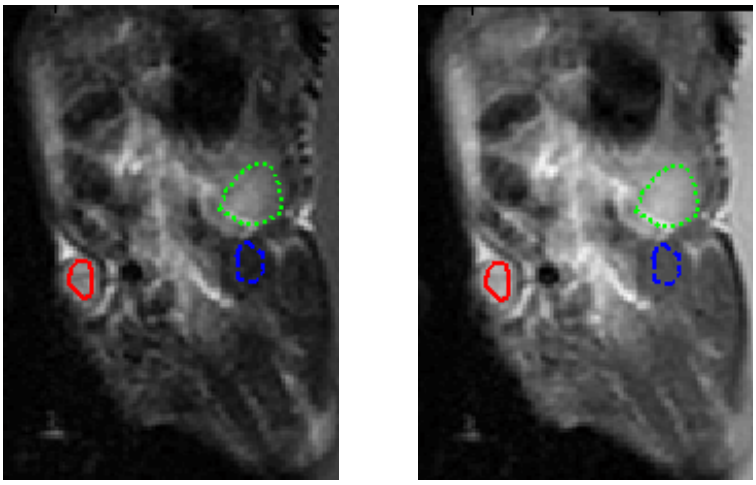

(a) (b)

Figure 3. *In vivo* MR images of a mouse at (a) TE = 96 ms and (b) TE = 56 ms. Region of interests used for CNR calculations tumour, muscle, and kidney as red (—), blue (--) and green (…) respectively. By using predicted TEmax; (b) has an 125% CNR compared to (a).

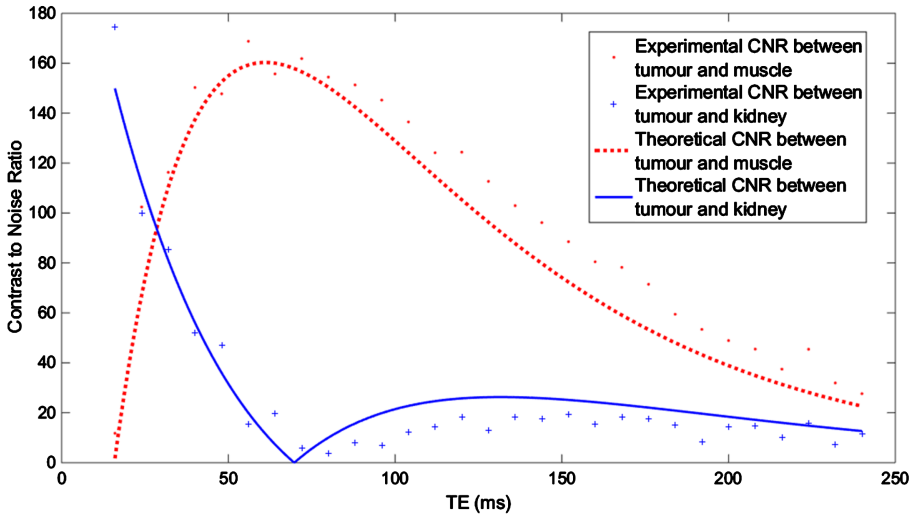

Figure 4. *In vivo* experimental and theoretical CNRas a function of TE comapring tumour with muscle and kidney.

thod has the ability to maximize CNR between healthy and malignant tissue, further work with patients is needed to investigate the differentiation of healthy prostate tissue from malignant tissue in humans and compare with biopsy [5].

The results have implication in many areas of MRI. Throughout the last few decades, numerous papers have been published regarding advances in MRI. Most of those involve some form of contrast enhancement [18]. The work presented here shows a simple method to obtain the maximum contrast between two samples or tissues. In practice, this method can be applied to other sequences within MR imaging to further improve CNR between desired tissues.

Further work will include performing similar experiments at different magnetic field strengths. The theoretical derivation shown exemplifies the spin echo sequence CNR optimization for T_2 weighted images.

5. Conclusion

The work presented showed it is possible to maximize the CNR by selecting proper TE in a SE pulse sequence.

This was validated by *in vivo* experiments in prostate cancer tumours. The work derived here has wide implications as the ability to increase CNR and differentiate between tissues is essential in many aspects of MR imaging. Our future work will incorporate T_1-weighted images, including TR values, into the CNR equation thus making it a partial derivative to obtain the maximum CNR. We will also compare CNR at different field strengths in order to show the potential of low field MRI to have an equal or even greater CNR compared to higher field strengths. Our end goal is to develop a robust program which can be used to calculate optimal TE, TR and other user defined MRI parameters in order to obtain an MR image with the highest CNR between two tissues of interest based on intrinsic parameters.

Acknowledgements

Work funded by NSERC Discovery.

References

[1] Heyn, C., Bowen, C.V., Rutt, B.K. and Foster, P.J. (2005) *Magnetic Resonance in Medicine*, **53**, 312-320. http://dx.doi.org/10.1002/mrm.20356

[2] Massoud, T.F. and Gambhir, S.S. (2003) *Genes & Development*, **17**, 545-580. http://dx.doi.org/10.1101/gad.1047403

[3] Barentsz, J.O., Richenberg, J., Clements, R., Choyke, P., Verma, S., Villeirs, G., Rouviere, O., Logager, V. and Fütterer, J.J. (2012) *European Radiology*, **22**, 746-757. http://dx.doi.org/10.1007/s00330-011-2377-y

[4] Langer, D.L., van der Kwast, T.H., Evans, A.J., Trachtenberg, J., Wilson, B.C. and Haider, M.A. (2009) *Journal of Magnetic Resonance Imaging*, **30**, 327-334. http://dx.doi.org/10.1002/jmri.21824

[5] Cheikh, A.B., Girouin, N., Colombel, M., Maréchal, J.-M., Gelet, A., Bissery, A., Rabilloud, M., Lyonnet, D. and Rouvière, O. (2009) *European Radiology*, **19**, 770-778. http://dx.doi.org/10.1007/s00330-008-1190-8

[6] Bangma, C.H., Roemeling, S. and Schröder, F.H. (2007) *World Journal of Urology*, **25**, 3-9. http://dx.doi.org/10.1007/s00345-007-0145-z

[7] Bartolini, M., Pekar, J., Chettle, D., McNeill, F., Scott, A., Sykes, J., Prato, F. and Moran, G. (2003) *Magnetic Resonance Imaging*, **21**, 541-544. http://dx.doi.org/10.1016/S0730-725X(03)00081-X

[8] Brown, R.W., Cheng, Y.-C.N., Haacke, E.M., Thompson, M.R. and Venkatesan, R. (2014) Magnetic Resonance imaging: Physical Principles and Sequence Design. 2nd Edition, John Wiley & Sons, Inc., Hoboken. http://dx.doi.org/10.1002/9781118633953

[9] Soltanian-Zadeh, H., Saigal, R., Windham, J.P., Yagle, A.E. and Hearshen, D.O. (1994) *IEEE Transactions on Medical Imaging*, **13**, 161-175. http://dx.doi.org/10.1109/42.276155

[10] Cornelis, N. and Bakker, C. (1986) *The Journal of Nuclear Medicine*, **27**, 281-286.

[11] Foley, W.D., Kneeland, J.B., Cates, J.D., Kellman, G.M., Lawson, T.L., Middleton, W.D. and Hendrick, R.E. (1987) *American Journal of Roentgenology*, **149**, 1155-1160. http://dx.doi.org/10.2214/ajr.149.6.1155

[12] Miao, H., Fukatsu, H. and Ishigaki, T. (2007) *European Journal of Radiology*, **61**, 297-302. http://dx.doi.org/10.1016/j.ejrad.2006.10.002

[13] Tofts, P., Ed. (2003) Quantitative MRI of the Brain: Measuring Changes Caused by Disease. Wiley, Chichester, Hoboken. http://dx.doi.org/10.1002/0470869526

[14] Reeder, S.B., Smith, M.R. and Hernando, D. (2016) *Magnetic Resonance in Medicine*, **75**, 1556-1564. http://dx.doi.org/10.1002/mrm.25744

[15] Sussman, M.S., Lindner, U., Haider, M., Kucharczyk, W., Hlasny, E. and Trachtenberg, J. (2013) *Magnetic Resonance in Medicine*, **70**, 333-340. http://dx.doi.org/10.1002/mrm.24830

[16] Bernstein, M.A., King, K.F. and Zhou, Z.J. (2004) Handbook of MRI Pulse Sequences. Academic Press, Amsterdam, Boston.

[17] DiFrancesco, M.W., Rasmussen, J.M., Yuan, W., Pratt, R., Dunn, S., Dardzinski, B.J. and Holland, S.K. (2008) *Medical Physics*, **35**, 3972. http://dx.doi.org/10.1118/1.2968092

[18] Artemov, D. (2003) *Journal of Cellular Biochemistry*, **90**, 518-524. http://dx.doi.org/10.1002/jcb.10660

Journal of Modern Physics, 2016, 7, 827-851
Published Online April 2016 in SciRes. http://www.scirp.org/journal/jmp
http://dx.doi.org/10.4236/jmp.2016.78076

Scientific Research Publishing

Emission Intensity in the Hydrogen Atom Calculated from a Non-Probabilistic Approach to the Electron Transitions

Stanisław Olszewski

Institute of Physical Chemistry, Polish Academy of Sciences, Warsaw, Poland
Email: olsz@ichf.edu.pl

Received 10 March 2016; accepted 26 April 2016; published 29 April 2016

Abstract

Quantum aspects of the Joule-Lenz law for the transmission of energy allowed us to calculate the time rate of energy transitions between the quantum states of the hydrogen atom in a fully non-probabilistic way. The calculation has been extended to all transitions between *p* and *s* states having main quantum numbers not exceeding 6. An evident similarity between the intensity pattern obtained from the Joule-Lenz law and the corresponding quantum-mechanical transition probabilities has been shown.

Keywords

Time Intervals for the Electron Transitions in the Hydrogen Atom, Non-Probabilistic Theory of Energy Emission in the Atom, Comparison of the Emission Intensities with the Quantum-Mechanical Transition Probabilities

1. Introduction

Since the very beginning of quantum theory the transition rate of energy connected with the occupation change of quantum states has been considered on a combined probabilistic-and-statistical footing [1]-[3]. Another formal probabilistic calculations of the rate of energy emitted in course of the electron transitions could be done on the basis of quantum mechanics; see e.g. [4] [5]. Experimentally a roughly precise measurement of the time of a single transition between two quantum levels seems to be hardly possible because of an extremely short interval of time expected to be associated with the transition phenomenon. In reality any experiment has its finite duration, so beyond of a short time of transition a whole electron population of transitions should be considered before the time of a single transition can be derived and estimated.

How to cite this paper: Olszewski, S. (2016) Emission Intensity in the Hydrogen Atom Calculated from a Non-Probabilistic Approach to the Electron Transitions. *Journal of Modern Physics*, **7**, 827-851. http://dx.doi.org/10.4236/jmp.2016.78076

However, the problem could obtain a new approach if the quantum background coupled with the Joule--Lenz law of the energy emission is taken into account. In this case the quantum aspects of that law discovered recently [6] [7] allowed us to make a step towards an understanding of the radiation theory which is much different in its character than a search for transition probabilities between the quantum states.

In effect we can calculate the transition time of a single electron particle between two quantum states. Further connection of such time with the energy rate of radiation becomes a simple task. An auxiliary component of this theory is the fact that it can be compared with the quantum-mechanical calculations giving a rather satisfactory assessment for the new, *i.e.* non-probabilistic, results.

This is so because the ratio of the intensities of two spectroscopic lines gives in fact the ratio of transition probabilities [8]. In emission spectra, the simplest conditions of excitation are those in which the excited states of the atoms are approximately in thermal equilibrium and the number of atoms in any given state is proportional to the Boltzmann factor. Usually in considering the ratio of intensities of two lines without specifying conditions, one practically assumes the temperature equilibrium at infinite temperature so that the Boltzmann factor is equal to unity. This assumption is realized especially well when the transitions originate from levels whose energies differ little from one another. Experimentally in flames and in certain parts of electric arcs the excitation corresponds approximately to thermal equilibrium, on the other hand in glow discharges the conditions of excitation are more complicated and it is not always possible to connect observed intensities with transition probabilities. However, if two lines have a common upper level their intensities will always be in the ratio of their transition probabilities [8].

In the present calculations of the changes of quantum states only the energy and time are involved. Therefore there is no reference to the selection rules of transitions given by such parameters like, for example, the orbital angular momentum.

2. Time Intervals Considered instead of Transition Probabilities

A characteristic step of a later Bohr's approach to the atomic spectra was a poposal of the Fourier analysis of the displacement vector associated with the position change of the particle submitted to transition [9]. This analysis was expected to give the probabilities of transitions between quantum states. But in our opinion a much more practical step than the displacement analysis is to examine the balance of time necessary to perform a transition. In fact this balance can be represented with the aid of the transition energy, too, because the components entering the balance of time can be defined with aid of the components of the transition energy. A complementary relation between energy and time becomes here especially of use if we note that the energy intervals are much more easy to calculate than the intervals of time.

In effect, because any elementary interval of energy has its corresponding interval of time, these elementary time intervals can be added together into full intervals necessary to be considered in description of a given quantum process. In result the rate of the electron transitions between rather distant quantum levels could be calculated as a function of the elementary intervals of energy. In the present paper we do such time analysis and apply it in calculating the rate of electron transitions in the hydrogen atom. Before we do that, the elementary properties of both energy and time entering the transitions will be represented.

3. Elementary and Combined Transitions and Their Properties

Elementary transition is that between two neighbouring quantum levels, say $n+1$ and n. Beginning with $n=1$ we obtain

$$\begin{aligned} E_2 - E_1 &= \Delta E_1, \\ E_3 - E_2 &= \Delta E_2, \\ E_4 - E_3 &= \Delta E_3, \cdots, \end{aligned} \tag{1}$$

in general

$$E_{n+1} - E_n = \Delta E_n.$$

But any transition energy ΔE_1 takes place in course of time Δt_1, the transition of ΔE_2 is done in course of Δt_2, the ΔE_3 is obtained in course of Δt_3, etc. So there are

$$\begin{aligned} t_2 - t_1 &= \Delta t_1, \\ t_3 - t_2 &= \Delta t_2, \\ t_4 - t_3 &= \Delta t_3, \end{aligned} \tag{2}$$

etc., in general

$$t_{n+1} - t_n = \Delta t_n. \tag{2a}$$

Because a complementarity relation deduced from the Joule-Lenz law does exist between the elementary energy interval and transition time interval we have

$$\Delta E_1 \Delta t_1 = \Delta E_2 \Delta t_2 = \Delta E_3 \Delta t_3 = \cdots = \Delta E_n \Delta t_n = h. \tag{3}$$

Evidently the $t_1, t_2, t_3, \cdots$ entering (2) with a minus sign are the beginning times of successive intervals, and $t_2, t_3, t_4, \cdots$ entering with a plus sign are the end times of these intervals. In the emission process we have $\Delta E_1, \Delta E_2, \Delta E_3, \cdots > 0$, the same property concerns by definition also the intervals $\Delta t_1, \Delta t_2, \Delta t_3, \cdots$

But still another kind of relations—similar to that introduced by Kramers and Heisenberg [10]—concerns ΔE and Δt. We have

$$a_1 \Delta E_1 = \frac{\Delta E_1}{\Delta t_1} = \frac{(\Delta E_1)^2}{h}, \tag{4}$$

$$a_2 \Delta E_2 = \frac{\Delta E_2}{\Delta t_2} = \frac{(\Delta E_2)^2}{h}, \tag{4a}$$

$$a_3 \Delta E_3 = \frac{\Delta E_3}{\Delta t_3} = \frac{(\Delta E_3)^2}{h}, \tag{4b}$$

$$a_4 \Delta E_4 = \frac{\Delta E_4}{\Delta t_4} = \frac{(\Delta E_4)^2}{h}, \cdots \tag{4c}$$

Here $a_1, a_2, a_3, \cdots$ denote the transition coefficients between states 2 and 1, 3 and 2, 4 and 3, etc., respectively. The coefficients lead to the emission rate represented in the last step of any formula in (4), (4a), (4b), (4c)... This step is due to application of the complementarity relation in (3).

Certainly the same relation can represent Δt_i giving

$$\frac{1}{\Delta t_i} = \frac{\Delta E_i}{h}. \tag{5}$$

From the formulae in (4) it is evident that any transition coefficient a_i satisfies the formula

$$a_i = \frac{1}{\Delta t_i}. \tag{6}$$

Simple properties of a_i are ready to calculate. By dividing Formula (4) by (4a), (4a) by (4b), (4b) by (4c), etc., we obtain

$$\frac{a_1}{a_2}\frac{\Delta E_1}{\Delta E_2} = \frac{(\Delta E_1)^2}{(\Delta E_2)^2} \to \frac{a_1}{a_2} = \frac{\Delta E_1}{\Delta E_2}, \tag{7}$$

$$\frac{a_2}{a_3}\frac{\Delta E_2}{\Delta E_3} = \frac{(\Delta E_2)^2}{(\Delta E_3)^2} \to \frac{a_2}{a_3} = \frac{\Delta E_2}{\Delta E_3}, \tag{7a}$$

$$\frac{a_3}{a_4}\frac{\Delta E_3}{\Delta E_4} = \frac{(\Delta E_3)^2}{(\Delta E_4)^2} \to \frac{a_3}{a_4} = \frac{\Delta E_3}{\Delta E_4}, \tag{7b}$$

etc. In effect

$$\frac{a_1^2}{a_2^2}=\frac{\left(\Delta E_1\right)^2}{\left(\Delta E_2\right)^2}=\frac{\Delta E_1/\Delta t_1}{\Delta E_2/\Delta t_2}=\frac{I_{2-1}}{I_{3-2}}, \tag{8}$$

$$\frac{a_2^2}{a_3^2}=\frac{\left(\Delta E_2\right)^2}{\left(\Delta E_3\right)^2}=\frac{\Delta E_2/\Delta t_2}{\Delta E_3/\Delta t_3}=\frac{I_{3-2}}{I_{4-3}}, \tag{8a}$$

$$\frac{a_3^2}{a_4^2}=\frac{\left(\Delta E_3\right)^2}{\left(\Delta E_4\right)^2}=\frac{\Delta E_3/\Delta t_3}{\Delta E_3/\Delta t_4}=\frac{I_{4-3}}{I_{5-4}}, \tag{8a}$$

etc., where

$$I_{2-1}, I_{3-2}, I_{4-3}, I_{5-4},\cdots \tag{9}$$

are respectively the intensities, or energy rates, of transitions from level 2 to 1, from 3 to 2, from 4 to 3, from 5 to 4, etc.

We see that the ratios of the coefficient squares are equal to the ratios of intensities.

4. Intensities in the Hydrogen Atom

The emitted energy intensity of transition between a paricular pair of quantum states is sometimes called a component of the spectral line [11]. When expressed in energy units (ergs) per second the intensity of such line is

$$I_{a-b}=N\left(a\right)h\nu A\left(a,b\right) \tag{10}$$

where $N\left(a\right)$ is the number of atoms in state a, $h\nu$ is the energy obtained in a single electron transition, and $A\left(a,b\right)$ is the emission probability. In fact an accurate $N\left(a\right)$ is hardly possible to be estimated, $A\left(a,b\right)$ is obtainable from rather tedious quantum mechanical calculations.

The aim of the present paper is to join, as far as possible, the calculations of the emission rate of single transitions given by the present theory with the former theory of the line spectra, or obtained from experiment. Since it is difficult to make an absolute comparison between the theory, or theories, or experiment, the calculations are referred mainly to the relative intensities of the spectral lines.

In fact we shall demonstrate that the Bohr energies of electron transitions in the hydrogen atom applied in the present theory can give a rather satisfactory approximation for the ratios of the transition probabilities between the atomic states given by the quantum-mechanical theory. To this purpose the transitions from the atomic states $n_{(p)}p$ where

$$n_{(p)}=2,3,4,5,6, \tag{11}$$

to the states $n_{(s)}s$ where

$$n_{(s)}=1,2,3,4 \text{ and } 5 \tag{12}$$

are considered because all results of calculations can be compared with the quantum-mechanical data listed in [11].

In examining the intensities due to the present framework we take into account the ratios

$$\frac{I_{n_{\alpha'}p-n_{\alpha''}s}}{I_{n_{\beta'}p-n_{\beta''}s}} \tag{13}$$

where

$$n_{\alpha'}>n_{\alpha''} \tag{14}$$

and

$$n_{\beta'}>n_{\beta''}. \tag{15}$$

Both the numerator (labelled by α) and denominator (labelled by β) entering (13) are expressed in terms

of the Bohr energy differences

$$\Delta E_{\alpha} = E_{\alpha'}^{(p)} - E_{\alpha''}^{(s)}, \tag{16}$$

$$\Delta E_{\beta} = E_{\beta'}^{(p)} - E_{\beta''}^{(s)}, \tag{17}$$

which are positive quantities, first in view of (14) and (15), second because of the energy components equal to

$$E_{\alpha'}^{(p)} = -\frac{1}{n_{\alpha'}^2}\frac{m_e e^4}{2\hbar^2}, \tag{18}$$

$$E_{\alpha''}^{(s)} = -\frac{1}{n_{\alpha''}^2}\frac{m_e e^4}{2\hbar^2}, \tag{19}$$

$$E_{\beta'}^{(p)} = -\frac{1}{n_{\beta'}^2}\frac{m_e e^4}{2\hbar^2}, \tag{20}$$

$$E_{\beta''}^{(s)} = -\frac{1}{n_{\beta''}^2}\frac{m_e e^4}{2\hbar^2}. \tag{21}$$

But the intensities entering (13) are represented by the formulae

$$I_{n_{\alpha'}(p)-n_{\alpha''}(s)} = \frac{E_{n_{\alpha'}}^{(p)} - E_{n_{\alpha''}}^{(s)}}{t_{n_{\alpha'}} - t_{n_{\alpha''}}^{(s)}} \tag{22}$$

and

$$I_{n_{\beta'}(p)-n_{\beta''}(s)} = \frac{E_{n_{\beta'}}^{(p)} - E_{n_{\beta''}}^{(s)}}{t_{n_{\beta'}} - t_{n_{\beta''}}^{(s)}} \tag{23}$$

which contain in general the time intervals different than the elementary intervals presented in (2). For example we can have

$$t_{n_{\alpha'}} - t_{n_{\alpha''}} = t_5 - t_1 \tag{24}$$

or

$$t_{n_{\beta'}} - t_{n_{\beta''}} = t_6 - t_3. \tag{25}$$

However such intervals can be decomposed into elementary ones, so we obtain

$$\begin{aligned} t_5 - t_1 &= \Delta t_4 + \Delta t_3 + \Delta t_2 + \Delta t_1 \\ &= t_5 - t_4 + t_4 - t_3 + t_3 - t_2 + t_2 - t_1 \\ &= \frac{h}{\Delta E_4} + \frac{h}{\Delta E_3} + \frac{h}{\Delta E_2} + \frac{h}{\Delta E_1}, \end{aligned} \tag{26}$$

or

$$\begin{aligned} t_6 - t_3 &= \Delta t_5 + \Delta t_4 + \Delta t_3 \\ &= t_6 - t_5 + t_5 - t_4 + t_4 - t_3 \\ &= \frac{h}{\Delta E_5} + \frac{h}{\Delta E_4} + \frac{h}{\Delta E_3}. \end{aligned} \tag{27}$$

The last steps in the Formulaes (26) and (27) come from (3). Evidently any term entering (16) and (17) can be decomposed into ΔE_i, for example

$$\begin{aligned} E_5^{(p)} - E_1^{(s)} &= E_5 - E_4 + E_4 - E_3 + E_3 - E_2 + E_2 - E_1 \\ &= \Delta E_4 + \Delta E_3 + \Delta E_2 + \Delta E_1 \end{aligned} \tag{28}$$

and

$$E_6^{(p)} - E_3^{(s)} = E_6 - E_5 + E_5 - E_4 + E_4 - E_3 = \Delta E_5 + \Delta E_4 + \Delta E_3. \tag{29}$$

On the right of (28) and (29) the indices *s* and *p* could be omitted because of the lack of dependence of the right-hand side of the formulae in (18)-(21) on *s* $(l=0)$ and *p* $(l=1)$.

It should be noted that for transitions between levels $n+2$ and *n*, say 3 and 1, we arrive at a very simple intensity formula similar to those given in (4)-(4c):

$$\frac{\Delta E_{3-1}}{\Delta t_{3-1}} = \frac{\Delta E_2 + \Delta E_1}{\Delta t_2 + \Delta t_1} = \frac{\Delta E_2 + \Delta E_1}{\frac{h}{\Delta E_2} + \frac{h}{\Delta E_1}} = \frac{\Delta E_2 + \Delta E_1}{h\left(\Delta E_1 + \Delta E_2\right)} \Delta E_1 \Delta E_2 = \frac{\Delta E_1 \Delta E_2}{h}. \tag{30}$$

A time ago Einstein has remarked that the time of transitions between deep-lying quantum states should be very small [12]. The present approach does confirm this view. For example the time between 2*p* and 1*s* is-because of the result obtained before [6] [7] that the transition time between two neighbouring quantum levels approaches approximately the time period of the lower lying quantum state-equal to

$$\Delta t_1 = T_1 = \frac{2\pi\hbar^3}{m_e e^4}. \tag{31}$$

This is the time period of the first quantum state in the hydrogen atom [13]. In fact the Formula (3) gives Δt_1 rather close to T_1:

$$\Delta t_1 = \frac{h}{\Delta E_1} = \frac{16\pi}{3}\frac{\hbar^3}{m_e e^4} \cong 4\times 10^{-16}\ \text{sec}. \tag{31a}$$

For large quantum numbers *n* and *m* there is evident the formula [see (6)]:

$$\frac{a_m}{a_n} = \frac{\Delta t_n}{\Delta t_m} = \frac{\Delta E_m}{\Delta E_n} = \frac{E_{m+1} - E_m}{E_{n+1} - E_n} = \frac{-\frac{1}{(m+1)^2} + \frac{1}{m^2}}{-\frac{1}{(n+1)^2} + \frac{1}{n^2}} = \frac{\frac{(m+1)^2 - m^2}{(m+1)^2 m^2}}{\frac{(n+1)^2 - n^2}{(n+1)^2 n^2}} \cong \frac{2m/m^4}{2n/n^4} = \frac{n^3}{m^3}, \tag{32}$$

whereas the ratio of the time periods of the hydrogen atom is also:

$$\frac{T_n}{T_m} = \frac{2\pi n^3\hbar^3}{m_e e^4} \cdot \frac{m_e e^4}{2\pi m^3\hbar^3} = \frac{n^3}{m^3}. \tag{32a}$$

Evidently the values of $\Delta t_n \approx T_n$ increase rapidly with increase of *n*.

5. Quantum-Mechanical Counterpart of the Intensity Calculations

The Formulaes (8)-(9) indicate a reference between the coefficients squares a_n^2 and a_{n+1}^2 to the intensity ratios between I_{n+1} and I_n in the sense that the ratio of the squares is equal to the ratio of intensities. This result has obtained its quantum-mechanical counterpart on the basis of the data collected in [11].

In fact we find that there exists an evident correspondence between the ratios of the quantum-mechanical transition probabilities

$$\frac{A\left(n_{\alpha'} p, n_{\alpha''} s\right)}{A\left(n_{\beta'} p, n_{\beta''} s\right)} \tag{33}$$

calculated for different pairs of transitions given by the $n'p$ and $n''s$ states $(n' > n'')$, and the intensity ratios

$$\frac{I_{n_{\alpha'}p-n_{\alpha''}s}}{I_{n_{\beta'}p-n_{\beta''}s}} \tag{13a}$$

calculated with the aid of the present method. In **Table 1** we present the formulae and intensity ratio (13) [or (13a)] obtained for each of the considered pair of transitions. In **Table 2** the quantum-mechanical ratios of probabilities (33) calculated for each transition pair are compared with the ratios calculated in **Table 1**. **Table 3** provides us with the abbreviated expressions for the energy intervals applied in the computations of **Table 1**.

In fact the ratio of two intensities obtained with the present theory referred to the corresponding ratio of the quantum-mechanical probabilities rather seldom exceeds number 2, although the ratios entering the calculations vary between the numbers being evidently smaller than unity [cases (61), (65), (86), (91)] to the numbers equal to several thousands [cases (13) and (14)].

The ratio equal to 2 is exceeded by the cases (6), (10), (31), (35), (56), (65), (86) and (91) where respectively there is obtained

$$\begin{aligned}\frac{\text{semiclassical ratio}}{\text{quantum-mechanical ratio}}:&\frac{43}{18.4}=2.3;\quad \frac{90}{32}=2.8;\quad \frac{1.48}{0.65}=2.3;\quad \frac{2.08}{1.13}=2.7;\\ &\frac{1.08}{0.49}=2.2;\quad \frac{0.38}{0.154}=2.5;\quad \frac{0.175}{0.082}=2.1;\quad \frac{0.081}{0.038}=2.1,\end{aligned} \tag{34}$$

but only in the case (99)

$$\frac{\text{quantum-mechanical ratio}}{\text{semiclassical ratio}}:\frac{92.9}{41.9}=2.2 \tag{34a}$$

exceeds 2.

A time ago Ornstein and Burger [16] considered three intensity ratios presented in **Table 1** and **Table 2**. These are:

$$(4p-2s):(4p-3s),(5p-2s):(5p-3s) \text{ and } (6p-2s):(6p-3s); \tag{35}$$

see items (51), (78) and (100) in **Table 1** and **Table 2**.

They have found respectively the following quantum-mechanical ratios for the transition probabilities:

$$3.55,\ 3.4 \text{ and } 3.2. \tag{36}$$

The experimental ratios of the intensities were found equal to [16]

$$2.6,\ 2.5 \text{ and } 2.0; \tag{37}$$

see also [11]. The data of the present theory are [see e.g. **Table 1**, items (51), (78) and (100)]

$$2.86,\ 2.66 \text{ and } 2.54, \tag{38}$$

so they are closer to the experimental data in (37) than the data given in (36).

6. Lifetime of the Excited States

The intensity I_{p-q} of the electron transition from a state p to a lower state q of the hydrogen atom is coupled with the quanta of energy ΔE_{p-q} and time Δt_{p-q} of the transition by the formula

$$I_{p-q}=\frac{\Delta E_{p-q}}{\Delta t_{p-q}}=a_{p-q}\Delta E_{p-q}. \tag{39}$$

The term a_{p-q} plays the role of transition probability from p to q; see e.g. [10].

Evidently on the basis of (39) we have

$$\frac{1}{\Delta t_{p-q}}=a_{p-q}. \tag{40}$$

Table 1. Intensity ratios of electron transitions between the *p* and *s* states in the hydrogen atom calculated by the present method. The applied intervals of energy are listed in **Table 3**. A comparison of the results of the present Table with the ratios of quantum-mechanical transition probabilities is done in **Table 2**.

No	Case		Formula for the intensity ratio and the value of that ratio
(1)	$\frac{2p-1s}{3p-1s}$	$\rightarrow$	$\frac{(\Delta E_1)^2}{\Delta E_1 \Delta E_2} = \frac{\Delta E_1}{\Delta E_2} = 5.4$,
(2)	$\frac{2p-1s}{3p-2s}$	$\rightarrow$	$\frac{(\Delta E_1)^2}{(\Delta E_2)^2} = 29.2$,
(3)	$\frac{2p-1s}{4p-1s}$	$\rightarrow$	$\frac{(\Delta E_1)^2}{\Delta E_{4-1}}\left(\frac{1}{\Delta E_1}+\frac{1}{\Delta E_2}+\frac{1}{\Delta E_3}\right) = 17.1$,
(4)	$\frac{2p-1s}{4p-2s}$	$\rightarrow$	$\frac{(\Delta E_1)^2}{\Delta E_2 \Delta E_3} = 83.3$,
(5)	$\frac{2p-1s}{4p-3s}$	$\rightarrow$	$\frac{(\Delta E_1)^2}{(\Delta E_3)^2} = 238$,
(6)	$\frac{2p-1s}{5p-1s}$	$\rightarrow$	$\frac{(\Delta E_1)^2}{\Delta E_{5-1}}\left(\frac{1}{\Delta E_1}+\frac{1}{\Delta E_2}+\frac{1}{\Delta E_3}+\frac{1}{\Delta E_4}\right) = 43$,
(7)	$\frac{2p-1s}{5p-2s}$	$\rightarrow$	$\frac{(\Delta E_1)^2}{\Delta E_{5-2}}\left(\frac{1}{\Delta E_2}+\frac{1}{\Delta E_3}+\frac{1}{\Delta E_4}\right) = 193$,
(8)	$\frac{2p-1s}{5p-3s}$	$\rightarrow$	$\frac{(\Delta E_1)^2}{\Delta E_3 \Delta E_4} = 514$,
(9)	$\frac{2p-1s}{5p-4s}$	$\rightarrow$	$\frac{(\Delta E_1)^2}{(\Delta E_4)^2} = 1110$,
(10)	$\frac{2p-1s}{6p-1s}$	$\rightarrow$	$\frac{(\Delta E_1)^2}{\Delta E_{6-1}}\left(\frac{1}{\Delta E_1}+\frac{1}{\Delta E_2}+\frac{1}{\Delta E_3}+\frac{1}{\Delta E_4}+\frac{1}{\Delta E_5}\right) = 90$,
(11)	$\frac{2p-1s}{6p-2s}$	$\rightarrow$	$\frac{(\Delta E_1)^2}{\Delta E_{6-2}}\left(\frac{1}{\Delta E_2}+\frac{1}{\Delta E_3}+\frac{1}{\Delta E_4}+\frac{1}{\Delta E_5}\right) = 390$,
(12)	$\frac{2p-1s}{6p-3s}$	$\rightarrow$	$\frac{(\Delta E_1)^2}{\Delta E_{6-3}}\left(\frac{1}{\Delta E_3}+\frac{1}{\Delta E_4}+\frac{1}{\Delta E_5}\right) = 987$,
(13)	$\frac{2p-1s}{6p-4s}$	$\rightarrow$	$\frac{(\Delta E_1)^2}{\Delta E_4 \Delta E_5} = 2045$,
(14)	$\frac{2p-1s}{6p-5s}$	$\rightarrow$	$\frac{(\Delta E_1)^2}{(\Delta E_5)^2} = 3765$,
(15)	$\frac{3p-1s}{3p-2s}$	$\rightarrow$	$\frac{\Delta E_1 \Delta E_2}{(\Delta E_2)^2} = \frac{\Delta E_1}{\Delta E_2} = 5.4$,
(16)	$\frac{3p-1s}{4p-1s}$	$\rightarrow$	$\frac{\Delta E_1 \Delta E_2}{\Delta E_{4-1}}\left(\frac{1}{\Delta E_1}+\frac{1}{\Delta E_2}+\frac{1}{\Delta E_3}\right) = 3.23$,
(17)	$\frac{3p-1s}{4p-2s}$	$\rightarrow$	$\frac{\Delta E_1 \Delta E_2}{\Delta E_2 \Delta E_3} = \frac{\Delta E_1}{\Delta E_3} = 15.4$,

Continued

(18)	$\frac{3p-1s}{4p-3s}$	$\rightarrow$	$\frac{\Delta E_1 \Delta E_2}{(\Delta E_3)^2} = 44.1$,
(19)	$\frac{3p-1s}{5p-1s}$	$\rightarrow$	$\frac{\Delta E_1 \Delta E_2}{\Delta E_{5-1}}\left(\frac{1}{\Delta E_1}+\frac{1}{\Delta E_2}+\frac{1}{\Delta E_3}+\frac{1}{\Delta E_4}\right) = 7.98$,
(20)	$\frac{3p-1s}{5p-2s}$	$\rightarrow$	$\frac{\Delta E_1 \Delta E_2}{\Delta E_{5-2}}\left(\frac{1}{\Delta E_2}+\frac{1}{\Delta E_3}+\frac{1}{\Delta E_4}\right) = 35.8$,
(21)	$\frac{3p-1s}{5p-3s}$	$\rightarrow$	$\frac{\Delta E_1 \Delta E_2}{\Delta E_3 \Delta E_4} = 95.4$,
(22)	$\frac{3p-1s}{5p-4s}$	$\rightarrow$	$\frac{\Delta E_1 \Delta E_2}{(\Delta E_4)^2} = 205.8$,
(23)	$\frac{3p-1s}{6p-1s}$	$\rightarrow$	$\frac{\Delta E_1 \Delta E_2}{\Delta E_{6-1}}\left(\frac{1}{\Delta E_1}+\frac{1}{\Delta E_2}+\frac{1}{\Delta E_3}+\frac{1}{\Delta E_4}+\frac{1}{\Delta E_5}\right) = 16.6$,
(24)	$\frac{3p-1s}{6p-2s}$	$\rightarrow$	$\frac{\Delta E_1 \Delta E_2}{\Delta E_{6-2}}\left(\frac{1}{\Delta E_2}+\frac{1}{\Delta E_3}+\frac{1}{\Delta E_4}+\frac{1}{\Delta E_5}\right) = 72.2$,
(25)	$\frac{3p-1s}{6p-3s}$	$\rightarrow$	$\frac{\Delta E_1 \Delta E_2}{\Delta E_{6-3}}\left(\frac{1}{\Delta E_3}+\frac{1}{\Delta E_4}+\frac{1}{\Delta E_5}\right) = 184$,
(26)	$\frac{3p-1s}{6p-4s}$	$\rightarrow$	$\frac{\Delta E_1 \Delta E_2}{\Delta E_4 \Delta E_5} = 379$,
(27)	$\frac{3p-1s}{6p-5s}$	$\rightarrow$	$\frac{\Delta E_1 \Delta E_2}{(\Delta E_5)^2} = 697$,
(28)	$\frac{3p-2s}{4p-1s}$	$\rightarrow$	$\frac{(\Delta E_2)^2}{\Delta E_{4-1}}\left(\frac{1}{\Delta E_1}+\frac{1}{\Delta E_2}+\frac{1}{\Delta E_3}\right) = 0.60$,
(29)	$\frac{3p-2s}{4p-2s}$	$\rightarrow$	$\frac{(\Delta E_2)^2}{\Delta E_2 \Delta E_3} = 2.86$,
(30)	$\frac{3p-2s}{4p-3s}$	$\rightarrow$	$\frac{(\Delta E_2)^2}{(\Delta E_3)^2} = 8.16$,
(31)	$\frac{3p-2s}{5p-1s}$	$\rightarrow$	$\frac{(\Delta E_2)^2}{\Delta E_{5-1}}\left(\frac{1}{\Delta E_1}+\frac{1}{\Delta E_2}+\frac{1}{\Delta E_3}+\frac{1}{\Delta E_4}\right) = 1.48$,
(32)	$\frac{3p-2s}{5p-2s}$	$\rightarrow$	$\frac{(\Delta E_2)^2}{\Delta E_{5-2}}\left(\frac{1}{\Delta E_2}+\frac{1}{\Delta E_3}+\frac{1}{\Delta E_4}\right) = 6.63$,
(33)	$\frac{3p-2s}{5p-3s}$	$\rightarrow$	$\frac{(\Delta E_2)^2}{\Delta E_3 \Delta E_4} = 17.6$,
(34)	$\frac{3p-2s}{5p-4s}$	$\rightarrow$	$\frac{(\Delta E_2)^2}{(\Delta E_4)^2} = 38.1$,
(35)	$\frac{3p-2s}{6p-1s}$	$\rightarrow$	$\frac{(\Delta E_2)^2}{\Delta E_{6-1}}\left(\frac{1}{\Delta E_1}+\frac{1}{\Delta E_2}+\frac{1}{\Delta E_3}+\frac{1}{\Delta E_4}+\frac{1}{\Delta E_5}\right) = 3.08$,

Continued

(36)	$\frac{3p-2s}{6p-2s}$	$\rightarrow$	$\frac{\left(\Delta E_2\right)^2}{\Delta E_{6-2}}\left(\frac{1}{\Delta E_2}+\frac{1}{\Delta E_3}+\frac{1}{\Delta E_4}+\frac{1}{\Delta E_5}\right)=13.4,$
(37)	$\frac{3p-2s}{6p-3s}$	$\rightarrow$	$\frac{\left(\Delta E_2\right)^2}{\Delta E_{6-3}}\left(\frac{1}{\Delta E_3}+\frac{1}{\Delta E_4}+\frac{1}{\Delta E_5}\right)=33.9,$
(38)	$\frac{3p-2s}{6p-4s}$	$\rightarrow$	$\frac{\left(\Delta E_2\right)^2}{\Delta E_4 \Delta E_5}=70.1,$
(39)	$\frac{3p-2s}{6p-5s}$	$\rightarrow$	$\frac{\left(\Delta E_2\right)^2}{\left(\Delta E_5\right)^2}=129,$
(40)	$\frac{4p-1s}{4p-2s}$	$\rightarrow$	$\frac{\Delta E_{4-1}}{\frac{1}{\Delta E_1}+\frac{1}{\Delta E_2}+\frac{1}{\Delta E_3}}\cdot\frac{1}{\Delta E_2 \Delta E_3}=4.76,$
(41)	$\frac{4p-1s}{4p-3s}$	$\rightarrow$	$\frac{\Delta E_{4-1}}{\frac{1}{\Delta E_1}+\frac{1}{\Delta E_2}+\frac{1}{\Delta E_3}}\cdot\frac{1}{\left(\Delta E_3\right)^2}=13.7,$
(42)	$\frac{4p-1s}{5p-1s}$	$\rightarrow$	$\frac{\Delta E_{4-1}}{\frac{1}{\Delta E_1}+\frac{1}{\Delta E_2}+\frac{1}{\Delta E_3}}\cdot\frac{\frac{1}{\Delta E_1}+\frac{1}{\Delta E_2}+\frac{1}{\Delta E_3}+\frac{1}{\Delta E_4}}{\Delta E_{5-1}}=2.47,$
(43)	$\frac{4p-1s}{5p-2s}$	$\rightarrow$	$\frac{\Delta E_{4-1}}{\frac{1}{\Delta E_1}+\frac{1}{\Delta E_2}+\frac{1}{\Delta E_3}}\cdot\frac{\frac{1}{\Delta E_2}+\frac{1}{\Delta E_3}+\frac{1}{\Delta E_4}}{\Delta E_{5-2}}=11.1,$
(44)	$\frac{4p-1s}{5p-3s}$	$\rightarrow$	$\frac{\Delta E_{4-1}}{\frac{1}{\Delta E_1}+\frac{1}{\Delta E_2}+\frac{1}{\Delta E_3}}\cdot\frac{1}{\Delta E_3 \Delta E_4}=29.5,$
(45)	$\frac{4p-1s}{5p-4s}$	$\rightarrow$	$\frac{\Delta E_{4-1}}{\frac{1}{\Delta E_1}+\frac{1}{\Delta E_2}+\frac{1}{\Delta E_3}}\cdot\frac{1}{\left(\Delta E_4\right)^2}=63.6,$
(46)	$\frac{4p-1s}{6p-1s}$	$\rightarrow$	$\frac{\Delta E_{4-1}}{\Delta E_{6-1}}\cdot\frac{\frac{1}{\Delta E_1}+\frac{1}{\Delta E_2}+\frac{1}{\Delta E_3}+\frac{1}{\Delta E_4}+\frac{1}{\Delta E_5}}{\frac{1}{\Delta E_1}+\frac{1}{\Delta E_2}+\frac{1}{\Delta E_3}}=5.14,$
(47)	$\frac{4p-1s}{6p-2s}$	$\rightarrow$	$\frac{\Delta E_{4-1}}{\Delta E_{6-2}}\cdot\frac{\frac{1}{\Delta E_2}+\frac{1}{\Delta E_3}+\frac{1}{\Delta E_4}+\frac{1}{\Delta E_5}}{\frac{1}{\Delta E_1}+\frac{1}{\Delta E_2}+\frac{1}{\Delta E_3}}=22.3,$
(48)	$\frac{4p-1s}{6p-3s}$	$\rightarrow$	$\frac{\Delta E_{4-1}}{\Delta E_{6-3}}\cdot\frac{\frac{1}{\Delta E_3}+\frac{1}{\Delta E_4}+\frac{1}{\Delta E_5}}{\frac{1}{\Delta E_1}+\frac{1}{\Delta E_2}+\frac{1}{\Delta E_3}}=56.8,$
(49)	$\frac{4p-1s}{6p-4s}$	$\rightarrow$	$\frac{\Delta E_{4-1}}{\Delta E_4 \Delta E_5}\cdot\frac{1}{\frac{1}{\Delta E_1}+\frac{1}{\Delta E_2}+\frac{1}{\Delta E_3}}=117,$

Continued

(50)	$\frac{4p-1s}{6p-5s}$	$\rightarrow$	$\frac{\Delta E_{4-1}}{\left(\Delta E_5\right)^2}\cdot\frac{1}{\frac{1}{\Delta E_1}+\frac{1}{\Delta E_2}+\frac{1}{\Delta E_3}}=216$,
(51)	$\frac{4p-2s}{4p-3s}$	$\rightarrow$	$\frac{\Delta E_2\Delta E_3}{\left(\Delta E_3\right)^2}=\frac{\Delta E_2}{\Delta E_3}=2.86$,
(52)	$\frac{4p-2s}{5p-1s}$	$\rightarrow$	$\frac{\Delta E_2\Delta E_3}{\Delta E_{5-1}}\left(\frac{1}{\Delta E_1}+\frac{1}{\Delta E_2}+\frac{1}{\Delta E_3}+\frac{1}{\Delta E_4}\right)=0.52$,
(53)	$\frac{4p-2s}{5p-2s}$	$\rightarrow$	$\frac{\Delta E_2\Delta E_3}{\Delta E_{5-2}}\left(\frac{1}{\Delta E_2}+\frac{1}{\Delta E_3}+\frac{1}{\Delta E_4}\right)=2.32$,
(54)	$\frac{4p-2s}{5p-3s}$	$\rightarrow$	$\frac{\Delta E_2\Delta E_3}{\Delta E_3\Delta E_4}=\frac{\Delta E_2}{\Delta E_4}=6.17$,
(55)	$\frac{4p-2s}{5p-4s}$	$\rightarrow$	$\frac{\Delta E_2\Delta E_3}{\left(\Delta E_4\right)^2}=13.2$,
(56)	$\frac{4p-2s}{6p-1s}$	$\rightarrow$	$\frac{\Delta E_2\Delta E_3}{\Delta E_{6-1}}\left(\frac{1}{\Delta E_1}+\frac{1}{\Delta E_2}+\frac{1}{\Delta E_3}+\frac{1}{\Delta E_4}+\frac{1}{\Delta E_5}\right)=1.08$,
(57)	$\frac{4p-2s}{6p-2s}$	$\rightarrow$	$\frac{\Delta E_2\Delta E_3}{\Delta E_{6-2}}\left(\frac{1}{\Delta E_2}+\frac{1}{\Delta E_3}+\frac{1}{\Delta E_4}+\frac{1}{\Delta E_5}\right)=4.68$,
(58)	$\frac{4p-2s}{6p-3s}$	$\rightarrow$	$\frac{\Delta E_2\Delta E_3}{\Delta E_{6-3}}\left(\frac{1}{\Delta E_3}+\frac{1}{\Delta E_4}+\frac{1}{\Delta E_5}\right)=11.9$,
(59)	$\frac{4p-2s}{6p-4s}$	$\rightarrow$	$\frac{\Delta E_2\Delta E_3}{\Delta E_4\Delta E_5}=24.6$,
(60)	$\frac{4p-2s}{6p-5s}$	$\rightarrow$	$\frac{\Delta E_2\Delta E_5}{\left(\Delta E_5\right)^2}=45.2$,
(61)	$\frac{4p-3s}{5p-1s}$	$\rightarrow$	$\frac{\left(\Delta E_3\right)^2}{\Delta E_{5-1}}\left(\frac{1}{\Delta E_1}+\frac{1}{\Delta E_2}+\frac{1}{\Delta E_3}+\frac{1}{\Delta E_4}\right)=0.18$,
(62)	$\frac{4p-3s}{5p-2s}$	$\rightarrow$	$\frac{\left(\Delta E_3\right)^2}{\Delta E_{5-2}}\left(\frac{1}{\Delta E_2}+\frac{1}{\Delta E_3}+\frac{1}{\Delta E_4}\right)=0.81$,
(63)	$\frac{4p-3s}{5p-3s}$	$\rightarrow$	$\frac{\left(\Delta E_3\right)^2}{\Delta E_3\Delta E_4}=\frac{\Delta E_3}{\Delta E_4}=2.16$,
(64)	$\frac{4p-3s}{5p-4s}$	$\rightarrow$	$\frac{\left(\Delta E_3\right)^2}{\left(\Delta E_4\right)^2}=4.67$,
(65)	$\frac{4p-3s}{6p-1s}$	$\rightarrow$	$\frac{\left(\Delta E_3\right)^2}{\Delta E_{6-1}}\left(\frac{1}{\Delta E_1}+\frac{1}{\Delta E_2}+\frac{1}{\Delta E_3}+\frac{1}{\Delta E_4}+\frac{1}{\Delta E_5}\right)=0.38$,
(66)	$\frac{4p-3s}{6p-2s}$	$\rightarrow$	$\frac{\left(\Delta E_3\right)^2}{\Delta E_{6-2}}\left(\frac{1}{\Delta E_2}+\frac{1}{\Delta E_3}+\frac{1}{\Delta E_4}+\frac{1}{\Delta E_5}\right)=1.64$,
(67)	$\frac{4p-3s}{6p-3s}$	$\rightarrow$	$\frac{\left(\Delta E_3\right)^2}{\Delta E_{6-3}}\left(\frac{1}{\Delta E_3}+\frac{1}{\Delta E_4}+\frac{1}{\Delta E_5}\right)=4.16$,

Continued

(68)	$\frac{4p-3s}{6p-4s}$	$\rightarrow$	$\frac{(\Delta E_3)^2}{\Delta E_4 \Delta E_5} = 8.59$,
(69)	$\frac{4p-3s}{6p-5s}$	$\rightarrow$	$\frac{(\Delta E_3)^2}{(\Delta E_5)^2} = 15.8$,
(70)	$\frac{5p-1s}{5p-2s}$	$\rightarrow$	$\frac{\Delta E_{5-1}}{\frac{1}{\Delta E_1}+\frac{1}{\Delta E_2}+\frac{1}{\Delta E_3}+\frac{1}{\Delta E_4}} \cdot \frac{1}{\Delta E_{5-2}} \left(\frac{1}{\Delta E_2}+\frac{1}{\Delta E_3}+\frac{1}{\Delta E_4} \right) = 4.49$,
(71)	$\frac{5p-1s}{5p-3s}$	$\rightarrow$	$\frac{\Delta E_{5-1}}{\frac{1}{\Delta E_1}+\frac{1}{\Delta E_2}+\frac{1}{\Delta E_3}+\frac{1}{\Delta E_4}} \cdot \frac{1}{\Delta E_3 \Delta E_4} = 11.9$,
(72)	$\frac{5p-1s}{5p-4s}$	$\rightarrow$	$\frac{\Delta E_{5-1}}{\frac{1}{\Delta E_1}+\frac{1}{\Delta E_2}+\frac{1}{\Delta E_3}+\frac{1}{\Delta E_4}} \cdot \frac{1}{(\Delta E_4)^2} = 25.8$,
(73)	$\frac{5p-1s}{6p-1s}$	$\rightarrow$	$\frac{\Delta E_{5-1}}{\frac{1}{\Delta E_1}+\frac{1}{\Delta E_2}+\frac{1}{\Delta E_3}+\frac{1}{\Delta E_4}} \cdot \frac{1}{\Delta E_{6-1}} \left(\frac{1}{\Delta E_1}+\frac{1}{\Delta E_2}+\frac{1}{\Delta E_3}+\frac{1}{\Delta E_4}+\frac{1}{\Delta E_5} \right) = 2.09$,
(74)	$\frac{5p-1s}{6p-2s}$	$\rightarrow$	$\frac{\Delta E_{5-1}}{\frac{1}{\Delta E_1}+\frac{1}{\Delta E_2}+\frac{1}{\Delta E_3}+\frac{1}{\Delta E_4}} \cdot \frac{1}{\Delta E_{6-2}} \left(\frac{1}{\Delta E_2}+\frac{1}{\Delta E_3}+\frac{1}{\Delta E_4}+\frac{1}{\Delta E_5} \right) = 9.05$,
(75)	$\frac{5p-1s}{6p-3s}$	$\rightarrow$	$\frac{\Delta E_{5-1}}{\frac{1}{\Delta E_1}+\frac{1}{\Delta E_2}+\frac{1}{\Delta E_3}+\frac{1}{\Delta E_4}} \cdot \frac{1}{\Delta E_{6-3}} \left(\frac{1}{\Delta E_3}+\frac{1}{\Delta E_4}+\frac{1}{\Delta E_5} \right) = 23.0$,
(76)	$\frac{5p-1s}{6p-4s}$	$\rightarrow$	$\frac{\Delta E_{5-1}}{\frac{1}{\Delta E_1}+\frac{1}{\Delta E_2}+\frac{1}{\Delta E_3}+\frac{1}{\Delta E_4}} \cdot \frac{1}{\Delta E_4 \Delta E_5} = 48.4$,
(77)	$\frac{5p-1s}{6p-5s}$	$\rightarrow$	$\frac{\Delta E_{5-1}}{\frac{1}{\Delta E_1}+\frac{1}{\Delta E_2}+\frac{1}{\Delta E_3}+\frac{1}{\Delta E_4}} \cdot \frac{1}{(\Delta E_5)^2} = 87.4$,
(78)	$\frac{5p-2s}{5p-3s}$	$\rightarrow$	$\frac{\Delta E_{5-2}}{\frac{1}{\Delta E_2}+\frac{1}{\Delta E_3}+\frac{1}{\Delta E_4}} \cdot \frac{1}{\Delta E_3 \Delta E_4} = 2.66$,
(79)	$\frac{5p-2s}{5p-4s}$	$\rightarrow$	$\frac{\Delta E_{5-2}}{\frac{1}{\Delta E_2}+\frac{1}{\Delta E_3}+\frac{1}{\Delta E_4}} \cdot \frac{1}{(\Delta E_4)^2} = 5.74$,
(80)	$\frac{5p-2s}{6p-1s}$	$\rightarrow$	$\frac{\Delta E_{5-2}}{\frac{1}{\Delta E_2}+\frac{1}{\Delta E_3}+\frac{1}{\Delta E_4}} \cdot \frac{1}{\Delta E_{6-1}} \left(\frac{1}{\Delta E_1}+\frac{1}{\Delta E_2}+\frac{1}{\Delta E_3}+\frac{1}{\Delta E_4}+\frac{1}{\Delta E_5} \right) = 0.46$,
(81)	$\frac{5p-2s}{6p-2s}$	$\rightarrow$	$\frac{\Delta E_{5-2}}{\frac{1}{\Delta E_2}+\frac{1}{\Delta E_3}+\frac{1}{\Delta E_4}} \cdot \frac{1}{\Delta E_{6-2}} \left(\frac{1}{\Delta E_2}+\frac{1}{\Delta E_3}+\frac{1}{\Delta E_4}+\frac{1}{\Delta E_5} \right) = 2.02$,

Continued

(82)	$\frac{5p-2s}{6p-3s}$	$\rightarrow$	$\frac{\Delta E_{5-2}}{\frac{1}{\Delta E_2}+\frac{1}{\Delta E_3}+\frac{1}{\Delta E_4}}\cdot\frac{1}{\Delta E_{6-3}}\left(\frac{1}{\Delta E_3}+\frac{1}{\Delta E_4}+\frac{1}{\Delta E_5}\right)=5.12,$
(83)	$\frac{5p-2s}{6p-4s}$	$\rightarrow$	$\frac{\Delta E_{5-2}}{\frac{1}{\Delta E_2}+\frac{1}{\Delta E_3}+\frac{1}{\Delta E_4}}\cdot\frac{1}{\Delta E_4\Delta E_5}=10.6,$
(84)	$\frac{5p-2s}{6p-5s}$	$\rightarrow$	$\frac{\Delta E_{5-2}}{\frac{1}{\Delta E_2}+\frac{1}{\Delta E_3}+\frac{1}{\Delta E_4}}\cdot\frac{1}{(\Delta E_5)^2}=19.5,$
(85)	$\frac{5p-3s}{5p-4s}$	$\rightarrow$	$\frac{\Delta E_3\Delta E_4}{(\Delta E_4)^2}=\frac{\Delta E_3}{\Delta E_4}=2.16,$
(86)	$\frac{5p-3s}{6p-1s}$	$\rightarrow$	$\frac{\Delta E_3\Delta E_4}{\Delta E_{6-1}}\left(\frac{1}{\Delta E_1}+\frac{1}{\Delta E_2}+\frac{1}{\Delta E_3}+\frac{1}{\Delta E_4}+\frac{1}{\Delta E_5}\right)=0.175,$
(87)	$\frac{5p-3s}{6p-2s}$	$\rightarrow$	$\frac{\Delta E_3\Delta E_4}{\Delta E_{6-2}}\left(\frac{1}{\Delta E_2}+\frac{1}{\Delta E_3}+\frac{1}{\Delta E_4}+\frac{1}{\Delta E_5}\right)=0.76,$
(88)	$\frac{5p-3s}{6p-3s}$	$\rightarrow$	$\frac{\Delta E_3\Delta E_4}{\Delta E_{6-3}}\left(\frac{1}{\Delta E_3}+\frac{1}{\Delta E_4}+\frac{1}{\Delta E_5}\right)=1.93,$
(89)	$\frac{5p-3s}{6p-4s}$	$\rightarrow$	$\frac{\Delta E_3\Delta E_4}{\Delta E_4\Delta E_5}=\frac{\Delta E_3}{\Delta E_5}=3.98,$
(90)	$\frac{5p-3s}{6p-5s}$	$\rightarrow$	$\frac{\Delta E_3\Delta E_4}{(\Delta E_5)^2}=7.32,$
(91)	$\frac{5p-4s}{6p-1s}$	$\rightarrow$	$\frac{(\Delta E_4)^2}{\Delta E_{6-1}}\left(\frac{1}{\Delta E_1}+\frac{1}{\Delta E_2}+\frac{1}{\Delta E_3}+\frac{1}{\Delta E_4}+\frac{1}{\Delta E_5}\right)=0.081,$
(92)	$\frac{5p-4s}{6p-2s}$	$\rightarrow$	$\frac{(\Delta E_4)^2}{\Delta E_{6-2}}\left(\frac{1}{\Delta E_2}+\frac{1}{\Delta E_3}+\frac{1}{\Delta E_4}+\frac{1}{\Delta E_5}\right)=0.35,$
(93)	$\frac{5p-4s}{6p-3s}$	$\rightarrow$	$\frac{(\Delta E_4)^2}{\Delta E_{6-3}}\left(\frac{1}{\Delta E_3}+\frac{1}{\Delta E_4}+\frac{1}{\Delta E_5}\right)=0.89,$
(94)	$\frac{5p-4s}{6p-4s}$	$\rightarrow$	$\frac{(\Delta E_4)^2}{\Delta E_4\Delta E_5}=\frac{\Delta E_4}{\Delta E_5}=1.84,$
(95)	$\frac{5p-4s}{6p-5s}$	$\rightarrow$	$\frac{(\Delta E_4)^2}{(\Delta E_5)^2}=3.39,$
(96)	$\frac{6p-1s}{6p-2s}$	$\rightarrow$	$\frac{\Delta E_{6-1}}{\frac{1}{\Delta E_1}+\frac{1}{\Delta E_2}+\frac{1}{\Delta E_3}+\frac{1}{\Delta E_4}+\frac{1}{\Delta E_5}}\cdot\frac{\frac{1}{\Delta E_2}+\frac{1}{\Delta E_3}+\frac{1}{\Delta E_4}+\frac{1}{\Delta E_5}}{\Delta E_{6-2}}=4.34,$
(97)	$\frac{6p-1s}{6p-3s}$	$\rightarrow$	$\frac{\Delta E_{6-1}}{\frac{1}{\Delta E_1}+\frac{1}{\Delta E_2}+\frac{1}{\Delta E_3}+\frac{1}{\Delta E_4}+\frac{1}{\Delta E_5}}\cdot\frac{\frac{1}{\Delta E_3}+\frac{1}{\Delta E_4}+\frac{1}{\Delta E_5}}{\Delta E_{6-3}}=11.02,$

Continued

(98)	$\frac{6p-1s}{6p-4s}$	$\rightarrow$	$\frac{\Delta E_{6-1}}{\frac{1}{\Delta E_1}+\frac{1}{\Delta E_2}+\frac{1}{\Delta E_3}+\frac{1}{\Delta E_4}+\frac{1}{\Delta E_5}}\cdot\frac{1}{\Delta E_4\Delta E_5}=22.8$,
(99)	$\frac{6p-1s}{6p-5s}$	$\rightarrow$	$\frac{\Delta E_{6-1}}{\frac{1}{\Delta E_1}+\frac{1}{\Delta E_2}+\frac{1}{\Delta E_3}+\frac{1}{\Delta E_4}+\frac{1}{\Delta E_5}}\cdot\frac{1}{(\Delta E_5)^2}=41.9$,
(100)	$\frac{6p-2s}{6p-3s}$	$\rightarrow$	$\frac{\Delta E_{6-2}}{\frac{1}{\Delta E_2}+\frac{1}{\Delta E_3}+\frac{1}{\Delta E_4}+\frac{1}{\Delta E_5}}\cdot\frac{\frac{1}{\Delta E_3}+\frac{1}{\Delta E_4}+\frac{1}{\Delta E_5}}{\Delta E_{6-3}}=2.54$,
(101)	$\frac{6p-2s}{6p-4s}$	$\rightarrow$	$\frac{\Delta E_{6-2}}{\frac{1}{\Delta E_2}+\frac{1}{\Delta E_3}+\frac{1}{\Delta E_4}+\frac{1}{\Delta E_5}}\cdot\frac{1}{\Delta E_4\Delta E_5}=5.25$,
(102)	$\frac{6p-2s}{6p-5s}$	$\rightarrow$	$\frac{\Delta E_{6-2}}{\frac{1}{\Delta E_2}+\frac{1}{\Delta E_3}+\frac{1}{\Delta E_4}+\frac{1}{\Delta E_5}}\cdot\frac{1}{(\Delta E_5)^2}=9.66$,
(103)	$\frac{6p-3s}{6p-4s}$	$\rightarrow$	$\frac{\Delta E_{6-3}}{\frac{1}{\Delta E_3}+\frac{1}{\Delta E_4}+\frac{1}{\Delta E_5}}\cdot\frac{1}{\Delta E_4\Delta E_5}=2.06$,
(104)	$\frac{6p-3s}{6p-5s}$	$\rightarrow$	$\frac{\Delta E_{6-3}}{\frac{1}{\Delta E_3}+\frac{1}{\Delta E_4}+\frac{1}{\Delta E_5}}\cdot\frac{1}{(\Delta E_5)^2}=3.8$,
(105)	$\frac{6p-4s}{6p-5s}$	$\rightarrow$	$\frac{\Delta E_4\Delta E_5}{(\Delta E_5)^2}=\frac{\Delta E_4}{\Delta E_5}=1.84$,

Table 2. Quantum-mechanical ratios of transition probabilities between the pairs of quantum levels (see [11]) compared with the intensity ratios calculated in **Table 1**.

No	Case		Quantum-mechanical ratio	Intensity ratio from **Table 1**
(1)	$\frac{2p-1s}{3p-1s}$	$\rightarrow$	$\frac{6.25}{1.64}=3.8$;	5.4
(2)	$\frac{2p-1s}{3p-2s}$	$\rightarrow$	$\frac{6.25}{0.22}=28.4$;	29.2
(3)	$\frac{2p-1s}{4p-1s}$	$\rightarrow$	$\frac{6.25}{0.68}=9.4$;	17.1
(4)	$\frac{2p-1s}{4p-2s}$	$\rightarrow$	$\frac{6.25}{0.095}=65.8$;	83.3
(5)	$\frac{2p-1s}{4p-3s}$	$\rightarrow$	$\frac{6.25}{0.030}=208$;	238
(6)	$\frac{2p-1s}{5p-1s}$	$\rightarrow$	$\frac{6.25}{0.34}=18.4$;	43
(7)	$\frac{2p-1s}{5p-2s}$	$\rightarrow$	$\frac{6.25}{0.049}=128$;	193

Continued

(8)	$\frac{2p-1s}{5p-3s}$	$\rightarrow$	$\frac{6.25}{0.016}=391;$	514
(9)	$\frac{2p-1s}{5p-4s}$	$\rightarrow$	$\frac{6.25}{0.0075}=833;$	1110
(10)	$\frac{2p-1s}{6p-1s}$	$\rightarrow$	$\frac{6.25}{0.195}=32;$	90
(11)	$\frac{2p-1s}{6p-2s}$	$\rightarrow$	$\frac{6.25}{0.029}=216;$	390
(12)	$\frac{2p-1s}{6p-3s}$	$\rightarrow$	$\frac{6.25}{0.0096}=651;$	987
(13)	$\frac{2p-1s}{6p-4s}$	$\rightarrow$	$\frac{6.25}{0.0045}=1390;$	2045
(14)	$\frac{2p-1s}{6p-5s}$	$\rightarrow$	$\frac{6.25}{0.0021}=2980;$	3765
(15)	$\frac{3p-1s}{3p-2s}$	$\rightarrow$	$\frac{1.64}{0.22}=7.45;$	5.4
(16)	$\frac{3p-1s}{4p-1s}$	$\rightarrow$	$\frac{1.64}{0.68}=2.41;$	3.2
(17)	$\frac{3p-1s}{4p-2s}$	$\rightarrow$	$\frac{1.64}{0.095}=17.3;$	15.4
(18)	$\frac{3p-1s}{4p-3s}$	$\rightarrow$	$\frac{1.64}{0.030}=54.7;$	44.1
(19)	$\frac{3p-1s}{5p-1s}$	$\rightarrow$	$\frac{1.64}{0.34}=4.82;$	7.98
(20)	$\frac{3p-1s}{5p-2s}$	$\rightarrow$	$\frac{1.64}{0.049}=33.5;$	35.8
(21)	$\frac{3p-1s}{5p-3s}$	$\rightarrow$	$\frac{1.64}{0.016}=102;$	95.4
(22)	$\frac{3p-1s}{5p-4s}$	$\rightarrow$	$\frac{1.64}{0.0075}=218;$	206
(23)	$\frac{3p-1s}{6p-1s}$	$\rightarrow$	$\frac{1.64}{0.195}=8.4;$	16.6
(24)	$\frac{3p-1s}{6p-2s}$	$\rightarrow$	$\frac{1.64}{0.029}=56.6;$	72.2
(25)	$\frac{3p-1s}{6p-3s}$	$\rightarrow$	$\frac{1.64}{0.0096}=171;$	184
(26)	$\frac{3p-1s}{6p-4s}$	$\rightarrow$	$\frac{1.64}{0.0045}=364;$	379

Continued

(27)	$3p-1s \over 6p-5s$	→	$1.64 \over 0.0021 = 781$;	697
(28)	$3p-2s \over 4p-1s$	→	$0.22 \over 0.68 = 0.32$;	0.60
(29)	$3p-2s \over 4p-2s$	→	$0.22 \over 0.095 = 2.32$;	2.86
(30)	$3p-2s \over 4p-3s$	→	$0.22 \over 0.030 = 7.33$;	8.16
(31)	$3p-2s \over 5p-1s$	→	$0.22 \over 0.34 = 0.65$;	1.48
(32)	$3p-2s \over 5p-2s$	→	$0.22 \over 0.049 = 4.49$;	6.63
(33)	$3p-2s \over 5p-3s$	→	$0.22 \over 0.016 = 13.8$;	17.6
(34)	$3p-2s \over 5p-4s$	→	$0.22 \over 0.0075 = 29.3$;	38.1
(35)	$3p-2s \over 6p-1s$	→	$0.22 \over 0.195 = 1.13$;	3.08
(36)	$3p-2s \over 6p-2s$	→	$0.22 \over 0.029 = 7.6$;	13.4
(37)	$3p-2s \over 6p-3s$	→	$0.22 \over 0.0096 = 22.9$;	33.9
(38)	$3p-2s \over 6p-4s$	→	$0.22 \over 0.0045 = 48.9$;	70.1
(39)	$3p-2s \over 6p-5s$	→	$0.22 \over 0.0021 = 105$;	129
(40)	$4p-1s \over 4p-2s$	→	$0.68 \over 0.095 = 7.14$;	4.76
(41)	$4p-1s \over 4p-3s$	→	$0.68 \over 0.030 = 22.7$;	13.7
(42)	$4p-1s \over 5p-1s$	→	$0.68 \over 0.34 = 2.0$;	2.47
(43)	$4p-1s \over 5p-2s$	→	$0.68 \over 0.049 = 13.9$;	11.1
(44)	$4p-1s \over 5p-3s$	→	$0.68 \over 0.016 = 42.5$;	29.5
(45)	$4p-1s \over 5p-4s$	→	$0.68 \over 0.0075 = 90.6$;	63.6
(46)	$4p-1s \over 6p-1s$	→	$0.68 \over 0.195 = 3.49$;	5.14

Continued

(47)	$\frac{4p-1s}{6p-2s}$	$\rightarrow$	$\frac{0.68}{0.029}=23.4$;	22.3
(48)	$\frac{4p-1s}{6p-3s}$	$\rightarrow$	$\frac{0.68}{0.0096}=70.8$;	56.8
(49)	$\frac{4p-1s}{6p-4s}$	$\rightarrow$	$\frac{0.68}{0.0045}=151$;	117
(50)	$\frac{4p-1s}{6p-5s}$	$\rightarrow$	$\frac{0.68}{0.0021}=324$;	216
(51)	$\frac{4p-2s}{4p-3s}$	$\rightarrow$	$\frac{0.095}{0.030}=3.17$;	2.86
(52)	$\frac{4p-2s}{5p-1s}$	$\rightarrow$	$\frac{0.095}{0.34}=0.28$;	0.52
(53)	$\frac{4p-2s}{5p-2s}$	$\rightarrow$	$\frac{0.095}{0.049}=1.94$;	2.32
(54)	$\frac{4p-2s}{5p-3s}$	$\rightarrow$	$\frac{0.095}{0.016}=5.94$;	6.17
(55)	$\frac{4p-2s}{5p-4s}$	$\rightarrow$	$\frac{0.095}{0.0075}=12.7$;	13.2
(56)	$\frac{4p-2s}{6p-1s}$	$\rightarrow$	$\frac{0.095}{0.195}=0.49$;	1.08
(57)	$\frac{4p-2s}{6p-2s}$	$\rightarrow$	$\frac{0.095}{0.029}=3.28$;	4.68
(58)	$\frac{4p-2s}{6p-3s}$	$\rightarrow$	$\frac{0.095}{0.0096}=9.9$;	11.9
(59)	$\frac{4p-2s}{6p-4s}$	$\rightarrow$	$\frac{0.095}{0.0045}=21.1$;	24.6
(60)	$\frac{4p-2s}{6p-5s}$	$\rightarrow$	$\frac{0.095}{0.0021}=45.2$;	45.2
(61)	$\frac{4p-3s}{5p-1s}$	$\rightarrow$	$\frac{0.030}{0.34}=0.09$;	0.18
(62)	$\frac{4p-3s}{5p-2s}$	$\rightarrow$	$\frac{0.030}{0.049}=0.61$;	0.81
(63)	$\frac{4p-3s}{5p-3s}$	$\rightarrow$	$\frac{0.030}{0.016}=1.88$;	2.16
(64)	$\frac{4p-3s}{5p-4s}$	$\rightarrow$	$\frac{0.030}{0.0075}=4.0$;	4.67
(65)	$\frac{4p-3s}{6p-1s}$	$\rightarrow$	$\frac{0.030}{0.195}=0.15$;	0.38
(66)	$\frac{4p-3s}{6p-2s}$	$\rightarrow$	$\frac{0.030}{0.029}=1.03$;	1.64

Continued

(67)	$\frac{4p-3s}{6p-3s}$	→	$\frac{0.030}{0.0096}=3.13$;	4.16
(68)	$\frac{4p-3s}{6p-4s}$	→	$\frac{0.030}{0.0045}=6.67$;	8.59
(69)	$\frac{4p-3s}{6p-5s}$	→	$\frac{0.030}{0.0021}=14.3$;	15.8
(70)	$\frac{5p-1s}{5p-2s}$	→	$\frac{0.34}{0.049}=6.94$;	4.49
(71)	$\frac{5p-1s}{5p-3s}$	→	$\frac{0.34}{0.016}=21.3$;	11.9
(72)	$\frac{5p-1s}{5p-4s}$	→	$\frac{0.34}{0.0075}=45.3$;	25.8
(73)	$\frac{5p-1s}{6p-1s}$	→	$\frac{0.34}{0.195}=1.74$;	2.09
(74)	$\frac{5p-1s}{6p-2s}$	→	$\frac{0.34}{0.029}=11.7$;	9.05
(75)	$\frac{5p-1s}{6p-3s}$	→	$\frac{0.34}{0.0096}=35.4$;	23.0
(76)	$\frac{5p-1s}{6p-4s}$	→	$\frac{0.34}{0.0045}=75.6$;	48.4
(77)	$\frac{5p-1s}{6p-5s}$	→	$\frac{0.34}{0.0021}=162$;	87.4
(78)	$\frac{5p-2s}{5p-3s}$	→	$\frac{0.049}{0.016}=3.06$;	2.66
(79)	$\frac{5p-2s}{5p-4s}$	→	$\frac{0.049}{0.0075}=6.53$;	5.74
(80)	$\frac{5p-2s}{6p-1s}$	→	$\frac{0.049}{0.195}=0.25$;	0.46
(81)	$\frac{5p-2s}{6p-2s}$	→	$\frac{0.049}{0.029}=1.69$;	2.02
(82)	$\frac{5p-2s}{6p-3s}$	→	$\frac{0.049}{0.0096}=5.10$;	5.12
(83)	$\frac{5p-2s}{6p-4s}$	→	$\frac{0.049}{0.0045}=10.9$;	10.6
(84)	$\frac{5p-2s}{6p-5s}$	→	$\frac{0.049}{0.0021}=23.3$;	19.5
(85)	$\frac{5p-3s}{5p-4s}$	→	$\frac{0.016}{0.0075}=2.13$;	2.16
(86)	$\frac{5p-3s}{6p-1s}$	→	$\frac{0.016}{0.195}=0.082$;	0.175

Continued

(87)	$\frac{5p-3s}{6p-2s}$	$\rightarrow$	$\frac{0.016}{0.029}=0.55$;	0.76
(88)	$\frac{5p-3s}{6p-3s}$	$\rightarrow$	$\frac{0.016}{0.0096}=1.67$;	1.93
(89)	$\frac{5p-3s}{6p-4s}$	$\rightarrow$	$\frac{0.016}{0.0045}=3.56$;	3.98
(90)	$\frac{5p-3s}{6p-5s}$	$\rightarrow$	$\frac{0.016}{0.0021}=7.62$;	7.32
(91)	$\frac{5p-4s}{6p-1s}$	$\rightarrow$	$\frac{0.0075}{0.195}=0.038$;	0.081
(92)	$\frac{5p-4s}{6p-2s}$	$\rightarrow$	$\frac{0.0075}{0.029}=0.26$;	0.35
(93)	$\frac{5p-4s}{6p-3s}$	$\rightarrow$	$\frac{0.0075}{0.0096}=0.78$;	0.89
(94)	$\frac{5p-4s}{6p-4s}$	$\rightarrow$	$\frac{0.0075}{0.0045}=1.67$;	1.84
(95)	$\frac{5p-4s}{6p-5s}$	$\rightarrow$	$\frac{0.0075}{0.0021}=3.57$;	3.39
(96)	$\frac{6p-1s}{6p-2s}$	$\rightarrow$	$\frac{0.195}{0.029}=6.72$;	4.34
(97)	$\frac{6p-1s}{6p-3s}$	$\rightarrow$	$\frac{0.195}{0.0096}=20.3$;	11.02
(98)	$\frac{6p-1s}{6p-4s}$	$\rightarrow$	$\frac{0.195}{0.0045}=43.3$;	22.8
(99)	$\frac{6p-1s}{6p-5s}$	$\rightarrow$	$\frac{0.195}{0.0021}=92.9$;	41.9
(100)	$\frac{6p-2s}{6p-3s}$	$\rightarrow$	$\frac{0.029}{0.0096}=3.02$;	2.54
(101)	$\frac{6p-2s}{6p-4s}$	$\rightarrow$	$\frac{0.029}{0.0045}=6.44$;	5.25
(102)	$\frac{6p-2s}{6p-5s}$	$\rightarrow$	$\frac{0.029}{0.0021}=13.8$;	9.66
(103)	$\frac{6p-3s}{6p-4s}$	$\rightarrow$	$\frac{0.0096}{0.0045}=2.10$;	2.06
(104)	$\frac{6p-3s}{6p-5s}$	$\rightarrow$	$\frac{0.0096}{0.0021}=4.6$;	3.8
(105)	$\frac{6p-4s}{6p-5s}$	$\rightarrow$	$\frac{0.0045}{0.0021}=2.14$;	1.84

Table 3. Energy intervals ΔE entering the calculations of **Table 1**. All presented ΔE values contain the common factor of $f = m_e e^4 / 2\hbar^2$.

$$\Delta E_1 = \left(\frac{1}{1^2} - \frac{1}{2^2}\right) f; \quad \Delta E_{4-1} = \left(\frac{1}{1^2} - \frac{1}{4^2}\right) f;$$

$$\Delta E_2 = \left(\frac{1}{2^2} - \frac{1}{3^2}\right) f; \quad \Delta E_{5-2} = \left(\frac{1}{2^2} - \frac{1}{5^2}\right) f; \quad \Delta E_{6-2} = \left(\frac{1}{2^2} - \frac{1}{6^2}\right) f;$$

$$\Delta E_3 = \left(\frac{1}{3^2} - \frac{1}{4^2}\right) f; \quad \Delta E_{6-3} = \left(\frac{1}{3^2} - \frac{1}{6^2}\right) f; \quad \Delta E_{6-1} = \left(\frac{1}{1^2} - \frac{1}{6^2}\right) f.$$

$$\Delta E_4 = \left(\frac{1}{4^2} - \frac{1}{5^2}\right) f; \quad \Delta E_{5-1} = \left(\frac{1}{1^2} - \frac{1}{5^2}\right) f;$$

$$\Delta E_5 = \left(\frac{1}{5^2} - \frac{1}{6^2}\right) f;$$

The lifetime of the excited state p is represented by a sum of

$$\frac{1}{a_{p-q}} = \Delta t_{p-q} \tag{41}$$

performed over all possible transitions from state p to states q which are lower than p (see [14]), *i.e.*

$$E_p > E_q. \tag{42}$$

In the hydrogen atom the lowest possible state q is represented by $n = 1$. This means that for $p = n = 2$ we have only one term:

$$\frac{1}{a_{2-1}} = \Delta t_{2-1} = \Delta t_1 = \frac{h}{\Delta E_1}; \tag{43}$$

for $p = n = 3$ we have two terms which are

$$\frac{1}{a_{3-2}} = \Delta t_{3-2} = \Delta t_2 = \frac{h}{\Delta E_2} \tag{44}$$

and

$$\frac{1}{a_{3-1}} = \Delta t_{3-1} = \Delta t_1 + \Delta t_2 = \frac{h}{\Delta E_1} + \frac{h}{\Delta E_2}; \tag{45}$$

for $p = n = 4$ we have three transitions giving

$$\frac{1}{a_{4-3}} = \Delta t_{4-3} = \Delta t_3 = \frac{h}{\Delta E_3}, \tag{46}$$

$$\frac{1}{a_{4-2}} = \Delta t_{4-2} = \Delta t_3 + \Delta t_2 = \frac{h}{\Delta E_3} + \frac{h}{\Delta E_2}, \tag{46a}$$

$$\frac{1}{a_{4-1}} = \Delta t_{4-1} = \Delta t_3 + \Delta t_2 + \Delta t_1 = \frac{h}{\Delta E_3} + \frac{h}{\Delta E_2} + \frac{h}{\Delta E_1}, \tag{46b}$$

etc. In the last steps of (46)-(46b) we applied the partition of the transition times into their component intervals similar to those applied in Section 3.

In general the lifetime of state p is

$$T_p^{\text{life}} = \sum_q \frac{1}{a_{p-q}} \tag{47}$$

where q are the states lower than p so they all satisfy (42). Next any reciprocal value of a_{p-q} is

$$\frac{1}{a_{p-q}} = \Delta t_{p-q} = h\sum_{i=q}^{i=p-q}\frac{1}{\Delta E_i}. \tag{48}$$

We have found before [6] [7] that the intervals ΔE_n and Δt_n satisfy the equation

$$\Delta t_n \Delta E_n = h \tag{49}$$

where for large n the formula

$$\Delta t_n = T_n = \frac{2\pi\hbar^3 n^3}{me^4} \tag{50}$$

is fulfilled with a good accuracy: the T_n is the time period of the electron circulation about the nucleus of the hydrogen atom. Roughly the Formula (50) can be applied also for small n. In this way we obtain the lifetime

$$T_2^{\text{life}} \cong T_1 = \frac{2\pi\hbar^3}{me^4} \approx 10^{-16} \text{ sec.} \tag{51}$$

for the level $p = n = 2$. The lifetime for the level $p = n = 3$ which is a sum of (44) and (45) becomes

$$T_3^{\text{life}} \cong T_1 + 2T_2 = \left(1^3 + 2\times 2^3\right)\frac{2\pi\hbar^3}{me^4}; \tag{52}$$

the lifetime for the level $p = n = 4$ is a sum of terms entering the Formulaes (46)-(48):

$$T_4^{\text{life}} \cong T_1 + 2T_2 + 3T_2 = \left(1^3 + 2\times 2^3 + 3\times 3^3\right)\frac{2\pi\hbar^3}{me^4}. \tag{53}$$

The procedure outlined above can be extended to an arbitrary n. We obtain [15]

$$T_n^{\text{life}} \approx \sum_{k=1}^{k=n-1} k^4 \frac{2\pi\hbar^3}{me^4} = \frac{1}{30}(n-1)n(2n-1)\left(3n^2-3n-1\right)\frac{2\pi\hbar^3}{me^4} \tag{54}$$

so for large n

$$T_n^{\text{life}} \approx \frac{1}{5}n^5\frac{2\pi\hbar^3}{me^4}. \tag{55}$$

Evidently the present calculations do not take into account the quantum numbers other than n.

The quantum-mechanical calculations done for the lifetimes of the excited levels in the hydrogen atom are represented in [14]. For $n \gg 1$ this formalism gives

$$T_n^{\text{life}} \sim n^{4.5}. \tag{56}$$

7. Transition Time and Emission Intensity between Energy States of the Hydrogen-Like Atom Having the Nuclear Charge Ze; $Z > 1$

In considering the transition times of electrons in the hydrogen-like atom a situation when the electron is moving in the field of the nucleus having the charge Ze where $Z > 1$ seems to be of interest. In particular the change with Z of the intervals ΔE and Δt between the nearest quantum states in the system is worth to be considered. For $Z = 1$ we demonstrated (see [6] [7]) that for such pairs of states the intervals of energy and time satisfy the relation

$$\Delta E \Delta t = h. \tag{57}$$

In fact both ΔE and Δt depend on Z. First we have that

$$\Delta E \sim Z^2 \tag{58}$$

because

$$E_n(Z) = Z^2 E_n(Z=1); \tag{59}$$

see e.g. [13]. Our aim is to calculate the dependence

$$\Delta t = \Delta t\left(Z\right). \tag{60}$$

This is an easy task if we note that the Joule-Lenz law gives

$$\frac{\Delta E}{\Delta t} = Ri^2 \tag{61}$$

where

$$R = \frac{V}{i} \cong \frac{\Delta E}{e^2} T_n \tag{62}$$

is the resistance of the current i induced by the energy transition ΔE and T_n is the time of the electron circulation involved in calculating ΔE. Since

$$i \cong \frac{e}{T_n} \tag{63}$$

equation (61) becomes approximately

$$\frac{\Delta E}{\Delta t} \approx \frac{\Delta E}{e^2} T_n \frac{e^2}{T_n^2} = \frac{\Delta E}{T_n} \tag{64}$$

so

$$\Delta t \approx T_n \tag{65}$$

holds irrespectively of the size of Z.

It is easy to show that $T_n\left(Z\right)$ in a hydrogen-like system should be

$$T_n\left(Z\right) \sim Z^{-2}; \tag{66}$$

see also [13]. For example let us note that according to the virial theorem

$$2E_{\text{kin}}^{(n)} + E_{\text{pot}}^{(n)} = 0 \tag{67}$$

we obtain

$$E_n = E_{\text{kin}}^{(n)} + E_{\text{pot}}^{(n)} = -E_{\text{kin}}^{(n)} = \frac{1}{2} E_{\text{pot}}^{(n)} \tag{68}$$

where

$$E_{\text{pot}}^{(n)} = -\frac{Ze^2}{r_n\left(Z\right)}. \tag{69}$$

Equation (59) together with (68) implies that

$$r_n\left(Z\right) = \frac{r_n\left(Z=1\right)}{Z} \tag{70}$$

which is in accordance with the well-known result; see e.g. [13]. On the other hand

$$\begin{aligned} E_{\text{kin}}^{(n)} &= \frac{m}{2} v_n^2\left(Z\right) = \frac{m}{2}\left[\frac{2\pi r_n\left(Z\right)}{T_n\left(Z\right)}\right]^2 = \frac{\left(2\pi\right)^2 r_n^2\left(Z=1\right)}{Z^2} \frac{1}{T_n^2\left(Z\right)} \frac{m}{2} \\ &= Z^2 E_{\text{kin}}^{(n)}\left(Z=1\right) = Z^2 \frac{m}{2} \frac{\left(2\pi\right)^2 r_n^2\left(Z=1\right)}{T_n^2\left(Z=1\right)}. \end{aligned} \tag{71}$$

This implies that

$$Z^4 T_n^2\left(Z\right) = T_n^2\left(Z=1\right) \tag{72}$$

or

$$T_n(Z) = Z^{-2} T_n(Z=1) \tag{73}$$

which is the result given in (66).

In effect because of (65)

$$\Delta E_n(Z)\Delta t_n(Z) \cong \Delta E_n(Z)\Delta T_n(Z) = Z^2 \Delta E_n(Z=1)\frac{1}{Z^2} T_n(Z=1) = h, \tag{74}$$

so the Formula (57) remains unchanged upon the change of *Z*.

But the result of (73) has an important consequence concerning the emission intensity which is

$$I = \frac{\Delta E}{\Delta t} \cong \frac{Z^2 \Delta E(Z=1)}{T_n(Z=1)\frac{1}{Z^2}} \cong Z^4 \frac{\Delta E(Z=1)}{\Delta t(Z=1)}, \tag{75}$$

so we obtain that the intensity of transitions in the hydrogen-like system having $Z>1$ is approximately Z^4 times larger than intensity of similar transitions obtained in the hydrogen atom having $Z=1$. An experimental verification of this result seems to be a not too difficult task.

8. Summary and Discussion

In the paper a semiclassical approach to the transition intensities between *p* and *s* quantum levels of the hydrogen atom is compared with the quantum-mechanical transition probabilities for the same pairs of levels. An evident convergence between the sets of the data calculated by the both methods is obtained.

The present method is fully a non-probabilistic one. This is so because the idea of probability became unnecessary to apply as far as we do not ask when (or why) the system is going to change. In fact we look for a definite change of the occupation of quantum states in the system and the energy connected with it. In this case there is no uncertainty, or search, in the system to obtain the interval of time necessary for transition. Formally the changes of the quanta of energy and time remain on an equal footing. A difference-especially evident in the case of the hydrogen atom-is mainly connected with the computational practice: The quanta of energy are easy to calculate (with the aid of the fundamental constants of nature taken into account), but we are unable to do the same thing with the intervals of time. In effect first the intervals of energy have to be obtained, next they serve us as a background for calculating the intervals of time.

Once the system "decides" to change its definite population into another one, the time necessary to perform the transition process is defined-together with the energy change connected with transition-by the complementary relation (3), or a superposition of (3). A single (3) is adequate for an emissive transition between two neighbouring energy levels. On the other hand, if for some (unknown) reasons, the atom "decides" to choose the energy change (emission) corresponding to a larger distance between the levels than described by a single Formula (3), the transition time should necessarily fit to this requirement. In this case the individual formulae (3) serve also to calculate the components of the whole time interval necessary for transition; see formulae (26) and (27).

Computationally this makes the semiclassical approach much more simple than the quantum-mechanical one. For example we readily obtain that the ratio of the intensities $(n+1)p-ns$ transition should be larger than the intensity of $(n+2)p-(n+1)s$ transition for any *n*. This is so because the ratio of the intensity of the first kind of transitions to the intensity of the second kind transitions is given by

$$\frac{(\Delta E_n)^2}{(\Delta E_{n+1})^2} \tag{76}$$

and we have (see **Table 3**) that

$$\Delta E_n > \Delta E_{n+1} \tag{77}$$

For a reason similar to (77) the intensity of $(n+2)p-ns$ should be larger than intensity $(n+3)p-(n+1)s$. This is so because the ratio of these intensities is given by

$$\frac{\Delta E_n \Delta E_{n+1}}{\Delta E_{n+1} \Delta E_{n+2}} = \frac{\Delta E_n}{\Delta E_{n+2}} \tag{78}$$

and we have

$$\Delta E_n > \Delta E_{n+2}. \tag{79}$$

It should be noted that when we consider space and time as elements of a common space-and-time system, the quantum theory "selects"the time variable to a treatment based on a fully different footing than it may concern the intervals in space. Because of Equation (3) the time is divided into portions, or quanta, similar to those of their energy partners ΔE .

In result a whole of the time interval between two events-which are the beginning and end of the emission-is divided into portions, or quanta, similar to those of the energy partners entering (3). In effect the time interval between two events is either elementary, *i.e.* defined by a single Δt entering one of the elementary formulae in (3), or the transition process is not elementary, *i.e.* its time interval is composed of a sum of Δt_i entering different elementary formulae in (3). A similar existence and selection of the elementary intervals defining the spatial behaviour of the electron particle seem to be yet unknown.

A simple example of an application of the Formula (30) can be given also for some cases of the ratios of the *s-p* transition intensities which have been not yet considered in the present paper. For example we have for the ratio

$$\frac{3s-2p}{4s-2p} \to \frac{\left(\Delta E_2\right)^2}{\Delta E_2 \Delta E_3} = \frac{\Delta E_2}{\Delta E_3} = \frac{\frac{1}{2^2}-\frac{1}{3^2}}{\frac{1}{3^2}-\frac{1}{4^2}} = 2.86, \tag{80}$$

wheras the quantum-mechanical ratio of transition probabilities is

$$0.63 : 0.25 = 2.52 \quad [11]\ [16]; \tag{81}$$

for the intensity ratio

$$\frac{4s-3p}{5s-3p} \to \frac{\left(\Delta E_3\right)^2}{\Delta E_3 \Delta E_4} = \frac{\Delta E_3}{\Delta E_4} = \frac{\frac{1}{3^2}-\frac{1}{4^2}}{\frac{1}{4^2}-\frac{1}{5^2}} = 2.16, \tag{82}$$

whereas the quantum-mechanical ratio of transition probabilities is

$$0.018 : 0.0085 = 2.12 \quad [11]\ [16] \tag{83}$$

and for the intensity ratio

$$\frac{5s-4p}{6s-4p} \to \frac{\left(\Delta E_4\right)^2}{\Delta E_4 \Delta E_5} = \frac{\Delta E_4}{\Delta E_5} = \frac{\frac{1}{4^2}-\frac{1}{5^2}}{\frac{1}{5^2}-\frac{1}{6^2}} = 1.84, \tag{84}$$

whereas the quantum-mechanical ratio of transition probabilities is

$$0.0065 : 0.0035 = 1.86 \quad [11]\ [16] \tag{85}$$

References

[1] Planck, M. (1910) Acht Vorlesungen ueber Theoretische Physik. S. Hirzel, Leipzig.

[2] Einstein, A. (1917) *Physikalische Zeitschrift*, **18**, 121-128.

[3] Van der Waerden, B.L. (1967) Sources of Quantum Mechanics. Dover, New York.

[4] Schiff, L.I. (1968) Quantum Mechanics. 3rd Edition, McGraw-Hill, New York.

[5] Bethe, H.A. and Jackiw, R.W. (1968) Intermediate Quantum Mechanics. 2nd Edition, Benjamin, New York.

[6] Olszewski, S. (2015) *Journal of Modern Physics*, **6**, 1277-1288. http://dx.doi.org/10.4236/jmp.2015.69133
Olszewski, S. *Quantum Matter*. (in press)

Olszewski, S. *Reviews in Theoretical Science*. (in press)

[7] Olszewski, S. (2016) *Journal of Modern Physics*, **7**, 162-174. http://dx.doi.org/10.4236/jmp.2016.71018

[8] Kuhn, H.G. (1962) Atomic Spectra. Academic Press, New York.

[9] Bohr, N. (1918) Kgl. Danske Vid. Selsk. Scr. natur-math. Afd., 8 Raekke IV.1, Part I.

[10] Kramers, H.A. and Heisenberg, W. (1925) *Zeitschrift für Physik*, **31**, 681-708. http://dx.doi.org/10.1007/BF02980624

[11] Condon, E.U. and Shortley, G.H. (1970) The Theory of Atomic Spectra. Cambridge University Press, Cambridge.

[12] Douglas Stone, A. (2013) Einstein and the Quantum. Princeton University Press, Princeton.

[13] Sommerfeld, A. (1931) Atombau und Spektrallinien. Vol. 1, 5th Edition, Vieweg, Braunschweig.

[14] Bethe, H. (1933) Quantenmechanik der Ein- and Zwei-Elektronenprobleme In: Geiger, H. and Scheel, K., Eds., *Handbuch der Physik*, Vol. 24, Part 1, Springer, Berlin, 273-560.

[15] Gradsztejn, I.S. and Ryzhik, I.M. (1963) Tables of Integrals, Sums, Series and Products. Izd. Fiziko-Matematiceskoi Literatury, Moscow. (In Russian)

[16] Ornstein, L.S. and Burger, H.C. (1930) *Zeitschrift für Physik*, **62**, 636-639.

Journal of Modern Physics, 2016, 7, 852-862
Published Online April 2016 in SciRes. http://www.scirp.org/journal/jmp
http://dx.doi.org/10.4236/jmp.2016.78077

Scientific Research Publishing

Arguing on Entropic and Enthalpic First-Order Phase Transitions in Strongly Interacting Matter

F. Wunderlich[1,2], R. Yaresko[1,2], B. Kämpfer[1,2]

[1]Helmholtz-Zentrum Dresden-Rossendorf, Institut für Strahlenphysik, Dresden, Germany
[2]Institut für Theoretische Physik, TU Dresden, Dresden, Germany
Email: f.wunderlich@hzdr.de, b.kaempfer@hzdr.de

Received 10 March 2016; accepted 26 April 2016; published 29 April 2016

Abstract

The pattern of isentropes in the vicinity of a first-order phase transition is proposed as a key for a sub-classification. While the confinement-deconfinement transition, conjectured to set in beyond a critical end point in the QCD phase diagram, is often related to an entropic transition and the apparently settled gas-liquid transition in nuclear matter is an enthalphic transition, the conceivable local isentropes w.r.t. "incoming" or "outgoing" serve as another useful guide for discussing possible implications, both in the presumed hydrodynamical expansion stage of heavy-ion collisions and the core-collapse of supernova explosions. Examples, such as the quark-meson model and two-phase models, are shown to distinguish concisely the different transitions.

Keywords

Entropic and Enthalpic Phase Transitions, Chiral Phase Transition, Isentropes, Quark-Meson Model, Linear Sigma Model with Linearized Fluctuations

1. Introduction

The beam energy scan at RHIC [1]-[7] is aimed at searching for a critical end point (CEP) in the phase diagram of strongly interacting matter, which is related to confinement-deconfinement effects. At a CEP [8]-[11], a line of first-order phase transitions (FOPT) is conjectured to set in. Still, the hypothetical CEP could not (yet) be localized by ab initio QCD calculations. Therefore, details of the FOPT curve and details of the equation of state in its vicinity are unsettled to a large extent.

The utmost importance of the search for a CEP is also manifested by the fact that further ongoing relativistic

How to cite this paper: Wunderlich, F., Yaresko, R. and Kämpfer, B. (2016) Arguing on Entropic and Enthalpic First-Order Phase Transitions in Strongly Interacting Matter. *Journal of Modern Physics*, **7**, 852-862.
http://dx.doi.org/10.4236/jmp.2016.78077

heavy-ion collision experiments, such as NA61/SHINE [12]-[15], have it on the their priority list, and planned experiments at FAIR, e.g. CBM [16], at NICA, e.g. by the MPD group [17], and at J-PARC, e.g. by the J-PARC heavy-ion collaboration [18], are primarily motivated by it. The proceedings of the CPOD conferences [19] [20] document well the theoretical expectations and experimental achievements in this field.

The CEP itself (which may occur also as a tricritical point [21]) is interesting, as it is expected to show up in specific fluctuation observables [22]-[27], related to critical exponents, however, also the emerging FOPT curve can give rise to interesting physics phenomena. If the hypothetical FOPT curve continues to small or even zero temperatures, astrophysical consequences for neutron stars [28]-[41] proto-neutron star formation and core-collapse supernova explosions [33] [36] [42]-[44] are directly related to the physics of heavy-ion collisions, supposed the FOPT curve is accessible in such experiments (cf. [45] for searches for two-phase mixture effects related to the deconfinement FOPT).

From the theory side, the famous Columbia plot (cf. [21] for an update) unravels the following qualitative features: (i) At zero chemical potential, three-flavor QCD in the chiral limit displays a first-order confinement-deconfinement transition which extends to non-zero strange-quark masses $m_s < m_s^{\mathrm{tri}}$ and light-quark masses $m_{u,d} \to 0$; the delineation curve to the region $m_{u,d,s} > 0$ is related to a 2nd order transition with $Z(2)$ symmetry, beyond which the transition turns into a cross over; for $m_s > m_s^{\mathrm{tri}}$ and $m_{u,d} \to 0$, the 2nd order transition line is related to $O(4)$ symmetry. The physical point $m_{u,d,s} > 0$ is in the cross over region. (ii) For $m_s > m_s^{\mathrm{tri}}$ and $m_{u,d} \to 0$, the phase structure in the temperature-chemical potential plane is determined by a 2nd order transition curve of presumably negative slope (with the above mentioned universal $O(4)$ scaling properties) which ends in a tri-critical point, where the 1st order transition sets in, expected to continue to zero temperature. (iii) Upon enlarging $m_{u,d}$ toward the physical values and keeping the conjectured $m_s > m_s^{\mathrm{tri}} > 0$, the 2nd oder transition curve turns into the pseudo-critical (cross over) curve which ends at non-zero chemical potential in a CEP. The latter one can be thought to arise from the previous tri-critical point along a 2nd order $Z(2)$ curve when enlarging $m_{u,d}$. Therefore, the expectation for 2 + 1 flavor QCD with physical quark masses is the existence of a CEP at a temperature below the pseudo-critical temperature of (154 ± 9) MeV and non-zero chemical potential and an emerging 1st oder transition curve going to zero temperature [21]. Present day lattice QCD evaluations attempt to quantify these features, cf. [46], for example.

In a recent series of papers [47]-[49], the authors promote a useful sub-classification of FOPTs by attributing the confinement-deconfinement transition to an entropic one, while the established gas-liquid transition in nuclear matter [8]-[11] is classified as enthalpic one. The key is the Clausius-Clapeyron equation

$$\frac{\mathrm{d}p_c(T)}{\mathrm{d}T} = \frac{s_1/n_1 - s_2/n_2}{1/n_1 - 1/n_2} \tag{1}$$

which relates the slope of the critical pressure, p_c, along the FOPT w.r.t. temperature, T, to entropy densities $s_{1,2}$ and baryon densities $n_{1,2}$. Denoting by the label "1" the dilute (confined/hadron) phase and by "2" the dense (deconfined/quark-gluon) phase, the slope of the critical pressure curve is positive, $\mathrm{d}p_c/\mathrm{d}T > 0$, for larger entropy per baryon in phase "1", meaning an enthalpic FOPT. In contrast, for larger entropy per baryon in phase "2" the critical curve has a negative slope, $\mathrm{d}p_c/\mathrm{d}T < 0$ meaning an entropic FOPT.

Some guidance for the trajectories of fluid elements is given by the isentropic curves, determined by $s/n = \mathrm{const}$, when having in mind the adiabatic expansion of matter created in the course of a heavy-ion collision as long as the respective fluid element is in a pure phase, "2" or "1". The details of the transit through the two-phase coexistence region depend on the latent heat and other details of the equation of state. With respect to investigations of the heavy-ion dynamics (cf. [50]) seeking for imprints of the conjectured QCD FOPT and CEP signatures, it seems tempting to clarify in a clear-cut picture the different patterns of isentropes being related to a FOPT.

Our note is organized as follows. In Section 2 we discuss obvious types of isentropic patterns which may accompany a FOPT in strongly interacting matter. The pattern classification is put in relation to the entropic and enthalpic sub-classes. We see enthalpic transitions either with incoming-only or incoming + outgoing isentropes, thus qualifying also the latter one for modeling the QCD deconfinement-confinement transition. Examples based on transparent models are presented in Section 3 and **Appendix**. In Section 4, we summarize.

2. Isentropic Patterns

We restrict our discussion to the grand canonical description of matter by an equation of state $p(T,\mu)$ with one conserved charge, e.g. baryon number, related to the chemical potential μ. Entropy density and baryon density are given by $s(T,\mu)=\partial p/\partial T$ and $n(T,\mu)=\partial p/\partial\mu$ and the Gibbs-Duhem relation $e+p=sT+n\mu$ holds (e is the energy density). Considering the region $s>0$ and $n>0$, the isobars $p=\text{const}$ have negative slopes in the T-μ diagram upon $\mathrm{d}T/\mathrm{d}\mu\big|_{\mathrm{d}p=0}=-n/s$. We assume locally a FOPT which is signaled by a kinky behavior of $p(T,u)$ over the T-μ plane, both in T and μ directions. $p(T,\mu)$ refers here to stable states; if multi-valued regions emerge, the branch with maximum pressure is the stable one. We further assume, for the sake of definiteness, the FOPT curve has a negative slope, $\mathrm{d}T_c(\mu)/\mathrm{d}\mu<0$. In fact, $\mathrm{d}\big(p_1(T,\mu)-p_2(T,\mu)\big)=0$ on the FOPT curve delivers $\mathrm{d}T_c/\mathrm{d}\mu=-(n_1-n_2)/(s_1-s_2)$, where we suppose $n_1<n_2$ and $s_1<s_2$.

We also recall from the equilibrium conditions $T_1=T_2$, $\mu_1=\mu_2$ and $p_1=p_2$ on the FOPT curve the relation

$$\frac{\mathrm{d}p_c(\mu)}{\mathrm{d}\mu}=\frac{n_1/s_1-n_2/s_2}{1/s_1-1/s_2} \tag{2}$$

which is another form of the Clausius-Clapeyron Equation (1).

From selected examples we can infer three different patterns of isentropes in the T-μ plane:

Type IA: Isentropes come in from the phase "2", enter the critical curve $T_c(\mu)$ and leave it toward the phase "1" at *lower* temperature, see **Figure 1**, left top panel. According to Clausius-Clapeyron (1) one has $\mathrm{d}p_c(T)/\mathrm{d}T>0$, *i.e.* a gas-liquid or enthalpic transition in the nomenclature of [49].

Type IB: Isentropes come in from the phase "2", enter the critical curve $T_c(\mu)$ and evolve toward phase "1" at *higher* temperature, see **Figure 1** middle top panel. Clausius-Clapeyron tells us for that case $\mathrm{d}p_c(T)/\mathrm{d}T<0$, *i.e.* a QCD type or entropic FOPT in the nomenclature of [49].

Type II: Isentropes come in from both sides, *i.e.* phases "1" and "2", enter the critical curve $T_c(\mu)$ and run down on it, see **Figure 1**, right top panel. According to our experience with a number of models, $s_2/n_2<s_1/n_1$ in a point on the critical curve, *i.e.* also a gas-liquid type or enthalpic FOPT with $\mathrm{d}p_c(T)/\mathrm{d}T>0$.

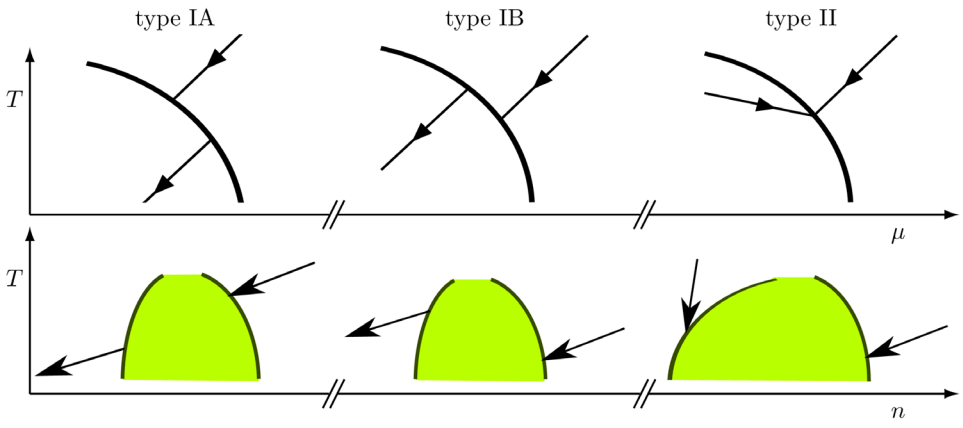

Figure 1. Schematic representation of isentropes (lines with arrows indicating the expansion path) for the FOPT types IA (left panels, $s/n=\text{const}$), IB (middle panels, $s/n=\text{const}$) and II (right panels, $s_1/n_1>s_2/n_2$) in the T-μ plane (upper row) and the T-n plane (lower row). States in "1" (see text) are left/below the phase border line (fat curves in the upper row), while states in "2" are right/above. The green areas in the lower row depict a part of the two-phase coexistence regions for the respective types. Note that the coexistence regions (green areas) can appear in quite different shapes.

The direction of isentropes is such to describe expansion, *i.e.* both temperature and density drop in pure phases. Type I is related to in-out (or going-through) isentropes, while type II has incoming-only. A prominent example for type II is the van der Waals equation of state, cf. [51] and Figure 1 in [52]. We emphasize the local character of our consideration, that is the restriction to the vicinity of a T-μ point on the presumed phase boundary. These patterns translate directly into the T-n plane, see bottom row of **Figure 1**, where one verifies that dropping temperatures along isentropes in pure phases imply in fact dropping densities, too, *i.e.* proper expansion. Types IA and IB are delineated by $s_1/n_1 = s_2/n_2$, resulting in $p_c(T) = \text{const}$. Types IA and II share as common feature flatter isobars than the critical curve $T_c(\mu)$; for type IB, the critical curve is flatter than the isobars. For the moment being we do not see the need to study further fine details, e.g. slopes and relative slopes of isentropes near the critical curve.

We would like to emphasize that also models of type IA could serve as an illustration of the possible structure of the phase diagram, despite they belong to the gas-liquid transition type: Suppose $n_1^c(T \to 0) > n_0$, where n_0 is the nuclear saturation density and n_1^c denotes the density of phase "1" at the critical curve, then nothing seems to speak against the scenario with an expanding and cooling fluid element initially in phase "2", which traverses the confinement transition region (two-phase coexistence) and arrives in the hadronic world of phase "1". That means, if "2" is a deconfined state, then both IA and IB allow for a graceful exit into the pure (hadronic) phase "1", while II ends locally in a two-phase mixture of "1 + 2" for adiabatic expansion dynamics, *i.e.* some part of matter remains in the deconfined state "2", e.g. as quark nuggets, contrary to our present expectations and in agreement with the failure of previous searches for them [53]-[57], (see however [58] [59] for considering them as candidates of dark matter). Whether realistic models can be designed to do so (cf. [60] for a recent attempt), in agreement with serving for two-solar mass neutron stars, is a question beyond the schematic phenomenological approaches. Anyhow, type IA supplements the considerations favored in [48] [49].

3. Examples

We are going to present a few examples for the above discussed transition types. For that, we select the quark-meson model[1] (cf. [63] for a description of the setting used here[2]) with linearized meson field fluctuations[3] and show that only shifting the nucleon/quark vacuum mass parameter m_q relative to the critical chemical potential at zero temperature μ_c^0 is sufficient to switch from IA to II. The latter one is to a large extent determined by the product of the sigma mass parameter m_σ and the (classical) vacuum expectation value of the sigma field $\langle\sigma\rangle_0$. We are fully aware of the shortcomings of such a model w.r.t. proper account of nuclear matter properties at low temperatures and QCD thermodynamics at high temperatures, as discussed in [48]. But in view of the pertinent complexity of the QCD degrees of freedom in the strong coupling regime such a model with chiral symmetry breaking and restoration may give some glimpses of what is conceivable, in principle.

Also our model for the type IB (cf. **Appendix**) has, at best, illustrative character: It is a two-phase construction with states in "2" modeled by the extrapolation of weakly interacting quarks and gluons, supplemented by an effective bag constant to account for some non-perturbative aspects, and states in "1" referring to thermal light-meson (pion) excitations and nucleons in some mean field approximation including a realistic incompressibility modulus.

Figure 2 exhibits the isobars $p = \text{const}$ over the T-μ plane for two parameter sets (see figure caption for the values) of the quark-meson model in linearized fluctuations approximation [63] [65]-[67]. These patterns look fairly similar at a first glance. The isobars are flatter than the phase border line (fat white curve). The CEP

[1]We chose this since in the chiral limit it obeys the same symmetries (an $O(4) \simeq SU(2) \times SU(2)$ [61]) as QCD [62] putting both into the same universality class and thus rendering the model a good prototype for studying the properties of the QCD chiral transition.

[2]In a nutshell, the employed model, also coined linear sigma model, is based on a doublett of quark degrees of freedom, an iso-scalar sigma field and an iso-triplett pion field with standard coupling among these fields.

[3]According to our experience with numerical evaluations, the account of linearized meson field fluctuations modifies significantly the results of the mean field approximation. (For the inclusion of the complete fluctuations spectrum within the functional renormalization group approach, see [64].) In particular, the fluctuating meson degrees of freedom deliver explicit contributions to the pressure.

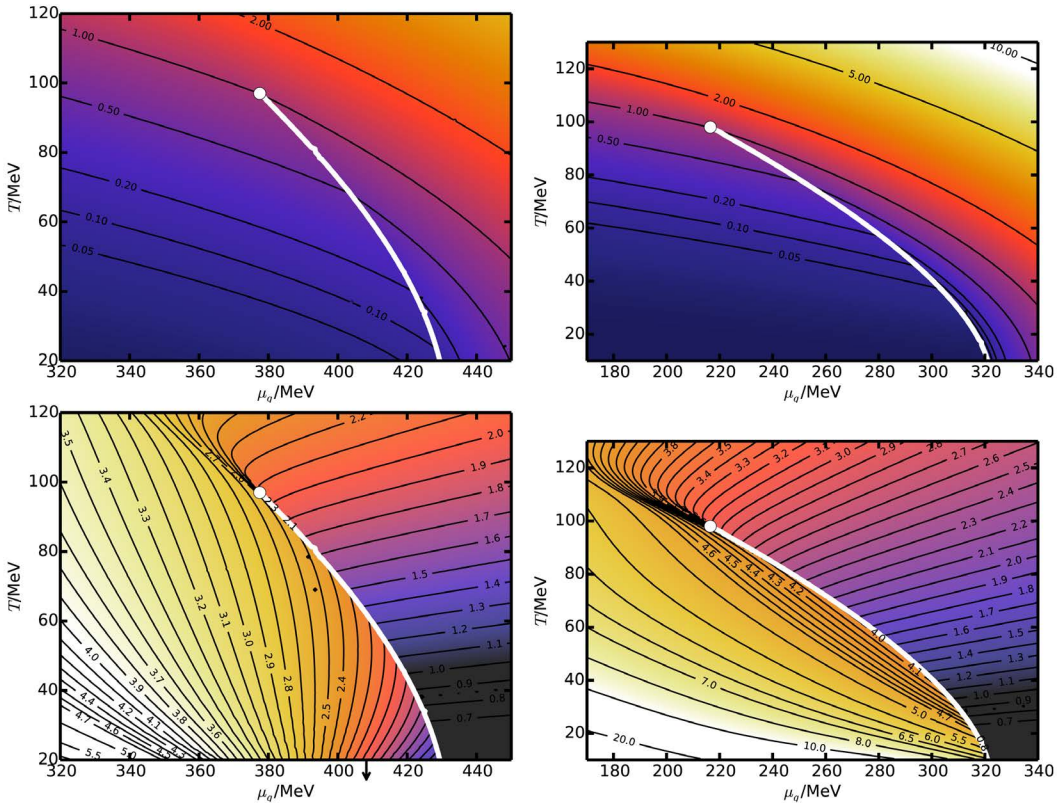

Figure 2. Contour plots of scaled pressure p/p_{CEP} (*i.e.* isobars, top row) and entropy per baryon s/n (*i.e.* isentropes, bottom row) for FOPTs of type IA (left column) and type II (right column) over the T-μ plane. Equation of state from the quark-meson model with linearized fluctuations applying the parameters $\langle\sigma\rangle_0 = 90$ MeV (expectation value of the sigma field in vacuum, as indicated by the label 0), $m_{\pi,0} = 138$ MeV (pion mass) as well as either $m_{\sigma,0} = 1284.4$ MeV (sigma mass), $m_{q,0} = 390$ MeV (quark mass) (left column) or $m_{\sigma,0} = 700$ MeV, $m_{q,0} = 360$ MeV (right column). The pressure is scaled by the pressure at the critical end point, *i.e.* with $p_{CEP} = 2.38\times10^8$ MeV^4 (left) and $p_{CEP} = 8.59\times10^8$ MeV^4 (right), respectively. The arrow in the bottom left plot points to a state where the density at $T = 0$ is equal to $n_0 = 0.17$ fm^{-3}. On the bottom right plot this point is located at the phase boundary.

coordinates are $(T_{CEP}, \mu_{CEP}) = (\mathcal{O}(97\text{ MeV}), \mathcal{O}(377.5\text{ MeV}))$ for the parameter set depicted on the left panels and $(\mathcal{O}(98\text{ MeV}), \mathcal{O}(216.5\text{ MeV}))$ on the right ones. (Note that we use actually quark chemical potential μ_q and net quark density n_q.) One must not consider these values as predictions of the CEP location since the proper account of fluctuations can significantly change them. Furthermore, the inclusion of some gluon dynamics, e.g. via a coupling to the Polyakov loop, thermal gluon fluctuations as well as extending the invoked hadron species can also cause substantial changes of the CEP coordinates.

Despite of the apparently marginal differences of the isobar patterns, the isentropes are drastically different. In the left bottom panel of **Figure 2**, type IA isentropes are seen which mean incoming from phase "2" and outgoing into phase "1" whenever they meet the critical curve. In contrast, the right bottom panel in **Figure 2** displays a type II FOPT with incoming-only isentropes into the critical curve.

Figure 3 exhibits the isentropes in pure phases "2" and "1" over the T-n plane. This presentation verifies that both the temperature and the density drop along the isentropes in pure phases. One can infer directly from the bottom panels of **Figure 2** the above claim w.r.t. outgoing isentropes from the low-density phase border curve $n_1(T)$ for type IA, see left panel of **Figure 3**, while for type II (right panel) only incoming isentropes appear (isentropes with $s/n > 5$ enter the two-phase region at smaller densities which are not displayed).

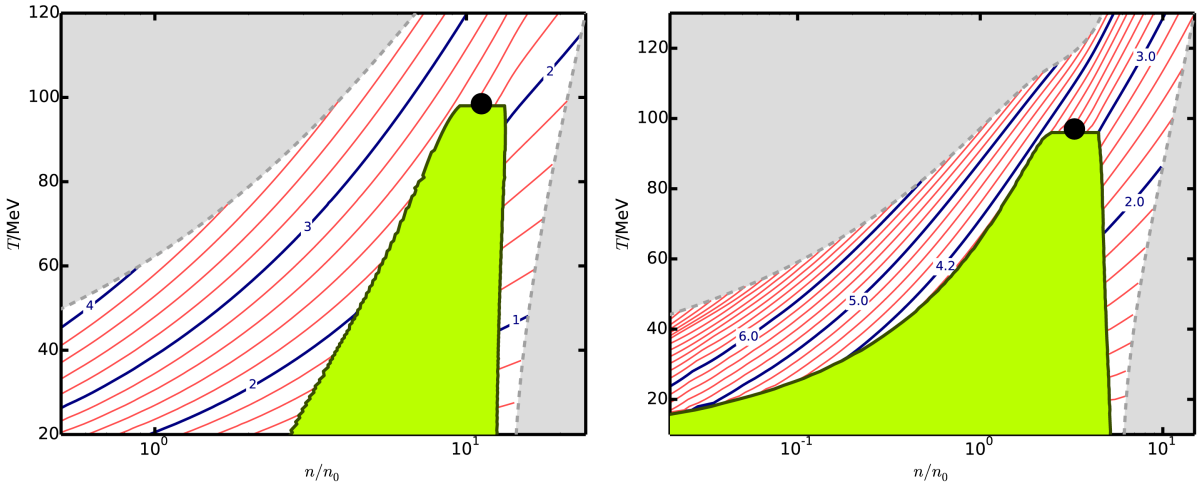

Figure 3. As **Figure 2** but for the isentropes in the *T*-*n* plane for pure phases only. The difference in *s*/*n* between two adjacent isentropes is 0.2 and the thick blue isentropes are labeled with their respective *s*/*n*. The two-phase coexistence regions are depicted as green areas with the CEP (black bullet) on top. The dashed grey curves enclose the regions in *T*-μ space displayed in **Figure 2**, *i.e.* the gray regions correspond to regions outside. The densities are scaled by the nuclear saturation density $n_0 = 0.17\ \mathrm{fm}^{-3}$.

Consistent to the Clausius-Clapeyron Equation (1), the critical pressure as a function of the temperature is increasing, see **Figure 4**. The inclined numbers at the top axis depict the (critical) chemical potential values corresponding to the temperature given at the lower axis thus highlighting the shape of $p_c(\mu)$ which is actually decreasing in agreement with (2).

We mention that the employed minimum set-up of the quark-meson model does not allow for type IB transitions since thermal gluon fluctuations are not included, *i.e.* the number of effective degrees of freedom accounting for thermal fluctuations is too small. One may, however, easily construct two-phase models with a high-temperature quark-gluon phase and a low-temperature hadron phase. **Figure 5** in the **Appendix** presents such an example. Without fine tuning, such models do not display a CEP at $\mu > 0$, instead the constructed phase border curve continues form the *T* axis down to the μ axis. Reference [68] provides an example of enforcing a CEP at $\mu > 0$ to obtain also a type IB transition.

The focus of the present note is on the isentropes relevant for the expansion dynamics in relativistic heavy-ion collisions. As emphasized, e.g. in [40] and references therein, analog considerations are useful for discussing the impact of peculiarities of the QCD phase diagram in core-collapse supernova explosions. There, one has to consider adiabatic paths along compression with proper leptonic contributions including also trapped neutrinos. For a first orientation, the pressure as a function of the energy density at suitable values of the entropy per baryon is to be analyzed to figure out whether the FOPT effects in iso-spin symmetric matter translate into modifications of neutron star configurations (with β stability, no trapped neutrinos) such as the occurrence of a third stable island (cf. [28]), nowadays often refered to as twin configurations [29]-[31] [37] [69]-[74], or modify the core collapse dynamics (with trapped neutrinos) toward proto-neutron stars or even black holes such as discussed in [40] [42] and references therein. We leave according investigations to separate dedicated analyses.

4. Conclusions and Summary

In summary we discuss options for modeling a hypothetical first-order phase transition which is related to a critical end point in a strongly interacting medium. Guided by the expectation that the QCD cross-over (as remnant of the transition of massless 2 + 1 flavor QCD, cf. [21]) at a temperature of about 150 MeV at small chemical potential turns, at the critical point at large chemical potential, into a first-order transition we consider scenarios where initially deconfined matter can evolve completely into confined (hadronic) matter. We emphasize that both enthalpic and entropic phase transitions are consistent with such an expectation provided a

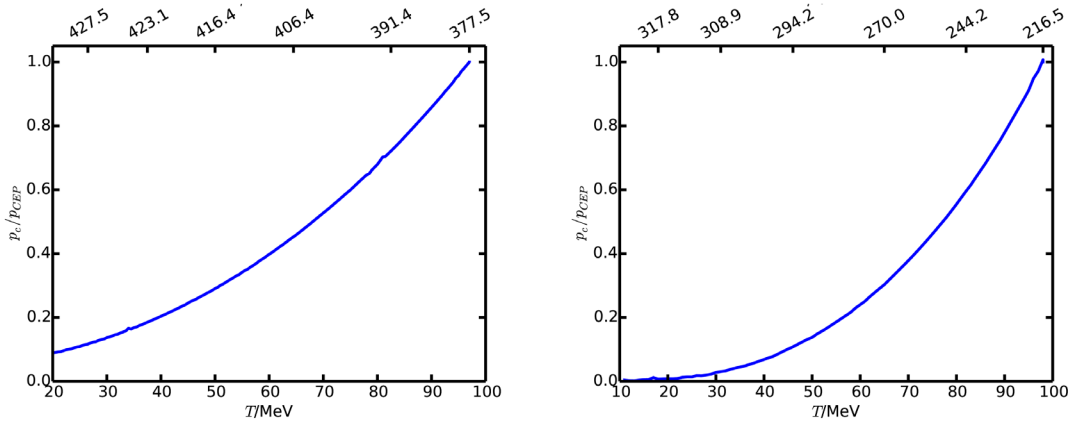

Figure 4. The critical pressure $p_c(T)$ as a function of temperature for FOPTs of type IA (left panel) and II (right panel). The numbers on the upper axis are the critical chemical potentials (in MeV) corresponding to the temperatures on the lower axis. Equation of state and critical pressures p_{CEP} as described in the caption of **Figure 2**.

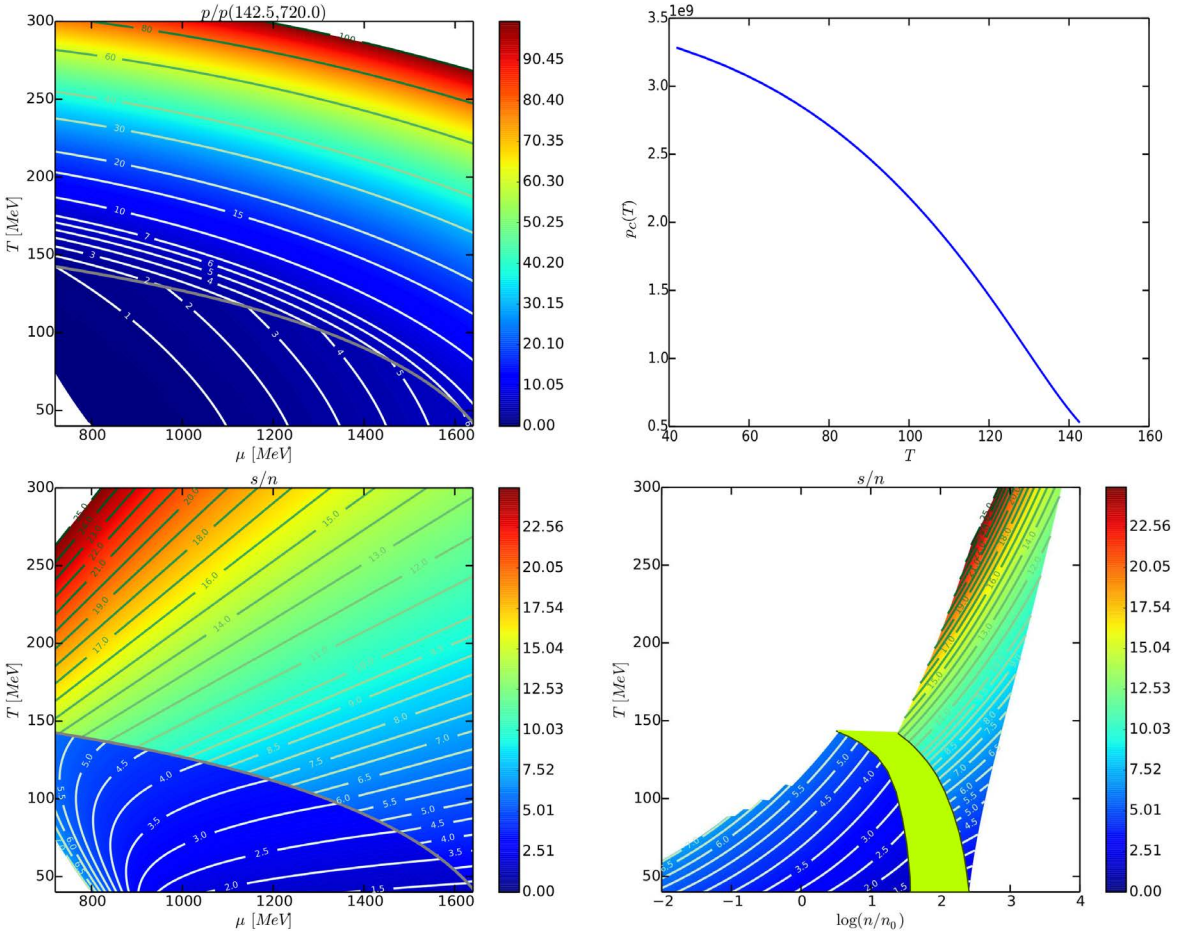

Figure 5. Isobars (left top panel) and the critical pressure p_c as a function of temperature (right top panel) as well as isentropes, both over the T-μ plane (left bottom) and over the T-n plane (right bottom) for the two-phase model of type IB FOPT, based on Equations (3-7). As in **Figure 3**, the coexistence region is depicted as green area. Our calculations do not map out completely the T-μ plane, thus leaving some uncharted regions in white in the left column and the bottom right panel.

graceful exit from the deconfined state into pure hadron matter is possible upon adiabatic expansion. At low temperature, the low density part of the two-phase coexistence region must be at larger densities than nuclear matter at saturation (for isospin symmetric nuclear matter). This implies that the pattern of isentropes must "go through" the phase border curve to be conform with the envisaged scenario. In contrast, the van der Waals type transition is of a different kind as it has locally incoming isentropes only. Obviously, more complicated phase border curves may allow for mixtures of the mentioned types. Our discussion also completely ignores flavor-locked color superconducting phases which are expected at larger densities.

Our discussion is based on equilibrium thermodynamics, and the medium is assumed to obey one conserved charge—the baryon density. Accounting for more conserved charges, e.g. related to isospin, strangeness, electric charge etc., complicates the picture. Transient states related to under saturated or over saturated gluons [75] or under saturated quark state occupation [76] give rise to many interesting phenomena beyond our discussion.

The lacking of ab intio information from first-principle calculations of QCD thermodynamics lets many options still be conceivable. This makes the concerted experimental hunt for signals of the critical end point and the related first-order transition so important.

Acknowledgements

We thank J. Randrup, V. Koch, F. Karsch, K. Redlich, M.I. Gorenstein, S. Schramm, H. Stöcker and B. Friman for enlightening discussions of phase transitions in nuclear matter. The work is supported by BMBF grant 05P12CRGH.

References

[1] Adare A., *et al.* (2012) *Physical Review Letters*, **109**, Article ID: 152301. http://dx.doi.org/10.1103/PhysRevLett.109.152301

[2] Adare A., *et al.* (2012) *Physical Review C*, **86**, Article ID: 064901. http://dx.doi.org/10.1103/PhysRevC.86.064901

[3] Adamczyk, L., *et al.* (2013) *Physical Review C*, **88**, Article ID: 014902. http://dx.doi.org/10.1103/PhysRevC.88.014902

[4] Adamczyk, L., *et al.* (2014) *Physical Review Letters*, **113**, Article ID: 052302. http://dx.doi.org/10.1103/PhysRevLett.113.052302

[5] Soltz, R.A. (2014) *Nuclear Physics A*, **931**, 780. http://dx.doi.org/10.1016/j.nuclphysa.2014.08.050

[6] Das, S. (2015) *EPJ Web of Conferences*, **90**, Article ID: 10003.

[7] McDonald, D. (2015) *EPJ Web of Conferences*, **95**, Article ID: 01009.

[8] Rischke, D.H. (2004) *Progress in Particle and Nuclear Physics*, **52**, 197. http://dx.doi.org/10.1016/j.ppnp.2003.09.002

[9] Stephanov, M.A. (2004) *Progress of Theoretical Physics Supplements*, **153**, 139. http://dx.doi.org/10.1143/PTPS.153.139

[10] Fukushima, K. and Hatsuda, T. (2011) *Reports on Progress in Physics*, **74**, Article ID: 014001. http://dx.doi.org/10.1088/0034-4885/74/1/014001

[11] Friman, B., *et al.* (2011) *Lecture Notes in Physics*, **814**, 1.

[12] Gazdzicki, M. (2008) *The European Physical Journal Special Topics*, **155**, 37-44. http://dx.doi.org/10.1140/epjst/e2008-00587-0

[13] Czopowicz, T. (2015) arXiv:1503.01619 [nucl-ex]

[14] Aduszkiewicz, A., *et al.* (2015) arXiv:1510.00163 [hep-ex]

[15] Mackowiak-Pawlowska, M. (2016) arXiv:1602.03682 [nucl-ex]

[16] Chattopadhyay, S. (2014) *Nuclear Physics A*, **931**, 267-276. http://dx.doi.org/10.1016/j.nuclphysa.2014.09.099

[17] Kekelidze, V., *et al.* (2015) *EPJ Web of Conferences*, **95**, Article ID: 01014. http://dx.doi.org/10.1051/epjconf/20159501014

[18] Sako, H. (2015) *JPS Conference Proceedings*, **8**, Article ID: 022010.

[19] (2013) *Proceedings of the* 8*th International Workshop on Critical Point and Onset of Deconfinement* (*CPOD* 2013), Napa, 1-15 March 12013.

[20] (2015) *Proceedings of the* 9*th International Workshop on Critical Point and Onset of Deconfinement* (*CPOD* 2014), Bielefeld, 17-21 November 2014.

[21] Ding, H.-T., Karsch, F. and Mukherjee, S. (2015) *International Journal of Modern Physics E*, **24**, Article ID: 1530007. http://dx.doi.org/10.1142/S0218301315300076

[22] Stephanov, M.A., Rajagopal, K. and Shuryak, E.V. (1999) *Physical Review D*, **60**, Article ID: 114028. http://dx.doi.org/10.1103/PhysRevD.60.114028

[23] Gupta, S. (2009) Finding the Critical End Point of QCD: Lattice and Experiment. 5*th International Workshop on Critical Point and Onset of Deconfinement*, Long Island, 8-12 June 2009, 025.

[24] Mohanty, B. (2009) *Nuclear Physics A*, **830**, 899C-907C. http://dx.doi.org/10.1016/j.nuclphysa.2009.10.132

[25] Adamczyk, L., *et al.* (2014) *Physical Review Letters*, **112**, Article ID: 032302. http://dx.doi.org/10.1103/PhysRevLett.112.032302

[26] Adamczyk, L., *et al.* (2014) *Physical Review Letters*, **113**, Article ID: 092301. http://dx.doi.org/10.1103/PhysRevLett.113.092301

[27] Almasi, G.A., Friman, B. and Redlich, K. (2016). arXiv:1601.00782 [hep-ph]

[28] Kämpfer, B. (1981) *Physics Letters B*, **101**, 366-368. http://dx.doi.org/10.1016/0370-2693(81)90065-4

Kämpfer, B. (1981) *Journal of Physics A*, **14**, L471. http://dx.doi.org/10.1088/0305-4470/14/11/009

Kämpfer, B. (1983) *Journal of Physics G*, **9**, 1487. http://dx.doi.org/10.1088/0305-4616/9/12/009

Kämpfer, B. (1983) *Astrophysics and Space Science*, **93**, 185-197. http://dx.doi.org/10.1007/BF02430922

Kämpfer, B. (1985) *Physics Letters B*, **153**, 121-123. http://dx.doi.org/10.1016/0370-2693(85)91410-8

[29] Schertler, K., Greiner, C., Sahu, P.K. and Thoma, M.H. (1998) *Nuclear Physics A*, **637**, 451-465. http://dx.doi.org/10.1016/S0375-9474(98)00330-3

[30] Schertler, K., Leupold, S. and Schaffner-Bielich, J. (1999) *Physical Review C*, **60**, Article ID: 025801. http://dx.doi.org/10.1103/PhysRevC.60.025801

[31] Schertler, K., Greiner, C., Schaffner-Bielich, J. and Thoma, M.H. (2000) *Nuclear Physics A*, **677**, 463-490. http://dx.doi.org/10.1016/S0375-9474(00)00305-5

[32] Macher, J. and Schaffner-Bielich, J. (2005) *European Journal of Physics*, **26**, 341. http://dx.doi.org/10.1088/0143-0807/26/3/003

[33] Dexheimer, V. and Schramm, S. (2008) *Astrophysical Journal*, **683**, 943. http://dx.doi.org/10.1086/589735

[34] Pagliara, G., Hempel, M. and Schaffner-Bielich, J. (2009) *Physical Review Letters*, **103**, Article ID: 171102. http://dx.doi.org/10.1103/PhysRevLett.103.171102

[35] Kurkela, A., Romatschke, P., Vuorinen, A. and Wu, B. (2010). arXiv:1006.4062 [astro-ph.HE]

[36] Fischer, T., *et al.* (2011) *The Astrophysical Journal Supplement Series*, **194**, 39. http://dx.doi.org/10.1088/0067-0049/194/2/39

[37] Alford, M.G., Han, S. and Prakash, M. (2013) *Physical Review D*, **88**, Article ID: 083013. http://dx.doi.org/10.1103/PhysRevD.88.083013

[38] Yasutake, N., *et al.* (2014) *Physical Review C*, **89**, Article ID: 065803. http://dx.doi.org/10.1103/PhysRevC.89.065803

[39] Zacchi, A., Stiele, R. and Schaffner-Bielich, J. (2015) *Physical Review D*, **92**, Article ID: 045022. http://dx.doi.org/10.1103/PhysRevD.92.045022

[40] Hempel, M., *et al.* (2015). arXiv:1511.06551 [nucl-th]

[41] Alvarez-Castillo, D.E. and Blaschke, D. (2015) Supporting the Existence of the QCD Critical Point by Compact Star Observations. 9*th International Workshop on Critical Point and Onset of Deconfinement*, Bielefeld, 17-21 November 2014, 045.

[42] Sagert, I., *et al.* (2009) *Physical Review Letters*, **102**, Article ID: 081101. http://dx.doi.org/10.1103/PhysRevLett.102.081101

[43] Nishimura, N., *et al.* (2012) *Astrophysical Journal*, **758**, 9. http://dx.doi.org/10.1088/0004-637X/758/1/9

[44] Pan, K.-C., Liebendrfer, M., Hempel, M. and Thielemann, F.-K. (2016) *Astrophysical Journal*, **817**, 72. http://dx.doi.org/10.3847/0004-637X/817/1/72

[45] Bugaev, K.A., *et al.* (2014). arXiv:1412.0718 [nucl-th]

[46] Bellwied, R., *et al.* (2015) *Physics Letters B*, **751**, 559-564. http://dx.doi.org/10.1016/j.physletb.2015.11.011

[47] Hempel, M., Dexheimer, V., Schramm, S. and Iosilevskiy, I. (2013) *Physical Review C*, **88**, Article ID: 014906. http://dx.doi.org/10.1103/PhysRevC.88.014906

[48] Steinheimer, J., Randrup, J. and Koch, V. (2014) *Physical Review C*, **89**, Article ID: 034901. http://dx.doi.org/10.1103/PhysRevC.89.034901

[49] Iosilevskiy, I. (2015). arXiv:1504.05850 [nucl-th]

[50] Steinheimer, J., *et al.* (2008) *Physical Review C*, **77**, Article ID: 034901. http://dx.doi.org/10.1103/PhysRevC.77.034901

[51] Johnston, D.C. (2014). arXiv:1402.1205 [cond-mat.soft]

[52] Yuen, A. and Barnard, J.J. (2015) *Physical Review E*, **92**, Article ID: 062307. http://dx.doi.org/10.1103/PhysRevE.92.062307

[53] Schaffner, J., Stoecker, H. and Greiner, C. (1991) *Nuclear Physics B-Proceedings Supplements*, **24**, 246-250. http://dx.doi.org/10.1016/0920-5632(91)90331-8

[54] Schaffner, J., Dover, C.B., Gal, A., Greiner, C. and Stoecker, H. (1993) *Physical Review Letters*, **71**, 1328. http://dx.doi.org/10.1103/PhysRevLett.71.1328

[55] Abelev, B.I., *et al.* (2007) *Physical Review C*, **76**, Article ID: 011901. http://dx.doi.org/10.1103/PhysRevC.76.011901

[56] Madsen, J. (2008) Strangelets in Cosmic Rays. 11*th Marcel Grossmann Meeting* (*MG*11), Berlin, 23-29 July 2006, 0098.

[57] Adriani, O., *et al.* (2015) *Physical Review Letters*, **115**, Article ID: 111101. http://dx.doi.org/10.1103/PhysRevLett.115.111101

[58] Gorham, P. (2012) *Physical Review D*, **86**, Article ID: 123005. http://dx.doi.org/10.1103/PhysRevD.86.123005

[59] Atreya, A., Sarkar, A. and Srivastava, A.M. (2014) *Physical Review D*, **90**, Article ID: 045010. http://dx.doi.org/10.1103/PhysRevD.90.045010

[60] Benic, S., Mishustin, I. and Sasaki, C. (2015) *Physical Review D*, **91**, Article ID: 125034. http://dx.doi.org/10.1103/PhysRevD.91.125034

[61] Tetradis, N. (2003) *Nuclear Physics A*, **726**, 93-119. http://dx.doi.org/10.1016/S0375-9474(03)01624-5

[62] Pisarski, R.D. and Wilczek, F. (1984) *Physical Review D*, **29**, 338(R). http://dx.doi.org/10.1103/PhysRevD.29.338

[63] Wunderlich, F. and Kämpfer, B. (2015) Photon Emission Rates near the Critical Point in the Linear Sigma Model. 9*th International Workshop on Critical Point and Onset of Deconfinement*, Bielefeld, 17-21 November 2014, 027.

[64] Tripolt, R.-A., Strodthoff, N., von Smekal, L. and Wambach, J. (2014) *Physical Review D*, **89**, Article ID: 034010. http://dx.doi.org/10.1103/PhysRevD.89.034010

[65] Mocsy, A., Mishustin, I. and Ellis, P. (2004) *Physical Review C*, **70**, Article ID: 015204. http://dx.doi.org/10.1103/PhysRevC.70.015204

[66] Bowman, E.S. and Kapusta, J.I. (2009) *Physical Review C*, **79**, Article ID: 015202. http://dx.doi.org/10.1103/PhysRevC.79.015202

[67] Ferroni, L., Koch, V. and Pinto, M.B. (2010) *Physical Review C*, **82**, Article ID: 055205. http://dx.doi.org/10.1103/PhysRevC.82.055205

[68] Steinheimer, J. and Randrup, J. (2012) *Physical Review Letters*, **109**, Article ID: 212301. http://dx.doi.org/10.1103/PhysRevLett.109.212301

[69] Drago, A. and Pagliara, G. (2016) *The European Physical Journal A*, **52**, 41. http://dx.doi.org/10.1140/epja/i2016-16041-2

[70] Zdunik, J.L. and Haensel, P. (2013) *Astronomy & Astrophysics*, **551**, Article No. A61. http://dx.doi.org/10.1051/0004-6361/201220697

[71] Chamel, N., Haensel, P., Zdunik, J.L. and Fantina, A.F. (2013) *International Journal of Modern Physics E*, **22**, Article ID: 1330018. http://dx.doi.org/10.1142/S021830131330018X

[72] Alvarez-Castillo, D.E. and Blaschke, D. (2015) *Physics of Particles and Nuclei*, **46**, 846-848. http://dx.doi.org/10.1134/S1063779615050032

[73] Blaschke, D., Alvarez-Castillo, D.E. and Benic, S. (2013) Astrophysics Constraints on the EOS. *8th International Workshop on Critical Point and Onset of Deconfinement*, 11-15 March 2013, Napa, 063.

[74] Benic, S., Blaschke, D., Alvarez-Castillo, D.E., Fischer, T. and Typel, S. (2015) *Astronomy & Astrophysics*, **577**, Article No. A40. http://dx.doi.org/10.1051/0004-6361/201425318

[75] Peshier, A. and Giovannoni, D. (2016) *Journal of Physics*: *Conference Series*, **668**, Article ID: 012076. http://dx.doi.org/10.1088/1742-6596/668/1/012076

[76] Stoecker, H., *et al.* (2016) *Journal of Physics G*, **43**, Article ID: 015105. http://dx.doi.org/10.1088/0954-3899/43/1/015105

[77] Buchwald, G., Csernai, L.P., Maruhn, J.A., Greiner, W. and Stocker, H. (1981) *Physical Review C*, **24**, 135. http://dx.doi.org/10.1103/PhysRevC.24.135

[78] Kurkela, A. and Vuorinen, A. (2016). arXiv:1603.00750 [hep-ph]

Appendix

A two-phase model for type IB

The constructed FOPT is based on the extrapolation of a hadron equation of state with pressure

$$p_1 = n_b^2 \left.\frac{\partial W}{\partial n_b}\right|_{\hat{s}} \tag{3}$$

to be calculated from

$$W = e/n_B = W_c + W_T \tag{4}$$

with

$$W_c = \frac{K}{18}\left(\frac{n_B - n_0}{n_B}\right)^2 + W_{\text{bind}} + m_N,$$

$$W_T = \frac{3}{2}T + \frac{\pi^2}{18}\frac{T^4}{n_B},$$

$$\hat{s} = \frac{s}{n_B} = \hat{s}_N + \hat{s}_\pi, \tag{5}$$

$$\hat{s}_N = 2.5 - \ln\left(\frac{n_B}{4}\left(\frac{2\pi}{T m_N}\right)^{3/2}\right),$$

$$\hat{s}_\pi = \frac{4}{3}\frac{\pi^2}{10}\frac{T^3}{n_B}.$$

The temperature $T(n_B, \hat{s})$ follows self consistently from

$$T = \frac{\partial W(n_B, \hat{s})}{\partial \hat{s}} \tag{6}$$

and the baryo-chemical potential is then $\mu_B = W + p/n_B - T\hat{s}$. We utilize the nucleon mass $m_N = 938\,\text{MeV}$, the nucleon binding energy $W_{\text{bind}} = -16\,\text{MeV}$, nuclear incompressibility coefficient $K = 235\,\text{MeV}$ and saturation density $n_0 = 0.17\,\text{fm}^{-3}$.[4] The equation of state in the high temperature phase is defined by the extrapolation of a quark-gluon equation of state from leading-order weak-coupling (cf. [78] for advanced calculations) supplemented by a bag constant B

$$p_2 = 16\frac{\pi^2}{90}T^4 + f_q\left(\frac{7}{8}\frac{\pi^2}{90}T^4 + \frac{1}{24}T^2\mu_B^2 + \frac{1}{48\pi^2}\mu_B^4\right) - B, \tag{7}$$

where we employ for the number of effective quark degrees of freedom $f_q = 2.5\times 3\times 2\times 2 = 30$ and $B = (235\,\text{MeV})^4$. These branches are matched by the above mentioned Gibbs criteria for equilibrium, $p_1 = p_2$, $T_1 = T_2$, $\mu_1 = \mu_2$. The resulting isobars, the critical pressure $p_c(T)$ as well as isentropes, both over the T-μ and the T-n-planes are exhibited in **Figure 5**.

[4]This is a model in the spirit of [77] for nuclear matter and pions.

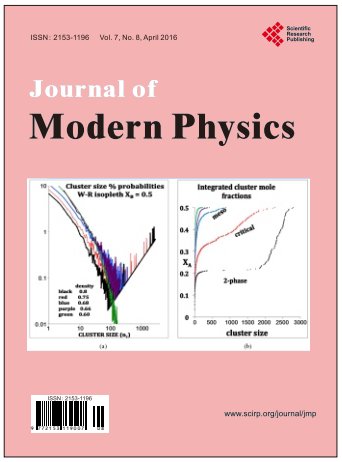

Call for Papers

Journal of Modern Physics

ISSN: 2153-1196 (Print) ISSN: 2153-120X (Online)
http://www.scirp.org/journal/jmp

Journal of Modern Physics **(JMP)** is an international journal dedicated to the latest advancement of modern physics. The goal of this journal is to provide a platform for scientists and academicians all over the world to promote, share, and discuss various new issues and developments in different areas of modern physics.

Editor-in-Chief

Prof. Yang-Hui He City University, UK

Executive Editor-in-Chief

Prof. Marko Markov Research International, Buffalo Office, USA

Subject Coverage

Journal of Modern Physics publishes original papers including but not limited to the following fields:

Biophysics and Medical Physics
Complex Systems Physics
Computational Physics
Condensed Matter Physics
Cosmology and Early Universe
Earth and Planetary Sciences
General Relativity
High Energy Astrophysics
High Energy/Accelerator Physics
Instrumentation and Measurement
Interdisciplinary Physics
Materials Sciences and Technology
Mathematical Physics
Mechanical Response of Solids and Structures
New Materials: Micro and Nano-Mechanics and Homogeneization
Non-Equilibrium Thermodynamics and Statistical Mechanics
Nuclear Science and Engineering
Optics
Physics of Nanostructures
Plasma Physics
Quantum Mechanical Developments
Quantum Theory
Relativistic Astrophysics
String Theory
Superconducting Physics
Theoretical High Energy Physics
Thermology

We are also interested in: 1) Short Reports—2-5 page papers where an author can either present an idea with theoretical background but has not yet completed the research needed for a complete paper or preliminary data; 2) Book Reviews—Comments and critiques.

Notes for Intending Authors

Submitted papers should not have been previously published nor be currently under consideration for publication elsewhere. Paper submission will be handled electronically through the website. All papers are refereed through a peer review process. For more details about the submissions, please access the website.

Website and E-Mail

http://www.scirp.org/journal/jmp **E-mail: jmp@scirp.org**

What is SCIRP?

Scientific Research Publishing (SCIRP) is one of the largest Open Access journal publishers. It is currently publishing more than 200 open access, online, peer-reviewed journals covering a wide range of academic disciplines. SCIRP serves the worldwide academic communities and contributes to the progress and application of science with its publication.

What is Open Access?

All original research papers published by SCIRP are made freely and permanently accessible online immediately upon publication. To be able to provide open access journals, SCIRP defrays operation costs from authors and subscription charges only for its printed version. Open access publishing allows an immediate, worldwide, barrier-free, open access to the full text of research papers, which is in the best interests of the scientific community.

- High visibility for maximum global exposure with open access publishing model
- Rigorous peer review of research papers
- Prompt faster publication with less cost
- Guaranteed targeted, multidisciplinary audience

Scientific Research Publishing

Website: http://www.scirp.org

Subscription: sub@scirp.org

Advertisement: service@scirp.org